A general non-stationarity measure : Application to biomedical image and signal processing

Yanli Zhang Xu

Numéro d'ordre: 2013-ISAL-0090 Année 2013

THÈSE

présentée devant

L'Institut National des Sciences Appliquées de Lyon

pour obtenir

LE GRADE DE DOCTEUR

ÉCOLE DOCTORALE: ÉLECTRONIQUE, ÉLECTROTECHNIQUE, AUTOMATIQUE
FORMATION DOCTORALE : SCIENCES DE L'INFORMATION, DES DISPOSITIFS ET DES SYSTÈMES

par

ZHANG Yanli

Une mesure de non-stationnarité générale: application en traitement d'images et de signaux biomédicaux

Soutenue le 04 Octobre 2013

Jury :

Jean-Marc CHASSERY	Directeur de Recherche CNRS	Rapporteur
Isabelle BLOCH	Professeur ENST	Rapporteur
Isabelle E. MAGNIN	Directeur de recherche INSERM	Directeur de thèse
Yue-Min ZHU	Directeur de recherche CNRS	Codirecteur de thèse
Jin LI	Professeur d'HEU	Examinateur
Ping LI	Professeur, Radiologue Hospitalier de HMU	Examinateur
Wan-Yu LIU	Professeur de HIT	Directeur de thèse

Yanli ZHANG
Thèse en traitement de l'image medicale / 2013
Institut national des sciences appliquées de Lyon

INSA Direction de la Recherche - Écoles Doctorales – Quinquennal 2011-2015

SIGLE	ECOLE DOCTORALE	NOM ET COORDONNEES DU RESPONSABLE
CHIMIE	**CHIMIE DE LYON** **http://www.edchimie-lyon.fr** Insa : R. GOURDON	M. Jean Marc LANCELIN Université de Lyon – Collège Doctoral Bât ESCPE 43 bd du 11 novembre 1918 69622 VILLEURBANNE Cedex Tél : 04.72.43 13 95 directeur@edchimie-lyon.fr
E.E.A.	**ELECTRONIQUE, ELECTROTECHNIQUE, AUTOMATIQUE** **http://edeea.ec-lyon.fr** Secrétariat : M.C. HAVGOUDOUKIAN eea@ec-lyon.fr	M. Gérard SCORLETTI Ecole Centrale de Lyon 36 avenue Guy de Collongue 69134 ECULLY Tél : 04.72.18 60 97 Fax : 04 78 43 37 17 Gerard.scorletti@ec-lyon.fr
E2M2	**EVOLUTION, ECOSYSTEME, MICROBIOLOGIE, MODELISATION** **http://e2m2.universite-lyon.fr** Insa : H. CHARLES	Mme Gudrun BORNETTE CNRS UMR 5023 LEHNA Université Claude Bernard Lyon 1 Bât Forel 43 bd du 11 novembre 1918 69622 VILLEURBANNE Cédex Tél : 04.72.43.12.94 e2m2@biomserv.univ-lyon1.fr
EDISS	**INTERDISCIPLINAIRE SCIENCES-SANTE** **http://ww2.ibcp.fr/ediss** Sec : Safia AIT CHALAL Insa : M. LAGARDE	M. Didier REVEL Hôpital Louis Pradel Bâtiment Central 28 Avenue Doyen Lépine 69677 BRON Tél : 04.72.68 49 09 Fax : 04 72 35 49 16 Didier.revel@creatis.uni-lyon1.fr
INFOMATHS	**INFORMATIQUE ET MATHEMATIQUES** **http://infomaths.univ-lyon1.fr**	M. Johannes KELLENDONK Université Claude Bernard Lyon 1 INFOMATHS Bâtiment Braconnier 43 bd du 11 novembre 1918 69622 VILLEURBANNE Cedex Tél : 04.72. 44.82.94 Fax 04 72 43 16 87 infomaths@univ-lyon1.fr
Matériaux	**MATERIAUX DE LYON** Secrétariat : M. LABOUNE PM : 71.70 –Fax : 87.12 Bat. Saint Exupéry **Ed.materiaux@insa-lyon.fr**	M. Jean-Yves BUFFIERE INSA de Lyon MATEIS Bâtiment Saint Exupéry 7 avenue Jean Capelle 69621 VILLEURBANNE Cédex Tél : 04.72.43 83 18 Fax 04 72 43 85 28 Jean-yves.buffiere@insa-lyon.fr
MEGA	**MECANIQUE, ENERGETIQUE, GENIE CIVIL, ACOUSTIQUE** Secrétariat : M. LABOUNE PM : 71.70 –Fax : 87.12 Bat. Saint Exupéry **mega@insa-lyon.fr**	M. Philippe BOISSE INSA de Lyon Laboratoire LAMCOS Bâtiment Jacquard 25 bis avenue Jean Capelle 69621 VILLEURBANNE Cedex Tél :04.72.43.71.70 Fax : 04 72 43 72 37 Philippe.boisse@insa-lyon.fr
ScSo	**ScSo*** M. OBADIA Lionel Sec : Viviane POLSINELLI Insa : J.Y. TOUSSAINT	M. OBADIA Lionel Université Lyon 2 86 rue Pasteur 69365 LYON Cedex 07 Tél : 04.78.69.72.76 Fax : 04.37.28.04.48 Lionel.Obadia@univ-lyon2.fr

Yanli ZHANG

Thèse en traitement de l'image medicale / 2013
Institut national des sciences appliquées de Lyon

A General Non-Stationarity Measure: Application to Biomedical Image and Signal Processing

Abstract

The intensity variation is often used in signal or image processing algorithms after being quantified by a measurement method. The method for measuring and quantifying the intensity variation is called a « change measure », which is commonly used in methods for signal change detection, image edge detection, edge-based segmentation models, feature-preserving smoothing, etc. In these methods, the « change measure » plays such an important role that their performances are greatly affected by the result of the measurement of changes.

The existing « change measures » may provide inaccurate information on changes, while processing biomedical images or signals, due to the high noise level or the strong randomness of the signals. This leads to various undesirable phenomena in the results of such methods. On the other hand, new medical imaging techniques bring out new data types and require new change measures. How to robustly measure changes in those tensor-valued data becomes a new problem in image and signal processing.

In this context, a « change measure », called the Non-Stationarity Measure (NSM), is improved and extended to become a general and robust « change measure » able to quantify changes existing in multidimensional data of different types, regarding different statistical parameters.

A NSM-based change detection method and a NSM-based edge detection method are proposed and respectively applied to detect changes in ECG and EEG signals, and to detect edges in the cardiac diffusion weighted (DW) images. Experimental results show that the NSM-based detection methods can provide more accurate positions of change points and edges and can effectively reduce false detections.

A NSM-based geometric active contour (NSM-GAC) model is proposed and applied to segment the ultrasound images of the carotid. Experimental results show that the NSM-GAC model provides better segmentation results with less iterations that comparative methods and can reduce false contours and leakages.

Last and more important, a new feature-preserving smoothing approach called « Nonstationarity adaptive filtering (NAF) » is proposed and applied to enhance human cardiac DW images. Experimental results show that the proposed method achieves a better compromise between the smoothness of the homogeneous regions and the preservation of desirable features such as boundaries, thus leading to homogeneously consistent tensor fields and consequently a more reconstruction of the coherent fibers.

Keywords: non-stationarity measure, change detection, edge detection, segmentation, adaptive filtering, diffusion tensor, magnetic resonance imaging, cardiac imaging

Une Mesure de Non-Stationnarité Générale: Application en Traitement d'Images et de Signaux Biomédicaux

Résumé

La variation des intensités est souvent exploitée comme une propriété importante du signal ou de l'image par les algorithmes de traitement. La grandeur permettant de représenter et de quantifier cette variation d'intensité est appelée « mesure de changement », elle est couramment employée dans les méthodes de détection de ruptures d'un signal, en détection de contours d'une image, dans les modèles de segmentation basés sur les contours, et dans les méthodes de lissage d'images avec préservation de discontinuités.

En traitement des images et des signaux biomédicaux, les mesures de changement existantes fournissent des résultats peu précis lorsque le signal ou l'image présentent un fort niveau de bruit ou un fort caractère aléatoire, ce qui conduit à des artefacts indésirables dans le résultat des méthodes basées sur la mesure de changement. D'autre part, de nouvelles techniques d'imagerie médicale produisent de nouveaux types de données dites à valeurs multiples, qui nécessitent le développement de mesures de changement adaptées. Mesurer le changement dans des données de tenseur pose alors de nouveaux problèmes.

Dans ce contexte, une mesure de changement, appelée « mesure de non-stationnarité (NSM) », est améliorée et étendue pour permettre de mesurer la non-stationnarité de signaux multidimensionnels quelconques (scalaires, vectoriels, tensoriels) par rapport à un paramètre statistique, ce qui en fait ainsi une mesure générique et robuste.

Une méthode de détection de changements basée sur la NSM et une méthode de détection de contours basée sur la NSM sont respectivement proposées et appliquées aux signaux ECG et EEG, ainsi qu'a des images cardiaques pondérées en diffusion (DW). Les résultats expérimentaux montrent que les méthodes de détection basées sur la NSM permettent de fournir la position précise des points de changement et des contours des structures tout en réduisant efficacement les fausses détections.

Un modèle de contour actif géométrique basé sur la NSM (NSM-GAC) est proposé et appliqué pour segmenter des images échographiques de la carotide. Les résultats de segmentation montrent que le modèle NSM-GAC permet d'obtenir de meilleurs résultats comparativement aux outils existants avec moins d'itérations et un temps de calcul plus faible tout en réduisant les faux contours et les ponts.

Enfin, et plus important encore, une nouvelle approche de lissage préservant les caractéristiques locales, appelée filtrage adaptatif de non-stationnarité (NAF), est proposée et appliquée pour améliorer les images DW cardiaques. Les résultats expérimentaux montrent que la méthode proposée peut atteindre un meilleur compromis entre le lissage des régions homogènes et la préservation des caractéristiques désirées telles que les bords ou frontières, ce qui conduit à des champs de tenseurs plus homogènes et par conséquent à des fibres cardiaques reconstruites plus cohérentes.

Mots Clés: mesure de Non-stationnarité, détection de changement, détection de contours, segmentation, filtrage adaptatif, tenseur de diffusion, imagerie par résonance magnétique, imagerie cardiaque

Acknowledgement

I owe my sincere gratitude to all the people who have made this dissertation possible and my graduate school experience a cherishable one.

I would like to express my deepest gratitude to my supervisors Madam Isabelle Magnin, Mr. Wan-Yu Liu and Mr. Yue-Min Zhu, not only for the guidance and supervision throughout the course of this work but also for their understanding, encouragement and kindness during these years. This thesis would not appear in its present form without their kind assistance and valuable suggestions. They have been phenomenal role models and special friends to me.

I would like to acknowledge the members of my thesis committee, especially the rapporteurs, Mr. Jean-Marc Chassery and Madam Isabelle Bloch. Thank you for agreeing to be my thesis rapporteurs and giving me valuable advice on my thesis. I would like to thank Professor Jin Li, president of the jury, for her valuable advice and kindness. I also thank Professor Ping Li for agreeing to be the member of my thesis committee.

I have had the priviledge of working in two outstanding labs: the Centre de Recherche en Acquisition et Traitement de l'Image pour la Santé (Creatis) and the HIT-INSA Sino-French Research Center for biomedical imaging. I would like to thank all members of both labs, past and present, for their support. In particular, I would like to thank Dr. Lihui Wang, Dr. Feng Yang and Shengfu Li for all their generous help. I also thank Dr. Pierre Croisille, Dr. Xin Song, Dr. Stanislas Rappachi, Dr. Carole Frindel and other researchers from Creatis for sharing their experiences and helpful discussions. And from the HIT-INSA Sino-French Research Center for biomedical imaging, I would also like to thank Jian-Ping Huang, Bin Gao, Kaixiang Zhang, Liu He, Dr. Li-Jun Bao, Qi Wu, Wen-Hui Liu, Shan Hu, Xiaoming Sun, and Jian-Wei Ma for their help.

I am profoundly grateful to my husband Jin-Zhe Xu and our parents for their unwavering love, understanding, and moral support during these years.

Contents

Content of Figures

Introduction Générale

Les images et les signaux biomédicaux sont connus pour leur faible intensité, leur faible rapport signal sur bruit (SNR) et leurs fortes propriétés aléatoires. Améliorer la performance des méthodes de traitement pour ces données biomédicales est l'une des tâches importantes dans le domaine du traitement d'image et du signal.

La variation des intensités est souvent exploitée comme une propriété importante du signal ou de l'image par les algorithmes de traitement. La grandeur permettant de représenter et de quantifier cette variation d'intensité est appelée « mesure de changement ». Par exemple, l'amplitude du gradient est souvent utilisée comme une mesure de changement pour quantifier l'intensité des contours en traitement d'images. La « mesure de changement » est couramment employée dans les méthodes de détection des changements d'un signal, en détection de contours dans des images, dans les modèles de segmentation basés contours, et dans les méthodes de lissage d'images avec préservation de caractéristiques.

Dans toutes ces méthodes basées sur la «mesure de changement », la précision de cette mesure influence directement la performance de la méthode. En traitement d'images et de signaux biomédicaux, les mesures de changement existantes fournissent des résultats peu précis lorsque le signal ou l'image présente un fort niveau de bruit ou un fort caractère aléatoire, ce qui conduit à une dégradation des performances des méthodes basées ce type de mesure.

Dans ce contexte, l'objectif de notre travail de thèse est d'étudier une « mesure de changement » robuste et de l'utiliser pour améliorer la performance des méthodes de traitement du signal et de l'image, vis-à-vis du bruit et des artefacts indésirables souvent observés dans les méthodes existantes.

D'autre part, de nouvelles techniques d'imagerie médicale produisent de nouveaux types de données dites à valeurs multiples, qui nécessitent le développement des mesures de changement correspondantes. Par exemple, pour traiter les données de tenseur fournies par le DT-MRI, qui a apparu au milieu des années 1990, de nombreux travaux ont porté sur le traitement des champs de valeurs matricielles. Mesurer le changement dans ces données de tenseur pose alors de nouveaux problèmes en traitement d'images.

La mesure de non-stationnarité (NSM) est une mesure de changement robuste avec une bonne immunité au bruit. Elle peut refléter et quantifier les changements dans une image ou dans un signal en mesurant son degré de non-stationnarité. Dans ce travail, la méthode NSM est améliorée et étendue, et plusieurs approches de traitement d'image et de signal basées sur la NSM sont proposées et appliquées aux diverses images médicales ayant des niveaux de bruit élevés et aux signaux fortement aléatoires. En outre, la NSM étendue permet de mesurer les changements dans les données vectorielles et tensorielles, devenant ainsi une mesure générique et robuste pour des données de types différents et de dimensions quelconques. Les recherches effectuées sont détaillées comme suit:

Tout d'abord, la NSM est améliorée et étendue. La notion de stationnarité de paramètre en général est introduite. Basée sur cette notion, la NSM est élaborée et expliquée et une

formulation générale de la NSM est donnée. Ensuite, le processus de construction des opérateurs de NSM est généralisé. Les sorties des opérateurs NSM dans plusieurs cas typiques sont formulées. L'avantage de l'opérateur NSM en termes d'immunité au bruit est théoriquement prouvé. Le choix des paramètres critiques est discuté. Enfin, l'opérateur de NSM est étendu pour traiter des données à N dimensions et pour mesurer les changements dans des données vectorielles et tensorielles, devenant ainsi une méthode de mesure de changement générique et robuste.

Deuxièmement, nous proposons une méthode de détection de changements ainsi qu'une méthode de détection de contours toutes deux basées sur la NSM. Nous l'appliquons aux signaux ECG et EEG, ainsi qu'a des images cardiaques pondérées en diffusion (DW), l'objectif visé étant de réduire les fausses alarmes et les mauvaises détections lors de la détection des changements dans ces signaux fortement aléatoires et bruités contenant de faux bords. . Les résultats expérimentaux montrent que les méthodes de détection basées sur la NSM permettent de fournir la position précise des points de changement et des bords avec un temps de calcul plus faible, et de réduire efficacement les fausses détections qui sont souvent présentes dans les résultats fournis par les autres méthodes de mesure de changement.

Troisièmement, en vue de résoudre le problème des faux contours et des fuites qui apparaissent lors de la segmentation d'images très bruitées, nous proposons un modèle de contour actif géométrique basé sur la NSM (NSM-GAC) et nous l'appliquons pour segmenter des images d'échographie carotidienne. Le modèle utilise la NSM au lieu de l'amplitude du gradient pour obtenir des informations de bord et guider l'évolution de l'ensemble de niveau zéro vers les positions souhaitées. Les résultats de segmentation sur des images de synthèse très bruitées et des images d'échographie carotidienne simulées et réelles montrent que le modèle NSM-GAC permet d'obtenir de meilleurs résultats avec moins d'itérations et un temps de calcul faible, et de réduire les faux contours et les fuites.

Enfin, et plus important encore, en se concentrant sur le difficile problème de compromis entre le lissage des régions homogènes et la préservation des caractéristiques désirées dans des images à faible RSB, nous développons une nouvelle approche de lissage préservant les discontinuités, appelée filtrage adaptatif de non-stationnarité (nonstationarity adaptive filtering—NAF, en anglais). Cette méthode estime l'intensité d'un pixel en faisant la moyenne des intensités sur un voisinage homogène adaptatif. Ce dernier est déterminé suivant cinq contraintes et la carte de NSM. L'approche proposée est appliquée pour améliorer les images DW cardiaques et comparée à la méthode de filtrage de diffusion anisotrope (FDA). Des résultats expérimentaux sur des données synthétiques montrent que l'indice de similarité structurelle moyenne (MSIMS, en anglais) des images DW lissées par le NAF est 120,3% plus élevé que celui des images bruitées, et est 22,6% plus élevé que celui des images lissées par la FAD. Les résultats expérimentaux sur des images DW cardiaques humaines montrent que la méthode proposée fournit un meilleur compromis entre le lissage des régions homogènes et la préservation des caractéristiques désirées telles que les bords ou frontières, ce qui conduit à des champs de tenseurs plus homogènes et par conséquent à des fibres plus cohérentes. Le temps de calcul du lissage NAF dépend de la taille de l'image traitée et de la taille du voisinage homogène de chaque pixel. Une façon très simple mais extrêmement

efficace pour réduire le coût de calcul est d'imposer une limite supérieure sur la taille du voisinage adaptatif.

Pour résumer, les méthodes de traitement d'images et du signal basées sur la NSM ci-dessous présentent une bonne immunité aux bruits, permettent de réduire les phénomènes indésirables induits par le bruit, et se prêtent bien au traitement des images très bruitées et des signaux fortement aléatoires.

Chapter 1

1 Introduction

Contents

Résumé en français

Ce chapitre d'introduction a pour objectif de présenter le contexte et l'importance du sujet de thèse, les problématiques, les théories impliquées, et les contributions de ce travail de thèse.

Premièrement, l'importance et la nécessité d'une étude sur la mesure robuste de variation sont abordées (Section 1.1). Deuxièmement, les mesures de variation fréquemment utilisées en traitement des signaux 1-D sont introduites. Leurs avantages et inconvénients sont analysés et énumérés. La mesure de changement dans les signaux 1-D se trouve souvent dans les méthodes de détection de changement. Pour les signaux fortement aléatoires tels que les signaux ECG et les signaux EEG, les fausses alarmes et les mauvaises détections sont des problèmes souvent rencontrés avec les méthodes existantes de mesure de changement (Section 1.2).

Troisièmement, les mesures de variation couramment utilisées en traitement d'images 2-D et 3-D sont introduites. Leurs avantages et inconvénients sont également détaillés. La mesure de variation dans l'image 2-D est couramment employée pour la détection des contours dans les images, dans les modèles de segmentation basés contours, et dans les méthodes de lissage d'images avec préservation de caractéristiques. Pour des images ayant des niveaux de bruit élevés, telles que les images DW et les images échographiques, de faux contours se produisent souvent avec les méthodes de détection de contour basées sur la mesure de variation, et de faux contours ainsi que des ponts apparaissent dans les résultats de segmentation basés contours. Dans tous ces problèmes, la difficulté se trouve dans le compromis entre la réduction du bruit et la préservation des caractéristiques importantes telles que les bords et les détails (Section 1.3).

Quatrièmement, les mesures de changement utilisées en traitement des données de type vecteurs et tenseurs sont introduites (Section 1.4)

En particulier, une approche de mesure du changement robuste, appelée mesure de non-stationnarité (en anglais, Non-Stationarity Measure, NSM), est introduite, y compris son contexte, ses applications et l'état de l'art dans ce domaine (Section 1.5).

En analysant les mesures de changement existantes et leurs applications, nous pouvons résumer les problèmes comme suit: (1) absence d'approches générales et robustes de mesure du changement; (2) fausses alarmes et mauvaises détections dans le cas de signaux fortement aléatoires ou faux bords dans le cas d'images très bruitées; (3) faux contours ou fuites lors de la segmentation d'images très bruitées; (4) difficulté d'obtention d'un compromis acceptable entre réduction du bruit et préservation des caractéristiques dans le lissage des images à faible RSB.

Afin d'aborder les problèmes mentionnés ci-dessus, nous proposons dans ce travail de thèse: (1) d'améliorer et de généraliser la méthode NSM; (2) d'étudier des méthodes de détection de changement dans un signal et la détection des contours ou des bords dans une image en s'appuyant sur la NSM; (3) de développer un modèle de segmentation GAC (Geometric Active Contour) basé sur la NSM et de l'appliquer; (4) d'étudier un filtre adaptatif basé sur la NSM et de l'appliquer.

1.1 Background and significance of the research

Biomedical images and signals are the visible manifestation of the physical, chemical, and biological phenomena produced by the body itself or stimulated by an external excitation. Some typical examples are the electro-cardiographic (ECG) signal, the electro-encephalographic (EEG) signal, ultrasound echographies, magnetic resonance images, etc. These data carry important functional information about organs, tissues, cells, even molecules, that is indispensable for clinical diagnosis.

Processing biomedical images and signals and extracting qualitative and quantitative biomarkers is of great help to assist the medical doctor to optimize diagnosis and treatment of diseases.

However, biomedical images and signals are known to exhibit weak intensities, high noises and strong randomness. For such images and signals, especially for those with high noise level, most processing approaches are unable to guarantee the desired result. Making existing methods more robust to noise by altering their designs or designing a new method which is more robust than the existing ones has always been an important topic in image and signal processing.

In addition, new medical imaging modalities offer new information (images) about organism which make possible to functionally study the microstructure of tissues and organs. However, owing to the complexity of the imaging formation process and environment, the obtained images are often corrupted by a high-level of noise, leading to a low SNR. For instance, diffusion tensor magnetic resonance imaging (DT-MRI, or DTI), coming into existence in the mid-1990s, appears to be the unique available technique of measuring the diffusion of water molecules in *ex vivo* and *in vivo* tissues and organs [Basser *et al.*, 1994]. DTI data can help to characterize the composition, microstructure and architecture of a tissue, and assess its changes in development, disease, and degeneration. However, important features of raw diffusion weighted (DW) magnetic resonance images, such as homogeneous regions, edges, and details, are often buried into speckled mosaic-like patterns aroused by high noise, which hampers the performance and the potentiality of DTI in studying *in vivo* tissues functionally [Basser *et al.*, 2000; Chen *et al.*, 2005; Ding *et al.*, 2005; Jones *et al.*, 2004]. For such emerging medical imaging modalities, there is an urgent need to develop image or signal processing methods that are robust against high-level noises.

The analysis of a large number of image and signal processing methods shows that most of them use information on changes within an image or a signal, and thus include operators to quantify these changes. Such an operator can be considered as a realization of a “change measure” method. It is used to measure and quantify changes, providing the magnitude of changes for various image and signal processing methods. For instance, the magnitude of a gradient is usually used as a “change measure” to quantify the edge strength contained in an image.

A “change measure” is commonly used in methods dedicated to signal change detection, image edge detection, edge-based segmentation models, and feature-preserving smoothing. Such methods are collectively referred as “change-measure based” methods in this work. The “change measure” plays such an important role that it can affect, to a large extent, the

performance of the "change measure-based" method itself. When dealing with biomedical images or signals, the existing change measures may provide inaccurate information on changes due to the high noise level or the strong randomness of the data, so leading to the degradation of the performance of the "change-measure based" methods and the generation of undesirable phenomena.

In this context, our research perspective is to study a "robust change measure" and to propose several processing methods based on it. These methods should be robust to noise, and also reduce undesirable phenomena which are often present in the processed data obtained by more conventional "change measure-based" methods.

Moreover, prompted by new medical imaging techniques, many multi-valued image processing methods are proposed, which require corresponding "change measures". Typically, to deal with the tensor-valued data provided by the DT-MRI, many works focused on the processing of matrix-valued fields [Burgeth *et al.*, 2011; Hamarnesh *et al.*, 2007; Welk *et al.*, 2007]. To this end, some definitions of the difference between two tensors are given [Arsigny *et al.*, 2006; Burgeth *et al.*, 2007; Demirci, 2007; Pennec *et al.*, 2006; Wang *et al.*, 2005; Wang *et al.*, 2004d]. So far, there has been no literature to discuss the robustness of these definitions. How to robustly measure variations in tensor-valued data becomes a new problem in image processing.

The Non-Stationarity Measure (NSM) studied in this work was proposed as a rupture detection method in 1994[Liu *et al*.] and mainly used for the edge detection and the segmentation of ultrasound images. In the early 1990s, ultrasound images were much more difficult to deal with than other images because of the presence of speckle, shadows, low contrast, and varying spatial resolution. The satisfactory segmentation results obtained by the NSM showed its advantage in noise immunity. As a matter of fact, the NSM can reflect and quantify changes in an image or a signal by locally measuring its degree of non-stationarity. It can therefore be considered as a "change measure".

In this work, we demonstrate that the NSM provides basic and important information on changes for various image and signal processing algorithms. Then, we propose several NSM based algorithms and we apply them to process data with high noise level and/or strong randomness. Additionally, we extend the NSM to measure changes in vector- and tensor-valued data. Finally we show that the NSM is a general and robust change measure which can deal with different forms, arbitrary dimensional data regarding multiple statistical parameters.

This work was supported by the French ANR 2009 (ANR-09-BLAN-0372-01), the National Natural Science Foundation of China (61271092), International S&T Cooperation Project of China (2007DFB30320), and the Program PHC-Cai Yuanpei 2012. It is done in the framework of the French CNRS Inserm GDR Stic Santé.

1.2 Change measures of a signal and their applications

1.2.1 Change measures of a signal

Detecting changes or ruptures present in a 1-D signal requires the use of a change measure. Different kinds of changes require different change detection methods which use different

change measures. For instance, in monitoring applications, such as monitoring of the heart rate [Yang *et al.*, 2006], air pollution [Chelani, 2011], or sleep apnoea [Severo *et al.*, 2006], any modification from an acceptable standard state of the process is considered as a change. To detect such changes, cumulative sum (CUSUM) based methods are often used, where the cumulative shift is taken as the change measure. In contrast, in the change detection method proposed in [Ensign *et al.*, 2010; Lavielle, 1999;2005], a signal change is usually considered as a transition between two adjacent properties of the signal. It occurs very fast with respect to the sampling period, if not instantaneously. To detect such a change, a dissimilarity or distance can be used to measure the difference between two successive segments before and after each time instant t_0 [Laurent *et al.*, 1998; Malegaonkar *et al.*, 2006] (see Fig. 1.1) or between two hypothetical situations (assuming a change or no change occurring at the central point t_0 of a segment) [Ajmera *et al.*, 2004; Tourneret, 1998]. In this work we focus on such changes as well as on change measures (dissimilarities or distances) and change detection methods.

At present, most change measures of a signal can be roughly grouped into the following three categories.

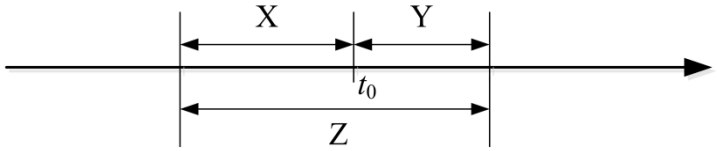

Fig. 1.1 Signal segments X , Y and Z involved in the measurement of the change at time t_0

1.2.1.1 Based on the Log Likelihood Ratio

The change measure based on the log likelihood ratio (LLR) [Delacourt *et al.*, 2000; Gish *et al.*, 1994] is a common type of change measure in signal processing.

Two signal segments X and Y can be represented by the vectors $\{x_1, x_2, \cdots, x_{n_x}\}$ of size n_x and $\{y_1, y_2, \cdots, y_{n_y}\}$ of size n_y respectively. The signal segment Z is the union of X and Y, such that $\mathrm{Z} = \mathrm{X} \cup \mathrm{Y} = \{z_1, z_2, \cdots, z_n\}$, $n = n_x + n_y$. Assuming that the data points in X and Y are independent and identically distributed (i.i.d.), the log likelihood of Z under the null hypothesis $\mathbf{H}_0$ (there is no change at time t_0) is calculated as

$$L_0 = \sum_{i=1}^{n_x} \log p\left(x_i | \theta_z\right) + \sum_{i=1}^{n_y} \log p\left(y_i | \theta_z\right), \tag{1.1}$$

where $p\left(x|\theta\right)$ is the likelihood of the data point x given θ. Here, θ_z is the maximum likelihood (ML) estimate of the parameters of the single Gaussian density of Z. The log likelihood of Z under the hypothesis $\mathbf{H}_1$ (there is a change at time t_0) is calculated as

$$L_1 = \sum_{i=1}^{n_x} \log p\left(x_i \middle| \theta_x\right) + \sum_{i=1}^{n_y} \log p\left(y_i \middle| \theta_y\right), \tag{1.2}$$

where θ_x and θ_y are the ML estimates of the parameters of the Gaussian densities of data set X and Y, respectively. Then, the change measure based on the LLR can be expressed as

$$\mathrm{LLR} = L_1 - L_0. \tag{1.3}$$

Although being simple, the change measure LLR has limited use because θ_z is estimated with the single Gaussian density. Ajmera et al. [Ajmera *et al.*, 2004] proposed to model the data with a Gaussian mixture model (GMM) with two Gaussian components instead of the single Gaussian density.

1.2.1.2 Based on the Bayesian Information Criterion

The change measure based on the Bayesian Information Criterion (BIC) is another common type of change measure in signal processing. Among these change measures, ΔBIC [Chen *et al.*, 1998; Cheng *et al.*, 2010; Huang *et al.*, 2005] is the most important one which can be expressed as

$$\begin{aligned} \Delta\mathrm{BIC} &= \mathrm{BIC}\left(\mathbf{H}_1, \mathrm{Z}\right) - \mathrm{BIC}\left(\mathbf{H}_0, \mathrm{Z}\right) \\ &= L_1 - L_0 - \lambda \log n \end{aligned}, \tag{1.4}$$

where λ is the penalty factor which should ideally be 1. ΔBIC is similar to LLR except the fact that the likelihoods now are penalized by the number of parameters used in the model. The decent measuring accuracy of this approach is widely recognized; however, as the length of the signal segment grows, it incurs a heavy computational cost due to numerous computations. To reduce the computational cost, Zhou and Hansen [Zhang *et al.*, 2011; Zhou *et al.*, 2005] integrated the Hotelling's T^2-Statistic, which has the advantage of low computations, with the BIC, known as the distance measure T^2-BIC.

Another change measure based on the BIC, called the bilateral scoring [Malegaonkar *et al.*, 2006; Malegaonkar *et al.*, 2007]., calculates the difference between two signal segments of equal length ($n_x = n_y$) before and after each time instant t_0

$$\left\{\log p\left(\mathrm{Y}\middle|\theta_x\right) - \log p\left(\mathrm{Y}\right)\right\} + \left\{\log p\left(\mathrm{X}\middle|\theta_y\right) - \log p\left(\mathrm{X}\right)\right\}. \tag{1.5}$$

1.2.1.3 Kullback-Leibler and J-divergence

The last of the dominant change measures is the Kullback-Leibler (KL) divergence (or relative entropy) which estimates the distance between two random distributions [Kuncheva, 2013; Noble *et al.*, 2006]. The KL divergence of a pair of distributions p and q is given as

$$\mathrm{KL}(p \,\|\, q) = \sum p(z_i) \log \frac{p(z_i)}{q(z_i)}. \tag{1.6}$$

If the two distributions are identical, the value of $\mathrm{KL}(p\|q)$ is 0. The larger the value, the higher the likelihood that p is different from q. In the real-life case, we do not have p and q but only approximations of them estimated from X and Y, respectively.

However, KL divergence is not symmetric and the most frequently used way to symmetrize it is the *J*-divergence given by

$$\mathrm{J}(p,q)=\frac{1}{2}\left(\mathrm{KL}(p\|q)+\mathrm{KL}(q\|p)\right). \tag{1.7}$$

Besides the above three dominant types, there are other change measures including the Kolmogorov distances, Küllback distance, "Jensen-like" divergence [Laurent *et al.*, 1998], the dissimilarity in the kernel method [Desobry *et al.*, 2005], the Pearson divergence [Liu *et al.*, 2012], etc.

1.2.2 Signal change detection

Change detection is a basic and longstanding issue in signal processing. The objective of change detection is to discover and locate abrupt property changes lying behind time-series data. In most cases, signal properties can be identified using some basic statistical parameters, such as mean [Lavielle, 2005; Lebarbier, 2005] and variance [Lavielle, 2005; Tourneret, 1998], or using some high-level representations, such as time-frequency representations [Laurent *et al.*, 1998], mel-cepstral coefficients [Cheng *et al.*, 2010], wavelet coefficients [Desobry *et al.*, 2005; Laurent *et al.*, 1998] in more complicated applications.

Existing change detection approaches include ones based on a model [La Rosa *et al.*, 2008; Malegaonkar *et al.*, 2007], based on models selection [Lebarbier, 2005; Rigaill *et al.*, 2012], and based on change measures (metrics) [Ajmera *et al.*, 2004; Al-Assaf, 2006; Chen *et al.*, 1998; Cheng *et al.*, 2010; Desobry *et al.*, 2005; Ensign *et al.*, 2010; Huang *et al.*, 2005; Huang *et al.*, 2006; Khalil *et al.*, 2000; Laurent *et al.*, 1998; Lavielle, 2005; Malegaonkar *et al.*, 2006; Malegaonkar *et al.*, 2007; Tourneret, 1998; Zhang *et al.*, 2011; Zhou *et al.*, 2005].

In all the above mentioned approaches, change measure (metric)-based ones have recently become popular because of their robustness and effectiveness for change detection without supervision. Those approaches first use a change measure method to highlight abrupt changes in a signal. Then, based on the obtained measurement curve which peaks usually indicate abrupt changes, they estimate the locations of the change points. However, when dealing with signals showing strong randomness, those curves often become fluctuating. To avoid fluctuations, they are often smoothed by low-pass filters [Delacourt *et al.*, 2000; Zhou *et al.*, 2005]. Such remedies effectively improve the robustness of the method, but they lack elegant mathematical basis and may increase the missing rate.

1.3 Change measures of an image and their applications

1.3.1 Change measures of an image

Change measures provide basic and important information on changes for various 2-D and 3-D image processing algorithms. The most typical change in an image is the brutal

modification of its mean value which is commonly referred to an edge. The magnitude of such a change is correspondingly referred to the edge strength. Existing change measures in 2-D and 3-D can be grouped into three categories: based on derivatives, based on phase congruency and local energy, and based on probability and statistics.

1.3.1.1 Based on derivatives

The magnitude of the gradient is the most commonly used change measure in image processing. Gradient is usually computed by differential operators, such as Sobel, Prewitt, Roberts, etc. The gradient magnitude measures a local intensity change in a simple and effective way, but it is sensitive to noise [Gonzalez *et al.*, 2002]. Therefore, in practice, it is reserved to deal with low noise images [Kawaguchi *et al.*, 2003; Laligant *et al.*, 2010], or images that have been pre-processed using smoothing techniques [Barcelos *et al.*, 2003; Chen, 2008; Direkoglu *et al.*, 2011; Xu *et al.*, 2009b].

An efficient optimization scheme to lessen the sensitivity of gradient to noise is the one performed by the Canny operator [Canny, 1986]. In the implementation, the Canny operator is approximated using the first derivative of a Gaussian function. Two steps can be distinguished in the change measurement procedure carried out by the Canny operator: first, the raw image is convolved with a Gaussian filter; second, the first derivatives in the horizontal direction and the vertical direction of the filtered image are returned by convolving the image with a classical edge detection operator, Roberts, Prewitt, Sobel, for example. Thereby, the magnitude of the gradient (edge strength) can be obtained. Since the Canny operator is essentially based on gradient, the resultant magnitude can contain false information on change in some noisy cases. To overcome this drawback, solutions were proposed that introduce remedial steps performed after the gradient-based change measurement, such as the embedded confidence [Meer *et al.*, 2001], the fused edge strength maps (ESM) [Shui *et al.*, 2012], the edge following algorithm [Somkantha *et al.*, 2011], and the edge membership degrees [Lopez-Molina *et al.*, 2011].

In 1992, Mallat combined the Canny operator with the multiscale wavelet, clearly explaining the significance of multiscale idea in image edge detection. In fact, at a single scale, the modulus [Mallat, 2009] of some particular analyzing wavelet [Heric *et al.*, 2007; Mallat *et al.*, 1992; Nes, 2012; Sun *et al.*, 2004], carrying the properties of abrupt signal changes such as edge slope and width, is equivalent to an intensity variation measure. However, the modulus at a finer scale, although representing edge position more accurately, is easily affected by noise. Therefore, in order to suppress spurious responses, the technique of maxima curves [Mallat, 2009] was employed to combine edge information at several scales.

Other derivative-based change measures, such as, the instantaneous coefficient of variation (ICOV) [Yu *et al.*, 2004], were also designed to provide better immunity to noise.

1.3.1.2 Based on phase congruency and local energy

In studies on the phenomenon of Mach band, Morrone et al. [Morrone *et al.*, 1986] found that there was a high phase congruency where features could be perceived in the image. Based on the theory of phase congruency, local energy was introduced to detect features. Morrone and Owens [Morrone *et al.*, 1987] and Morrone and Burr [Morrone *et al.*, 1988] calculated

the local energy using the original signal and its 1-D Hilbert transform. However in practice, it is not convenient to compute the local energy on the horizontal and vertical orientations, separately. Subsequently, Kovesi developed a novel algorithm to calculate the local energy by using the odd and even log Gabor wavelet [Kovesi, 2000]. Then the authors of [Ke *et al.*, 2011] introduced the 2-D discrete Hilbert transform to simplify the calculation of the local energy, and to improve the result of feature detection.

Since phase congruency marks a line feature with a single response and since its magnitude is largely independent of the local contrast [Kovesi, 2000], it is often used in the processing of images with abundant line features [Struc *et al.*, 2009; Wong *et al.*, 2008; Zhang *et al.*, 2012]. However, the phase congruency is very sensitive to noise. Future work is required to improve the algorithm of phase congruency to control noise more efficiently.

1.3.1.3 Based on probability and statistics

In a local area, usually determined by a neighborhood window, the variance [Chuang *et al.*, 1993; Park *et al.*, 1995] or the weighted variance [Hou *et al.*, 2003; Law *et al.*, 2007] were computed as discontinuity measures. In [Kim *et al.*, 2004], the authors computed the difference between the average intensities of two pixel groups formed by the ideal binary pattern as edge strength.

The log-likelihood ratio was also used as a local measure of edge strength in edge detection [Konishi *et al.*, 2003a; Konishi *et al.*, 2003b] and in image segmentation [Zhu *et al.*, 1996].

These statistical change measures are more effective than the gradient magnitude in noisy cases, but computationally more demanding.

Besides the change measures mentioned above, there also exist other interesting change measure methods. For instance, in [Bouda *et al.*, 2008; Lopez-Molina *et al.*, 2010; Sun *et al.*, 2007], physics-based methods were proposed that use either the “universal gravitational force” or the “electric field” to measure image intensity variations.

All the change measures mentioned above have their advantages and disadvantages. Their common problem is however the decrease of their performance in high-level noise cases. Therefore, it is still a challenge issue to design a change measure with excellent noise immunity.

1.3.2 Image processing tasks involving change measures

Edge detection, edge-based segmentation, and feature-preserving smoothing are the three image processing tasks in which change measures of an image are often used.

1.3.2.1 Edge detection

Edge detection is a fundamental task in image processing, machine vision and computer vision. The results of edge detection particularly affects some high level tasks, such as feature extraction, target recognition, and image understanding.

Change measure-based edge detection approaches are basic and important because of their objectiveness and non-supervision. They first use a measurement method to highlight edges occurring between objectives, between regions, or between target and background. Then,

based on the obtained edge strength map, they estimate the locations of edges using subsequent processing steps. The Canny detector is considered to be one of the most successful approach of edge detection, and still widely used in many image processing tasks [Li *et al.*, 2010; Shacham *et al.*, 2007; Zhang *et al.*, 2010]. The three steps of edge detection proposed in the Canny detector, estimation of the gradient magnitude, non maxima suppression, and hysteresis thresholding, have become an usual procedure of edge detection, except that different change measures other than gradient magnitude are designed in order to better highlight edges [Lopez-Molina *et al.*, 2011; Shui *et al.*, 2012].

In a change measure-based edge detection approach, change measure plays such an important role that the detected edges are greatly dependent on the results of the change measurement. When dealing with biomedical images, like DW magnetic resonance images, the existing change measures may provide inaccurate information on edges due to the high noise level, which leads to the generation of false edges in the results.

1.3.2.2 Edge-based segmentation

Segmentation is the process of partitioning an image into different regions. In medical imaging, these regions often correspond to different tissue classes, organs, pathologies, or other biologically relevant structures. Medical image segmentation is made difficult by low contrast, noise, and other imaging ambiguities.

Edge-based schemes and region-based schemes are two major types of image segmentation methods. Traditional edge-based segmentation schemes are performed based on edges obtained from edge detectors. However, in noisy cases, the obtained edges may not form closed contours. To separate topologically unconnected objects, these unclosed edges must be extended and connected to construct closed contours at approximate boundaries. In the early 90's, the geometric active model (GAC) formed through a combination of level set and active contour [Caselles *et al.*, 1993; Malladi *et al.*, 1995] was introduced into the field of image processing and computer vision. The GAC has several advantages, such as, handling topological changes in a natural and efficient way, and performing numerical computations on a fixed Cartesian grid without having to parameterize the points on a contour. Since its first application to the edge-based segmentation, the GAC has become increasingly popular as a general framework for image segmentation.

The edge-based GAC model guides the motion of the zero level set and stops the level set evolution using the image gradient magnitude in the external energy term. However, in highly noisy cases, the gradient may provide inaccurate information on edges for the edge-based GAC model so that such model can easily produce false contours or pass through weak object boundaries, called leakages.

1.3.2.3 Feature-preserving smoothing

As a special case of filtering, image smoothing is commonly applied in a processing chain to improve the visual appearance of an image and to simplify subsequent image processing stages such as feature extraction, image segmentation or motion estimation [Jähne, 1997]. As smoothing is sometimes applied to remove small details from an image prior to large object extraction and to bridge small gaps in lines or curves [Gonzalez *et al.*, 2002], the term of

feature preserving smoothing (FPS) is used to emphasize another type of smoothing which aims to reduce undesirable distortions, due to the presence of noise or the poor image acquisition process, while preserving important features such as homogeneous regions, discontinuities, edges and textures [Grazzini *et al.*, 2009; Saintmarc *et al.*, 1991; Tomasi *et al.*, 1998].We focus on such smoothing in this work.

Traditional filters usually perform fixed operations on fixed neighborhoods, that is, their parameters cannot adapt themselves to the local image features. The most obvious side effect created by these nonadaptive filters is the significant blurring caused by averaging of distinct populations on the boundaries between two regions.

To avoid the undesirable phenomenon of blurring, there has been in particular substantial efforts in developing adaptive filters. A generic idea underlying most of them is to update a pixel's intensity through a local weighted averaging of its neighbor pixels' intensities within a neighborhood. They can adjust either the averaging weights or the neighborhood to the local image features. The filters having adaptive weights usually operate within a fixed neighborbood, such as nonlinear diffusion filters [Ding *et al.*, 2005; Perona *et al.*, 1990; Weickert, 1998] or Bilateral filters [Elad, 2002; Paris *et al.*, 2008]. And the filters having adaptive neighborhoods often perform a fixed operation, such as, adaptive median filter [Gonzalez *et al.*, 2002], amoeba dynamic structuring element [Lerallut *et al.*, 2007], adaptive geodesic neighbourhood [Grazzini *et al.*, 2009]. These adaptive filters are more robust than nonadaptive filters and appropriate for FPS.

In such adaptive filters, the intensity gradient often exists to provide information on the local image intensity variations so that they can intrinsically allow the processing of image pixels with different strategies depending on the region where they are positioned. However, when dealing with biomedical images, the intensity gradient may provide inaccurate information on change due to the high noise level, which is one of the reasons for the degradation of the performance of these adaptive filters. For low-SNR images, it is hard to achieve a good compromise between noise reduction and feature preserving. There is a need for better adaptive schemes and robust change measures.

1.4 Change measures of vector- and tensor-valued data

1.4.1 Change measures of vector-valued data

Currently, change measures of vector-valued data are often used for processing color images, and relatively rarely used for processing biomedical images. The Euclidean distance and the orientation difference between two vectors are change measures that were once applied to restore direction fields in DTI [Coulon *et al.*, 2004] and to detect edges in multiple channel images [Lukac *et al.*, 2007].

Minkowski Distance and orientation difference

There are two common change measures of vector-valued data: the Minkowski distance and the orientation difference. The Minkowski distance between two vectors $U=(u_1,u_2,\cdots,u_n)\in\mathbf{R}^n$ and $V=(v_1,v_2,\cdots,v_n)\in\mathbf{R}^n$ can be expressed as

$$d(U,V)=\left(\sum_{i=1}^{n}|u_i-v_i|^p\right)^{1/p}. \tag{1.8}$$

This definition is typically used with p being 1 or 2. The latter is the Euclidean distance, also written as $\|U-V\|$, while the former is sometimes known as the Manhattan distance.

The orientation difference between U and V is defined as

$$d(U,V)=\arccos\left(\frac{U\cdot V}{|U|\cdot|V|}\right), \tag{1.9}$$

where "$\cdot$" is the scalar product of the two vectors.

Based on statistics

Scharcanski et al. defined the change measure of a vector-valued image at an arbitrary pixel (x_0,y_0) as the magnitude of the "gradient" [Scharcanski *et al.*, 1997], although the "gradient" was obtained with two directional operators of size $(2w+1)\times(2w+1)$.

$$\begin{aligned}\Delta U_x(x_0,y_0)&=\Delta U_{x+}(x_0,y_0)-\Delta U_{x-}(x_0,y_0)\\&=\frac{1}{w(2w+1)}\sum_{y=y_0-w}^{y=y_0+w}\sum_{x=x_0+1}^{x=x_0+w}U(x,y)-\frac{1}{w(2w+1)}\sum_{y=y_0-w}^{y=y_0+w}\sum_{x=x_0-1}^{x=x_0-w}U(x,y)\end{aligned} \tag{1.10}$$

and

$$\begin{aligned}\Delta U_y(x_0,y_0)&=\Delta U_{y+}(x_0,y_0)-\Delta U_{y-}(x_0,y_0)\\&=\frac{1}{w(2w+1)}\sum_{y=y_0+1}^{y=y_0+w}\sum_{x=x_0-w}^{x=x_0+w}U(x,y)-\frac{1}{w(2w+1)}\sum_{y=y_0-1}^{y=y_0-w}\sum_{x=x_0-w}^{x=x_0+w}U(x,y).\end{aligned} \tag{1.11}$$

Therefore, the magnitude of the "gradient" at pixel (x_0,y_0) can be expressed as $\sqrt{\|\Delta U_x(x_0,y_0)\|^2+\|\Delta U_y(x_0,y_0)\|^2}$. It is seen that, in order to obtain noise immunity, multiple vectors are averaged for calculating the gradient.

Demirci [Demirci, 2007] used the average of eight dissimilaries between the current point U and its 8-neighbors $V_i, i=1,\cdots,8$ as the change measure :[Demirci, 2007]

$$d(U)=\frac{1}{8}\sum_{i=1}^{8}d(U,V_i), \tag{1.12}$$

where $d(U,V_i)$ can be the Euclidean distance or the orientation difference of two vectors defined in (1.8) and (1.9). In this definition, the average of multiple differences of two vectors is calculated for noise immunity.

Based on rank ordering

In edge detection of a vector field, the change measures based on rank ordering, such as the minimal spanning tree (MST) ordering in [Theoharatos *et al.*, 2005] and the minimum vector dispersion (MVD) in [Trahanias *et al.*, 1993;1996], usually possess good noise immunity,. Among these ranking schemes, the MVD, expressed as

$$\mathrm{MVD} = \min_{j}\left(\left\| U_{n-j+1} - \frac{1}{l}\sum_{i=1}^{l} U_i \right\|\right), \quad j = 1,2,\cdots,k;\ k,l < n, \tag{1.13}$$

is well known for its improved noise performance since the minimum operation makes it insensitive to long-tailed noise and the averaging operation makes it insensitive to short-tailed noise.

Sometimes, in order to obtain good noise immunity, the change measure of vector-valued data may be designed to be very complex, for example, the magnitude of the maximum variation rate proposed in [Kuo *et al.*, 2007].

1.4.2 Change measures of tensor-valued data

At present, change measures of tensor-valued data are often used in the segmentation and the smoothing of diffusion tensor images and texture images. These change measures are restricted to the differences between two tensors.

Frobenius norm

The Frobenius norm, sometimes also called the Euclidean norm, of two matrices $\mathbf{M}_1$ and $\mathbf{M}_2$ is defined as

$$\left\|\mathbf{M}_1, \mathbf{M}_2\right\|_F = \sqrt{tr[(\mathbf{M}_1 - \mathbf{M}_2)^T(\mathbf{M}_1 - \mathbf{M}_2)]}, \tag{1.14}$$

where $\left\|\square\right\|_F$ represents the calculation of the Frobenius norm, and $tr(\cdot)$ the calculation of the trace of the matrix. The Frobenius norm is the change measure first used for processing tensor-valued data, for instance, the smoothing [Welk *et al.*, 2007] and the segmentation [Rousson *et al.*, 2004; Wang *et al.*, 2004b; Wiegell *et al.*, 2003] of diffusion tensor magnetic resonance images. This straightforward measure a priori leads to simple computations. Unfortunately, although the Frobenius norm is well adapted to general square matrices, it is unsatisfactory for tensors, positive definite symmetric matrices. Typical problems in Euclidean operations on tensors include nonpositive eigenvalues, tensor swelling, asymmetric tensors, etc.

Dissimilarity measure based on *J*-divergence

A diffusion tensor "distance" was defined as the square root of the *J*-divergence of two probability distributions [Wang *et al.*, 2005; Wang *et al.*, 2004d], i.e.,

$$d\left(\mathbf{T}_1, \mathbf{T}_2\right) = \sqrt{\mathrm{J}\left(p(\mathbf{r} \mid t, \mathbf{T}_1), p(\mathrm{r} \mid t, \mathbf{T}_2)\right)}, \tag{1.15}$$

where $p(\mathbf{r}|t,\mathbf{T})$ represents the probability density of the displacement $\mathbf{r}$ of water molecules starting from a given location at time t, given a diffusion tensor $\mathbf{T}$. If $p(\mathbf{r}|t,\mathbf{T})$ can be described as a Gaussian distribution, then

$$d(\mathbf{T}_1,\mathbf{T}_2)=\frac{1}{2}\sqrt{tr(\mathbf{T}_1^{-1}\mathbf{T}_2+\mathbf{T}_2^{-1}\mathbf{T}_1)-2n}\,, \tag{1.16}$$

where n is the size of the square matrix $\mathbf{T}$. This definition was used in the segmentation of texture images [Wang *et al.*, 2004d] and diffusion tensor images [Wang *et al.*, 2005; Wang *et al.*, 2004d].

Riemannian metrics

To fully circumvent the difficulties in Euclidean operations on tensors, affine-invariant Riemannian metrics have been recently proposed for tensors by several teams. Among these Riemannian metrics, the most well-known is the one proposed in [Pennec *et al.*, 2006] which can be expressed as

$$d\left(\mathbf{T}_1,\mathbf{T}_2\right)=\left\|\log\left(\mathbf{T}_1^{-1/2}\cdot\mathbf{T}_2\cdot\mathbf{T}_1^{-1/2}\right)\right\|, \tag{1.17}$$

where $\|\cdot\|$ is an Euclidean norm on symmetric matrices.

Lenglet et al. also ended up with the same metric tensors, called geodesic distance [Lenglet *et al.*, 2006b]. In [Lenglet *et al.*, 2006a], the geodesic distance was compared to the Frobenius norm, and the *J*-divergence in the segmentation of tensor fields. The article suggested that the geodesic distance offered a better segmentation result.

These Riemannian metrics were applied for interpolation [Batchelor *et al.*, 2005; Pennec *et al.*, 2006], segmentation [Guo *et al.*, 2008; Lenglet *et al.*, 2006a; Lenglet *et al.*, 2006b; Malcolm *et al.*, 2007], and regularization [Castano-Moraga *et al.*, 2007; Pennec *et al.*, 2006] of tensor fields.

With affine-invariant metrics, symmetric matrices with negative and null eigenvalues are at an infinite distance from any tensor and the swelling effect disappears. Practically, this prevents nonpositive eigenvalues to appear, which is particularly difficult to avoid in Euclidean algorithms. However, the price paid for this success is a high computational cost spent on matrix inverses, square roots, logarithms, and exponentials.

Log-Euclidean metric

Affine-invariant Riemannian metrics have excellent theoretical properties, but also lead to complex and slow algorithms in practice. To remedy this limitation, a simple similarity-invariant Log-Euclidean metric [Arsigny *et al.*, 2006] was proposed, which is given by

$$d\left(\mathbf{T}_1,\mathbf{T}_2\right)=\left\{tr\left[\log\left(\mathbf{T}_1\right)-\log\left(\mathbf{T}_2\right)\right]^2\right\}^{1/2}. \tag{1.18}$$

Although not yielding full affine-invariance as the affine-invariant metrics, this metric is invariant by similarity (orthogonal transformation and scaling) [Vincent Arsigny, 2005], but with much simpler and faster computations.

1.5 Background on the Non-Stationarity Measure

From the 1950s through the 1970s, different types of medical imaging equipment appeared, including magnetic resonance imaging (MRI), ultrasound, X-ray and computed tomography (CT) scans. Since the late 1970s to the early 1980s, they began to be applied to assist in the diagnosis of illness and injury. Although different in the imaging principles and parameters, they all create images of the human body for clinical purposes or medical science. Since the late 1980s to the early 1990s, methods used to process these medical images began to appear in large numbers. At that time, the ultrasound image segmentation was strongly difficult because of speckle, shadows, and low contrast, as well as low spatial resolution.

A review on image segmentation techniques [Pal et al., 1993] suggested that: at that time, most techniques were not suitable for noisy environments; although Markov random field (MRF) model and neural network architecture (NNA) were robust to noise, they are computationally involved which was an insurmountable problem at that time. In contrast, the segmentation method proposed in [Liu, 1994; Liu *et al.*, 1995], based on the Non-Stationarity Measure (NSM) together with thresholding and thinning, provided a satisfactory result with good noise immunity and less computation.

The NSM was first proposed in 1994 [Liu, 1994] and mainly used for the edge detection and segmentation in ultrasound images. Based on the concept of stationarity in the random process theory, the authors established a multidimensional geometric space where the geometric meaning of stationarity and nonstationarity of signal was explained. Each point in the space, corresponding to a signal segment in the time domain, represents a (non-)stationary state. The NSM is defined as a distance from any non-stationary point to the stationary line in a given space. This distance is mapped into the time domain and considered as the NSM of the central point of a signal segment. The NSM measures the difference between two states, represented in a multidimensional geometric space, the non-stationary state and a stationary state, while conventional methods consider the difference between two intensities or the weighted sums of these differences as change measures. The impact of noise is much smaller on the measurement of the NSM than on the simple difference between two intensities in the time-domain. This is why the NSM is particularly robust to noise compared to conventional techniques based on derivatives. The advantage of the NSM operator in terms of noise immunity is theoretically proved in [Liu, 1994; Liu *et al.*, 1995].

Unfortunately, the research results in [Liu, 1994] had not been published except several short meeting papers [Liu *et al.*, 1993a; Liu *et al.*, 1992;1993b] and a French article [Liu *et al.*, 1995]. Additionally, no following study was carried out afterwards. But the good noise immunity of the NSM has been proved by its long term use in the software package *Creatools* developed by the Creatis.

1.6 Existing problems and contents of this research

Change measure is commonly used in methods for signal change detection, image edge detection, edge-based segmentation model, and feature-preserving smoothing. When dealing with biomedical images with high noise level and signals of strong randomness, the existing change measures may provide inaccurate information on change, which leads to the degradation of the performance of the change measure-based method and thus the generation of undesirable phenomena.

Analyzing the existing change measures from literature and their applications, we can summarize the problems encountered:

(1) *lack of general and robust change measure*

So far, there has been a wide variety of change measurement methods serving for the image and signal processing. They are based on different principles and possess various advantages and disadvantages. However, most of them cannot measure changes regarding multiple statistical parameters, changes in data of arbitrary dimension, and changes in data of different types. There is a lack of a general change measure robust to noise able to deal with different types of data, arbitrary dimensional signals regarding multiple statistical parameters.

(2) *false alarms and misdetections occurring in change detection of strong random signals and false edges occurring in edge detection of highly noisy images*

Signal change detection and image edge detection are the two most direct applications of change measures. In signal change detection, change measure-based methods have recently become popular because of their robustness, effectiveness, and non-supervision. However, for strong random signals, false alarms and misdetections often occur spoiling the results. With respect to image edge detection, approaches based on change measures have the advantages of being objective and unsupervised. However, for highly noisy images, false edges often occur so polluting the results.

(3) *false contours and leakages in segmentation of highly noisy images*

The edge-based GAC model guides the motion of the zero level set and stops the level set evolution using the image gradient magnitude from the external energy term. In highly noisy cases, the gradient provides inaccurate information for the edge-based GAC model so that such model may easily produce false contours or pass through weak object boundaries (leakages).

(4) *Difficulty in making a compromise between noise reduction and feature preservation in smoothing of low-SNR images*

Intensity gradient often exists in adaptive filters which aim to reduce undesirable distortions caused by noise while preserving important features. When dealing with low-SNR biomedical images, like diffusion weighted magnetic resonance images, the intensity gradient may provide inaccurate information on change due to the high noise level, which is one of the reasons for the degradation of the performance of such technique. It is difficult to achieve a

good compromise between noise reduction and feature preserving while smoothing low-SNR images.

Aiming to bring solutions to the above problems, we propose 4 contributions in this work:

(1) *Improvement and extension of the Non-Stationarity Measure*

Despite various change measurement methods, there is a lack of a general and robust change measure able to deal with different forms, arbitrary dimensional data regarding multiple statistical parameter.

Compared with other change measures, the NSM appears to be more robust to noise. Moreover, analyzing its principle, shows that the NSM possesses an intrinsic expansibility. In this work, the NSM will be improved and extended to a general change measure able to quantify changes in scalar-, vector-, and tensor-valued data of N -dimensions regarding the r^{th}-order moment.

(2) *NSM-based signal change detection and image edge detection methods and their applications*

For strongly random signals, false alarms and misdetections often occur in the change detection results. Focusing on the problem, we will propose a NSM-based change detection method and apply it to detect changes in biomedical signals: ECG and EEG.

For highly noisy images, false edges often occur in the edge detection results. Focusing on the problem, we will propose a NSM-based edge detection method and apply it to detect edges in biomedical images: cardiac diffusion weighted (DW) magnetic resonance images.

(3) *NSM-based GAC image segmentation model and its application*

In highly noisy cases, the edge-based GAC with gradient as the change measure may easily produce false contours or pass through weak object boundaries (leakages) during the segmentation process.

In this work, we will design a NSM-based geometric active contour (NSM-GAC) model and apply it to segment ultrasound images of the carotid.

(4) *NSM-based adaptive filter and its application*

When smoothing low-SNR biomedical images, it is hard to achieve a good compromise between noise reduction and feature preserving.

In fact, for any image pixel, a better operation to update its intensity is to average intensities of the pixels within its homogeneous neighborhood. So we design a new feature-preserving smoothing approach that appropriately choose the homogeneous neighborhood with the help of the robust NSM, and we apply it to enhance cardiac DW images.

The main contents and the organization of the thesis are shown in Fig. 1.2.

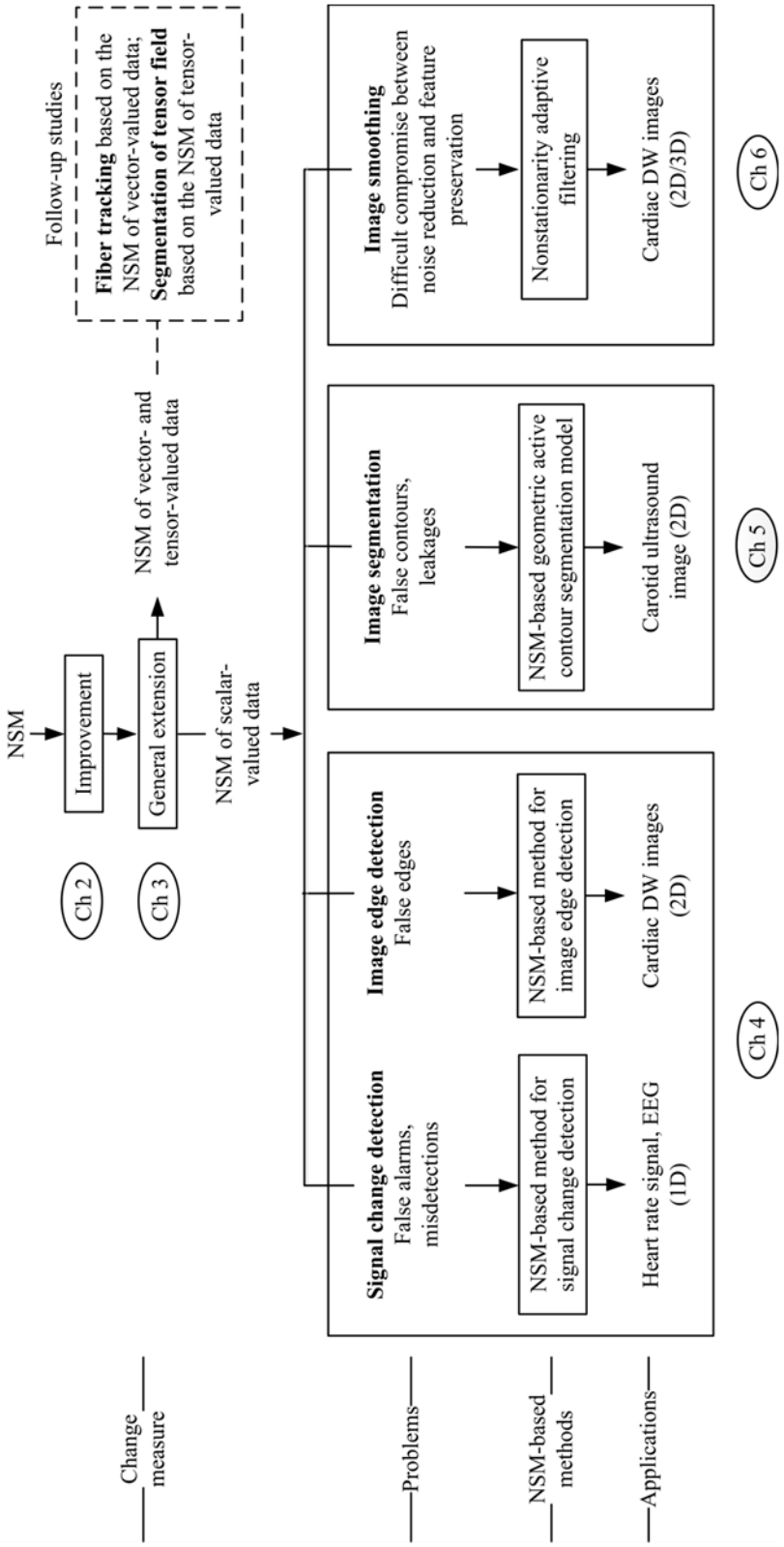

Fig. 1.2 Main contents and the organization of the thesis

Chapter 2

2 Improvement of the non-stationarity measure

Contents

Résumé en français

La mesure de nonstationarité (NSM) avait été proposée initialement comme technique de détection de rupture. Elle reflète les changements d'une image ou d'un signal et les quantifie en mesurant le degré de nonstationarité locale. Elle peut donc être considérée comme une mesure de changement. Dans le présent travail, en tant que méthode de mesure du changement, la NSM fournit des informations importantes de base pour les algorithmes de traitement d'images ou de signaux.

La méthode NSM initialement proposée présente cependant certaines limitations: a) la notion de (non-) stationnarité sur laquelle est fondée la NSM ne peut pas être utilisée pour étudier la stationnarité ou nonstationnarité des données vectorielles ou tensorielles; b) certaines notions utilisées dans la définition initiale de la NSM ne conviennent plus aux données vectorielles ou tensorielles; c) le comportement des opérateurs NSM n'a pas été étudié en détail et en profondeur; d) la sélection des paramètres cruciaux n'a pas été abordée.

Nous étions ainsi conduits à pallier ces insuffisances et à améliorer la méthode. Dans ce cadre, nous avons d'abord proposé la notion de stationnarité d'un paramètre en général comme base pour la méthode NSM. Par rapport à la notion de stationnarité classique, cette nouvelle notion définit la stationnarité par rapport à un paramètre (caractéristique) statistique du signal, et n'impose pas de forme concrète pour le paramètre et pour le signal, ce qui rend cette nouvelle notion de stationnarité plus générale, adaptative et évolutive. A partir de cette notion de stationnarité plus générale, nous avons calculé des paramètres statistiques glissants à l'aide d'une fenêtre, et construit ainsi un espace de paramètres statistiques glissant, ce qui nous a permis d'en déduire la mesure de non-stationnarité. Ensuite, le processus de construction de l'opérateur de mesure de la non-stationnarité a été formulé, et la réponse de l'opérateur à des signaux d'entrée typiques a été calculée analytiquement, ce qui nous a permis de démontrer de manière théorique la robustesse de l'opérateur d'ordre deux de mesure de la non-stationnarité. Enfin, le choix de la largeur de la fenêtre impliquée dans l'opérateur de mesure de non-stationnarité a été étudié en détail.

2.1 Introduction

Non-Stationarity Measure (NSM) was proposed as a rupture detection method in 1994 [Liu, 1994]. In fact, the NSM can reflect and quantify changes in an image or a signal through measuring its degree of non-stationarity, and therefore can be considered as a change measure. In this work, as a change measurement method, the NSM provides basic and important information of changes for various image and signal processing algorithms.

The original NSM method, however, has the following inadequacies: a) the basic concept of (non-) stationarity cannot be used to investigate the stationarity or non-stationarity of the vector- or tensor-valued signal; b) some notions, vector space for example, used in the definition of the NSM are no longer appropriate for the vector- or tensor-valued signal; c) the behaviors of the NSM operators have not been studied thoroughly; d) the selection of critical parameters was not investigated.

In this chapter, the original NSM is further improved and extended. On the one hand, the notion of general parameter stationarity (GPS) is introduced as the basis of the NSM method in Section 2.2.1. Based on the GPS, the principle of the NSM is elaborated using more appropriate notions, and a general formulation of the NSM is given (Sections 2.2.2 and 2.2.3). On the other hand, Section 2.3.1 generalizes the construction of a NSM operator; Section 2.3.2 studies the outputs of NSM operators in several typical cases; Section 2.3.3 provides the theoretical proof of the advantage of NSM operators in terms of noise immunity; Section 2.3.4 studies the selection of critical parameters.

2.2 Concept of non-stationarity measure

2.2.1 General parameter stationary

The inverse of change is stationarity. If certain feature (usually quantified by a statistical parameter) of a signal remains invariant in some sense, the signal is considered "stationary" regarding to the feature. More specifically, a signal $x(n)$ is said "stationary regarding θ" or "θ stationary" if its statistical parameter $\theta(n)$ is a constant C independent of n:

$$\theta(n) = C . \tag{2.1}$$

The statistical parameter $\theta(n)$ can be mean, variance, higher order moments, even more complex statistics that can describe the signal feature at each time instant. In addition, in respect of data type, θ can be a vector or matrix other than scalars. In this case, the constant C is correspondingly a vector-valued or a matrix-valued constant which does not change with time. Owing to the diversity of θ, the "θ stationary" can be considered the "general parameter stationary".

The GPS is different from the strict-sense stationarity (SSS) and the wide-sense stationarity (WSS) in stochastic process. Either the SSS or the WSS defines a stationary random process by requiring multiple statistical parameters to be independent of n. However, in some cases, we want to know the stationarity or non-stationarity of the signal regarding its certain statistical parameter; for instance, we want to know if a signal contains a change in its mean

but no change in its variance (its variance is independent of n, but its mean not). With the GPS, we can say that the signal is stationary regarding its variance and non-stationary regarding its mean, while it is simply considered non-stationary according to the WSS or the SSS. Different from the concept of (non-) stationarity used by the original NSM, the proposed GPS allows investigating the stationarity or non-stationarity of the vector- or tensor-valued signal.

Generally, real signals are not globally stationary but stationary only over short periods. In this work, we study the stationarity or non-stationarity of a signal within an observation window. If the statistical parameters within a $2W+1$ wide observation window g (centered on time $n=k$) satisfy

$$\theta(k-W)=\cdots=\theta(k)=\cdots=\theta(k+W), \tag{2.2}$$

the signal $x(n)$ is then locally stationary over the duration of length $2W+1$. On the contrary, with statistical parameters not satisfying (2.2), the signal $x(n)$ is locally non-stationary. For simplicity purpose, we will use the term "stationary" and "non-stationary" to mean "locally stationary" and "locally non-stationary" in the following.

With respect to the statistical parameter $\theta(n)$, it is derived from a number of signal samples. Yet, in most cases, the signal to be processed is obtained in a single acquisition. Therefore, intensities around the current time are often used as substitutes for those obtained from multiple acquisitions to estimate $\theta(n)$. For instance, time averages (or more exactly, time interval averaging) calculated within a sliding window h are often substituted for ensemble averages to estimate the r^{th}-order moment of a signal $x(n)$:

$$\hat{m}_r(n)=\sum_{i=n-L}^{n+L} h(i-n)\cdot x^r(i)=\frac{1}{2L+1}\sum_{i=n-L}^{n+L} x^r(i), \tag{2.3}$$

where L is the half width of the sliding window h. The statistical parameter estimated using a sliding window is called the moving statistical parameter in the present study. And then, the signal feature described by the moving statistical parameter is correspondingly called the moving feature.

2.2.2 Moving feature space

In this subsection, a multidimensional geometric space, called the moving feature space, is constructed based on the notion of the GPS, the moving statistical parameter and the moving feature. This space is essentially a vector space in the case of the scalar-valued signal, as it was called in the original NSM method [Liu, 1994]. In this work, the NSM is generalized to deal with the vector- and the tensor-valued data as well as the scalar-valued data. In the case of the vector- or the tensor-valued data, the multidimensional space is no longer a vector space. Therefore, instead of the notion of the vector space, the moving feature space is used in the present NSM to cover all the three cases. In the following, the NSM will be elaborated and explained using more appropriate notions like the moving feature space, the GPS, and the moving statistical parameter, etc.

The moving feature space is a $(2W+1)$-dimensional geometric space, written as $\mathbf{R}^{2W+1}$. The dimension of the moving feature space $\mathbf{R}^{2W+1}$ equals the width of the observation window g in time domain. The coordinates of a point K in the moving feature space $\left(\hat{\theta}_1, \hat{\theta}_2, \cdots, \hat{\theta}_{2W+1}\right)$ correspond to the moving statistical parameters inside the observation window g, that is, $\hat{\theta}_1 = \hat{\theta}(k-W), \cdots, \hat{\theta}_{W+1} = \hat{\theta}(k), \cdots, \hat{\theta}_{2W+1} = \hat{\theta}(k+W)$. If the coordinates of the point K equal each other, namely $\hat{\theta}_1 = \cdots = \hat{\theta}_{W+1} = \cdots = \hat{\theta}_{2W+1}$, that is, $\hat{\theta}(k-W) = \cdots = \hat{\theta}(k) = \cdots = \hat{\theta}(k+W)$, the point K then represents a stationary state corresponding to a stationary signal segment $x(k-W) = \cdots = x(k) = \cdots = x(k+W)$. All the stationary state points constitute a line Δ, called the stationary subspace, which passes through the origin. In contrast, the point whose coordinates are not all equal represents a non-stationary state corresponding to a non-stationary signal segment. All the non-stationary state points constitute a non-stationary subspace, which is the complementary part of Δ within $\mathbf{R}^{2W+1}$.

Taking Fig. 2.1 as an example, we elaborate the relationship between the time-domain signal $x(n)$ and the moving feature space $\mathbf{R}^{2W+1}$. There exists an abrupt change (or transition) at time o in the mean of the noisy signal $x(n)$. With the sliding window h, the moving statistical parameter $\hat{\theta}(n)$ (the 1st-order moment in the present example) is estimated. Moving the observation window g along $\hat{\theta}(n)$, point by point, it is observed that: 1) in the time period T_a before the change time o, the moving statistical parameters inside the observation window g nearly equal each other, namely $\hat{\theta}(k-W) = \cdots = \hat{\theta}(k) = \cdots = \hat{\theta}(k+W) = a$, therefore the signal segments $x(k-W) = \cdots = x(k) = \cdots = x(k+W)$ in T_a correspond to the same stationary point A in $\mathbf{R}^{2W+1}$; 2) in the close vicinity of the change time o, the moving statistical parameters inside the observation window g are not all equal, no longer satisfying (2.2) - the signal segments in this interval correspond to the points on the transition trajectory Γ in the non-stationary subspace; 3) in the time period T_b after the change time o, the moving statistical parameters inside the observation window g nearly equal each other, namely $\hat{\theta}(k-W) = \cdots = \hat{\theta}(k) = \cdots = \hat{\theta}(k+W) = b$, and therefore signal segments $x(k-W) = \cdots = x(k) = \cdots = x(k+W)$ in T_b correspond to the same stationary point B in $\mathbf{R}^{2W+1}$.

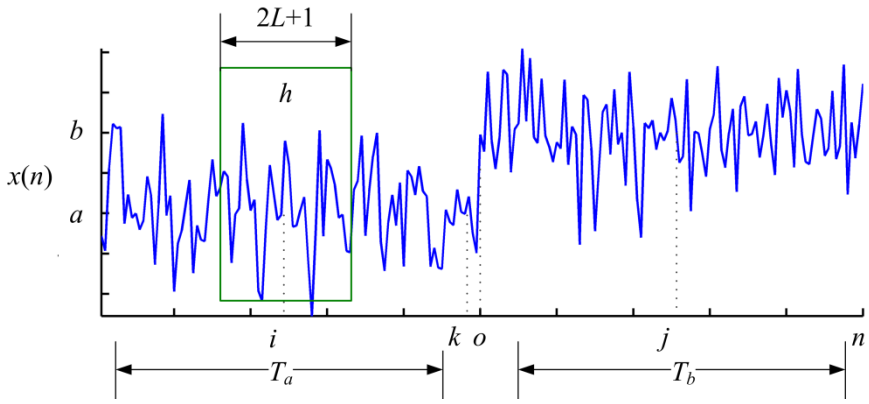

(a)

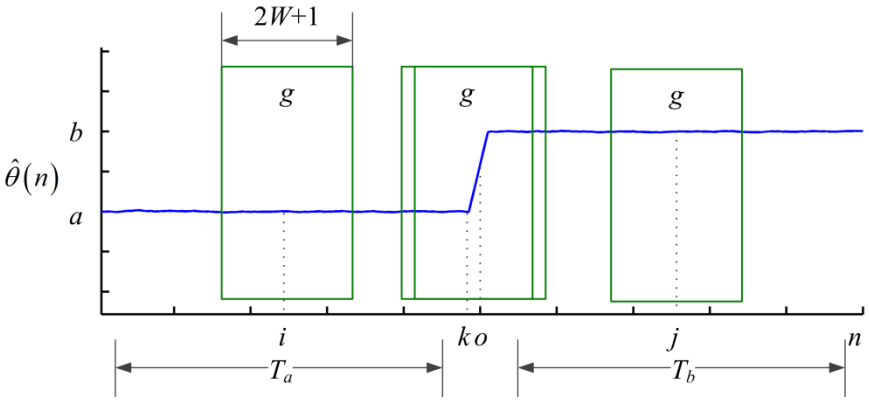

(b)

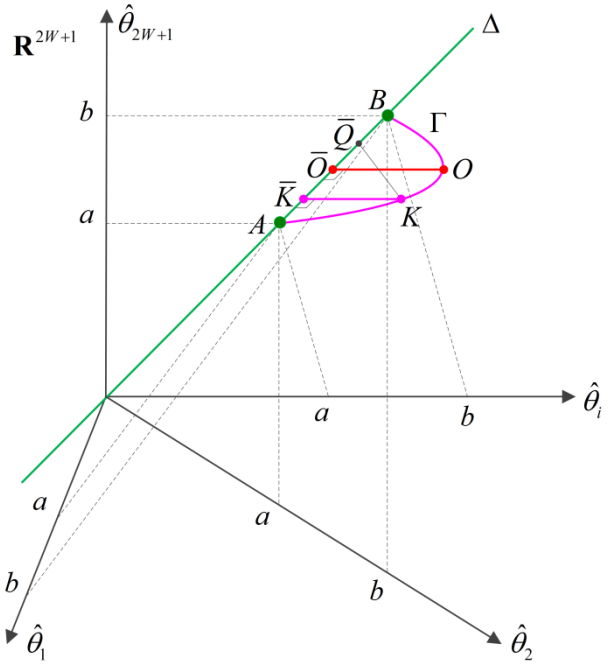

(c)

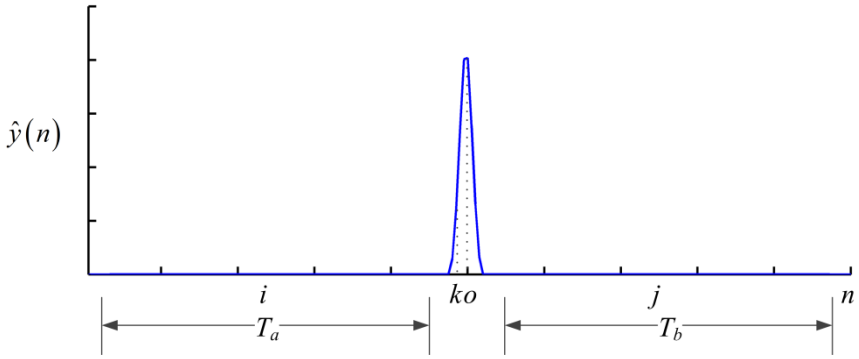

(d)

Fig. 2.1 Relationship among the signal $x(n)$, the moving statistical parameter $\hat{\theta}(n)$, the moving feature space $\mathbf{R}^{2W+1}$, and the NSM $\hat{y}(n)$. (a) Signal $x(n)$ with a transition at time o. (b) Moving statistical parameter $\hat{\theta}(n)$. (c) Multidimensional moving feature space $\mathbf{R}^{2W+1}$. (d) NSM $\hat{y}(n)$ of the signal $x(n)$.

2.2.3 Non-stationarity measure

The non-stationarity measure (NSM) is defined as a distance $d(K,\Delta)$ from the state point K to the stationary line Δ in the moving feature space $\mathbf{R}^{2W+1}$, see Fig. 2.1(c). This distance is mapped into the time domain and taken as the NSM of the central point of the observation window, see Fig. 2.1(d). Using Ψ to represent the operation of the NSM operator, we have

$$y(n) = \Psi[x(n)] = d(K,\Delta). \tag{2.4}$$

If $K \in \Delta$, that is, $\theta_i = \text{constant}$, then $d(K,\Delta) = 0$;

If $K \notin \Delta$, that is, $\theta_i \neq \text{constant}$, then $d(K,\Delta) \neq 0$,

where $i = 1,2,\cdots,2W+1$. According to the definition of the distance from a point to a line, the NSM is then calculated as

$$d(K,\Delta) = \min_{\bar{Q}\in\Delta} d(K,\bar{Q}) = d(K,\bar{K}), \tag{2.5}$$

where $\bar{Q}$ is an arbitrary point on the stationary line Δ, and $\bar{K}$ is the stationary point which makes $d(K,\Delta)$ minimal. The maximal distance from the transition trajectory Γ to the stationary line Δ in the case of Fig. 2.1 is obtained at the non-stationary point O, which is expressed as

$$d(O,\Delta) = \max_{K\in\Gamma} d(K,\Delta) = \max_{K\in\Gamma} \min_{\bar{Q}\in\Delta} d(K,\bar{Q}) = d(O,\bar{O}). \tag{2.6}$$

The signal segments in the time periods T_a and T_b respectively correspond to the stationary points $A \in \Delta$ and $B \in \Delta$, and the output $\hat{y}(n)$ of the NSM operator in the two periods equals zero (Fig. 2.1(d)). For the signal segments in the interval between T_a and T_b, the corresponding transition trajectory Γ gradually deviates from the stationary line Δ,

achieves the maximum distance at the point O, then gradually approaches the line Δ, and ends at the point B. Plotting the distances from the non-stationary state points in Γ to the stationary line Δ arrives at the NSM curve, see Fig. 2.1(d). It is seen that the NSM curve presents a symmetrical peak, whose position of indicates the location of the abrupt change, and the height of the peak giving the magnitude of the change.

In principle, any definition of the distance d can be used to calculate the NSM as long as it can appropriately quantify the distance between the non-stationary state point and the stationary line Δ. In this work, following the definition of the *p*-norm, we define the distance from point K to its stationary point $\bar{K}$ as

$$d\left(K,\bar{K}\right)=\sqrt[p]{\sum_{i=1}^{2W+1} g(i)\cdot\left[dis\left(\hat{\theta}_i,\bar{\theta}\right)\right]^p}, \tag{2.7}$$

where $dis\left(\hat{\theta}_i,\bar{\theta}\right)$, $i=1,2,\cdots,2W+1$, represents the dissimilarity between the coordinate $\hat{\theta}_i$ of point K and the coordinate $\bar{\theta}$ of the stationary point $\bar{K}$, and it is usually defined as $\left|\hat{\theta}_i-\bar{\theta}\right|$ for the scalar-valued signal; $g(i)$, the weighted coefficient of $dis\left(\hat{\theta}_i,\bar{\theta}\right)$, determines the observation window function g with $\sum_{i=1}^{2W+1} g(i)=1$. Usually, we substitute d^p for d to counteract the operation of the p^{th} root in the definition of d. Therefore, we have

$$d\left(K,\bar{K}\right)=\sum_{i=1}^{2W+1} g(i)\cdot\left[dis\left(\hat{\theta}_i,\bar{\theta}\right)\right]^p. \tag{2.8}$$

Here *p*, a non-zero natural number, is taken as the order of the NSM operator. In addition, the coordinate $\bar{\theta}$ of $\bar{K}$ can be estimated by setting to zero the partial derivative of d with respect to $\bar{\theta}$, $\partial d/\partial\bar{\theta}=0$.

To sum up, the NSM $\hat{y}(n)$ of the scalar-valued signal $x(n)$ in time domain can be expressed as

$$\hat{y}(n)=\square\left[x(n)\right]=\sum_{i=n-W}^{n+W} g(i)\cdot\left|\hat{\theta}(i)-\bar{\theta}\right|^p. \tag{2.9}$$

The NSM measures the difference between two states in a multidimensional geometric space, the non-stationary state (corresponding to the current moment in time domain) and a stationary state, while other methods take the difference between intensities at two moments or the weighted sums of these differences as change measures. The impact of noise is much smaller on the measurement of NSM than on the simple difference between two intensities in time-domain. This is why the NSM is particularly robust to noise compared to conventional techniques based on the derivative.

2.3 Operators of non-stationarity measure

2.3.1 Construction of NSM operators

The construction of a NSM operator needs to account for two points:

a. The signal feature to study, which helps determine the statistical parameter θ in (2.8).

b. The choice of the distance between the non-stationary state point and the stationary line Δ, which amounts for determining $dis\left(\hat{\theta}_i, \bar{\theta}\right)$, the weighted coefficient $g(i)$ and the order p of the NSM in (2.8).

The procedure of calculating the NSM of a signal, see Fig. 2.2, includes:

1. estimate the moving statistical parameter $\hat{\theta}$ with a sliding window h;
2. formulate the NSM according to the statistical parameter $\hat{\theta}$ and the distance d;
3. estimate $\bar{\theta}$ by $\partial d / \partial \bar{\theta} = 0$;
4. calculate $d\left(K, \bar{K}\right)$ as the NSM of signal $x(n)$ at the current time, the center of the observation window g.

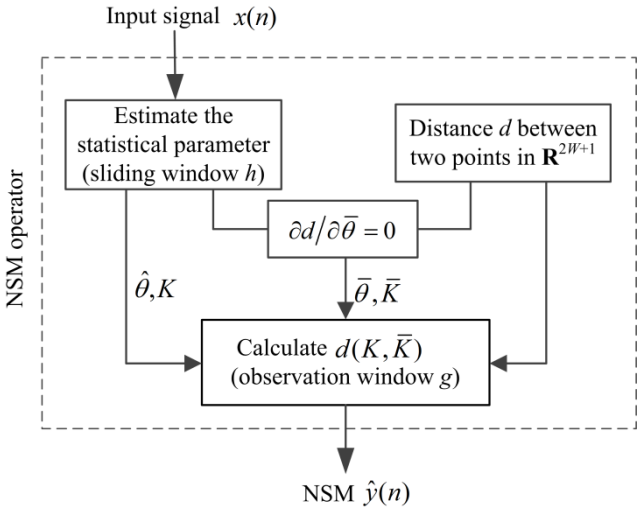

Fig. 2.2 Diagram for the calculation of the NSM $\hat{y}(n)$

We now elaborate the construction of a NSM operator by taking the 1st-order moment and the Euclidean norm as an example. The order p of the NSM in (2.9) then takes the value 2. First, we use a rectangular window function $h(n)$ of width $2L+1$ to estimate the moving statistical parameter

$$\begin{aligned}\hat{\theta}(n) &= \hat{m}_1(n) \\ &= \sum_{i=n-W}^{n+W} h(i-n)\cdot x(i) \\ &= \frac{1}{2W+1}\sum_{i=n-W}^{n+W} x(i).\end{aligned} \tag{2.10}$$

Second, according to (2.9), the 2nd-order NSM of $x(n)$ regarding the 1st-order moment can be expressed as

$$\hat{y}_1(n) = \Box\left[x(n)\right] = \sum_{i=n-W}^{n+W} g(i-n)\cdot\left|\hat{m}_1(i)-\bar{m}_1\right|^2, \tag{2.11}$$

where $\bar{m}_1$ is the coordinate of the stationary state point $\bar{K}$. Setting $\partial d/\partial\bar{\theta}=0$, the analytical expression of $\bar{m}_1$ is obtained as

$$\bar{m}_1 = \sum_{i=n-W}^{n+W} g(i-n)\cdot\hat{m}_1(i)\,. \tag{2.12}$$

Substituting equation (2.12) into (2.11), we arrive at

$$\hat{y}_1(n) = \sum_{i=n-W}^{n+W} g(i-n)\cdot\left[\hat{m}_1(i)\right]^2 - \left[\sum_{i=n-W}^{n+W} g(i-n)\cdot\hat{m}_1(i)\right]^2, \tag{2.13}$$

which is illustrated by the block diagram in Fig. 2.3.

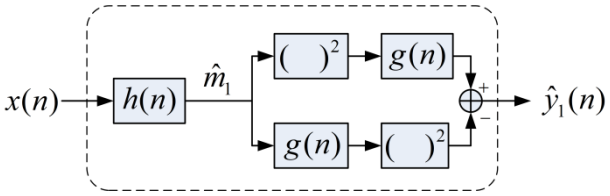

Fig. 2.3 Block diagram of the 2nd-order NSM operator regarding the 1st-order moment of the signal $x(n)$

Usually, the half width L of the sliding window h takes the same value as the half width W of the observation window g, that is, $L=W$.

2.3.2 Outputs of NSM operators

The basic properties of the outputs of NSM operators are first given in this section. Then the outputs of the NSM operators in a number of typical cases are studied. To keep the theoretical analysis simple, continuous signals instead of discrete ones are addressed in the section.

Assume that the input signal $x(t)$ is composed of a useful signal $s(t)$ (containing a discontinuity) and a zero mean noise $n(t)$:

$$x(t) = s(t) + n(t)\,. \tag{2.14}$$

The response of the p^{th}-order NSM operator to $x(t)$ can be expressed as:

$$\begin{aligned}\hat{y}_x(t) &= \int_{\Re} \left|(x*h)(\tau) - (x*h*g)(\tau)\right|^p g(t-\tau)d\tau \\ &= \int_{\Re} \left|(s*h)(\tau) - (s*h*g)(\tau) + (n*h)(\tau) - (n*h*g)(\tau)\right|^p g(t-\tau)d\tau\end{aligned}, \tag{2.15}$$

where both the sliding window function $h(t)$ and the observation window function $g(t)$ are symmetric and normalized. When $n(t) = 0$, the response of the NSM operator to the useful signal $s(t)$ is expressed as

$$\hat{y}_s(t) = \int_{\Re} \left|(s*h)(\tau) - (s*h*g)(\tau)\right|^p g(t-\tau)d\tau\,. \tag{2.16}$$

Obviously, $\hat{y}_s(t)$ has three properties [Liu, 1994]:

Property 1 *Amplitude-shift invariance*

When the amplitude of the input signal shifts to an arbitrary magnitude κ, that is, $s(t)$ shifts to $s(t)+\kappa$, the NSM remains invariant

$$\hat{y}_{s+\kappa}(t) = \hat{y}_s(t)\,. \tag{2.17}$$

Property 2 *Multiplication by a constant*

If the input signal $s(t)$ is multiplied by a constant κ, namely $\kappa \cdot s(t)$, the NSM becomes κ^p times greater than before

$$\hat{y}_{\kappa\cdot s}(t) = |\kappa|^p \cdot \hat{y}_s(t)\,. \tag{2.18}$$

Property 3 *Symmetry*

If the input signal curve shows odd symmetry after translation, that is $s(t) = -s(-t)$, the NSM of $s(t)$ also exhibits even symmetry

$$\hat{y}_s(-t) = \hat{y}_s(t)\,. \tag{2.19}$$

The original NSM [Liu, 1994] gave an analysis on the distances (the NSM) corresponding to $p=1$, $p=2$, and $p=\infty$. Compared with the case of $p=1$ or $p=\infty$, theoretical results can be obtained more easily with $p=2$. We take three typical 2nd-order NSM operators ($p=2$) as examples, and study their responses to three typical input signals. The 2nd-order NSM operator can be expressed, in continuous form, as

$$\begin{aligned}\hat{y}_s(t) &= \square\left[s(t)\right] \\ &= \left[(s*h)^2 * g\right](t) - (s*h*g)^2(t)\end{aligned}, \tag{2.20}$$

where $h(t)$ is a rectangular window function of width $2W$:

$$h(t)=\frac{1}{2W}rect\left(\frac{t}{2W}\right). \tag{2.21}$$

2.3.2.1 Three typical input signals

The ideal step signal s_1 describes the abrupt modification of its mean value, which is the most typical change in theory, see Fig. 2.4(a). s_1 is mathematically defined as

$$s_1(t)=u(t)=\begin{cases}0, & t\le 0\\ 1, & t>0\end{cases}. \tag{2.22}$$

The step signal with a transition band s_2 represents a common case in practice, where the change might not be instantaneous, see Fig. 2.4(b). s_2 is mathematically defined as

$$s_2(t)=\begin{cases}0, & t\le -\alpha/2\\ t/\alpha+1/2, & -\alpha/2<t\le\alpha/2\\ 1, & t>\alpha/2\end{cases}, \tag{2.23}$$

where α represents the width of the transition band, which is in general shorter than the observation window width $2W$.

The step signal mixed with a ramp s_3 describes the fact that, sometimes, slow changes exist in the background, so that the profile of a clear edge gradually varies over a wide range, see Fig. 2.4(c). s_3 can be mathematically defined as

$$s_3(t)=u(t)+\beta\cdot t, \tag{2.24}$$

where β is the slope of the ramp. If $\beta\ge 0$, the step is in the same direction as the ramp; if $\beta\le 0$, the step and the ramp are in reverse directions.

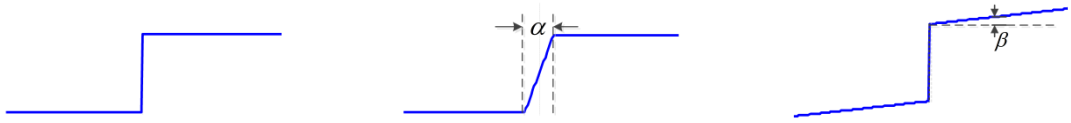

(a) (b) (c)

Fig. 2.4 Three typical input signals. (a) Ideal step s_1. (b) Step with transition band s_2. (c) Mixture of step and ramp s_3.

2.3.2.2 Three representative observation windows

Different observation window functions can result in different distances d, leading to different NSM operators. The original NSM studied the behavior of the NSM operator using a rectangular window function. In this section, another two representative observation window functions are given, and the typical outputs of the corresponding NSM operators are studied.

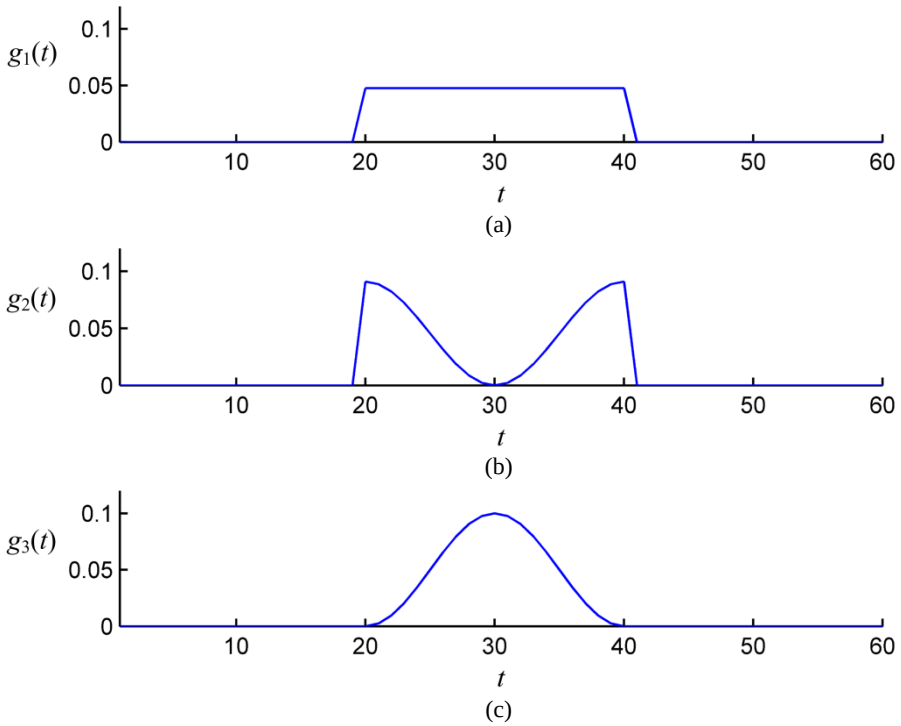

Fig 2.5 Three typical observation window functions *g*. (a) Rectangular g_1. (b) Concave g_2. (c) Convex g_3.

To differentiate the three window functions, g_1, g_2 and g_3 are used to designate the rectangular, the concave and the convex function respectively. They are mathematically expressed as:

$$g_1(t) = \frac{1}{2W} rect\left(\frac{t}{2W}\right), \tag{2.25}$$

$$g_2(t) = \frac{1-\cos(\pi t/W)}{2W}, \tag{2.26}$$

$$g_3(t) = \frac{1+\cos(\pi t/W)}{2W}, \tag{2.27}$$

and illustrated in Fig. 2.5.

2.3.2.3 Typical outputs of the NSM operators

All the three typical input signals show odd symmetry after translation, so their NSM curves present even symmetric peaks. The positions of the apexes indicate the locations of the changes, and the heights of the peaks reflect the magnitudes of the changes.

Table 2.1 gives the theoretical heights of the output peaks regarding to three typical input signals s_1, s_2, s_3 and three representative window functions g_1, g_2 and g_3. Their deductions are provided in Appendices A to C, and the heights of the output peaks corresponding to the rectangular window function g_1 were given in [Liu *et al.*, 1995]. In

order to differentiate the heights of different output peaks, H_{ij} is used to represent the peak height corresponding to the input signal s_i and the window function g_j. Fig 2.6 shows the corresponding output curves of the NSM operators.

From the theoretical results in Table 2.1 and the experimental ones in Fig. 2.6, we can obtain the following statements.

(1) The outputs of the NSM operators present symmetric peaks. The widths of these peak feet are related to the input signals s_1, s_2, s_3 and the observation/sliding window width $2W$. For the input signals s_1 and s_3, the feet of the peaks are $4W$ wide, while for the input signal s_2, they are $4W+\alpha$.

(2) For the same observation window function, the responses of the NSM operators to different input signals show similar shapes but different heights $H_{3j} > H_{1j} > H_{2j}$. The transition band in s_2 decreases the abruptness of the step change, hence s_2 is not so non-stationary as s_1, therefore $H_{1j} > H_{2j}$. The change in s_3 consists of both the step as in s_1 and the ramp, therefore $H_{3j} > H_{1j}$.

Table 2.1 Heights of the output peaks regarding to typical input signals and window functions

Input signal	Observation window	Heights of the output peaks of NSM operators
Ideal step s_1	Rectangular g_1	$H_{11} = \frac{1}{12}$
	Concave g_2	$H_{12} = \frac{1}{12} + \frac{1}{2\pi^2}$
	Convex g_3	$H_{13} = \frac{1}{12} - \frac{1}{2\pi^2}$
Step with transition band s_2	Rectangular g_1	$H_{21} = \frac{1}{12} - \frac{1}{24}\gamma^2 + \frac{13}{960}\gamma^3$
	Concave g_2	$H_{22} = \frac{1}{12} - \frac{\gamma^2}{24} + \frac{13\gamma^3}{960} - \frac{1}{4\pi^3}\sin(\gamma\pi) - \frac{\gamma}{16\pi^2} + \frac{3}{8\pi^4\gamma} + \frac{1}{4\pi^2} - \frac{3}{4\pi^4\gamma}\cos(\gamma\pi) + \frac{1}{4\pi^3\gamma}\sin(\gamma\pi) + \frac{3}{8\pi^5\gamma^2}\sin(\gamma\pi)$
	Convex g_3	$H_{23} = \frac{1}{12} - \frac{\gamma^2}{24} + \frac{13\gamma^3}{960} + \frac{1}{4\pi^3}\sin(\gamma\pi) + \frac{\gamma}{16\pi^2} - \frac{3}{8\pi^4\gamma} - \frac{1}{4\pi^2} + \frac{3}{4\pi^4\gamma}\cos(\gamma\pi) - \frac{1}{4\pi^3\gamma}\sin(\gamma\pi) - \frac{3}{8\pi^5\gamma^2}\sin(\gamma\pi)$
Mixture of step and ramp s_3	Rectangular g_1	$H_{31} = \frac{(2\beta W+1)^2}{12}$
	Concave g_2	$H_{32} = (2\beta W+1)^2(\frac{1}{12} + \frac{1}{2\pi^2})$
	Convex g_3	$H_{33} = (2\beta W+1)^2(\frac{1}{12} - \frac{1}{2\pi^2})$

Note $\gamma = \alpha / 2W$ and $0 < \gamma \le 1$.

(3) For the same input signal, the outputs of the NSM operators corresponding to different window functions show different heights: $H_{i2} > H_{i1} > H_{i3}$. It is seen from Table 2.1 that, for

s_1 and s_3, there is clearly $H_{12} > H_{11} > H_{13}$ and $H_{32} > H_{31} > H_{33}$. For s_2, the similar conclusion arises even though it is not apparent because of the complicated expression form. From the trend graph of H_{2j} in Fig. 2.7, it is directly seen that $H_{22} > H_{21} > H_{23}$ when $0 \le \gamma \le 1$, namely, $0 \le \alpha \le 2W$.

(4) Using the convex window function g_3, the output peaks may have flat tops, which make it difficult to locate the exact positions of the changes.

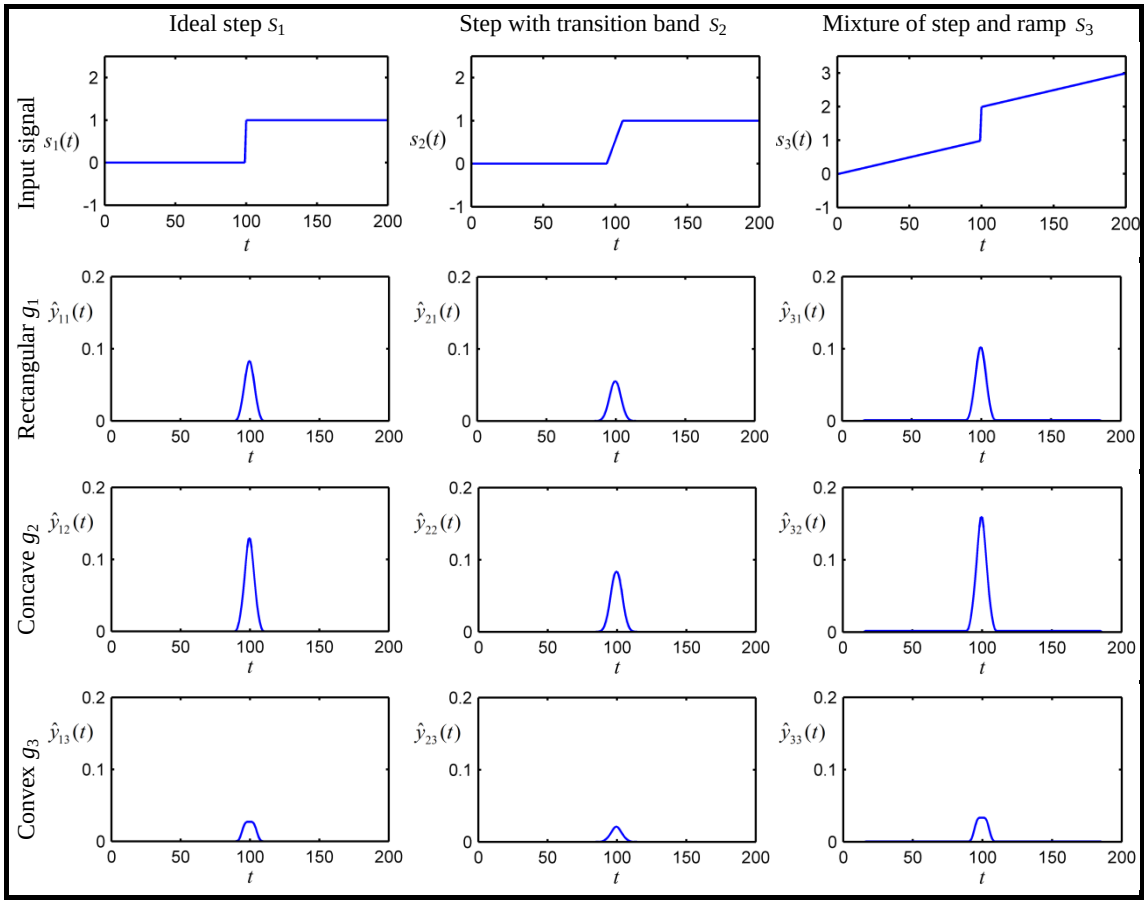

Fig. 2.6 Output peaks of NSM operators regarding to typical input signals and window functions

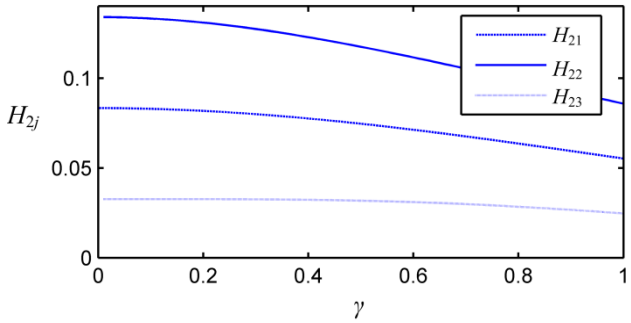

Fig. 2.7 Trend graph of H_{2j} for the step with transition band s_2

Fig. 2.8 shows the responses of the NSM operators to the three typical input signals corrupted by Gaussian noises with zero mean and 0.33 standard deviation. Note that, in this work, the quality of the input signal is usually evaluated with the Contrast-to-Noise Ratio (CNR) which is defined as the ratio of the amplitude of the change to the standard deviation of the noise, A/σ_n. The CNRs of these noisy input signals are about 3. It is seen that, despite low input CNRs, the NSM operators using the rectangular and concave window functions achieve higher output SNRs (theoretical analysis on the output SNRs is given in the next Section 2.3.3). From the apexes of the output peaks, the positions of changes can be located accurately in such noisy cases, which demonstrates the excellent noise-immunity abilities of the NSM operators.

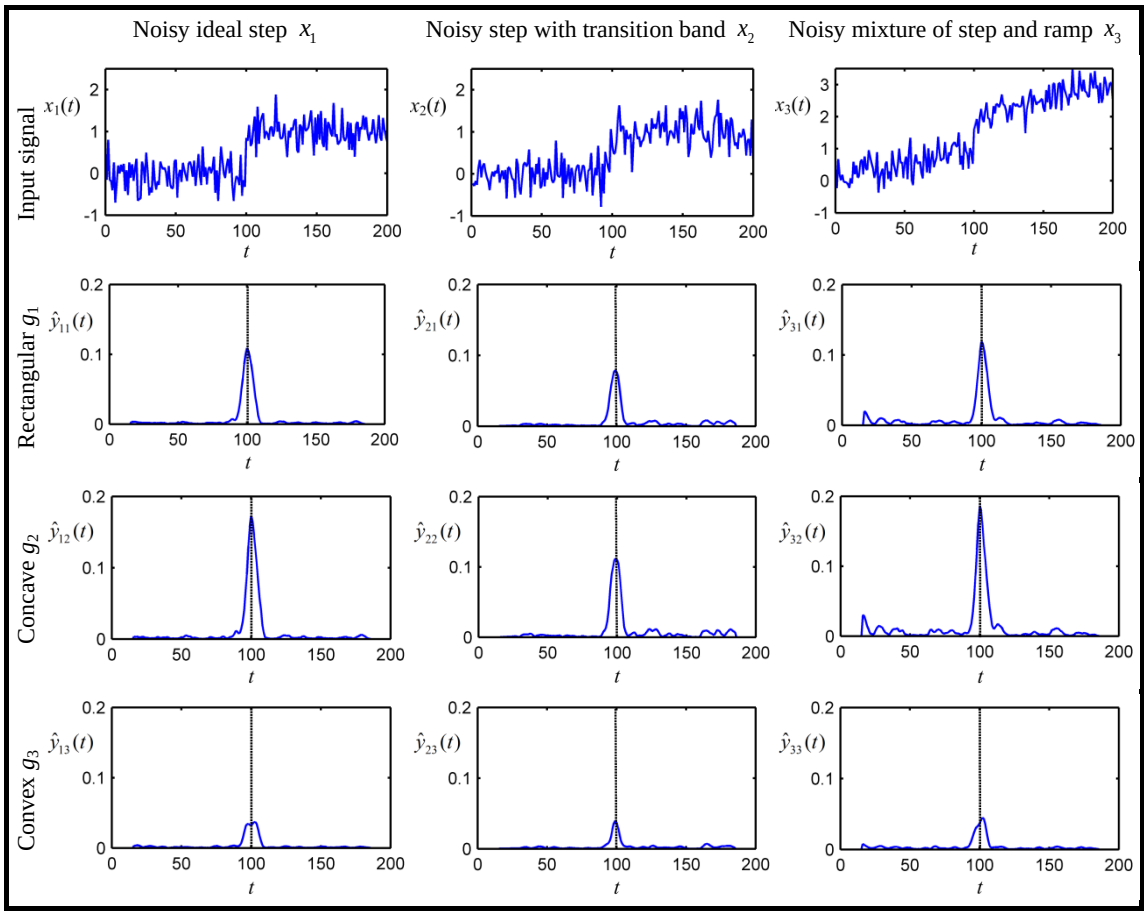

Fig. 2.8 Response peaks of the NSM operators to noisy input signals.

From the theoretical analyses and experimental results, it is concluded that:

(1) the observation window function influences the output of NSM operators: choosing the rectangular or concave function instead of convex function can generate a higher output SNR;

(2) the concave window function g_2 would be the best choice in practice as long as it can be implemented with a fast algorithm, since it provides the highest output SNR;

(3) the rectangular function g_1 is a good choice in practice because it requires less computation time and provides a high output SNR;

(4) similar to other change measures using sliding windows, the resolution of the NSM operator is related to the width of the window. Generally, changes at the details smaller than the width of the window might not be measured accurately.

In the above discussion, the heights of the step-like changes in the three input signals equal 1. According to the properties of the output of the NSM operator, it is known that, for the change of height *A*, the output peak will be A^p times higher than before, where p is the order of the operator.

2.3.3 Output signal to noise ratio

The output SNRs of the 2nd-order NSM operators adopting the three typical observation windows are studied and compared with that of the Canny operator. The noise-immunity ability of the NSM operator is proved theoretically and demonstrated by means of representative experiments.

Assume the input signal $x(t)$ is composed of a step signal $A \cdot u(t)$ and an additive white Gaussian noise $n(t)$ with mean 0 and standard deviation σ_n, that is,

$$x(t) = A \cdot u(t) + n(t) . \tag{2.28}$$

The output signal-to-noise ratio (SNR) is defined as the ratio of the height of the response peak to the step signal and the square root of the mean-squared noise response [Canny, 1986], expressed as

$$\Sigma = \frac{\hat{y}_{A \cdot u}(0)}{\sqrt{D^2\left(\hat{y}_n(t)\right)}}, \tag{2.29}$$

where $D^2\left(\hat{y}_n(t)\right)$ is the variance of the noise response, equivalent to the mean-squared noise response.

2.3.3.1 Output SNR of the NSM operator

$\Sigma_{\mathrm{NSM},1}$, $\Sigma_{\mathrm{NSM},2}$ and $\Sigma_{\mathrm{NSM},3}$ are respectively used to denote the output SNRs of the 2nd-order NSM operators corresponding to the three window functions g_1, g_2 and g_3. When using the rectangular function g_1, the height of the response peak to the step signal $A \cdot u(t)$ is written as $\hat{y}_{A \cdot u}(0) = A^2/12$ (refer to Table 2.1 and the property 2 of the output of the NSM operator in Section 2.3.2), and the square root of the mean-squared noise response is expressed as

$$D^2(\hat{y}_n(t)) = \frac{\sigma_n^4}{45W^2} . \tag{2.30}$$

According to (2.29), the output SNR of the NSM operator corresponding to the rectangular function g_1 is obtained as

$$\Sigma_{\mathrm{NSM},1} = \frac{A^2/12}{\sqrt{\sigma_n^4/45W^2}} \approx 0.28\left(\frac{A}{\sigma_n}\right)^2 (2W). \tag{2.31}$$

When using the concave function g_2, we have $\hat{y}_{A\cdot u}(0) = A^2(1/12 + 1/2\pi^2)$ and

$$D^2(\hat{y}_n(t)) = \frac{\sigma_n^4}{45W^2} + \frac{\sigma_n^4}{12\pi^2W^2} + \frac{55\sigma_n^4}{32\pi^4W^2}. \tag{2.32}$$

Therefore, the output SNR of the NSM operator corresponding to the concave function g_2 is

$$\Sigma_{\mathrm{NSM},2} = \frac{\frac{A^2}{12} + \frac{A^2}{2\pi^2}}{\sqrt{\frac{\sigma_n^4}{45W^2} + \frac{\sigma_n^4}{12\pi^2W^2} + \frac{55\sigma_n^4}{32\pi^4W^2}}} \approx 0.30\left(\frac{A}{\sigma_n}\right)^2 (2W). \tag{2.33}$$

When using the convex function g_3, we have $\hat{y}_{A\cdot u}(0) = A^2(1/12 - 1/2\pi^2)$ and

$$D^2(\hat{y}_n(t)) = \frac{\sigma_n^4}{45W^2} + \frac{\sigma_n^4}{12\pi^2W^2} - \frac{73\sigma_n^4}{32\pi^4W^2}. \tag{2.34}$$

So, we have

$$\Sigma_{\mathrm{NSM},3} = \frac{\frac{A^2}{12} - \frac{A^2}{2\pi^2}}{\sqrt{\frac{\sigma_n^4}{45W^2} + \frac{\sigma_n^4}{12\pi^2W^2} - \frac{73\sigma_n^4}{32\pi^4W^2}}} \approx 0.19\left(\frac{A}{\sigma_n}\right)^2 (2W). \tag{2.35}$$

The deductions of $\Sigma_{\mathrm{NSM},1}$, $\Sigma_{\mathrm{NSM},2}$ and $\Sigma_{\mathrm{NSM},3}$ are provided in Appendix D.

2.3.3.2 Comparison with the Canny operator

The response of the Canny operator to the step signal $A\cdot u(t)$ is given by

$$y_{A\cdot u}(t) = \int_{-\infty}^{\infty} A\cdot u(\tau) * G'_\sigma(t-\tau)d\tau, \tag{2.36}$$

where $G'_\sigma(t)$ is the first derivative of a Gaussian function, which is used to approximate the optimal form of the Canny operator, and σ is the standard deviation of the Gaussian function $G_\sigma(t)$. The height of the response peak to the step signal $A\cdot u(t)$ is obtained at $t=0$, equal to $\frac{A}{\sqrt{2\pi}\sigma}$, and the square root of the mean-squared noise response is calculated as

$$D^2\left(y_n(t)\right) = \sigma_n^2\int_{-\infty}^{\infty}\left(G'(t)\right)^2 dt = \frac{\sigma_n^2}{4\sqrt{\pi}\sigma^3}. \tag{2.37}$$

It follows that the output SNR of the Canny operator is given by

$$\Sigma_{\text{Canny}} = \frac{A/\left(\sqrt{2\pi}\sigma\right)}{\sigma_n\sqrt{1/\left(4\sqrt{\pi}\sigma^3\right)}} \approx 1.06\frac{A}{\sigma_n}\sqrt{\sigma}\,. \tag{2.38}$$

The 2nd-order NSM operators corresponding to the rectangular window g_1 are chosen to be compared with the Canny operator. Both the NSM operator and the Canny operator are the change measures using sliding windows, and their responses to a change therefore appear as peaks with certain widths. For a fair comparison, the two operators are compared based on the notion of "normalized width L_n". The normalized width L_n is defined as the total area of the response to an ideal step signal divided by the height of the output peak [Liu *et al.*, 1995].

For the NSM operator, the normalized width is calculated as:

$$L_{n,\text{NSM}} = \frac{\int_{-\infty}^{\infty}\hat{y}_u(t)dt}{1/12} = \frac{4}{5}\times 2W = \frac{8}{5}W\,. \tag{2.39}$$

For the Canny operator, the normalized width is calculated as:

$$L_{n,\text{Canny}} = \frac{\int_{-\infty}^{\infty}u(t)*G'_\sigma(t)dt,}{A/\sqrt{2\pi}\sigma} = \sqrt{2\pi}\sigma. \tag{2.40}$$

Let $L_{n,\text{NSM}}$ equal $L_{n,\text{Canny}}$, we then get

$$\sigma = \frac{8}{5\sqrt{2\pi}}W \approx 0.32\times 2W\,. \tag{2.41}$$

So the output SNR of the Canny operator becomes

$$\Sigma_{\text{Canny}} = \frac{A}{\sigma_n}\sqrt{\frac{16W}{5\pi\sqrt{2}}} \approx 0.60\frac{A}{\sigma_n}\sqrt{2W}\,. \tag{2.42}$$

It can be seen from (2.31) and (2.42) that, w.r.t. the window width $2W$, $\Sigma_{\text{NSM},1}$ is a straight line whose slope is equal to $0.28\left(A/\sigma_n\right)^2$, while Σ_{Canny} is a part of a hyperbola. A series of curve pairs of $\Sigma_{\text{NSM},1}$ and Σ_{Canny} can be drawn corresponding to different input CNR A/σ_n. The higher the input CNR is, the steeper the curve pair becomes. The two curves of output SNR cross at the point $\left(4.59\sigma_n^2/A^2, 1.29\right)$. With the increase of the input CNR A/σ_n, the intersection moves towards the origin along the horizontal line $\Sigma_{\text{NSM},1} = \Sigma_{\text{Canny}} = 1.29$. Above the line $\Sigma_{\text{NSM},1} = \Sigma_{\text{Canny}} = 1.29$, we always have $\Sigma_{\text{NSM},1} > \Sigma_{\text{Canny}}$. The possibility for $\Sigma_{\text{NSM},1} < \Sigma_{\text{Canny}}$ exists in the small area under the line. However, such case is meaningless in practice, since the two output SNRs are so low that both of them are not reliable for deciding

the presence of a change or not. Fig. 2.9 shows two pairs of curves corresponding to the input CNRs 3 and 2.15 respectively.

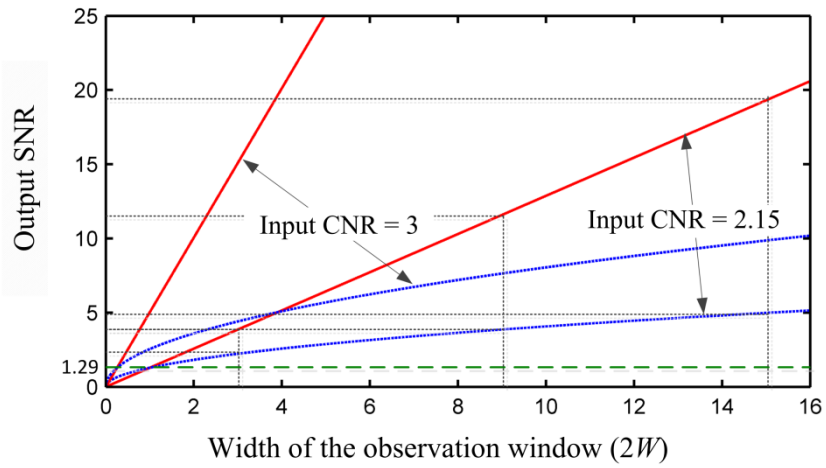

Fig. 2.9 Curves of output SNR of the NSM and the Canny operators. Red solid line: the NSM operator. Blue dashed line: the Canny operator.

In order to study the performance of the two change measures in low input CNR case, an experience of simulation is given corresponding to the above theoretical analysis. Fig. 2.10(a) shows a highly noisy input signal whose input CNR equals 2.15. The signal is a step of height $A=1$ corrupted by a Gaussian centered noise. The responses of the NSM operator and the Canny operator are normalized to allow for quantitative comparisons. When the window width takes a small value like 3, see Fig. 2.10(b), it is difficult to locate the discontinuity from both outputs because of the low output SNRs ($\Sigma_{\mathrm{NSM},1}\approx 3.88$, $\Sigma_{\mathrm{Canny}}\approx 2.24$ estimated from (2.31) and (2.42)). With the increase of $2W$, the two operators' abilities to suppress noise improve to varying degrees, as well as their output SNRs. In Fig. 2.10(c) ($2W=9$), noise is substantially reduced by the NSM operator ($\Sigma_{\mathrm{NSM},1}\approx 11.65$), and consequently the peak marking the discontinuity definitely emerges from the disturbing waves. However, for the Canny operator, the output still shows large fluctuations ($\mathrm{SNR}_{\mathrm{Canny}}\approx 3.87$) although better than in Fig. 2.10(b). With the continuing increase of the window width ($2W=15$), the NSM operator exhibits much better performance, as shown in Fig. 2.10(d) where most of the NSM values related to the two stationary periods approach zero while achieving a high maximum ($\Sigma_{\mathrm{NSM},1}\approx 19.41$) at the location of the discontinuity. In contrast, the performance of the Canny operator improves little ($\Sigma_{\mathrm{Canny}}\approx 4.99$). Hence the NSM offers a real and reliable knowledge about changes immersed within the noisy input signal, whereas less confidence can be given to the Canny operator that may present some false information in such a noisy context. But it is necessary to mention that increasing the window width $2W$ leads to lower the resolution. According to (2.39), the normalized width L_n equals 2.4 with $2W=3$, 7.2 with $2W=9$, and 12 with $2W=15$.

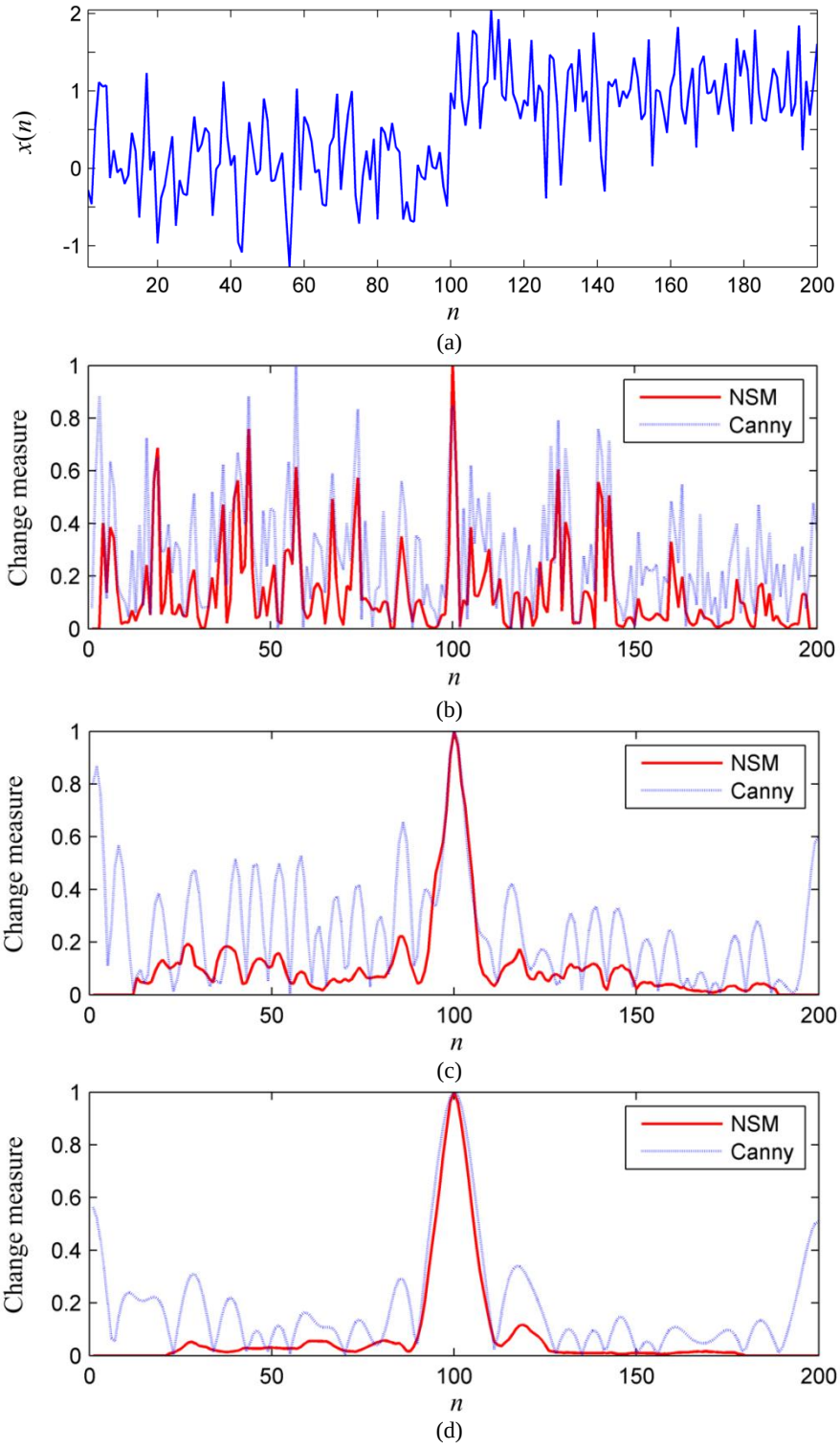

Fig. 2.10 Comparison between the responses of the NSM operator and the Canny operator to the input signal with $CNR = 2.15$. (a) Unit step signal with a discontinuity at $t = 100$ corrupted by a white centered Gaussian noise. (b) $2W = 3$, $\sigma = 0.96$. (c) $2W = 9$, $\sigma = 2.88$. (d) $2W = 15$, $\sigma = 4.80$. All the outputs are normalized by their own maxima since the contrast is the thing that really matters in this comparison.

2.3.4 Selection of window width

Two window functions $h(t)$ and $g(t)$ are used in the design of the NSM operator. The sliding window function $h(t)$ is used to estimate the moving statistical parameter of the signal, while the observation window function $g(t)$ is used for the definition of the distance between the non-stationary state point and the stationary line Δ in the moving feature space $\mathbf{R}^{2W+1}$. Usually the two window functions take the same width $2W$ ($2W+1$ in discrete form).

The window width $2W$ is an important parameter in the design of NSM operators. The original NSM did not discuss the selection of the window width. In the following, a range of W is given to guide its practical choice. The choice of W depends on the noise level of the input signal and the size of the smallest detail to be captured.

The noise level of the input signal limits the minimum size of W. If W is smaller than the minimum value, the number of samples will be too small to correctly estimate the statistical parameter. If the rectangular sliding window $h(t)$ is used to estimate the r^{th}-order moment of $x(t)$, we have

$$\hat{m}_r(t) = (h * x^r)(t), \tag{2.43}$$

where $h(t)$ satisfies the following two conditions

$$\int_R h(t)dt = 1, \tag{2.44}$$

$$\lim_{W\to\infty} \int_R h^2(t)dt = 0. \tag{2.45}$$

The variance of the estimate of the r^{th}-order moment $\hat{m}_r$ is given by

$$D^2(\hat{m}_r) = (m_{2r} - m_r^2)/2W. \tag{2.46}$$

For a stationary segment, a small $D^2(\hat{m}_r)$ means that $\hat{m}_r$ is a good estimator of m_r. An inequality $D^2(\hat{m}_r) \le \varepsilon$ can be used to indicate the desired level of approximation, where ε is usually a small positive number. This naturally provides the lower bound of W

$$W \ge (m_{2r} - m_r^2)/2\varepsilon. \tag{2.47}$$

On the other hand, the size of the smallest detail that we want to preserve limits the maximum size of W. If W is greater than the maximum value, some smaller temporal or spatial details might not be identified accurately through the output of the NSM operator. The height and the position of the apex of the output peak indicate the magnitude and the location of the change. The calculation of the value of such apex usually involve intensities within the range of width $4W$ around the apex. If a detail of width L_d is modeled as two adjacent discontinuities, see Fig. 2.11, to accurately measure changes at the L_d wide detail, the window width $2W$ should

be smaller than L_d to ensure that the value of the apex is only related to one single discontinuity/change, that is, $W \le L_d/2$.

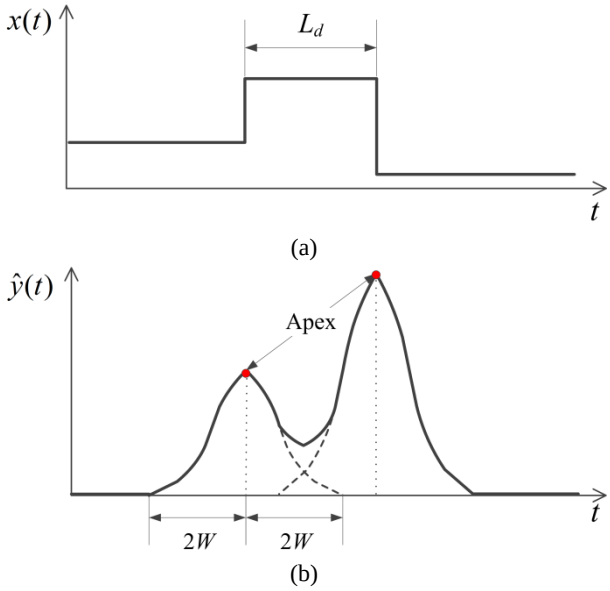

Fig. 2.11 Determination of the maximum of the window width. (a) A detail of width L_d. (b) The NSM of the detail.

2.4 Conclusion

In this chapter, the NSM has been improved in the following aspects. Firstly, the notion of general parameter stationarity (GPS) has been introduced as the basis of the present NSM method. Different from the concept of (non-) stationarity used by the original NSM, the proposed GPS allows investigating the stationarity or non-stationarity of the vector- or tensor-valued signal. That is, in respect of data form, θ can be scalar, vector or matrix. In addition, the statistical parameter θ in the GPS can be any statistic which describes the signal feature in time domain. Owing to the diversity of θ, the NSM method based on the GPS thus can be extended in many ways.

Secondly, based on the GPS, the NSM has been elaborated and explained using more appropriate notions and a general formulation of the NSM has been given. The NSM measures the difference between a non-stationary state and a stationary state in the moving feature space, while other methods take the difference between intensities at two moments or the weighted sums of these differences as change measures. The impact of noise is much smaller on the NSM than on the simple difference between two intensities in time-domain. This is why the NSM is particularly robust to noise compared to conventional techniques based on the derivative.

Thirdly, the outputs of NSM operators using another two representative observation window functions, the concave and the convex, corresponding to three typical input signals,

have been studied. The theoretical analyses and experimental results showed that the concave function can provide the highest output SNR but with complex computations. In practice, the rectangular function is still a good choice because it requires less computation time and provides a high output SNR.

Fourthly, the construction process of the NSM operator has been generalized and the selection of the observation/sliding window size has been discussed. Similar to other change measures using sliding windows, the resolution of the NSM operator depends on the width of the window. Generally, changes at the details smaller than the width of the window might not be measured accurately.

Chapter 3

3 General extension of the non-stationarity measure

Contents

Résumé en français

Jusqu'à présent, beaucoup de méthodes de mesure de changement ont été proposées dans la littérature pour le traitement des données de dimensions et de types différents. Elles sont basées sur des principes différents et possèdent des avantages divers. Cependant, la plupart d'entre elles ne peuvent mesurer que des changements par rapport à un paramètre statistique spécifique, ou des changements de données monodimensionnelles, ou de données scalaires.

Dans le chapitre 2, nous avons amélioré la méthode NSM afin de pallier les déficiences existant dans sa forme originale. La présente méthode NSM après amélioration nous permet d'explorer les stationnarités d'un signal par rapport à une propriété statistique quelconque, et n'impose de limitations ni sur la forme des propriétés statistiques ni sur le type des données signal. Ainsi cette nouvelle méthode présente une grande souplesse.

Dans ce chapitre, L'extension à n-dimensions (n-D) de l'opérateur de mesure de non-stationnarité a également été effectuée. D'abord, nous avons défini la mesure de non-stationnarité pour des signaux n-D, et donné l'algorithme général de calcul de cette mesure. Ensuite, nous avons expliqué le principe de la mesure de non-stationnarité pour des données vectorielles et tensorielles, déduit les formules de calcul, et donné des illustrations à l'aide d'exemples. Nous prenons aussi des moments d'ordre supérieur comme exemples pour montrer la généralité de la méthode NSM dans la mesure des changements de divers paramètres statistiques. Des exemples similaires peuvent aussi être trouvés dans [Liu, 1994].

Avec le dernier chapitre, la méthode NSM a été améliorée et étendue en une mesure générique et robuste de changements, qui permet de quantifier les changements existants dans des données multidimensionnelles et de différents types et par rapport à différents paramètres statistiques.

3.1 Introduction

We can notice that many change measurement methods are dedicated to the processing of data in different dimensions and of different value types. They are based on different principles and possess various advantages. However, most of them can only measure changes regarding either a specific statistical parameter, or a single dimension, or a single value types. On the contrary, it can be known that the improved NSM possesses an intrinsic expansibility. In this chapter, the NSM is extended to deal with data regarding higher order moments, N-dimensional (N-D) data, and vector-valued or tensor-valued data.

This chapter is organized as follows. First, Section 3.2 takes higher order moments as an example to show the generality of the NSM method in measuring changes related to various statistical parameters. Although most of its contents are contained in [Liu, 1994], Section 3.2 is still included here because it is an important part of the NSM methodology. Section 3.3 discusses the possibility to extend the NSM to process N-D data and gives the procedure to calculate the NSM of multidimensional data. Recently, change measures dedicated to vector-valued and tensor-valued data have often been used to process color images, texture images, dynamic images and diffusion tensor images. To answer that needs, the NSM is extended, in Section 3.4, to process vector-valued and tensor-valued data.

3.2 NSM of a signal regarding its r^{th}-order moment

Moments are important statistical descriptors describing the characteristics of a signal. In this section, higher order moments are taken as examples to show the generality of the NSM method in measuring changes related to various statistical parameters. The 2nd-order NSM of a signal regarding the r^{th}-order moment is discussed as follows [Liu *et al.*, 1995].

The moving r^{th}-order moment $m_r(n)$ of the signal $x(n)$ can be estimated by sliding a $2W+1$ wide rectangular window function $h(n)$ along the signal, such that,

$$\begin{aligned}\hat{\theta}(n) &= \hat{m}_r(n) \\ &= \sum_{i=n-W}^{n+W} h(i-n)\cdot x^r(i) \\ &= \frac{1}{2W+1}\sum_{i=n-W}^{n+W} x^r(i).\end{aligned} \tag{3.1}$$

The 2nd-order NSM of the signal $x(n)$ regarding its moving r^{th}-order moment $\hat{m}_r(n)$ can be expressed as

$$\hat{y}_r(n) = \sum_{i=n-W}^{n+W} g(i-n)\cdot\left[\hat{m}_r(i)\right]^2 - \left[\sum_{i=n-W}^{n+W} g(i-n)\cdot\hat{m}_r(i)\right]^2, \tag{3.2}$$

and illustrated in Fig. 3.1.

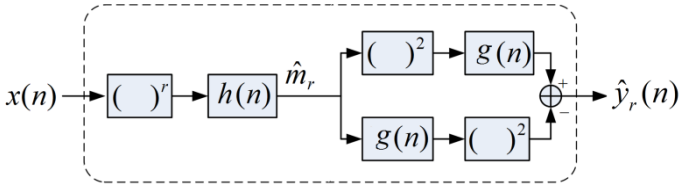

Fig. 3.1 Block diagram of the 2nd-order NSM regarding the r^{th}-order moment of the signal $x(n)$

The NSMs of a signal involving from the 2nd-order to the 4th-order moments are respectively shown in Section 3.2.1 to 3.2.3.

3.2.1 NSM of a signal regarding its 2nd-order moment

The 2nd-order central moment (variance) is a mathematical expectation of the average squared deviations from the mean, measuring the dispersion of a set of data points around their mean value.

A signal $x(n)$ containing a step in its 2nd-order central moment can be designed as

$$x(n) = [1 + A \cdot u(n)]\sin(wn + \varphi_0) + \eta(n), \tag{3.3}$$

where A is a positive real number, $u(n)$ the unit step signal, w the angular frequency, φ_0 the initial phase that is a random number between $[-\pi, \pi]$, and $\eta(n)$ the noise. From the definition, it comes that the 1st and 2nd-order central moments of $x(n)$ (3.3) can be written

$$m_1 = E[x(n)] = 0,$$

$$m_2 = E[(x - m_1)^2] = \frac{1}{2}[1 + (2A + A^2) \cdot u(n)] + \sigma_\eta^2.$$

Fig. 3.2(a) shows the corresponding synthetic signal, defined by (3.3), whose size is 1000 samples with $A = 1$, $w = 0.28\pi$, $\varphi_0 = 0.91$. The signal is corrupted by an additive Gaussian noise with $\mu_\eta = 0$ and $\sigma_\eta = 0.5$. We can observe that a step occurs at $n = 501$ in the 2nd-order moment of the signal. It is seen that, as expected, since the signal is stationary regarding the 1st-order moment, the corresponding NSM curve $\hat{y}_1(n)$ in Fig 3.2(b) is very close to zero (along the x-axis). In contrast, the signal is non-stationary regarding its 2nd-order moment. Taking advantage of the NSM curve $\hat{y}_2(n)$ in Fig 3.2(c), the change occurring between $n = 500$ and $n = 501$ can be easily spotted.

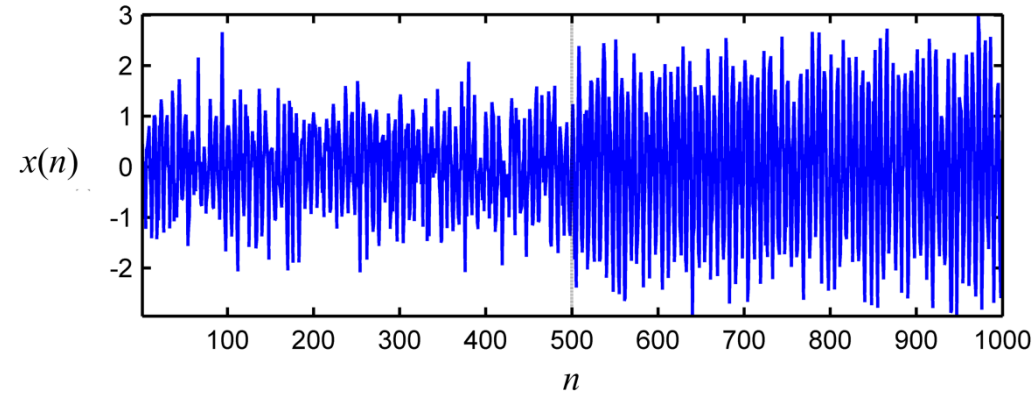

(a)

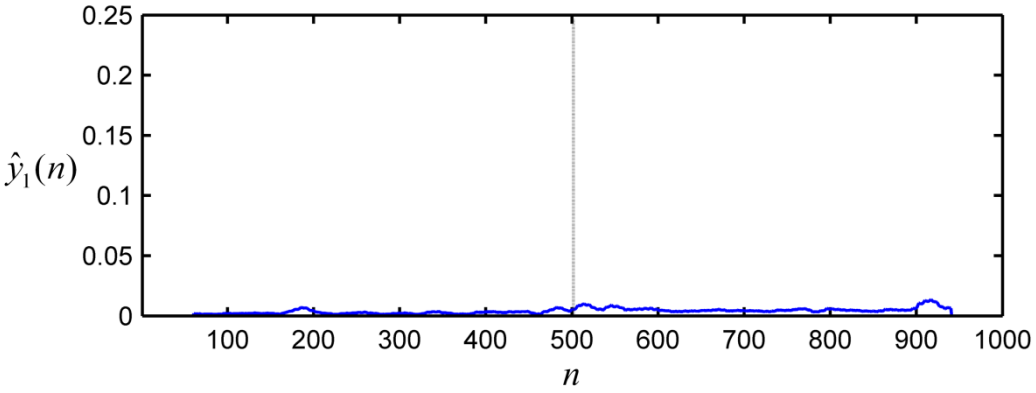

(b)

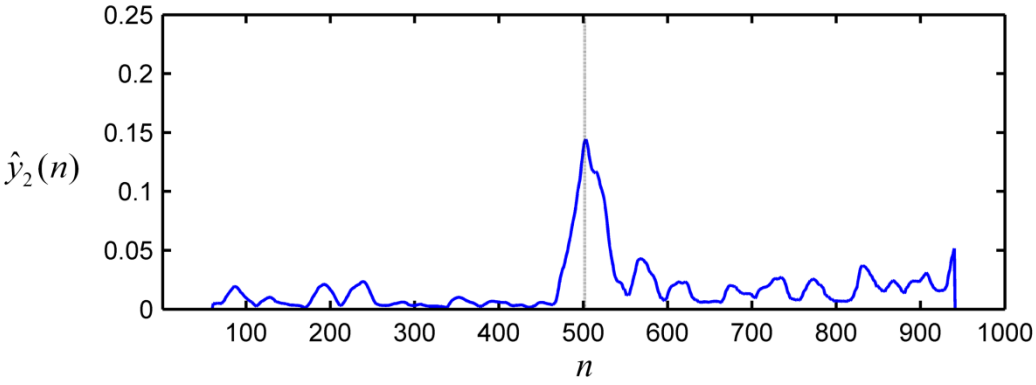

(c)

Fig.3.2 NSMs of a noisy signal containing a step in its 2nd-order moment. (a) $x(n)$: noisy signal with a step at $n = 501$ in its 2nd-order moment. (b) $\hat{y}_1(n)$: NSM regarding the 1st-order moment ($W = 20$). (c) $\hat{y}_2(n)$: NSM regarding the 2nd-order moment ($W = 20$).

3.2.2 NSM of a signal regarding its 3rd order moment

The 3rd-order central moment (skewness) describes asymmetry from the normal distribution of a set of statistical data. Skewness can be either a "negative skewness" or a "positive

skewness", depending on whether the data points are skewed to the left (negative skew) or to the right (positive skew) of the data average.

A signal $x(n)$ containing a change in its 3rd-order central moment but not in its 1st-order and 2nd-order moments can be designed as follows. Let us suppose that the value of a random variable x depends on a binary event. If the outcome of the event is 1, the conditional probability $p(x|1)$ is p_1; if the outcome is 0, $p(x|0)$ is p_2. After a time n_0, x has the probability p_3 for the result 1 and has p_4 for the result 0. So the probability of x is given by

$$\begin{aligned} p_x(n) &= p(x|1)\cdot p(1) + p(x|0)\cdot p(0) \\ &= \begin{cases} p_1 p(1) + p_2 p(0) & n < n_0 \\ p_3 p(1) + p_4 p(0) & n \geq n_0 \end{cases}, \end{aligned} \tag{3.4}$$

where p_1 and p_3 are two uniform distributions with values in the range $\left[\mu_1 - \frac{1}{2}, \mu_1 + \frac{1}{2}\right]$ and $\left[\mu_3 - \frac{1}{2}, \mu_3 + \frac{1}{2}\right]$, p_2 and p_4 are two Gaussian distributions $N(\mu_2, \sigma_2^2)$ and $N(\mu_4, \sigma_4^2)$, and $p(1) = p(0) = 0.5$. The moments of the signal $p_x(n)$ are given as follows:

$$m_1(n) = \begin{cases} \frac{1}{2}(\mu_1 + \mu_2) & n < n_0 \\ \frac{1}{2}(\mu_3 + \mu_4) & n \geq n_0 \end{cases},$$

$$m_2(n) = \begin{cases} \frac{1}{2}\left[\mu_1^2 + \frac{1}{12} + \mu_2^2 + \sigma_2^2\right] & n < n_0 \\ \frac{1}{2}\left[\mu_3^2 + \frac{1}{12} + \mu_4^2 + \sigma_4^2\right] & n \geq n_0 \end{cases},$$

$$m_3(n) = \begin{cases} \frac{1}{2}\mu_1\left[\mu_1^2 + \frac{1}{2}\right] + \frac{1}{2}\mu_2\left[\mu_2^2 + 3\sigma_2^2\right] & n < n_0 \\ \frac{1}{2}\mu_3\left[\mu_3^2 + \frac{1}{2}\right] + \frac{1}{2}\mu_4\left[\mu_4^2 + 3\sigma_4^2\right] & n \geq n_0 \end{cases}.$$

If $\mu_1 + \mu_2 = 0$, $\mu_1 + \mu_3 = 0$, $\mu_2 + \mu_4 = 0$ and $\sigma_2 = \sigma_4$, then the signal $p_x(n)$ possesses the following moments:

$$m_1(n) = 0,$$

$$m_2(n) = \frac{1}{2}\left[2\mu_1^2 + \frac{1}{12} + \sigma_2^2\right],$$

$$m_3(n)=\begin{cases}\frac{1}{2}\mu_1\left[\frac{1}{2}-3\sigma_2^2\right] & n<n_0\\ -\frac{1}{2}\mu_1\left[\frac{1}{2}-3\sigma_2^2\right] & n\geq n_0\end{cases}.$$

In the experiment shown in Fig. 3.3, $\mu_1=-2$, $\mu_2=2$, $\mu_3=2$, $\mu_4=-2$, and $\sigma_2=\sigma_4$=1. The signal thus obtained possesses the following moments:

$$m_1(n)=0,\leq n\leq 4096,$$

$$m_2(n)=109/24,1\leq n\leq 4096,$$

$$m_3(n)=\begin{cases}5/2,1\leq n\leq 2048\\ -5/2,2048<n\leq 4096\end{cases}.$$

As expected, since the signal is stationary regarding the 1st-order and the 2nd-order moments, the corresponding NSM curves $\hat{y}_1(n)$ and $\hat{y}_2(n)$ in Fig 3.3(b) and (c) are very close to zero (along the *x*-axis). In contrast, the signal is non-stationary regarding its 3rd-order moment. Taking advantage of the NSM curve $\hat{y}_3(n)$ in Fig 3.3(d), a change occurring in the 3rd-order moment around at $n=2049$ can be easily spotted.

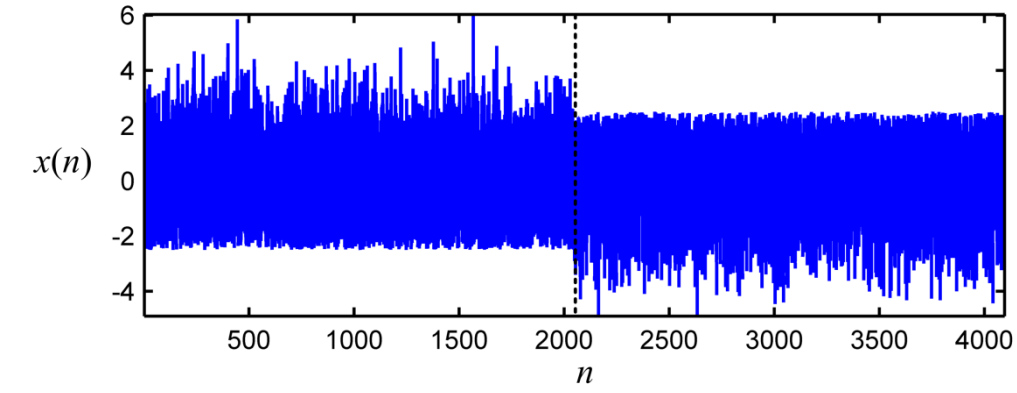

(a)

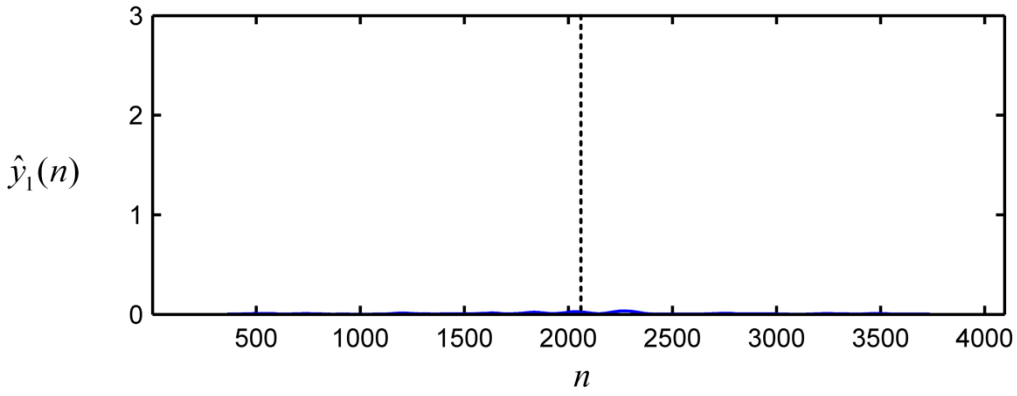

(b)

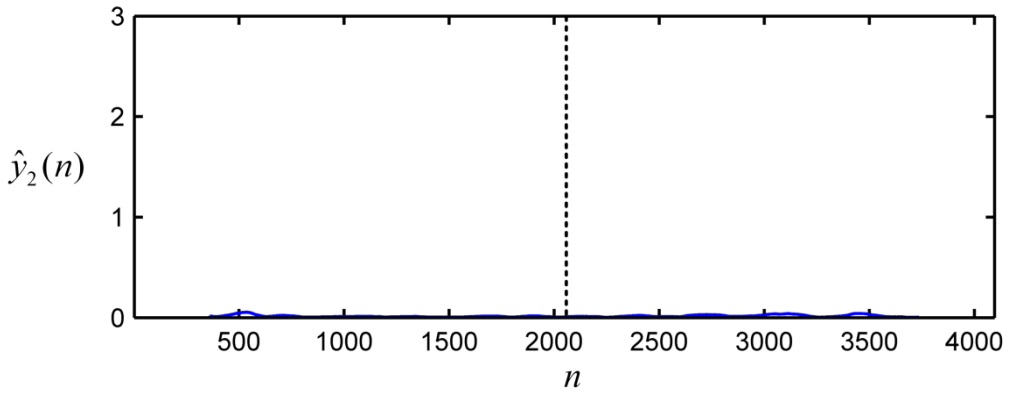

(c)

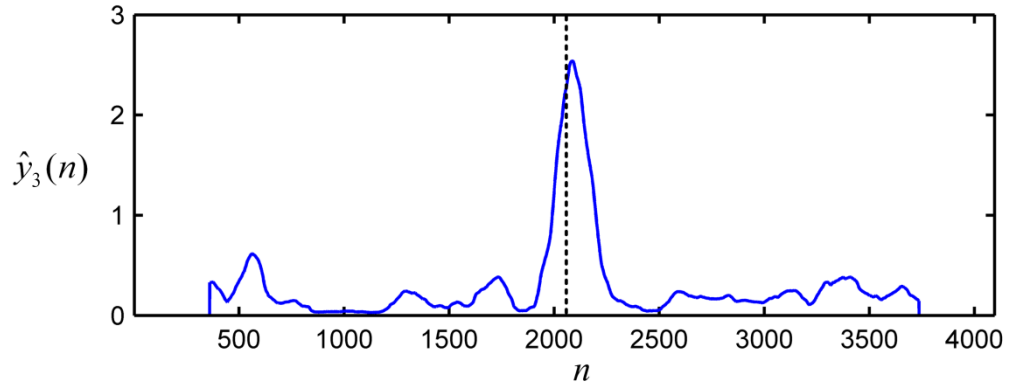

(d)

Fig. 3.3 NSMs of a random signal containing a change in its 3rd-order moment. (a) $x(n)$: random signal with a change at $n = 2049$ in its 3rd-order moment. (b) $\hat{y}_1(n)$: NSM regarding the 1st-order moment ($W = 120$). (c) $\hat{y}_2(n)$: NSM regarding the 2nd-order moment ($W = 120$). (d) $\hat{y}_3(n)$: NSM regarding the 3rd-order moment ($W = 120$).

3.2.3 NSM of a signal regarding its 4th-order moment

The 4th-order central moment (kurtosis) is a measure of the relative concentration (flatness or peakedness) of data values in the center versus in the tails when compared with a normal distribution. Distributions having higher kurtosis have fatter tails or more extreme values, and those with lower kurtosis have fatter middles or fewer extreme values.

A signal $x(n)$ containing a step in its 4th-order central moment can be designed as

$$x(n) = a(n)\mathrm{sgn}[\sin(wn + \varphi_0)] + b(n)\sin(wn + \varphi_0) + \eta(n), \tag{3.5}$$

where sgn designates the signum function, and φ_0, the initial phase, is a random number of uniform distribution between $[-\pi, \pi]$, $\eta(n)$ the noise. The r^{th}-order moment of $x(n)$ is

$$\begin{aligned} m_r(n) &= \frac{1}{2\pi}\int_{-\pi}^{\pi} x^r(\varphi)d\varphi \\ &= \frac{1}{2\pi}\sum_{i=0}^{r} C_r^i a^i(n) b^{r-i}(n)\int_{-\pi}^{\pi}\left[\operatorname{sgn}\left(\sin\varphi\right)\right]^r \left|\sin\varphi\right|^{r-i} d\varphi \end{aligned} . \tag{3.6}$$

When *r* is an odd number, $m_r(n)=0$. When *r* is an even number,

$$m_r(n) = \frac{1}{\pi}\sum_{i=0}^{r} C_r^i a^i(n) b^{r-i}(n)\int_0^{\pi}\sin^{r-i}(\varphi)d\varphi .$$

So, we have

$$m_2(n) = a^2(n) + b^2(n)/2 + 4a(n)b(n)/\pi ,$$

$$m_4(n) = a^4(n) + 8a^3(n)b(n)/\pi + 3a^2(n)b^2(n) + 16a(n)b^3(n)/3\pi + 3b^4(n)/8 .$$

In the experiment shown in Fig. 3.4,

$$a(n) = \begin{cases} 1 & 1 \le n \le 2000 \\ 1/\sqrt{2} & 2000 < n \le 4000 \end{cases},$$

$$b(n) = \begin{cases} 1 & 1 \le n \le 2000 \\ \sqrt{2} & 2000 < n \le 1000 \end{cases}.$$

The signal thus obtained possesses the following moments:

$$m_1(n) = m_3(n) = 0,$$

$$m_2(n) = 3/2 + 4/\pi ,$$

$$m_4(n) = \begin{cases} 35/8 + 40/3\pi & 1 \le n \le 2000 \\ 19/4 + 44/3\pi & 2000 < n \le 4000 \end{cases}.$$

The amplitude of the step occurring in the 4th-order moment at $n=2001$ is $3/8+4/3\pi$. The signal $x(n)$ is corrupted by an additive Gaussian noise with mean 0 and standard deviation 0.04. As expected, since the signal is stationary regarding the 1st-order, the 2nd-order and the 3rd-order moments, the corresponding NSM curves $\hat{y}_1(n)$, $\hat{y}_2(n)$ and $\hat{y}_3(n)$ in Fig 3.4 (b), (c) and (d) are very close to zero (along the *x*-axis). In contrast, the signal is non-stationary regarding its 4th-order moment. Taking advantage of the NSM curve $\hat{y}_4(n)$ in Fig 3.4(e), the change occurring between $n=2000$ and $n=2001$ can be easily spotted.

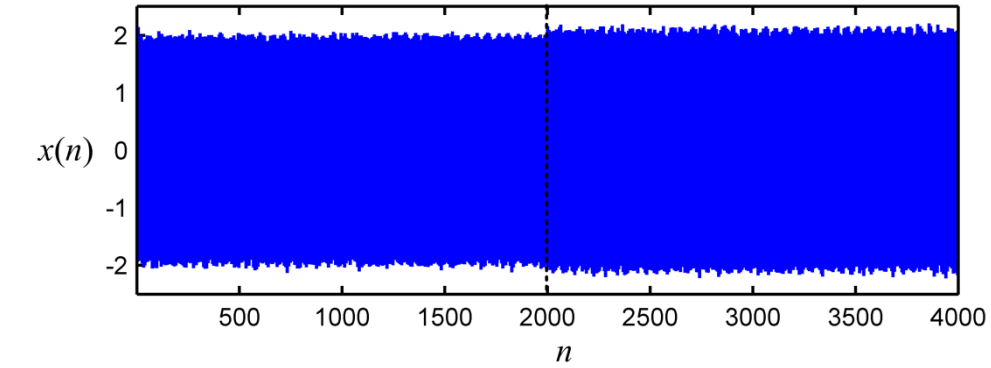

(a)

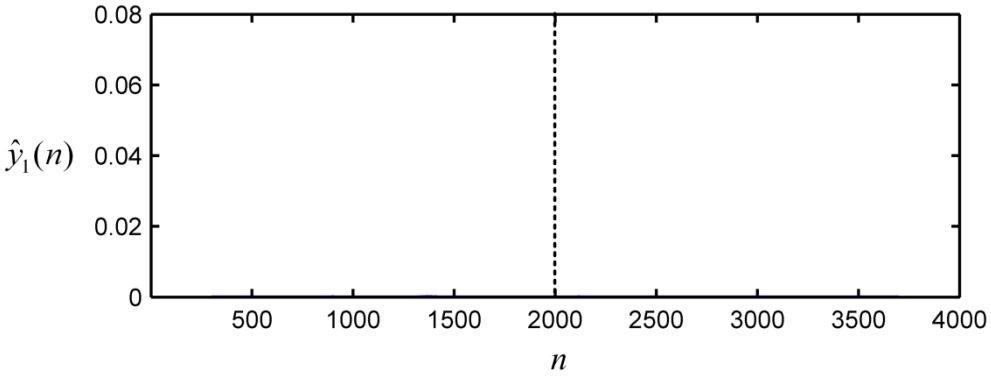

(b)

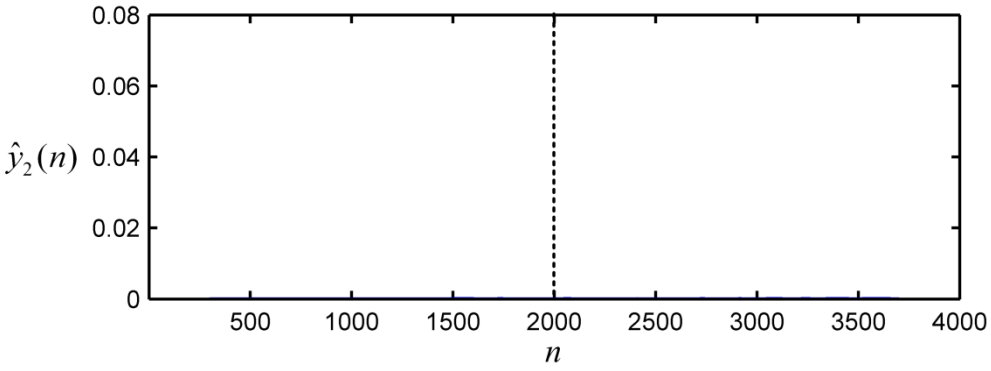

(c)

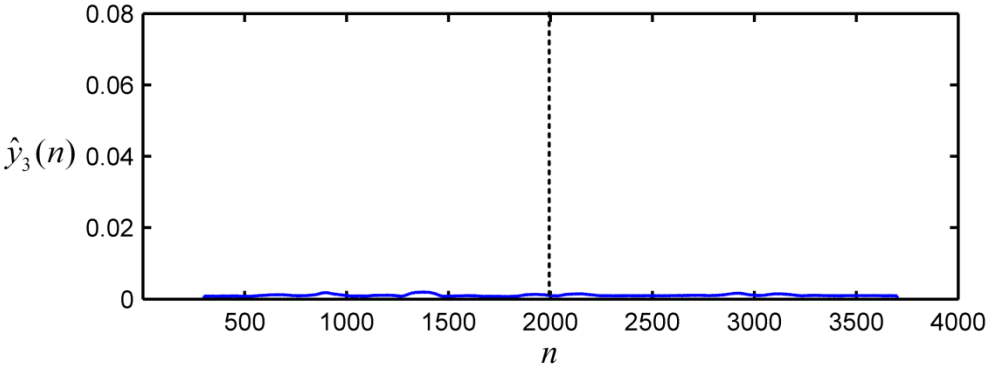

(d)

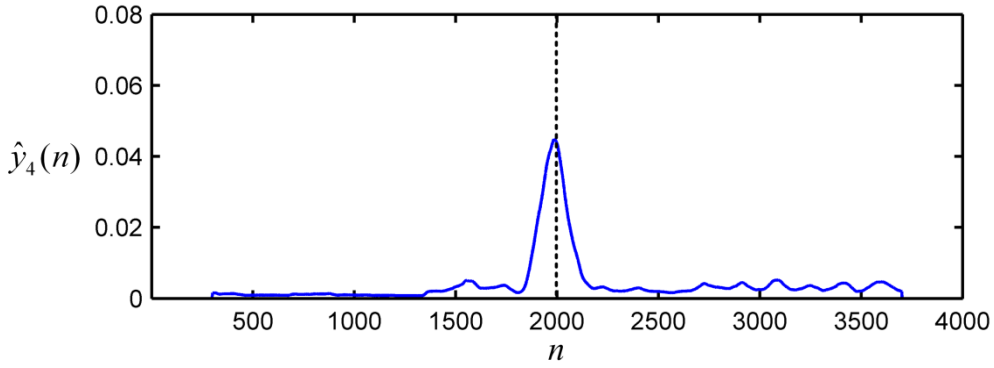

(e)

Fig. 3.4 NSMs of a noisy signal containing a change in its 4th-order moment. (a) $x(n)$: noisy signal with a change at $n = 2001$ in its 4th-order moment. (b) $\hat{y}_1(n)$: NSM regarding the 1st-order moment ($W = 100$). (c) $\hat{y}_2(n)$: NSM regarding the 2nd-order moment ($W = 100$). (d) $\hat{y}_3(n)$: NSM regarding the 3rd-order moment ($W = 100$). (e) $\hat{y}_4(n)$: NSM regarding the 4th-order moment ($W = 100$).

3.3 Extension of the NSM to process *N*-dimensional data

This section discusses the possibility to extend the NSM to process N -D data, and gives the steps to calculate the NSM of N -D data.

In order to measure the non-stationarity of a signal, we need to construct a multidimensional moving feature space, since the NSM is defined as the distance between a non-stationary state point and the stationary line in the same space. For 1-D signals, the state point is determined by the sequence of statistical parameters within the 1-D observation window in the time domain. The number of dimensions of the moving feature space equals the width of the observation window. For example, the observation window width $2W+1$ equals 21 (that is, 21 samples of the signal are contained in the sliding observation window), the moving feature space has 21 dimensions.

For multidimensional data, we study the NSM in a multidimensional sliding observation window. The statistical parameters within the multidimensional window can be arranged into an ordered sequence. Similar to the 1-D case, the sequence corresponds to a point in the moving feature space whose dimension equals the size of the observation window. The distance from the point to the stationary line is mapped into the time domain and considered as the NSM of the central point of the multidimensional sliding observation window. Such arrangement makes the extension straightforward and has no impact on the distance although it affects the location of the point.

Fig. 3.5 illustrates how to determine the state point in the moving feature space for 1-D to N -D data. Taking a 2-D image for example, the statistical parameters within the $(2W+1)\times(2W+1)$ sliding observation window can be arranged into an ordered sequence of length $(2W+1)^2$ which corresponds to a state point in the $(2W+1)^2$ dimensional moving feature space.

In practical applications, the NSM of multidimensional data can be calculated in four steps:

1. estimate the statistical parameter $\hat{\theta}(n)$ with a multidimensional sliding window h;
2. formulate the NSM according to the statistical parameter $\hat{\theta}(n)$ and the distance d;
3. estimate $\bar{\theta}$ by $\partial d / \partial \bar{\theta} = 0$;
4. calculate $d\left(K, \bar{K}\right)$ as the NSM of the central point of the multidimensional sliding observation window g in the time domain.

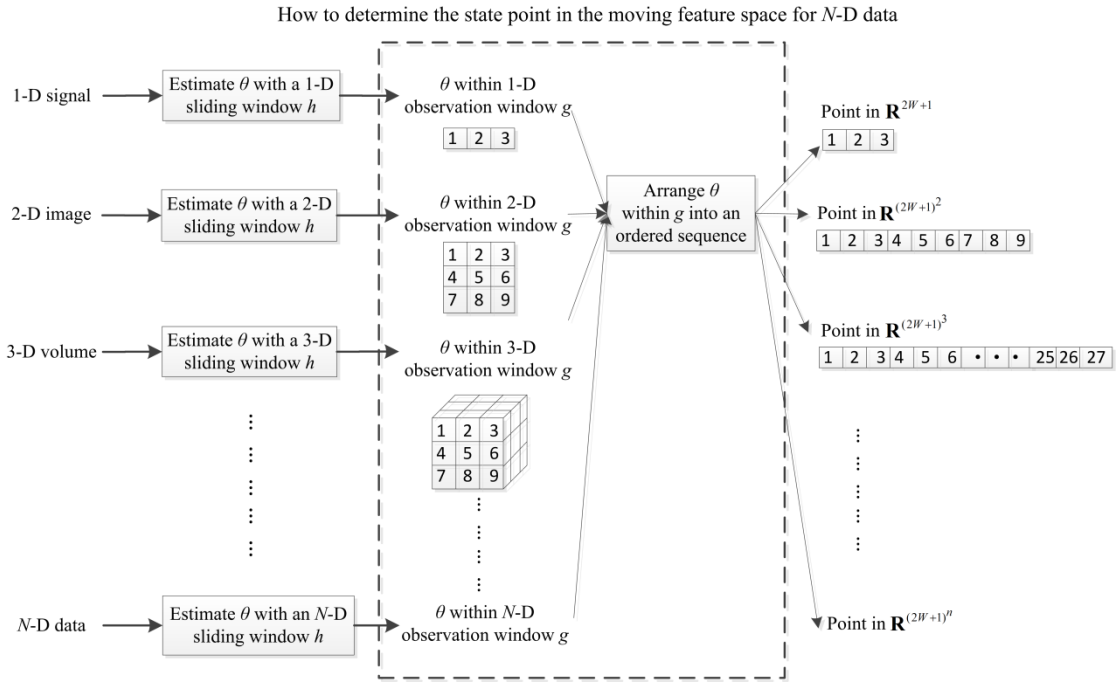

Fig.3.5 Determination of the state point in the moving feature space for 1-D to *N*-D data

3.4 Extension of the NSM to process vector-valued and tensor-valued data

From the general formulation of the NSM (see (2.8)) it comes that:

$$d\left(K, \bar{K}\right) = \sum_{i=1}^{2W+1} g_i \cdot \left[dis\left(\hat{\theta}_i, \bar{\theta}\right)\right]^p ,$$

it can be seen that the NSM is the sum of the weighted differences between the coordinate $\hat{\theta}_i$ of the state point K and the coordinate $\bar{\theta}$ of the stationary point $\bar{K}$. Therefore, as long as we can estimate the moving statistical parameter of the vector-valued or the tensor-valued data and we can define the dissimilarity between two vectors or two tensors properly, the NSM can be extended to process the vector-valued and the tensor-valued data.

3.4.1 NSM of vector-valued data

For vector-valued data, each state point K in the moving feature space is determined by a sequence of vectorial coordinates $\left(\hat{\boldsymbol{\theta}}_1,\hat{\boldsymbol{\theta}}_2,\cdots,\hat{\boldsymbol{\theta}}_{2W+1}\right)$, where $\hat{\boldsymbol{\theta}}_i$ is a vector with $i=1,\cdots,2W+1$. The stationary point which makes $d(K,\Delta)$ minimal is written as $\bar{K}=\left(\bar{\boldsymbol{\theta}},\bar{\boldsymbol{\theta}},\cdots,\bar{\boldsymbol{\theta}}\right)$, where $\bar{\boldsymbol{\theta}}$ is also a vector. The NSM of the vector-valued signal $\boldsymbol{v}(n)$ is generally formulated as:

$$\begin{aligned}\hat{y}(n) &= \square\left[\boldsymbol{v}(n)\right] \\ &= d\left(K,\bar{K}\right) \\ &= \sum_{i=1}^{2W+1} g_i \cdot \left[dis\left(\hat{\boldsymbol{\theta}}_i,\bar{\boldsymbol{\theta}}\right)\right]^p\end{aligned} \tag{3.7}$$

with $dis\left(\hat{\boldsymbol{\theta}}_i,\bar{\boldsymbol{\theta}}\right)$ representing the dissimilarity between two vectors, the coordinate $\hat{\boldsymbol{\theta}}_i$ of point K and the coordinate $\bar{\boldsymbol{\theta}}$ of point $\bar{K}$.

We now elaborate the construction of a 2nd-order NSM operator for the vector-valued signal $\boldsymbol{v}(n)$. If we want to study the stationarity/non-stationarity of the signal $\boldsymbol{v}(n)$ regarding its mean, we first use a rectangular window function $h(n)$ of width $2W+1$ to estimate the moving statistical parameter

$$\begin{aligned}\hat{\boldsymbol{\theta}}(n) &= \hat{\boldsymbol{m}}_1(n) \\ &= \sum_{i=n-W}^{n+W} h(i-n)\cdot\boldsymbol{v}(i). \\ &= \frac{1}{2W+1}\sum_{i=n-W}^{n+W}\boldsymbol{v}(i)\end{aligned} \tag{3.8}$$

Using the definition of the orientation difference between two vectors, see (1.7), according to (3.7) and (3.8), the 2nd-order NSM of the signal $\boldsymbol{v}(n)$ regarding its 1st-order moment can be expressed as:

$$\hat{y}_1(n) = \square\left[\boldsymbol{v}(n)\right] = \sum_{i=n-W}^{n+W} g(i-n)\cdot\left[\arccos\left(\frac{\hat{\boldsymbol{m}}_1(i)\cdot\bar{\boldsymbol{m}}_1}{\left|\hat{\boldsymbol{m}}_1(i)\right|\cdot\left|\bar{\boldsymbol{m}}_1\right|}\right)\right]^2, \tag{3.9}$$

where $\bar{\boldsymbol{m}}_1$ is the coordinate vector of the stationary state point $\bar{K}$. By $\partial d/\partial\bar{\boldsymbol{m}}_1=0$, the analytical formula of $\bar{\boldsymbol{m}}_1$ is given by:

$$\bar{\boldsymbol{m}}_1 = \sum_{i=n-W}^{n+W} g(i-n)\cdot\hat{\boldsymbol{m}}_1(i). \tag{3.10}$$

Fig. 3.6(a) shows a vector-valued signal of length 100, with the first fifty vectors equal to $[1,1,0]$ and the last fifty ones equal to $[-1,1,0]$. That is, there exists a change at time $n=51$ in the 1st-order moment of the signal. Using the NSM operator defined in (3.9), with both

$g(n)$ and $h(n)$ being a rectangular window function of width 3, the NSM of the vector-valued signal regarding its 1st-order moment can be obtained and is shown in Fig. 3.6(b). We note that the NSM values corresponding to the two periods before and after the change time $n=51$ equal zero, which indicates that the signal is locally stationary regarding the 1st-order moment in the two periods. Around the time $n=51$, the NSM curve $\hat{y}_1(n)$ presents a symmetrical peak with the position of the apex indicating the location of the abrupt change occurring between $n=50$ and $n=51$.

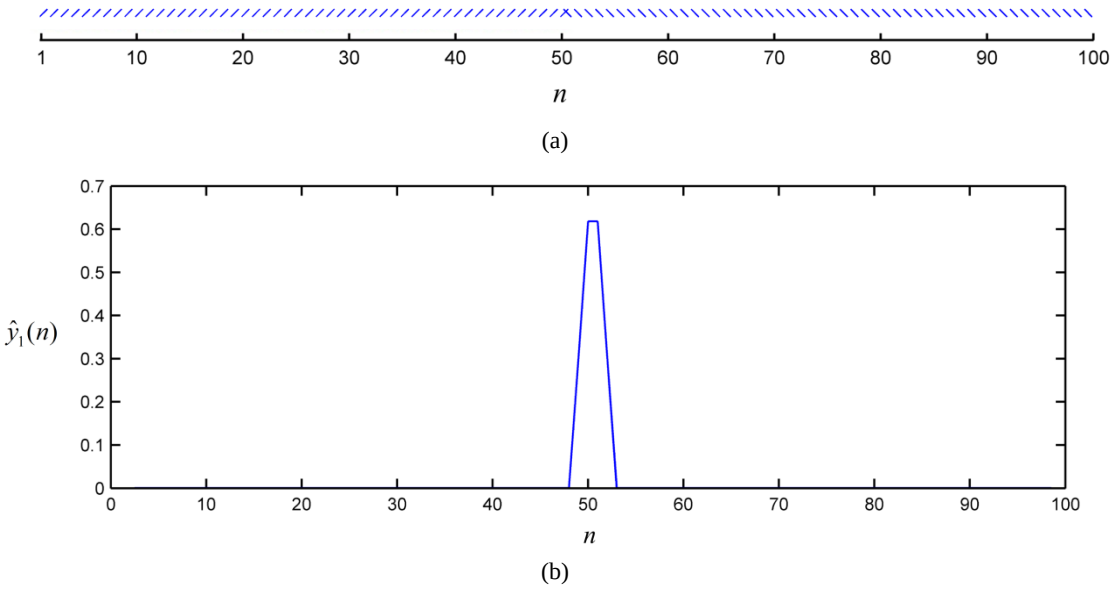

Fig.3.6 1-D vector-valued signal and its NSM. (a) 1-D vector-valued signal. (b) $\hat{y}_1(n)$: NSM of the 1-D vector-valued signal.

Fig. 3.7(a) shows a 2-D vector field of size 33×45 which contains three sets of vectors $\boldsymbol{v}_1$, $\boldsymbol{v}_2$ and $\boldsymbol{v}_3$. The angle between $\boldsymbol{v}_1$ and $\boldsymbol{v}_2$ is 30°, and the angle between $\boldsymbol{v}_2$ and $\boldsymbol{v}_3$ is 60° (see Fig. 3.7(b)). According to the procedure to calculate the NSM of multidimensional data described in Section 3.3, the NSM operator defined in (3.9) can be extended to process 2-D vector fields. With both $g(n)$ and $h(n)$ being a rectangular window function of size 3×3, the NSM map of the 2-D vector field regarding its 1st-order moment can be obtained and is shown in Fig. 3.7(c). From the brightness of the 2-D NSM map, we can observe the positions and the magnitudes of changes occurring in the vector field. Obviously, the difference between $\boldsymbol{v}_2$ and $\boldsymbol{v}_3$ is larger than that between $\boldsymbol{v}_1$ and $\boldsymbol{v}_2$. From the horizontal profile of the NSM map, see Fig. 3.7(d), we can clearly see that the magnitude of the right change (between $\boldsymbol{v}_2$ and $\boldsymbol{v}_3$) occurring at column 30 is twice that of the left change (between $\boldsymbol{v}_1$ and $\boldsymbol{v}_2$) occurring at column 15.

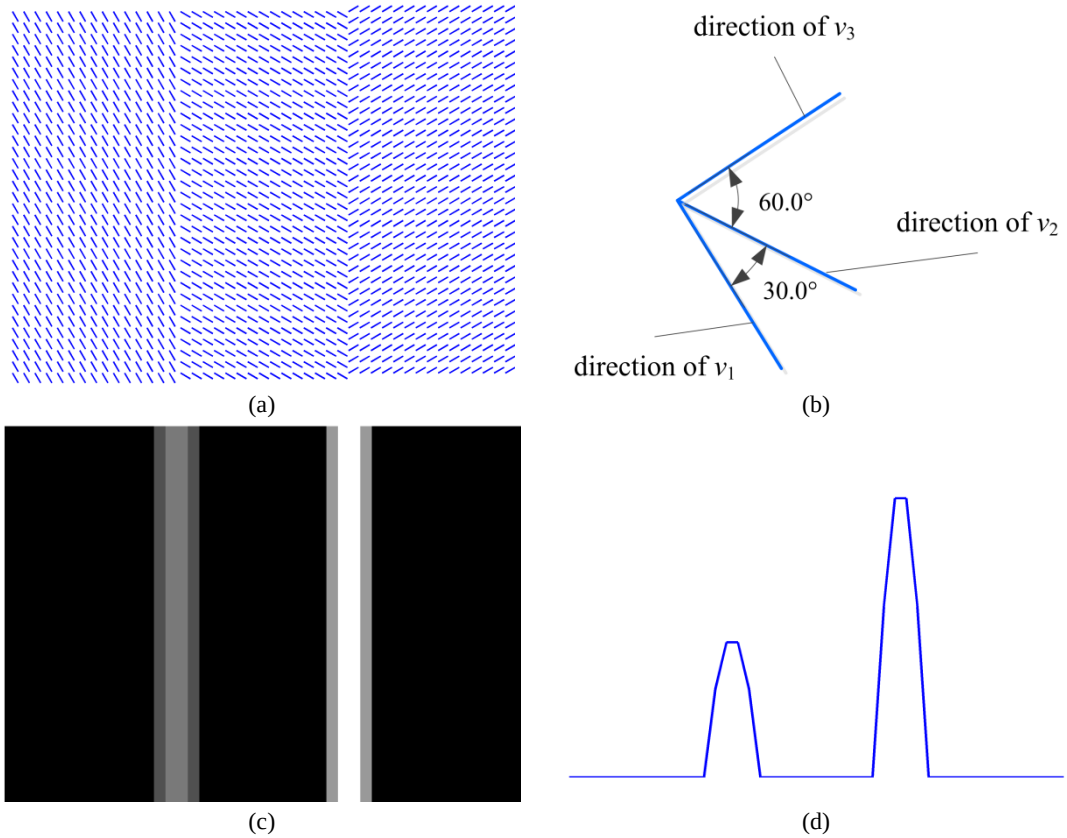

Fig.3.7 2-D vector field and its NSM map. (a) 2-D vector field composed of $\boldsymbol{v}_1$, $\boldsymbol{v}_2$, $\boldsymbol{v}_3$ successively. (b) relative angular orientations of the three vector field. (c) NSM map of the 2-D vector field regarding its 1st-order moment. (d) Horizontal profile of (c).

3.4.2 NSM of tensor-valued data

A mathematical or a physical quantity $\mathbf{T}$ can be described in a Cartesian coordinate system Z by 3^n elements $t_{ij\cdots m}$, the so-called translation invariants. Here the number of indices $i, j, \cdots, m$ is exactly equal to n $(n \geq 0)$. The indices are ordered, and each of them takes the values 1, 2 and 3. If under a coordinate transformation from Z to $\tilde{Z}$, the new elements are defined as:

$$\tilde{t}_{\mu\nu\cdots\rho} = \sum_{i=1}^{3}\sum_{j=1}^{3}\cdots\sum_{m=1}^{3} a_{\mu i} a_{\nu j} \cdots a_{\rho m} t_{ij\cdots m}\,, \tag{3.11}$$

where $a_{\mu i}, a_{\nu j}, \cdots, a_{\rho m}$ $(\mu, \nu, \rho = 1, 2, 3)$ are the coefficients of a linear transformation from Z to $\tilde{Z}$, then $\mathbf{T}$ is called a tensor of rank n, and the elements $t_{ij\cdots m}$ with ordered indices are the components of the tensor $\mathbf{T}$ [Bronshtein *et al.*, 2007]. From the point of view of isomorphism, a scalar is a tensor of rank zero, a vector is a tensor of rank 1, and a 3×3 matrix is a tensor of rank 2. In diffusion tensor magnetic resonance imaging (DT-MRI, or simply DTI), the

diffusion ellipsoid is mathematically represented by a tensor of rank 2. The tensor is most commonly represented by a 3×3 symmetric positive definite real matrix with 6 independent components.

This subsection focuses on studying the NSM with respect to the tensors in the DTI. In order to circumvent the problems in usual Euclidean operations on tensors, such as nonpositive eigenvalues, tensor swelling, and asymmetric tensors, the computations on tensors involved in the NSM of tensor-valued data are performed according to the Log-Euclidean Metrics [Arsigny *et al.*, 2006; Vincent Arsigny, 2005]. Under the Log-Euclidean framework, the matrix logarithm $\log(\mathbf{T})$ of a tensor $\mathbf{T}$ can be calculated in three steps [Arsigny *et al.*, 2006]:

1. perform a diagonalization of $\mathbf{T}$, which provides a rotation matrix $\mathbf{R}$ and a diagonal matrix $\mathbf{D}$ with the eigenvalues λ_1, λ_2, λ_3 of $\mathbf{T}$ in its diagonal, with the equality: $\mathbf{T}=\mathbf{R}\cdot\mathbf{D}\cdot\mathbf{R}^T$;
2. transform each diagonal element of $\mathbf{D}$ (which is necessarily positive, since it is an eigenvalue of $\mathbf{T}$) into its natural logarithm in order to obtain a new diagonal matrix $\tilde{\mathbf{D}}=\mathrm{diag}(\log\lambda_1,\log\lambda_2,\log\lambda_3)$;
3. recompose $\tilde{\mathbf{D}}$ and $\mathbf{R}$ to obtain the logarithm with the formula $\log(\mathbf{T})=\mathbf{R}\cdot\tilde{\mathbf{D}}\cdot\mathbf{R}^T$.

Conversely, the matrix exponential $\exp(\mathbf{T})$ is obtained by replacing the natural logarithm with the scalar exponential.

For tensor-valued data, each state point K in the moving feature space is determined by a sequence of matrix coordinates $\left(\hat{\Theta}_1,\hat{\Theta}_2,\cdots,\hat{\Theta}_{2W+1}\right)$, where $\hat{\Theta}_i$ is a 3×3 symmetric positive definite real matrix with $i=1,\cdots,2W+1$. The stationary point which makes $d(K,\Delta)$ minimal is written as $\bar{K}=\left(\bar{\Theta},\bar{\Theta},\cdots,\bar{\Theta}\right)$, where $\bar{\Theta}$ is also a matrix like $\hat{\Theta}_i$. The NSM of the tensor-valued signal $\boldsymbol{t}(n)$ is generally formulated as:

$$\begin{aligned}\hat{y}(n)&=\Im\left[\boldsymbol{t}(n)\right]\\&=d\left(K,\bar{K}\right)\\&=\sum_{i=1}^{2W+1}g_i\cdot\left[dis\left(\hat{\Theta}_i,\bar{\Theta}\right)\right]^p\end{aligned}\tag{3.12}$$

with $dis\left(\hat{\Theta}_i,\bar{\Theta}\right)$ representing the dissimilarity between two matrices, the coordinate $\hat{\Theta}_i$ of point K and the coordinate $\bar{\Theta}$ of point $\bar{K}$.

We now elaborate the construction of a 2nd-order NSM operator for the tensor-valued signal $\boldsymbol{t}(n)$. If we want to study the stationarity/non-stationarity of the signal $\boldsymbol{t}(n)$ regarding its mean, we first use a rectangular window function $h(n)$ of width $2W+1$ to estimate the moving evolving statistical parameters

$$\hat{\Theta}(n)=\hat{\boldsymbol{\mu}}_1(n)=\exp\left(\frac{1}{2W+1}\sum_{i=n-W}^{n+W}\log\left(\boldsymbol{t}(i)\right)\right).\tag{3.13}$$

Using the definition of the similarity-invariant Log-Euclidean metric, see (1.19), according to (3.12) and (3.13), the 2nd-order NSM of the signal $\boldsymbol{t}(n)$ can be expressed as:

$$\hat{y}_1(n) = \tilde{\square}\left[\boldsymbol{t}(n)\right] = \sum_{i=n-W}^{n+W} g(i-n)\cdot \mathrm{Trace}\left\{\left[\log\left(\hat{\boldsymbol{\mu}}_1(i)\right) - \log\left(\bar{\boldsymbol{\mu}}_1\right)\right]^2\right\}, \tag{3.14}$$

where $\bar{\boldsymbol{\mu}}_1$ is the coordinate vector of the stationary state point $\bar{K}$. By $\partial d/\partial \bar{\boldsymbol{\mu}}_1 = 0$, the analytical formula of $\bar{\boldsymbol{\mu}}_1$ is obtained as:

$$\bar{\boldsymbol{\mu}}_1 = \sum_{i=n-W}^{n+W} g(i-n)\cdot \hat{\boldsymbol{\mu}}_1(i)\,. \tag{3.15}$$

Fig. 3.8(a) shows a tensor-valued signal of length 100, with the first fifty tensors equal to $[1,0,0;0,2,0;0,0,1]$ and the last fifty ones equal to $[1,0,0;0,1,0;0,0,2]$. That is, there exists a change at time $n=51$ in the 1st-order moment of the tensor-valued signal. Using the NSM operator defined in (3.14), with both $g(n)$ and $h(n)$ being the rectangular window function of width 3, the NSM of the tensor-valued signal regarding its 1st-order moment can be obtained and is shown in Fig. 3.8(b). We note that the NSM values corresponding to the two periods before and after the change time $n=51$ equal zero, which indicates that the signal is locally stationary regarding the 1st-order moment in the two periods. Around the time $n=51$, the NSM curve $\hat{y}_1(n)$ presents a symmetrical peak with the position of the apex indicating the location of the abrupt change occurring between $n=50$ and $n=51$.

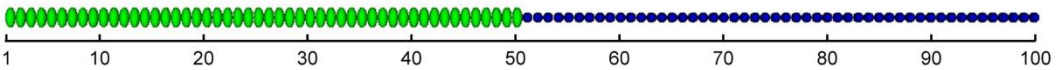

(a)

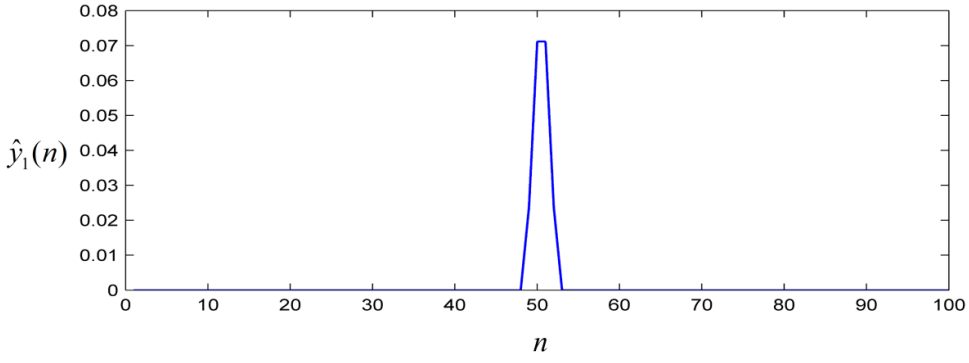

(b)

Fig. 3.8 1-D tensor signal and its NSM. (a) 1-D tensor signal. (b) $\hat{y}_1(n)$: NSM of the 1-D tensor signal with the detection of a 1st order moment change.

Fig. 3.9(a) shows a 2-D tensor field of size 33×45 which contains three sets of tensors:

$$\mathbf{T}_1 = \begin{bmatrix} 0.5 & 0 & 0 \\ 0 & 0.5 & 0 \\ 0 & 0 & 0.5 \end{bmatrix},\ \mathbf{T}_2 = \begin{bmatrix} 0.5 & 0 & 0 \\ 0 & 1 & 0 \\ 0 & 0 & 0.5 \end{bmatrix} \text{ and } \mathbf{T}_3 = \begin{bmatrix} 0.9 & 0.3 & 0 \\ 0.3 & 0.7 & 0 \\ 0 & 0 & 0.5 \end{bmatrix}$$

According to the procedure described in Section 3.3, the NSM operator defined in (3.14) can be extended to process 2-D tensor fields. With both $g(n)$ and $h(n)$ being a rectangular window function of size 3×3, the NSM of the 2-D tensor field regarding its 1st-order moment can be obtained and is shown in Fig. 3.9(b). From the brightness of the 2-D NSM map, we can observe the positions and the magnitudes of changes occurring in the tensor field. Obviously, the difference between $\mathbf{T}_2$ and $\mathbf{T}_3$ is larger than that between $\mathbf{T}_1$ and $\mathbf{T}_2$.

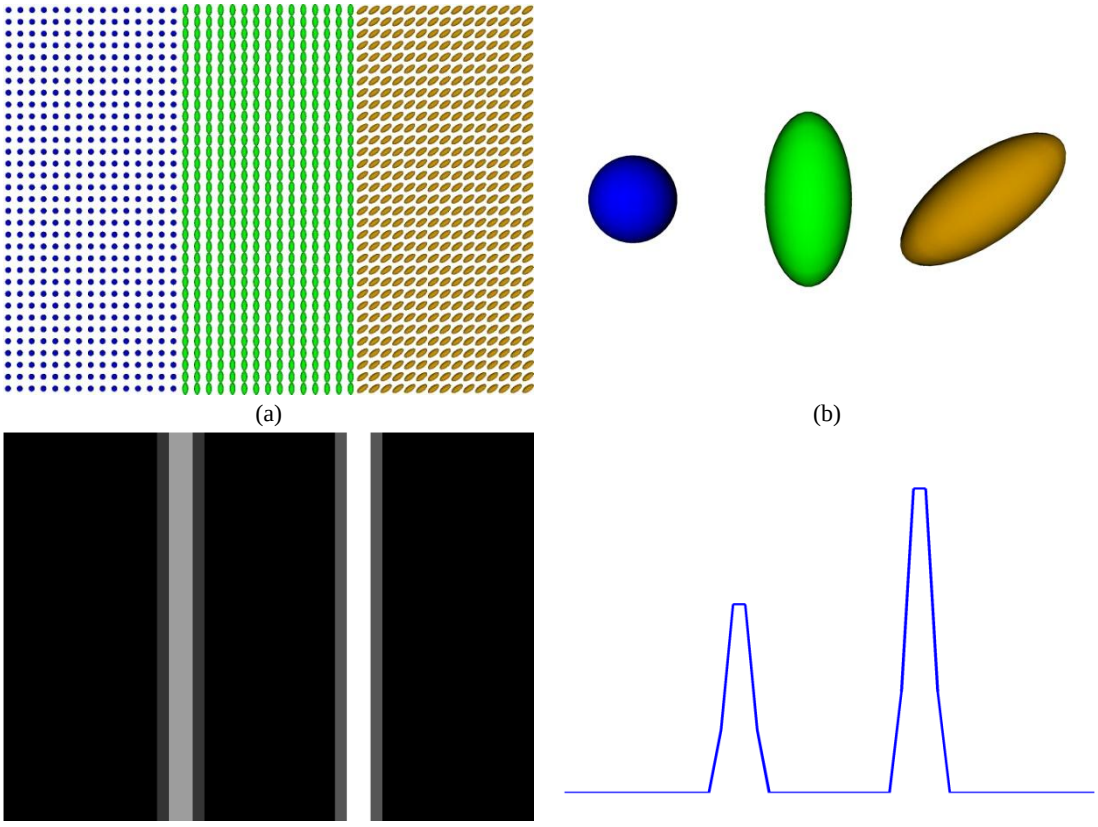

Fig. 3.9 2-D tensor field and its NSM map. (a) 2-D tensor fields composed of successively $\mathbf{T}_1$, $\mathbf{T}_2$, and $\mathbf{T}_3$. (b) Ellipsoid $\mathbf{T}_1$, $\mathbf{T}_2$, and $\mathbf{T}_3$ (from left to right). (c) NSM map of the 2-D tensor field showing two changes of their 1st order moment. (d) Horizontal profile of (c).

3.5 Conclusion

In this chapter, the NSM method is extended in three aspects: the NSM regarding different statistical parameters, the NSM of *N*-D data, and the NSM of vector- and tensor-valued data.

First, the NSM can be used to measure the degree of non-stationarity of a signal regarding given statistical parameters, thus reflecting changes existing in a specific signal feature. Since moments are important statistical parameters describing the characteristics of a signal, Section 3.2 has given the NSM of a signal regarding its r^{th}-order moment.

Second, the possibility to extend the NSM to process *N*-D data has been discussed and the procedure to calculate the NSM of multidimensional data has been given. The examples of using the NSM operator to process 1-D signal can be found in Section 4.2, and those concerning the NSM map of 2-D image can be found in Section 3.4 and Chapters 4 to 6.

Third, the NSM has been extended to process vector-valued and tensor-valued data. The extended NSM could be used for processing color images, textured images, dynamic images and diffusion tensor images. Due to limited research time, more and deep study on the subject will be carried on in the future.

Together with the last chapter, the NSM method has been improved and extended to become a general and robust change measure which can quantify changes existing in multidimensional data of various types, regarding different statistical parameters.

Chapter 4

4 NSM-based methods for signal change detection and image edge detection

Contents

Résumé en français

La détection de changements dans un signal et la détection des contours dans une image sont deux applications les plus simples de mesures de changement. Les méthodes basées sur la mesure du changement dans ces deux applications sont généralement conçues de manière similaire: premièrement utiliser la mesure du changement afin de mettre en évidence les changements brusques dans le signal ou les bords dans l'image; puis, estimer les positions de ces changements ou des bords a partir de l'amplitude des changements obtenus.

Les méthodes basées sur des mesures de changement sont récemment devenues populaires en raison de leur robustesse, de leur 'efficacité et de leur caractère non supervisé. Toutefois, pour les signaux fortement aléatoires, les résultats des mesures de changements sont souvent fluctuants, ce qui peut conduire à la génération de fausses alarmes et de fausses détections lorsqu'on utilise ce genre de méthode.

Les méthodes de détection de bords basées sur des mesures de changement sont fondamentales et importantes en raison de leur caractère objectif et non supervisé. Toutefois, lorsqu'il s'agit d'images biomédicales avec un niveau de bruit élevé, certaines mesures de changement existantes peuvent fournir des informations inexactes sur les bords, ce qui peut engendrer de faux bords. Cherchant à résoudre le problème des fausses alarmes et des fausses détections rencontrées dans les signaux extrêmement aléatoires, nous en sommes arrivés à proposer une méthode de détection de changement basée sur la NSM. En effet, grâce à sa robustesse au bruit, la méthode basée sur la NSM permet la détection des changements de manière précise et fiable, même dans des cas très bruités.

Les résultats sur des images synthétiques et sur des images réelles telle que DW cardiaques ont montré que la méthode basée sur NSM est effectivement capable de réduire les faux bords qui se produisent avec d'autres méthodes de détection de bord basées sur la mesure du changement.

4.1 Introduction

Signal change detection and image edge detection are two most straightforward applications of change measures. The change measure-based methods in the two applications are usually designed in a similar way: first use the change measurement method to highlight abrupt changes in the signal or edges in the image; then, based on the obtained magnitude of the changes, estimate the locations of the change points or edges.

In signal change detection, the methods based on change measures have recently become popular because of their robustness, effectiveness, and non-supervision. However, for strong random signals, their change measurement curves often become fluctuated, which may lead to the generation of false alarms and misdetections in these change measure-based detection methods. In section 4.2, a change detection method based on the robust NSM is introduced in subsection 4.2.1 and applied to detect change points in heart rate signals (subsection 4.2.2) and EEG signals (subsection 4.2.3).

The edge detection methods based on change measures are basic and important because of their objectiveness and non-supervision. However, when dealing with biomedical images with high noise levels, existing change measures may provide inaccurate information on edges, which can induce false edges in the methods based on these change measures. In section 4.3, a NSM-based edge detection method is proposed in subsection 4.3.1, evaluated on synthetic image in section 4.3.2, and applied to the edge detection of cardiac diffusion weighted (DW) images in section 4.3.3. Finally, conclusion is given in section 4.4.

4.2 NSM-based method for signal change detection

4.2.1 NSM-based change detection method

Similar to the usual detection procedure based on change measure, the NSM-based change detection method first highlights abrupt changes in signal using the NSM operator, and then estimates the locations of change points by examining the local maxima of the NSM curve above a threshold.

Two change detection situations are given below to explain the method visually. The noisy synthetic signal $x_1(n)$ contains three steps respectively at $n=200$, 300, and 500 regarding its 1st-order moment (Fig. 4.1(a)). The magnitude of the first two steps is 1, and that of the third step is 2. The minimal CNR of the signal $x_1(n)$ is only 2. According to (3.1) and (3.2), with $r=1$ and $h(n)=g(n)=\mathrm{rect}\left(n/21\right)/21$, the NSM curve $\hat{y}_1(n)$ is obtained and shown in Fig. 4.1(c). Above the threshold 0.05, there are three local maxima which indicate accurate positions of the three steps in the signal $x_1(n)$.

The noisy synthetic signal $x_2(n)$ contains three steps respectively at $n=200$, 300, and 500 regarding its 2nd-order moment, see Fig. 4.1(b). Similarly, according to (3.1) and (3.2), with $r=2$ and $h(n)=g(n)=\mathrm{rect}\left(n/21\right)/21$, the NSM curve $\hat{y}_2(n)$ is obtained and shown in Fig. 4.1(d). Above the threshold 0.37, there are three local maxima indicating the positions of the three steps in the signal $x_2(n)$.

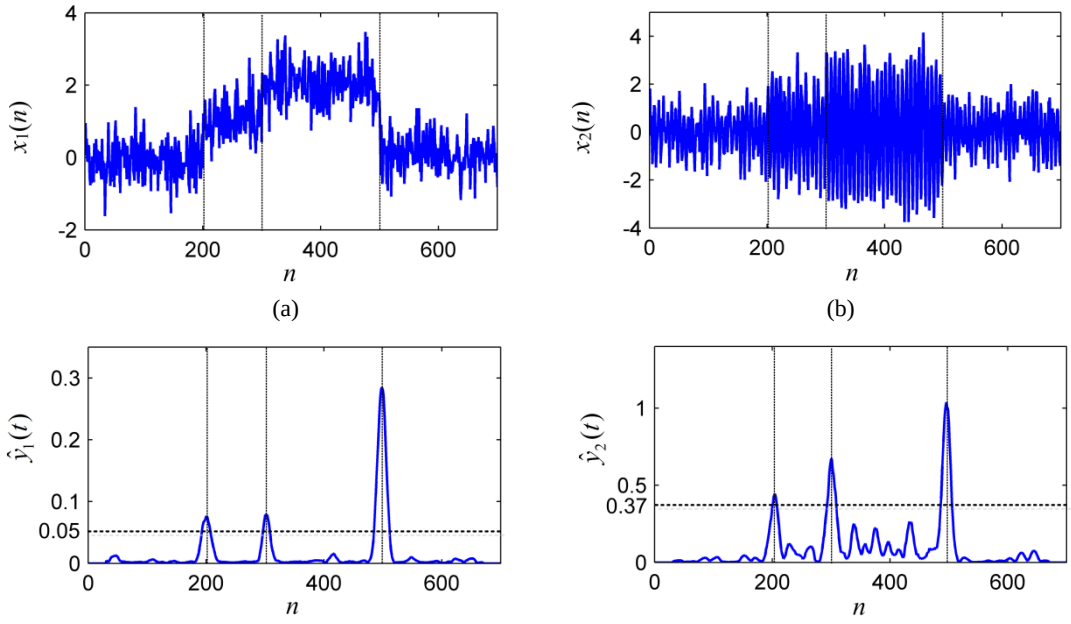

Fig. 4.1 Change detection of noisy synthetic signals. (a) Noisy synthetic signal $x_1(n)$ with three steps in its 1st-order moment. (b) Noisy synthetic signal $x_2(n)$ with three steps in its 2nd-order moment. (c) $\hat{y}_1(n)$: NSM of the noisy synthetic signal $x_1(n)$. (d) $\hat{y}_2(n)$: NSM of the noisy synthetic signal $x_2(n)$.

4.2.2 Change detection of heart rate signals

Heart rate is easy to acquire. Nowadays, the heart rate signal can even be acquired with people feeling nothing. As such acquisition has almost no effect on sleep, the heart rate signals thus acquired are of great significance in understanding sleep and discovering illnesses concerning sleep.

In this subsection, the NSM-based change detection method is used to detect change points in a heart rate signal of a new born baby to identify a heavy sleep period in it. External measurements (such as that of the eye-lids' movements) allow us to know that the heavy sleep period is approximately between data 1300 and data 3200. The signal was once used in [Lavielle, 1999].

The method based on the NSM is compared with other three change detection methods. Two of them are change measure-based methods, the classic ΔBIC [Chen *et al.*, 1998] and a recent method which is based on the relative Pearson divergence [Liu *et al.*, 2012]. The third one [Lavielle, 2005] is based on model selection and referred to as the DCPC (Detection of Changes using a Penalized Contrast). For all of the three change measure-based methods, the more abrupt the change, the higher local maxima. For each method, we localize the same number of changes one by one according to the local maxima of the measurement curves from higher to lower. For the model selection method, the DCPC, the number of changes is set the same as the latter, so that these methods are made comparable to some extend. The

specific parameter settings are listed as follows. For the ΔBIC, the size of the signal segment Z is 330, and the penalty factor $\lambda = 1$. For the method based on the Pearson divergence, the starting point $n = 50$, the window size $k = 10$, and the relative coefficient $\alpha = 0$. For the NSM, the order of the moment $r = 1$, and the half size of the observation window $W = 30$. Since seven change points are located in the three change measure-based methods, the number of segments in the DCPC is set as $K = 8$.

The heart rate signal of the new born baby is shown in Fig. 4.2(a). Its change measurement curves obtained using the ΔBIC, the Pearson divergence, and the NSM are respectively shown in Fig. 4.2 (b), (c) and (d) where the seven change points are marked with numbers. It is seen from Fig. 4.2 that

1) the heart rate signal shows strong randomness;
2) different change measurement curves are obtained for the three change measure-based methods due to their different principles;
3) the ΔBIC method gives a rough curve with several maxima around a single change point, which makes it difficult to determine the position of the change;
4) the NSM-based method gives the best smooth curve among the three change measure-based methods.

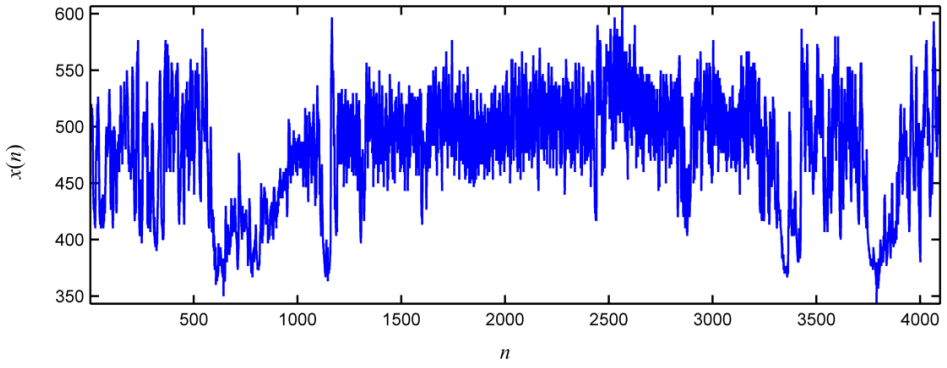

(a)

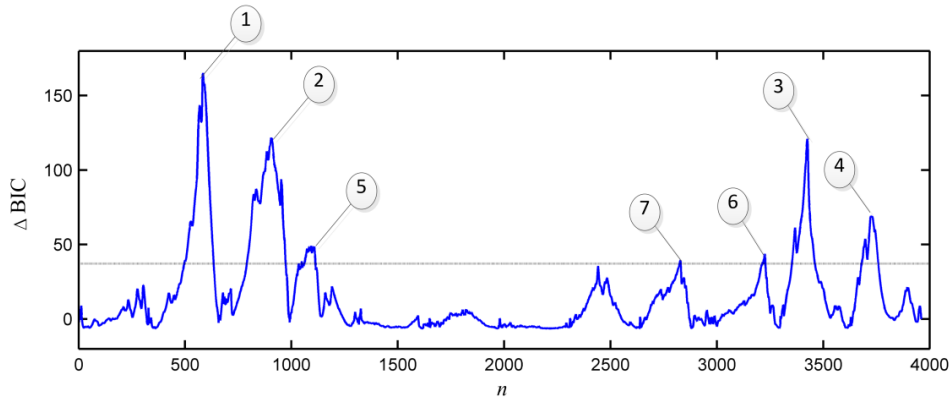

(b)

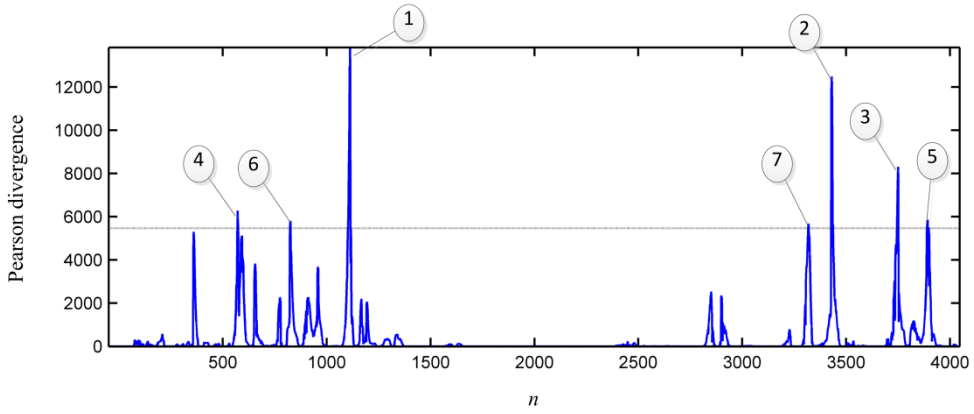

(c)

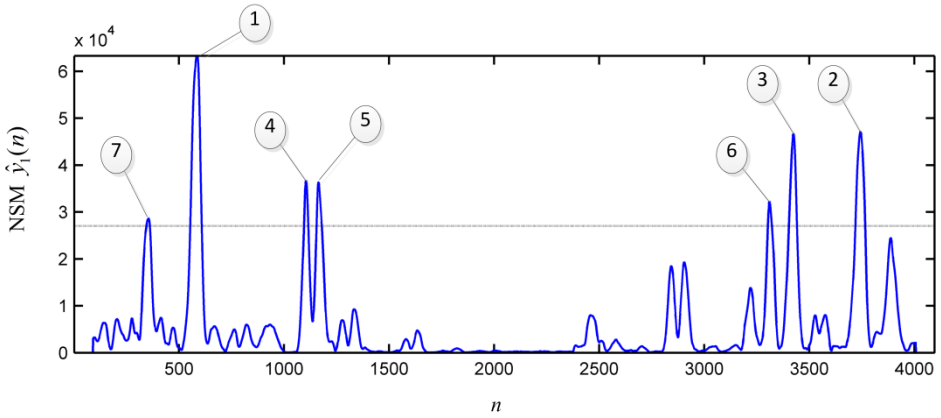

(d)

Fig. 4.2 Heart rate signal of a new born baby and its change measurement curves. (a) The heart rate signal. (b) to (d) Change measurement curves obtained using the ΔBIC, the Pearson divergence, and the NSM $\hat{y}_1(n)$, respectively. Signal is courtesy of Lavielle 1999.

The positions of the seven change points detected by the four methods are marked in Fig. 4.3 with different colors. Note that the heavy sleep period determined by the external measurements is indicated by the two blue vertical lines. It is seen that

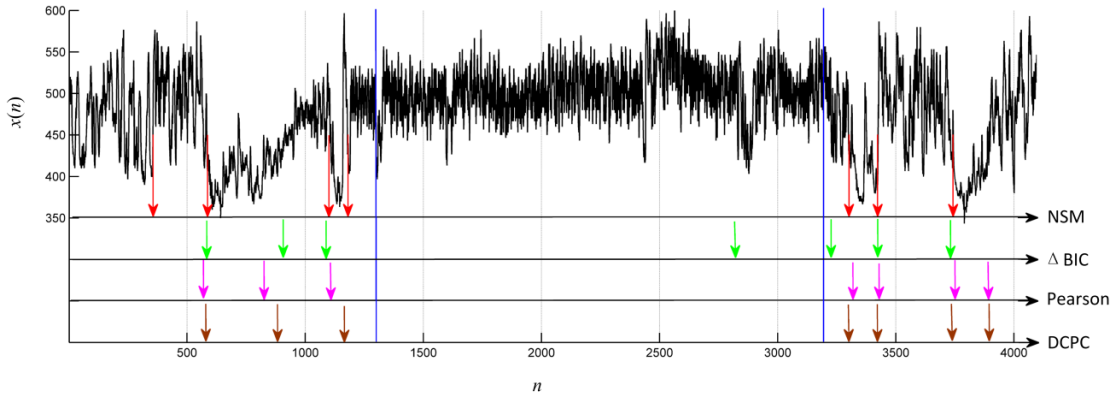

Fig. 4.3 Change detection of the heart rate of a new born baby. Red arrows: the NSM-based method; green arrows: the ΔBIC-based method; magenta arrows: the Pearson divergence-based method; brown arrows: the DCPC.

1) all the change detection results agree with the external measurements except for the ΔBIC which indicates a change during the heavy sleep period;
2) outside of the period, the methods based on the Pearson divergence and the DCPC give similar results which are different from those obtained with our method. For example, they indicate changes around 856 and 3895 which are visually not as abrupt as those at 1135 and 1197 indicated by the NSM-based method.

4.2.3 Change detection of EEG signal

EEG, which records the brain's spontaneous electrical activity, has attracted much attention of both researchers and clinical doctors owing to its non-invasive nature and high temporal resolution. The alpha wave presenting a fusiform amplitude modulation and a frequency ranging from 8 Hz to 12 Hz is considered a basic rhythmic EEG activity of a normal adult in a quiet state. Clinically, the state of alpha waves is used as an important criterion for assessing brain function.

In this subsection, the NSM-based change detection method is used to detect change points in an EEG signal to identify the start moment of an alpha wave in it. The feature of alpha wave allows us to know that the wave starts from 700 in the signal. The signal was once used in [Lavielle, 2005].

As in the last subsection, the NSM-based method is compared with the ΔBIC method [Chen *et al.*, 1998], the method based on the Pearson divergence [Liu *et al.*, 2012], and the DCPC method [Lavielle, 2005]. Change points are located in the same way as that described in the last subsection. The specific parameter settings are listed as follows. For the ΔBIC, the size of the signal segment Z is 300, and the penalty factor $\lambda = 1$. For the method based on the Pearson divergence, the starting point $n = 50$, the window size $k = 10$, and the relative coefficient $\alpha = 0$. For the NSM, the order of the moment $r = 2$, and the half size of the observation window $W = 12$. Since only one change point is located in the three change measure-based methods, the number of segments in the DCPC is set as $K = 2$.

An EEG signal is shown in Fig. 4.4(a). Its change measurement curves obtained using the ΔBIC, Pearson divergence, and NSM methods are respectively shown in Fig. 4.4(b), (c) and (d) where one change point is marked. It is seen from Fig. 4.4 that

1) the EEG signal shows strong randomness;
2) The three change measure-based methods did not generate the same change measurement curves because of their different principles;
3) the methods based on the ΔBIC and the Pearson divergence give complex curves presenting a lot of variations, which makes it difficult to determine the position of the change;
4) the NSM-based method gives the most simple curve among the three change measure-based methods.

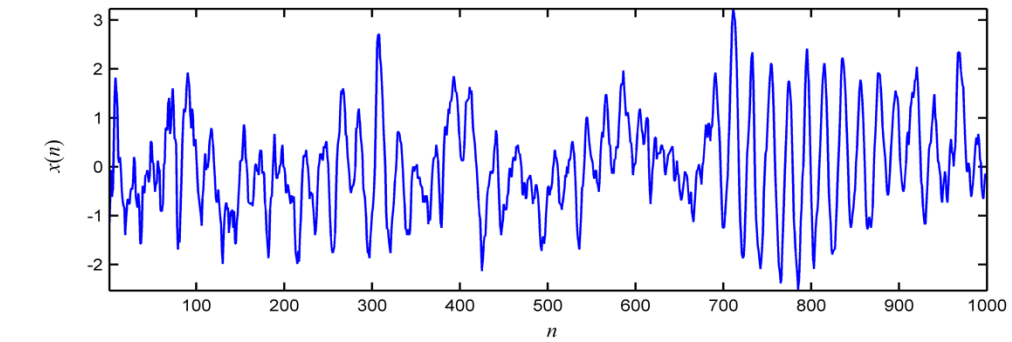

(a)

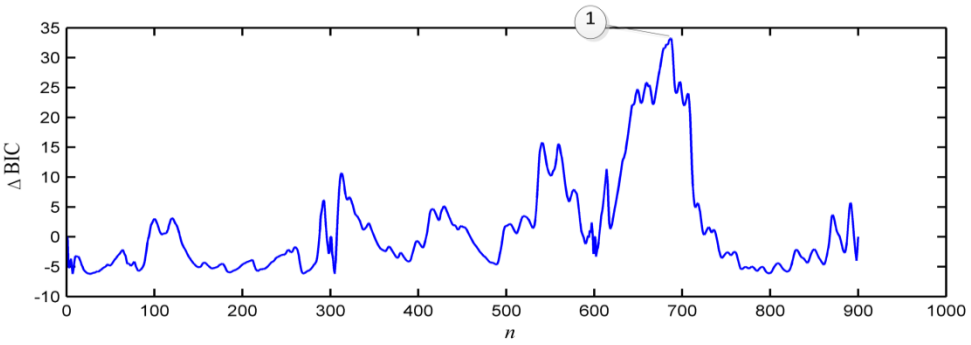

(b)

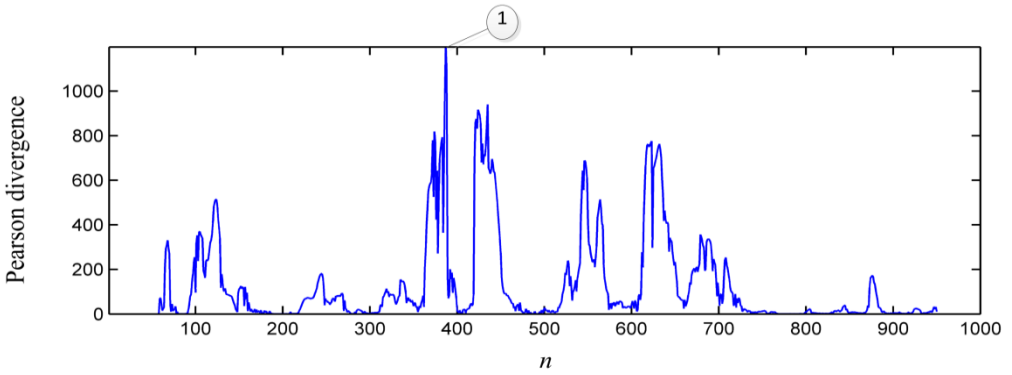

(c)

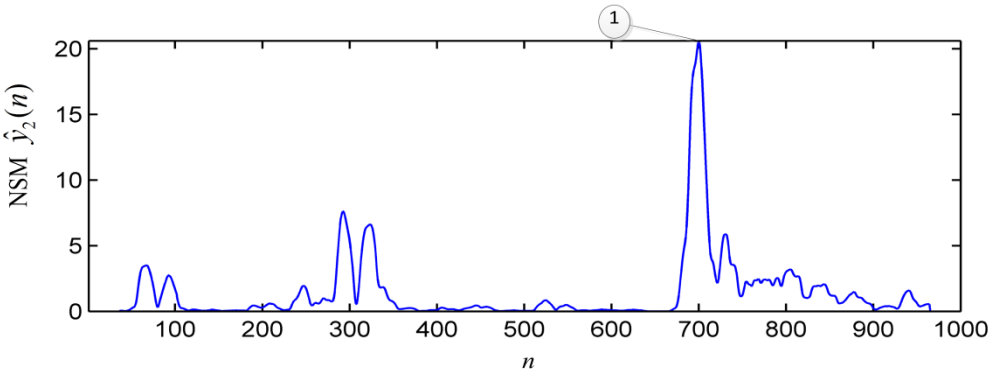

(d)

Fig. 4.4 EEG signal and its change measurement curves. (a) EEG signal. (b) to (d) Change measurement curves using the ΔBIC, the Pearson divergence and the NSM $\hat{y}_2(n)$ respectively. Signal is courtesy of Lavielle 2005.

The positions of the change point detected by the four methods are sketched in Fig. 4.5 with different colors. Note that the start moment of the alpha wave is indicated by the blue vertical line. It is seen that

1) both the ΔBIC and the DCPC indicate a change point near the blue line;
2) the NSM-based method gives an accurate position of the start moment of the alpha wave;
3) the method based on the Pearson divergence indicates a change far away from the blue line, creating an obvious false detection and misdetection.

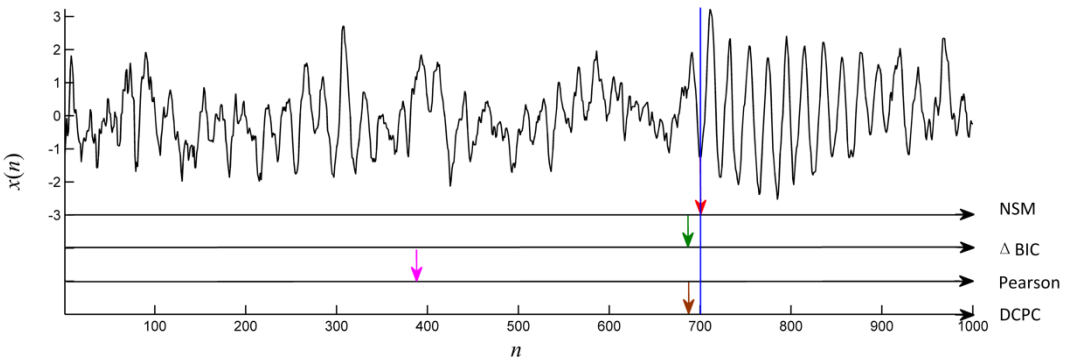

Fig. 4.5 Change detection of an EEG signal. Red arrows: the NSM-based method; green arrows: the ΔBIC-based method; magenta arrows: the Pearson divergence-based method; brown arrows: the DCPC.

The results on the heart rate and EEG signals showed that the NSM-based method is robust to noise and can more efficiently reduce false alarms and misdetections compared to other change measure-based methods.

4.3 NSM-based method for image edge detection

4.3.1 NSM-based edge detection method

The NSM-based edge detection method includes three steps:

1. *Calculation of the NSM map of the image*. The NSM map of the input image is calculated using a 2-D NSM operator;
2. *Nonmaxima suppression*. Two virtual neighbors are defined at the intersections of the gradient direction with the 3×3 sampling grid and the NSM for these neighbors is interpolated from the adjacent pixels, see Fig. 4.6. The pixel at the center of the 3×3 neighborhood is retained for further processing only if its NSM is the largest of the three values.
3. *Hysteresis thresholding*: Two thresholds are defined T_l and T_h with $T_l < T_h$. All the pixels with their NSM values $\Phi(\boldsymbol{p}) \geq T_h$ are retained for the edge map, while all the pixels with $\Phi(\boldsymbol{p}) \leq T_l$ are discarded. The pixels with $T_l < \Phi(\boldsymbol{p}) < T_h$ are retained only if they already have at least one neighbor in the edge map. This step is repeated till convergence.

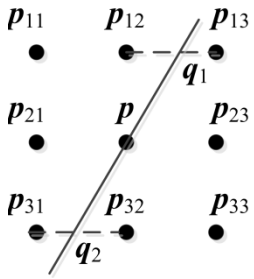

Fig. 4.6 Nonmaxima suppression.

4.3.2 Edge detection of synthetic images

To test the performance of the NSM-based edge detection method in suppressing false edges, a number of experiments on a highly noisy image is done. The original image of size 270×270 contains three gray level values (0, 128 and 255) and two gray level changes of magnitude 128 (0-128 and 128-255). The image is corrupted by an additive Gaussian white noise with mean 0 and standard deviation $\sigma_n = 43$, see Fig. 4.7(a1). The minimal CNR of the image is 3.

The NSM-based method is compared with other three change measure-based edge detection methods: a derivative-based nonlinear filtering scheme (NLFS) [Laligant *et al.*, 2010], the classic Canny filter [Canny, 1986], and a recent method based on the fused edge strength (FES) [Shui *et al.*, 2012]. The specific parameter settings are listed as follows. For the NFLS, no parameter need to be set. For the Canny operator, the standard deviation of the Gaussian function $\sigma = 1.6$. For the FES method, $\sigma^2 = 44.9$, $\rho^2 = 8$, $P = 16$, and $p_f = 0.05$. For the NSM-based method, both the sliding window function $h(n)$ and the observation window function $g(n)$ are the rectangular function of size 5×5, that is $W = 2$. All the measurement results are normalized by their own maxima.

In Fig. 4.7, the change measurement maps of the noisy image obtained by the above four methods are respectively shown from the second to bottom rows. For clearer observations, the upper left part of each map and a horizontal profile of the part marked by a red dashed line are respectively shown in the middle and the right column. It is seen that

(1) for the derivative-based NFLS, the measurement result is most susceptible to noise, with misdetections (for example, the first change from left in (b3)), masses of false responses in flat areas (see (b1) and (b2)) and, the low output SNR (see (b3));
(2) the Canny filter and the FES method give better measurement results than the NFLS, with more salient responses to edges (see (c1), (c2), (d1) and (d2)), less false responses in flat areas and higher output SNRs (see (c3) and (d3));
(3) the NSM operator provides the most robust change measurement map of the noisy image, with the least false responses (see (e1) and (e2)) and the highest output SNR (see (e3));

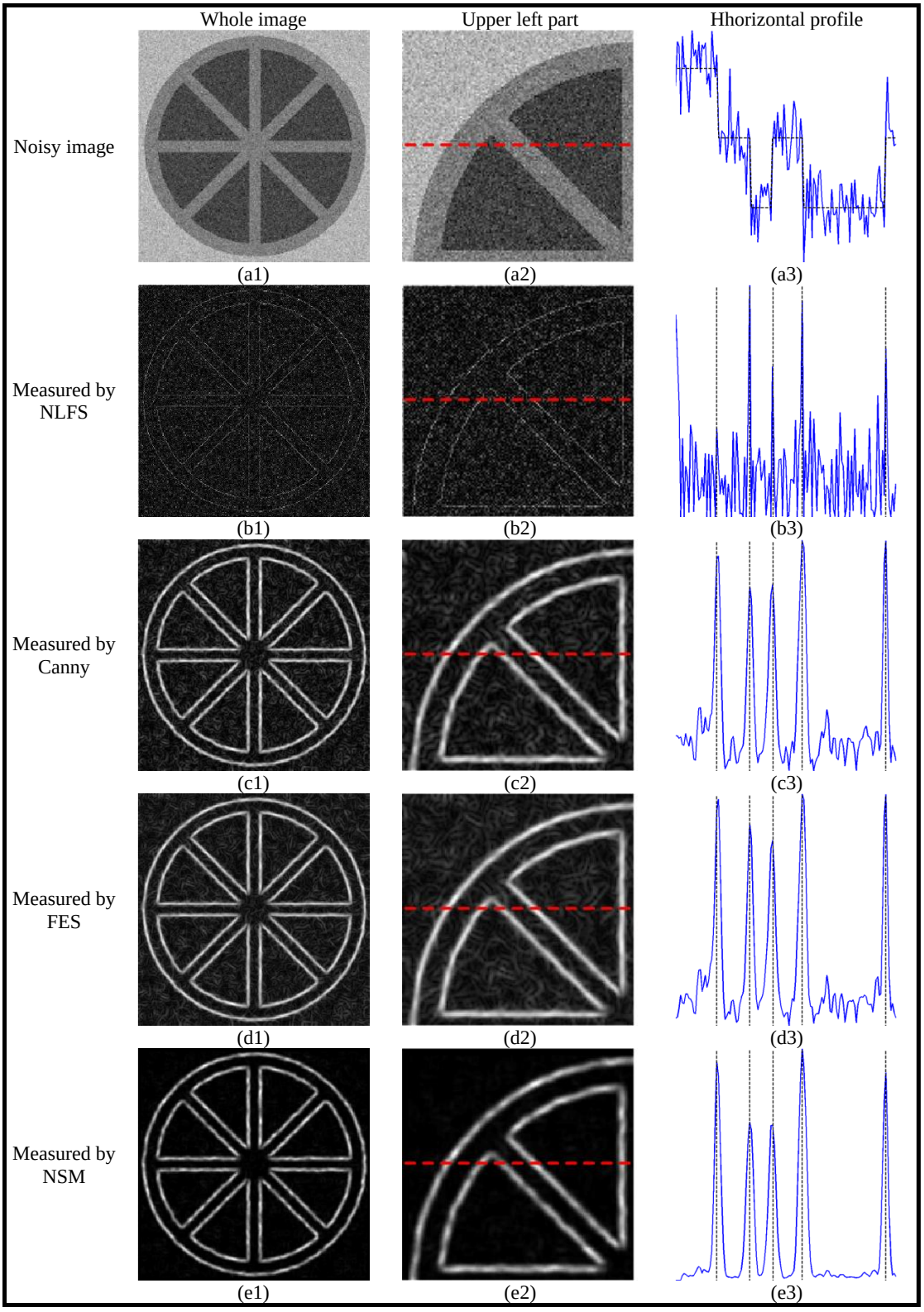

Fig. 4.7 Noisy synthetic image and its change measurement maps obtained by the NLFS, the Canny filter, the FES method and the NSM operator.

(4) The responses of the Canny filter, the FES method and the NSM operator to edges present as ridges, whose widths depend on the sizes of the sliding windows used in these methods;
(5) image details smaller than the window width are not be measured well (see corners in (c1), (c2), (d1), (d2), (e1) and (e2)).

After measuring edge strength by the four methods, nonmaxima suppression and hysteresis thresholding are carried out, yielding the edges shown in Fig. 4.8. Note that, for a fair comparison, the same thresholds $T_h = 0.3$ and $T_l = 0.12$ are used. It is seen that more or less false edges are present in the results of the NLFS, the Canny filter and the FES method. Compared to the three methods, the NSM-based method generates more reasonable results with less false edges ((d1) and (d2)).

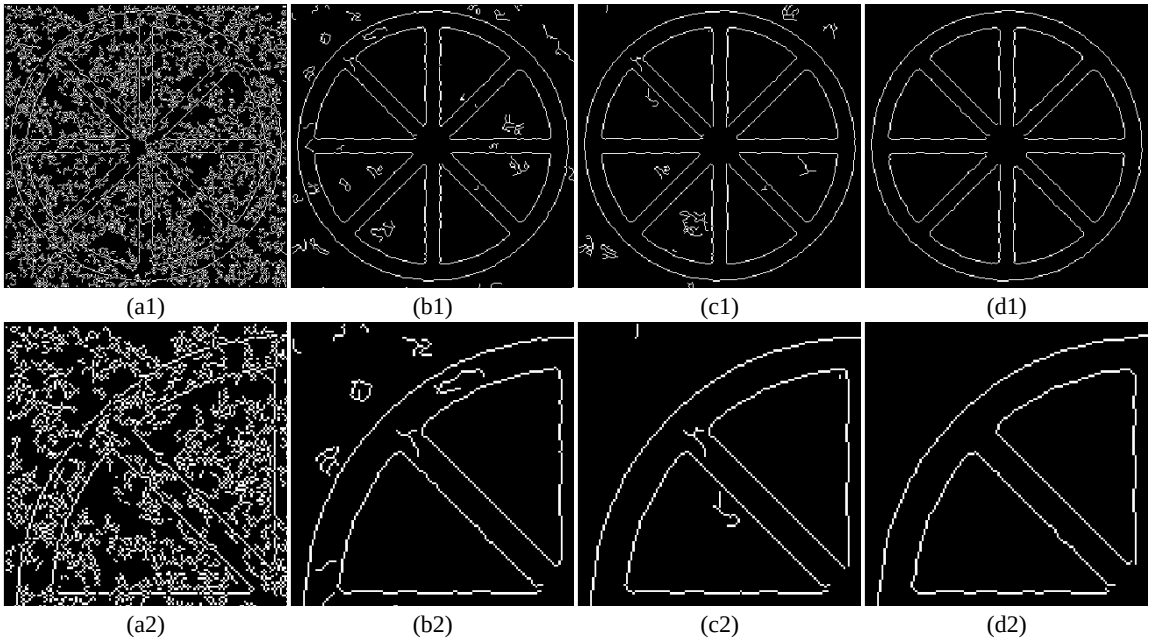

Fig. 4.8 Edge detection of a noisy synthetic image. (a1) to (d1) Edges detected by the NLFS, the Canny filter, the FES method and the NSM-based method, respectively. (a2) to (d2) Upper left parts of (a1) to (d1).

4.3.3 Edge detection of cardiac diffusion weighted images

The myocardium is the basic muscle that makes up the heart. The death of a part of the cardiac muscle is known as myocardial infarction or heart attack, which could in turn lead to a complete cessation of the heart muscles, known as cardiac arrest. Therefore, studies on the myocardial fibers have great significance for the analysis of the heart function and the prevention and treatment of serious heart diseases.

Diffusion tensor magnetic resonance imaging (DT-MRI, or DTI) appears currently as the unique imaging modality to investigate noninvasively both *ex vivo* and *in vivo* myocardial fiber architectures of the human heart. Although promising for studying the microstructure of

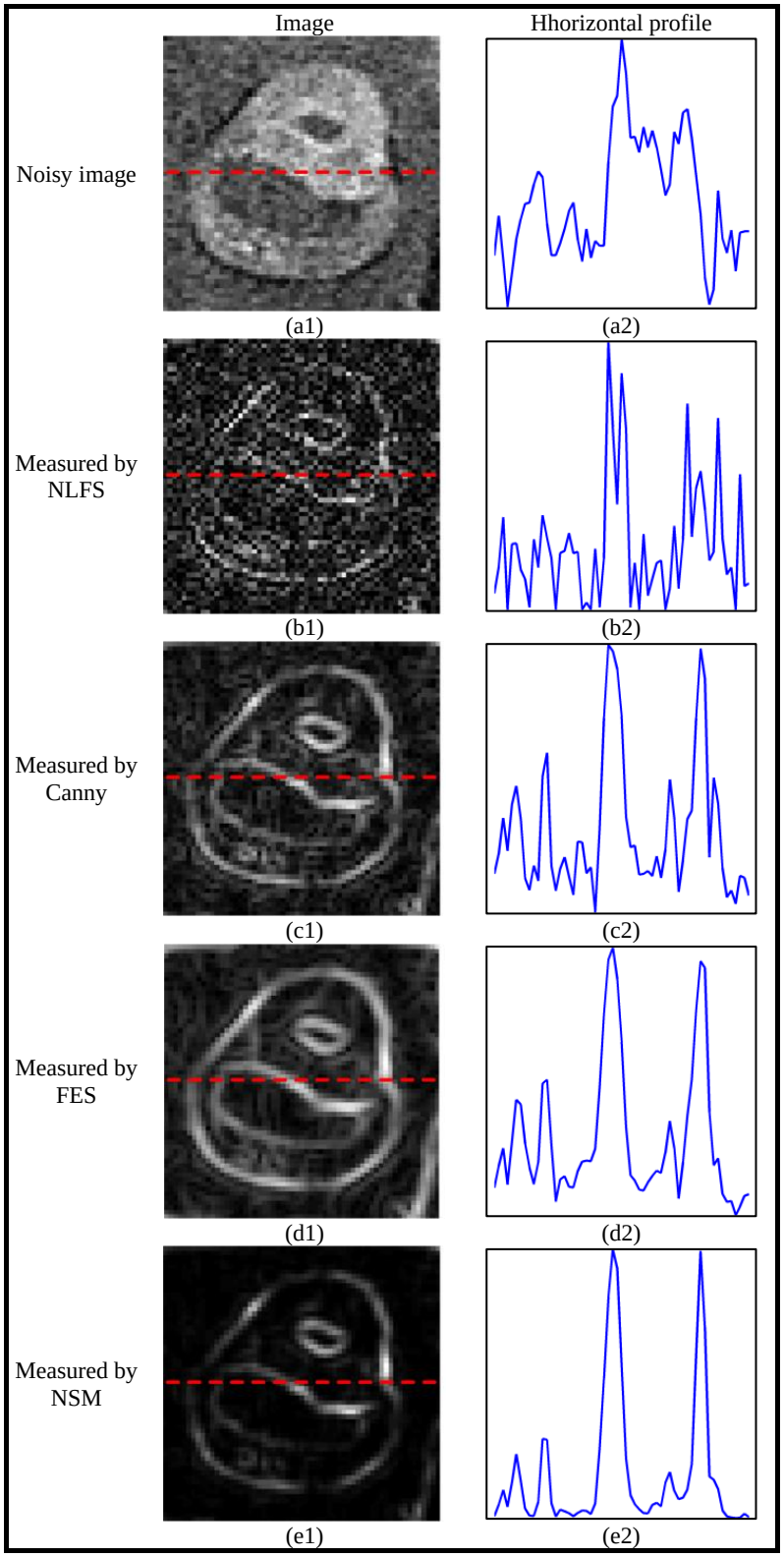

Fig. 4.9 Cardiac diffusion weighted image and its change measurement maps obtained by the NLFS, the Canny filter, the FES method and the NSM operator respectively. Images are courtesy of Pierre Croisille.

in vivo tissues, the performance and the potentiality of DTI are hampered by the presence of high-level noise in diffusion weighted (DW) images [Basser *et al.*, 2000; Chen *et al.*, 2005; Ding *et al.*, 2005; Jones *et al.*, 2004]. These images are corrupted so severely that their features, such as edges, can be buried in the speckled mosaic-like patterns aroused by noise.

In this subsection, the NSM-based edge detection method is used to detect edges of cardiac DW images. As in the experiments on synthetic images, the NLFS [Laligant *et al.*, 2010], the Canny filter [Canny, 1986], and the FES method [Shui *et al.*, 2012] are used as comparison methods. In the implementation of these methods, parameters in the four methods are the same as those used in the experiments on the synthetic images. Also, the measurement results are normalized by their own maxima as we did in the last subsection.

A DW image corresponding to one slice of the acquired 3D volumes in one direction is shown in Fig. 4.9(a1). Its change measurement maps obtained by the four methods are respectively shown from the second row to the bottom in the left column. For clearer observations, a horizontal profile of each map marked by a red dashed line is shown in the right column. It is seen from the results that

(1) similar to the experiments on synthetic images, the measurement result with the derivative-based NFLS is most susceptible to noise, with responses to real edges buried in false responses aroused by noise (see (b1) and (b2));
(2) the Canny filter and the FES method give better measurement results than the NFLS, with more salient responses to edges (see (c1) and (d1)), less false responses in flat areas and higher output SNRs (see (c2) and (d2));
(3) the NSM operator provides the most robust change measurement map, with the least false responses (see (e1)) and the highest output SNR (see (e2)).

After measuring edge strength by the four methods, nonmaxima suppression and hysteresis thresholding are carried out, yielding the edges shown in Fig. 4.10. For a fair comparison, different thresholds adapted to each method are used. It is seen that the NLFS, the Canny filter and the FES methods yield more or less false edges. In contrast, the NSM-based method generates more clean results, see (d).

(a) (b) (c) (d)

Fig. 4.10 Edge detection of a cardiac DW image. Edges detected by (a) the NLFS ($T_h = 0.25, T_l = 0.088$), (b) the Canny filter ($T_h = 0.45, T_l = 0.158$), (c) the FES method ($T_h = 0.4, T_l = 0.14$) and (d) the NSM-based method ($T_h = 0.22, T_l = 0.077$), respectively.

4.4 Conclusion

Aiming at the problem of false alarms and misdetections in the change detection of highly random signals, a NSM-based change detection method has been proposed. Because of the robustness of the NSM to noise, the method based on the NSM allows for accurate and reliable change detection even in highly noisy cases. The results on the heart rate and EEG signals showed that the NSM-based method can more efficiently reduce false alarms and misdetections compared to other change measure-based methods.

Aiming at the problem of false edges in the edge detection of highly noisy images, a NSM-based edge detection method has been proposed. The method based on the NSM enables the edges to be accurately and reliably detected. The results on both synthetic images and real cardiac DW images showed that the NSM-based method can effectively reduce false edges occurring with other change measure-based edge detection methods.

Chapter 5

5 NSM-based geometric active contour segmentation model

Contents

Résumé en français

La segmentation d'images médicales est rendue difficile à cause du faible contraste, du bruit important et d'autres ambiguïtés dans les images. Aujourd'hui, le modèle géométrique actif (GAC), introduit au début des années 90, est devenu un cadre général de plus en plus populaire pour la segmentation des images en particulier biomédicales. Comme type principal de modèle GAC, le modèle GAC basé contours utilise souvent l'amplitude du gradient pour guider les déplacements de l'ensemble de niveau zéro et pour arrêter l'évolution de l'ensemble de niveau. Toutefois, dans les cas très bruités, le gradient peut fournir des informations inexactes sur les bords de telle sorte que le modèle GAC basé contours peut facilement produire de faux contours autour des formes induite par le bruit ou des ponts au niveau des contours faiblement marqués des objets.

Dans ce travail, nous nous sommes focalisés sur le problème des faux positifs et de la délocalisation des contours dans des images très bruitées. Nous proposons de remplacer l'amplitude du gradient par la NSM robuste comme mesure de variation, pour fournir des informations sur l'intensité des contours au modèle GAC basé contour. Ce nouveau modèle GAC est appelé modèle NSM-GAC.

Le mécanisme du modèle réside dans l'exploitation de la robustesse de l'opérateur 2D de mesure de non-stationnarité pour mesurer l'intensité des contours et guider le contour actif vers les contours cibles contenus dans l'image. Les résultats sur des images de synthèse montrent que le modèle est particulièrement robuste au bruit gaussien et que le résultat de segmentation se dégrade peu avec l'augmentation du niveau de bruit. Sur des images ultrasonores de la carotide, la méthode proposée est plus performante que les méthodes DRLSE et C-V et plus robuste au bruit spatial de« speckle » propre aux images ultrasonores. Le temps de calcul est réduit et la précision de segmentation (moins de faux contours, moins de délocalisation de contours) comparativement meilleure.

5.1 Introduction

Medical image segmentation is made difficult by low contrast, noise, and other imaging ambiguities. So far, the geometric active (GAC) model, introduced in the early 90's [Caselles *et al.*, 1993; Malladi *et al.*, 1995], has become increasingly popular as a general segmentation framework used for segmenting various types of images and among them biomedical images. The edge-based GAC model usually guides the motion of the zero level set and stops the level set evolution using the image gradient magnitude computed in the external energy term [Gao *et al.*, 2011; Li *et al.*, 2010]. However, in highly noisy cases, the gradient may provide inaccurate information on edges so that the edge-based GAC model can easily produce false contours around noise-induced patterns or leakages at weak object boundaries.

In this chapter, we propose to modify the classical edge-based GAC model by replacing the gradient magnitude change measure by the NSM . Thus, a NSM-based GAC model, called the NSM-GAC model, is proposed in Section 5.2.1. Its flow chart is given in Section 5.2.2. Thanks to the robustness of the NSM, the new model should be immune to noise, reducing false contours and leakages which are often present in the output of the GAC models using the gradient magnitude as change measure.

In order to thoroughly analyze its performance in noisy cases, the proposed model is tested on synthetic images with different noise levels in Section 5.3. In Section 5.4, the model is applied to segment ultrasound images of the carotid. The conclusion is in Section 5.5.

5.2 The NSM-GAC segmentation model

5.2.1 Design of the NSM-GAC model

Let $\phi:\Omega\in R$ be a level set function defined on a domain Ω. The active contour C can be represented as the zero level set of ϕ by $\{C:\phi(x,y,t)=0\}$, and thus the initial contour C_0 is expressed as $\phi_0=\phi(x,y,0)$. We define an energy function $E(\phi)$ by

$$E(\phi)=E_{ext}(\phi)+\mu\Re(\phi)\,. \tag{5.1}$$

The first term $E_{ext}(\phi)$ is the external energy, depending on the input image. It guides the zero level set (the active contour C) towards the object boundary. The energy $E_{ext}(\phi)$ is designed such that it achieves a minimum when the zero level set of ϕ is located at the object boundary. Specifically, $E_{ext}(\phi)$ is defined as

$$E_{ext}(\phi)=\lambda L_e(\phi)+\alpha A_e(\phi), \tag{5.2}$$

where $\lambda>0$ and α are, two weighting coefficients of, respectively, the energy function $L_e(\phi)$ and $A_e(\phi)$, defined by

$$L_e(\phi)=\int_\Omega e(x,y)\cdot\delta_\varepsilon(\phi)\left|\nabla\phi\right|dxdy \tag{5.3}$$

and

$$A_e(\phi) = \int_\Omega e(x,y) \cdot H_\varepsilon(-\phi) dxdy\,, \tag{5.4}$$

where the Dirac delta function is defined as

$$\delta_\varepsilon(x) = \begin{cases} [1+\cos(2\pi x/3)]/3, & |x| \le 3/2 \\ 0 \qquad\qquad\quad , & |x| > 3/2 \end{cases}, \tag{5.5}$$

and the Heaviside function

$$H_\varepsilon(x) = \begin{cases} \left[1 + x/\varepsilon + \sin\left(\pi x/\varepsilon\right)/\pi\right]/2, & |x| \le \varepsilon \\ 0, & x > \varepsilon \\ 1, & x < -\varepsilon \end{cases}. \tag{5.6}$$

Like other edge-based GAC models, the NSM-GAC model includes an edge indicator function e to control the level set evolution. Traditionally, the function e is defined as [Caselles *et al.*, 1993; Li *et al.*, 2010]

$$e = \frac{1}{1+\left|\nabla G_\sigma * I\right|^2} \tag{5.7}$$

where G_σ is a Gaussian kernel with a standard deviation σ, and $\left|\nabla G_\sigma * I\right|$ is the gradient magnitude obtained by the Canny operator. Although being an efficient scheme to lessen the sensitivity of the gradient to noise, the Canny operator, essentially based on derivatives, may produce false responses in noisy cases anyway. In our model, the NSM $\tilde{I}$ is substituted for $\left|\nabla G_\sigma * I\right|$ to construct a new edge indicator function such that:

$$e = \frac{1}{1+\left(\nabla \tilde{I}\right)^2}. \tag{5.8}$$

This function e takes smaller values at the object boundaries than elsewhere. It can slow down the level set evolution at the locations where the intensity greatly varies and speed it up in flat areas. Being more robust than the Canny operator (see subsection 2.3.3.2), the NSM operator can provide more accurate edge strength to the function e, and thereby improve the performance of the edge-based GAC model.

In the second term of (5.1), $\mu > 0$ is a constant, and $\Re(\phi)$ is a distance regularization term [Li *et al.*, 2010] given by

$$\Re(\phi) = \int_\Omega p(|\nabla\phi|) dxdy\,, \tag{5.9}$$

where p represents the double-well potential function defined as

$$p(s) = \begin{cases} \dfrac{1}{(2\pi)^2}\left[1-\cos(2\pi s)\right] & s \le 1 \\ \dfrac{1}{2}(s-1)^2 & s \ge 1 \end{cases}. \tag{5.10}$$

This distance regularization term forces the gradient magnitude of the level set function toward one of its minimum points, thereby maintaining a desired shape of the level set function, particularly a signed distance profile near its zero level set. The distance

regularization completely eliminates the need for reinitialization which is usually used in conventional level set formulations.

To sum up, the energy function of (5.1) can be expressed as

$$E(\phi)=\lambda\int_{\Omega}\frac{1}{1+(\nabla I)^2}\cdot\delta_{\varepsilon}(\phi)|\nabla\phi|dxdy+\alpha\int_{\Omega}\frac{1}{1+(\nabla I)^2}\cdot H_{\varepsilon}(-\phi)dxdy+\mu\int_{\Omega}p(|\nabla\phi|)dxdy. \quad (5.11)$$

This energy function can be minimized by solving the following gradient flow:

$$\frac{\partial\phi}{\partial t}=\lambda\delta_{\varepsilon}(\phi)\mathrm{div}\left(\frac{1}{1+(\nabla I)^2}\cdot\frac{\nabla\phi}{|\nabla\phi|}\right)+\alpha\frac{\delta_{\varepsilon}(\phi)}{1+(\nabla I)^2}+\mu\mathrm{div}\left(\frac{p'(|\nabla\phi|)}{|\nabla\phi|}\nabla\phi\right). \quad (5.12)$$

5.2.2 Flow chart of the NSM-GAC model

In the implementation of the NSM-GAC model, an image I can be segmented according to the flow chart shown in Fig. 5.1. Like other GAC models, in the implementation, the computation time mainly depends on the number of iterations Υ.

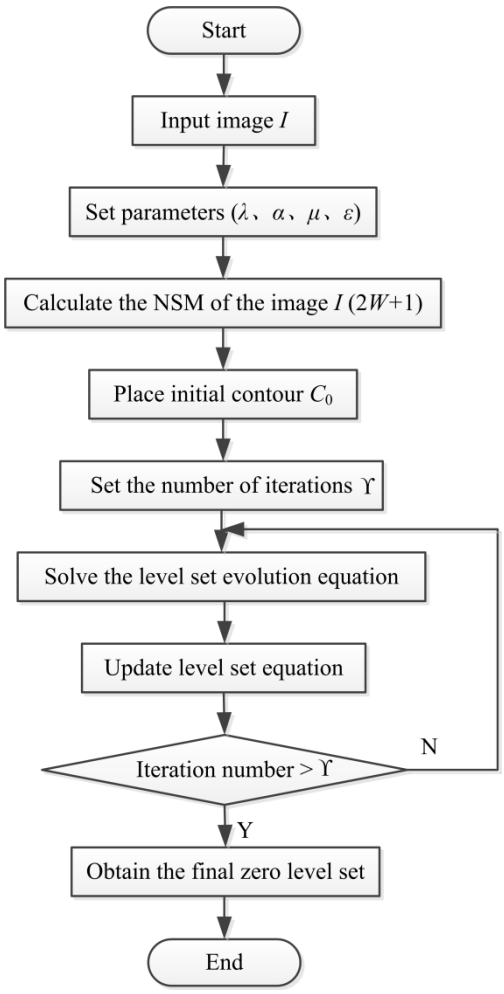

Fig. 5.1 Flow chart of the NSM-GAC model

5.3 Segmentation of synthetic images

5.3.1 Segmentation of images with different noise levels

To test the performance of the NSM-GAC model in segmenting images with different noise levels, four sets of experiments are done on synthetic images corrupted by an additive white Gaussian noise with mean 0 and variance 0, 25, 45 and 65 (see the first row in Fig. 5.2) respectively. These synthetic images contain various shapes, such as two ellipses, a right-angled triangle, and a concave shape. These shapes are used to evaluate the performance of the model in segmenting different geometric shapes. The noise-free image of size 128×128 includes three gray level values (0, 128 and 255) and two gray level changes of magnitude 128 (0-128 and 128-255) and 255 (0-255). With the increase of the noise variance (25, 45 and 65), the minimal CNR of the noisy synthetic image decreases (5.12, 2.84 and 1.97).

The distance regularized level set evolution (DRLSE) [Li *et al.*, 2010], a recently proposed edge-based GAC model, is used as a comparison method. In the DRLSE formulation, the gradient magnitude $|\nabla G_\sigma * I|$ is used as the change measure to provide information on edges for the level set evolution. The parameters (the weighting coefficient α, the iteration number Υ, the standard deviation of the Gaussian function σ, the width of the sliding and the observation window $2W+1$) of the two models have been experimentally optimized to produce the best segmentation results with less iteration. The Parameters remaining constant are: $\lambda = 5.0$, $\mu = 0.04$, $\Delta t = 5.0$, and $\varepsilon = 1.5$.

The same initial contour marked with a red rectangle is used in the four sets of experiments (see the input images in the first row of Fig. 5.2). The images in the second and third rows are respectively the segmentation results of the DRLSE and the NSM-GAC model. It is seen that

(1) with the increase of the noise level, more and more false contours and leakages are present in the results of the DRLSE model;

(2) the NSM-GAC model gives good segmentation results for all the noisy images;

(3) the NSM-GAC model always perform better than the DRLSE model in noisy cases.

These results are quantitatively evaluated using four indices which are the Jaccard similarity (JS) coefficient, Dice coefficient, false positive rate (FPR) and false negative rate (FNR). The JS coefficient measures similarity between two sample sets, and is defined as

$$JS = \frac{|SR \cap GT|}{|SR \cup GT|}, \tag{5.13}$$

where *SR* (Segmentation Result) and *GT* (Ground Truth) respectively represent the set of pixels contained in the segmented object and in the object of reference, and where $|\square|$ is the operation of counting their number. The closer to 1 the *JS* value is, the more similar the *SR* and the *GT* are.

The Dice coefficient is also a similarity measure between two sets, which definition is not very different from the *JS* coefficient. The Dice coefficient is defined as

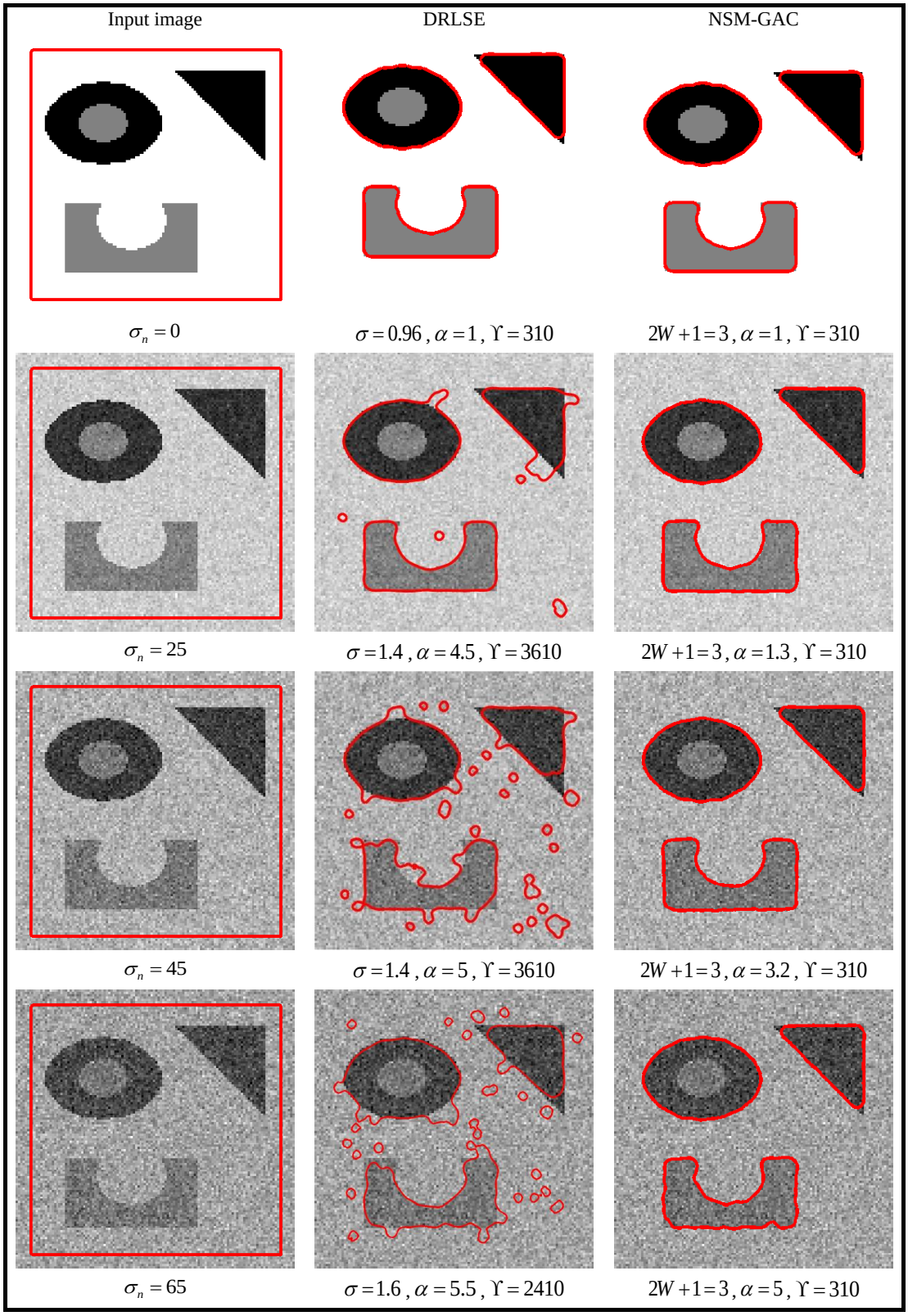

Fig. 5.2 Segmentation of synthetic images with different noise levels.

$$Dice = \frac{2|SR \cap GT|}{|SR| + |GT|}. \tag{5.14}$$

Like the JS coefficient, the Dice coefficient ranges between zero and one. Also, the closer to 1 the *Dice* value is, the more similar the *SR* and the *GT* are.

The FPR is equivalent to the false alarm rate: it is the proportion of pixels contained in the *SR* that do not belong to the *GT*. The FPR is defined as

$$FPR = \frac{|SR| - |SR \cap GT|}{|GT|}. \tag{5.15}$$

The FNR is equivalent to the missing alarm rate: its represents the proportion of pixels contained in the *GT* that do not belong to the *SR*. The FNR is defined as

$$FNR = \frac{|GT| - |SR \cap GT|}{|GT|}. \tag{5.16}$$

Table 5.1 reports the values of the JS coefficient, Dice coefficient, FPR and FNR corresponding to the results in Fig. 5.2. We can see from the table that

(1) For the noise-free image, the segmentation result of the DRLSE model is highly similar to the ground truth ($JS = 0.99$, $Dice = 1.00$) with few false and missing alarms ($FPR = 0$, $FNR = 0.98\%$), while for the noisy images, the results have a low similarity to the ground truth (the minimum *JS* and *Dice* are respectively 0.77 and 0.87) and high false and missing alarm rates (the maximum *FPR* and *FNR* are respectively 15.3% and 10.7%).

(2) For the NSM-GAC model, all the segmentation results are highly similar to the ground truth (the minimum *JS* and *Dice* are respectively 0.97 and 0.98) with few false and missing alarms (the maximum *FPR* and *FNR* are respectively 0.6% and 2.6%);

(3) The four indices computed on the segmentation results of the NSM-GAC model experience no significant changes while the noise level present in the images increases.

Table 5.1 *JS* coefficient, Dice coefficient, FPR and FNR of segmentation results in Fig. 5.2

Model	Index	$\sigma_n = 0$	$\sigma_n = 25$	$\sigma_n = 45$	$\sigma_n = 65$
DRLSE	*JS*	0.99	0.91	0.80	0.77
	Dice	1.00	0.95	0.89	0.87
	FPR	0	5.5%	16.5%	15.3%
	FNR	0.98%	4.0%	6.5%	10.7%
NSM-GAC	*JS*	0.99	0.99	0.98	0.97
	Dice	1.00	0.99	0.99	0.98
	FPR	0	0.2%	0.2%	0.6%
	FNR	0.95%	1.0%	1.3%	2.6%

Both qualitative and quantitative analyses show that the NSM-GAC model is robust to noise, and that using the NSM as the change measure can improve the performance of the edge-based GAC model in segmenting images corrupted by Gaussian noise.

5.3.2 Segmentation of an image with a high noise level

To test the performance of the NSM-GAC model in reducing false contours and leakages which usually occur in the segmentation results of highly noisy images, a set of experiments is done on a synthetic image corrupted by an additive white Gaussian noise with mean 0 and variance 65 (see Fig. 5.3 (a)). The minimal CNR of the noisy synthetic image is only 1.97.

The edge-based DRLSE model [Li *et al.*, 2010] and the classical region-based C-V model [Chan *et al.*, 2001] are used as comparison methods. The parameters (the weighting coefficient α, the iteration number Υ, the standard deviation of the Gaussian function σ, the width of the sliding and the observation window $2W+1$) of the three models have been experimentally optimized to produce the best segmentation results with the smaller number of iterations. The specific parameter settings are listed as follows. For the DRLSE model, $\Upsilon = 2410$, $\sigma = 1.6$, $\alpha = 5.5$, $\lambda = 5.0$, $\mu = 0.04$, $\Delta t = 5.0$, $\varepsilon = 1.5$. For the C-V model, $\Upsilon = 810$. For the NSM-GAC model, $\Upsilon = 310$, $2W+1 = 3$, $\alpha = 5$, $\lambda = 5.0$, $\mu = 0.04$, $\Delta t = 5.0$, $\varepsilon = 1.5$.

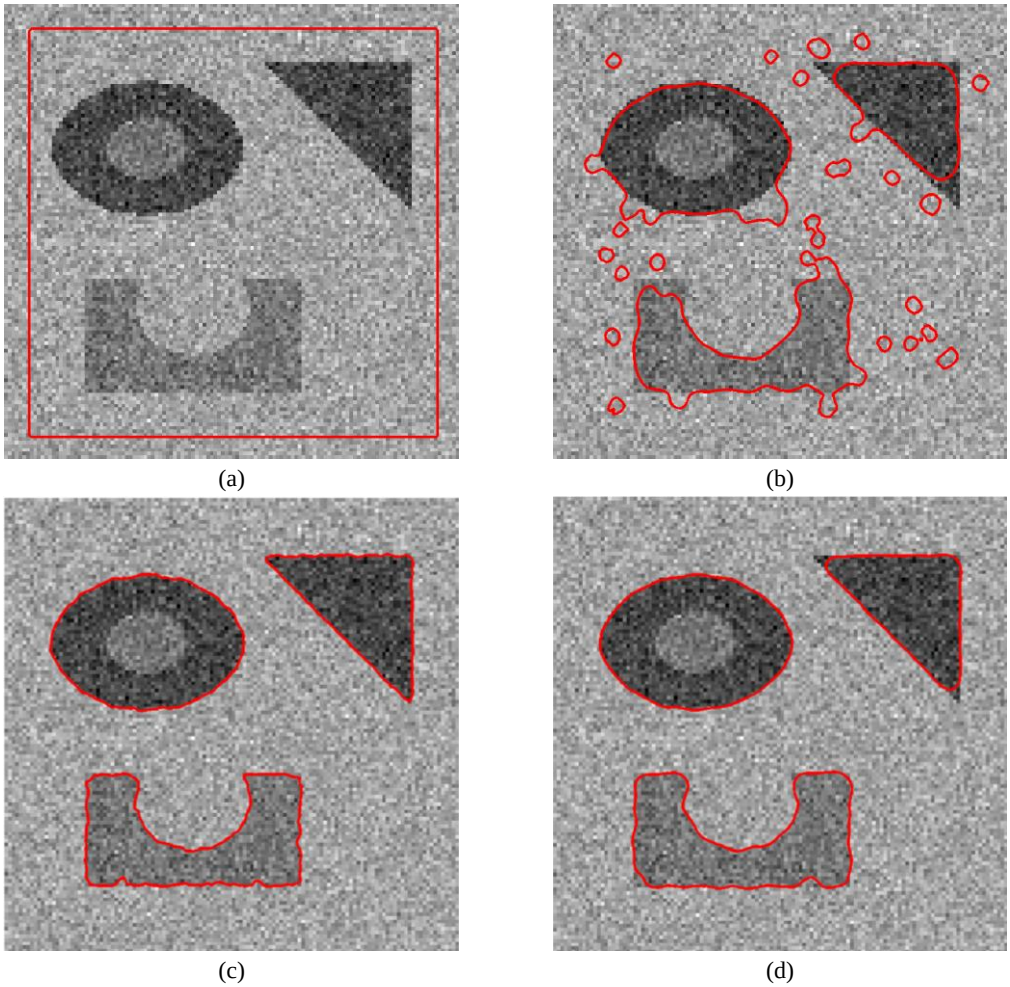

(a) (b) (c) (d)

Fig. 5.3 Segmentation of synthetic image corrupted by Gaussian noise. (a) Noisy synthetic image and the initial contour. (b) to (d) Segmentation result of the DRLSE model, the C-V model and the NSM-GAC model.

The same initial contour, marked with a red rectangle in the input image shown in Fig. 5.3 (a), is used in the three experiments. The segmentation results of the DRLSE model, the C-V model, and the NSM-GAC model are respectively shown in (b) to (d). We can see that

(1) the segmentation result of the DRLSE model contains a number of false contours and an obvious leakage at the upper left corner of the concave shape;

(2) both the region-based C-V model and the NSM-GAC model provide good segmentation results with no false contour and no obvious leakage;

(3) the NSM-GAC model only iterates 410 times to produce a segmentation result as good as that of the C-V model which is obtained after 810 iterations;

(4) the contours in the result of the NSM-GAC model have rounded corners, which is a common problem for the edge-based models which use sliding windows to estimate the edge strength.

Table 5.2 reports the values of the *JS* coefficient, the Dice coefficient, the FPR and the FNR corresponding to the results in Fig. 5.3. We see from the table that

(1) the result of the DRLSE model has low similarity with the ground truth ($JS = 0.77$, $Dice = 0.87$) and high false and missing alarm rates ($FPR = 15.3\%$, $FNR = 10.7\%$);

(2) the results of the C-V model and the NSM-GAC model are highly similar to the ground truth (C-V: $JS = 0.98$, $Dice = 0.99$; NSM-GAC: $JS = 0.97$, $Dice = 0.98$) with few false and missing alarms (C-V: $FPR = 1.1\%$, $FNR = 2.2\%$; NSM-GAC: $FPR = 0.6\%$, $FNR = 2.6\%$);

Both qualitative and quantitative analyses show that, for noisy images corrupted by Gaussian noise, the NSM-GAC model can provide better segmentation results with fewer false contours and leakages than the GAC model with the gradient magnitude as the change measure.

We recorded the CPU times consumed by the three models: 33.77s for the DRLSE model, 7.03s for the C-V model, and 5.49s for the NSM-GAC model. The CPU times are obtained by running the Matlab programs on a PC with Intel (R) Core (TM) 2 Duo CPU, E7300, 2.66 GHz, 3.25GB RAM, with Matlab 7.10.0.499 (R2010a) on Windows XP Professional SP3. From the consumed times and the above segmentation results, we demonstrate that the proposed NSM-GAC model can provide better results with less iterations and less computation time.

Table 5.2 JS coefficient, Dice coefficient, FPR and FNR of segmentation results shown in Fig. 5.3

Evaluation index	DRLSE	C-V	NSM-GAC
JS	0.77	0.98	0.97
Dice	0.87	0.99	0.98
FPR	15.3%	1.1%	0.6%
FNR	10.7%	2.2%	2.6%

5.4 Segmentation of ultrasound images of the carotid

The good condition or bad condition of the carotid artery are closely related to the good or bad global cardiovascular state of a patient. The evaluation of this condition plays an important role in identifying the danger of asymptomatic patients. Ultrasound imaging is the most commonly used modality to image the carotid artery. However, segmenting ultrasound image is strongly difficult because of the speckle, shadows, low contrast, as well as low spatial resolution inherent to that type of images.

5.4.1 Segmentation of a simulated ultrasound image

To test the performance of the NSM-GAC model in segmenting ultrasound images, a set of experiments is done on a simulated carotid image. According to the simulation method presented in [Bamber *et al.*, 1980; Yu *et al.*, 2002], the simulated image shown in Fig. 5.4 (b) is obtained with a 128×128 echogenicity model shown in Fig. 5.4 (a). The specific parameter settings in the simulation are: the center frequency 12MHz, the propagation speed 1540 m/s, the pulse-width of the transmitting ultrasonic wave 2 MHz, the beam-width of transmitting ultrasonic wave 1.5 MHz, and the variance of the Gaussian fluctuation 1 MHz. The large noise variance results in blurring the arterial walls and providing a low CNR in the simulated image.

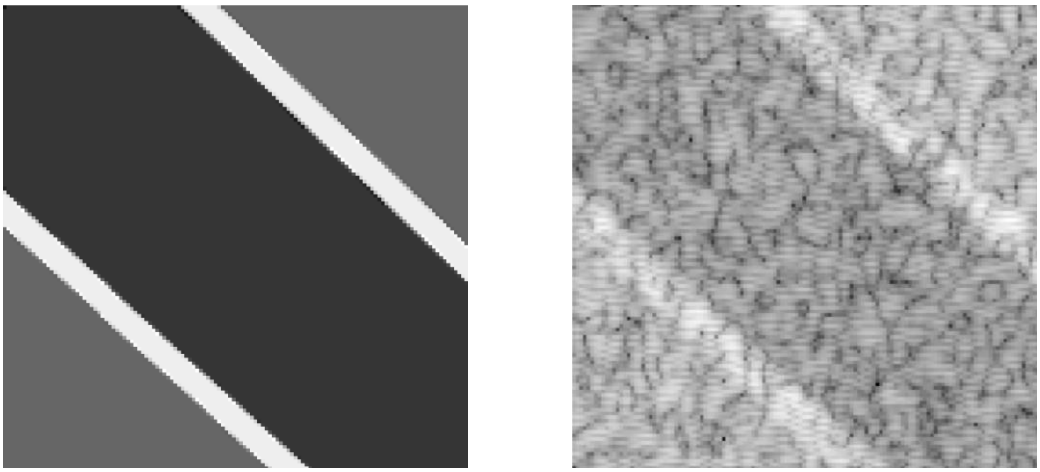

(a) (b)

Fig. 5.4 Simulated data. (a) backscatter cross section distribution. (b) Simulated ultrasound image of a carotid.

The edge-based DRLSE model [Li *et al.*, 2010] and the classic region-based C-V model [Chan *et al.*, 2001] are used as comparison methods. The parameters of the three models have been experimentally optimized to produce better segmentation results with the less iterations as possible. For the DRLSE model, $\Upsilon = 910$, $\sigma = 2.88$, $\alpha = -2.5$, $\lambda = 5.0$, $\mu = 0.04$, $\Delta t = 5.0$, $\varepsilon = 1.5$. For the C-V model, $\Upsilon = 460$. For the NSM-GAC model, $\Upsilon = 460$, $W = 3$, $\alpha = -1.7$, $\lambda = 5.0$, $\mu = 0.04$, $\Delta t = 5.0$, $\varepsilon = 1.5$.

The same initial contour, marked with a red rectangle in the input image shown in Fig. 5.5 (a), is used in the three experiments. The segmentation results of the DRLSE model, the C-V model, and the NSM-GAC model are respectively shown in (b) to (d). We can see that

(1) the segmentation result of the DRLSE model contains two false contours at the bottom right corner and an obvious leakage in the upper middle part;

(2) different from the case of the synthetic image corrupted by Gaussian noise, the region-based C-V model fails to segment the simulated ultrasound image, mainly because, unlike the zero mean Gaussian noise, the impact of speckle noise on the average intensity of the image inside and outside the active contour is hardly eliminated by the averaging;

(3) the NSM-GAC model provides a good result with no false contour and no obvious leakage;

(4) the NSM-GAC model only iterates 460 times and produces the best segmentation result, while the DRLSE model iterates 910 times.

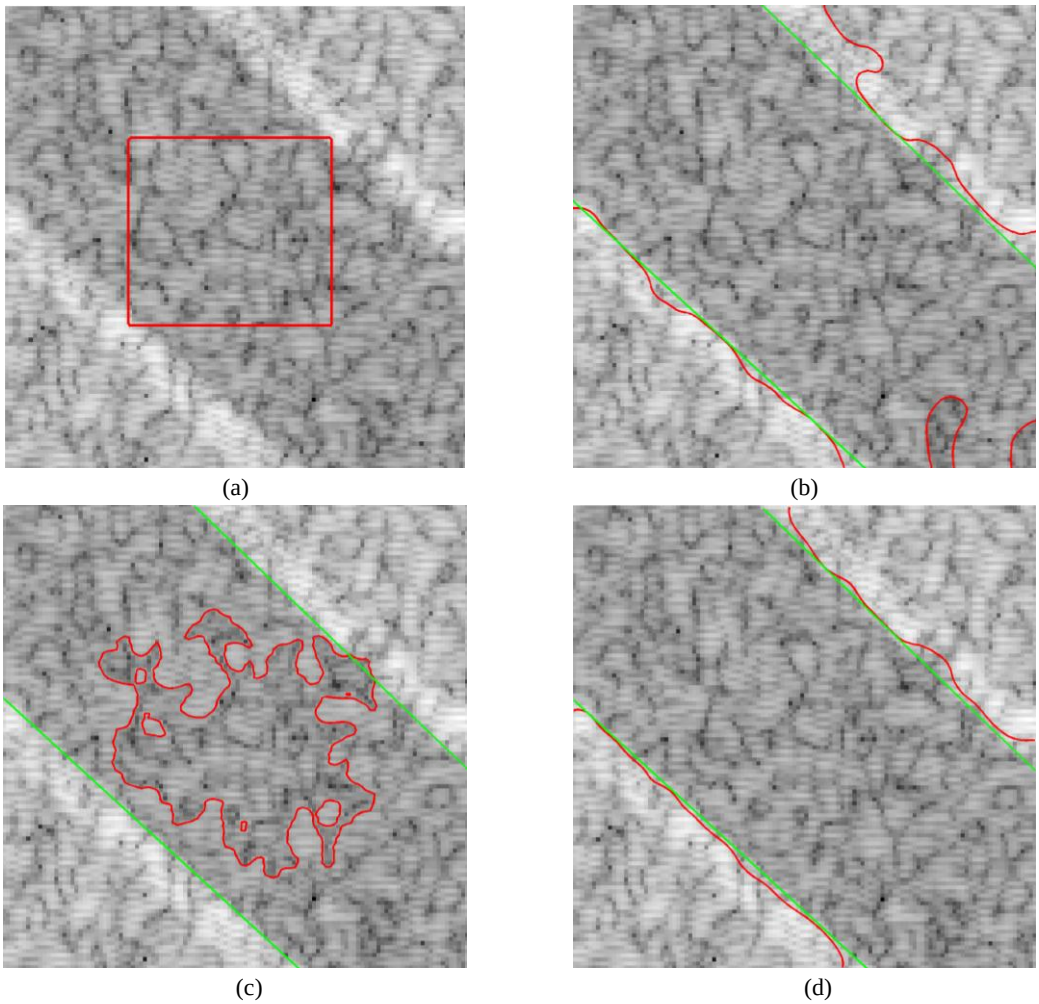

Fig. 5.5 Segmentation of a simulated ultrasound image. (a) Simulated image and the initial contour in red. (b) to (d) Segmentation results in green of the DRLSE model, the C-V model and the NSM-GAC model.

Table 5.3 reports the values of the *JS* coefficient, the Dice coefficient, the FPR and the FNR corresponding to the results shown in Fig. 5.5. It comes from the table that

(1) the segmentation result of the C-V model has the lowest similarity to the ground truth ($JS = 0.26$, $Dice = 0.41$) and the highest missing alarm rate ($FNR = 74\%$);

(2) the result of the DRLSE model has a moderate similarity to the ground truth ($JS = 0.92$, $Dice = 0.96$) but a higher false alarm rate ($FPR = 6.2\%$);

(3) the result of the NSM-GAC model has the highest similarity to the ground truth ($JS = 0.98$, $Dice = 0.99$) and the lowest false and missing alarm rates ($FPR = 1.8\%$, $FNR = 0.2\%$).

Both qualitative and quantitative analyses show that the NSM-GAC model is immune to the speckle noise and can effectively reduce false contours and leakages which usually occur while segmenting highly noisy ultrasound images.

The CPU times consumed by the three models are recorded: 12.95s for the DRLSE model, 3.83s for the C-V model, and 8.47s for the NSM-GAC model. Although the C-V model consumed a shorter computation time, its result cannot be improved by prolonging the running time, i.e., increasing the number of iterations.

Table 5.3 JS coefficient, Dice coefficient, FPR and FNR of the segmentation results shown in Fig. 5.5

Evaluation index	DRLSE	C-V	NSM-GAC
JS	0.92	0.26	0.98
Dice	0.96	0.41	0.99
FPR	6.2%	0.0%	1.8%
FNR	2.5%	74%	0.2%

5.4.2 Segmentation of a real ultrasound image of the carotid

In order to test the performance of the NSM-GAC model on real data, a set of experiments is done on a real ultrasound image of the carotid, aiming to segment the artery out. Compared with the simulated image, the real carotid image has a higher CNR, but still with strong speckle noise and weak edges.

Similar to the simulation experiment, the DRLSE model [Li *et al.*, 2010] and the C-V model [Chan *et al.*, 2001] are used as comparison methods. Still, the parameters of the three methods are experimentally optimized to produce the best segmentation results with the smaller number of iterations. For the DRLSE model, $\Upsilon = 1210$, $\sigma = 2.88$, $\alpha = -2$, $\lambda = 5.0$, $\mu = 0.04$, $\Delta t = 5.0$, $\varepsilon = 1.5$. For the C-V model, $\Upsilon = 1610$. For the NSM-GAC model, $\Upsilon = 610$, $W = 2$, $\alpha = -1.4$, $\lambda = 5.0$, $\mu = 0.04$, $\Delta t = 5.0$, $\varepsilon = 1.5$.

The same initial contour, marked with a red rectangle in the real carotid image shown in Fig. 5.6 (a), is used in the three experiments. The segmentation results of the DRLSE, the C-V model, and the NSM-GAC model are respectively shown in (b) to (d). We can see that

(1) the segmentation result of the DRLSE model contains four obvious false contours indicated with green arrows and two leakages indicated with magenta arrows;

(2) although after 1610 iterations, the result of the C-V model contains a number of undesirable false contours, most of them created by the speckle noise;

(3) a good segmentation result, with no false contour and no obvious leakage, is obtained by the NSM-GAC model after 610 iterations, which is only half of that of the DRLSE model, and one third of the C-V model.

We recorded the CPU times consumed by the three models: 186.81s for the DRLSE model, 65.90s for the C-V model, and 97.84s for the NSM-GAC model. Generally speaking, the NSM-GAC model can produce a better result with less iteration time and shorter running time than the other two models.

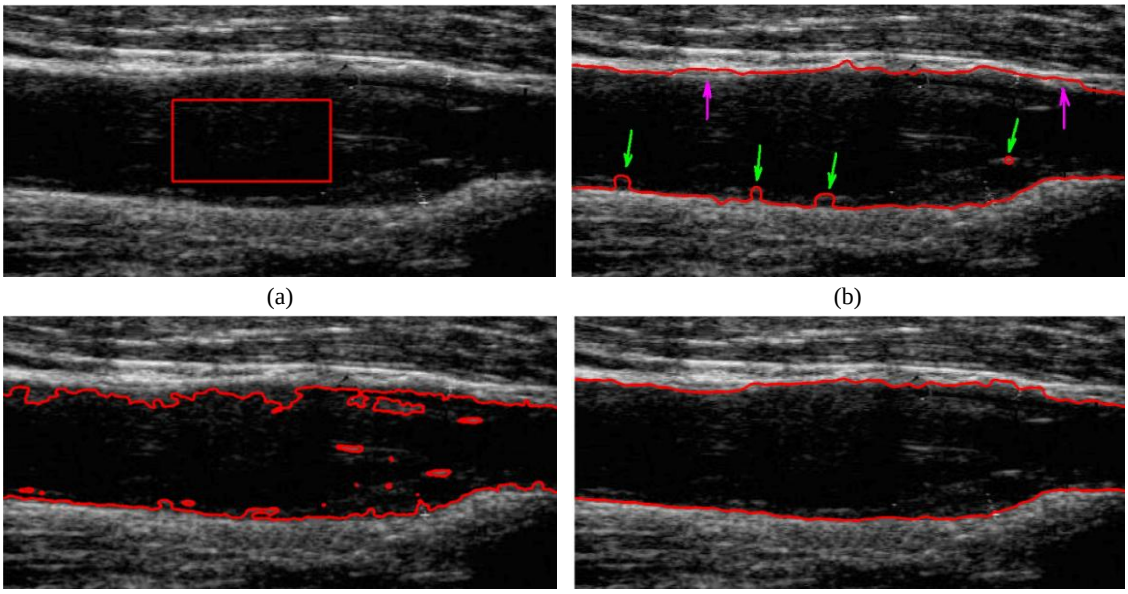

Fig. 5.6 Segmentation of a real ultrasound image of a carotid. (a) Carotid image and the initial contour in red. (b) to (d) Segmentation results of the DRLSE model, the C-V model and the NSM-GAC model. Image is courtesy of Ping Li.

5.5 Conclusion

We have presented a NSM-GAC model to overcome false contours and leakages while segmenting highly noisy images.

By qualitatively and quantitatively analyzing the segmentation results on noisy synthetic images, a simulated ultrasound image and a real ultrasound image of a carotid, we can derive the following conclusions

(1) The NSM-GAC model is immune to the Gaussian noise, the most common noise encountered in biomedical images, and to the speckle noise.

(2) For images with a high noise level, the NSM-GAC model can provide good segmentation results with few false contour s and obvious leakages.

(3) Like other GAC models, the running time of the NSM-GAC model mainly depends on the number of iterations. The experimental results show that the proposed model can provide better segmentation results with less iteration time and shorter running time than classical GAC models.

(4) Thanks to the NSM, the NSM-GAC model is more robust to noise than the GAC model using the gradient magnitude as change measure.

Chapter 6

6 Nonstationarity adaptive filtering and smoothing of human cardiac diffusion weighted images

Contents

6.1 Introduction

De nouvelles modalités d'imagerie médicale, qui rendent possible l'étude des microstructures d'organes humains, ouvrent de nouvelles perspectives pour le traitement et la prévention des maladies graves. Cependant, à cause du principe même de ces nouvelles modalités d'imagerie, conjugué avec la complexité des tissus imagés, les images obtenues contiennent souvent des bruits importants, et présentent ainsi de faibles rapport signal sur bruit. Les images à faible RSB peuvent limiter l'utilisation de ces nouvelles modalités d'imagerie et la potentialité de ces dernières. L'amélioration de la qualité de ces images à faible RSB a attiré l'attention des chercheurs. Dans ce domaine, la difficulté se trouve dans le compromis difficile à trouver entre réduction du bruit et préservation des caractéristiques importantes (bords, contours, détails, etc.) de l'image. L'imagerie par résonance magnétique du tenseur de diffusion (DT-MRI ou simplement DTI en anglais), qui est une nouvelle méthode d'imagerie, permet de mesurer la diffusion des molécules d'eau dans des directions différentes, fournissant ainsi des informations biologiquement et cliniquement pertinentes sur les tissus étudiés [Basser *et al.*, 1994]. Ces informations peuvent aider à caractériser la composition, la microstructure et l'architecture du tissu, et à évaluer son éventuel changement durant le développement, ou en cas de maladie ou de dégénérescence. L'Imagerie du tenseur de diffusion a été intensivement étudiée pour le cerveau humain [Alexander *et al.*, 2007; Assaf *et al.*, 2008; Xu *et al.*, 2009a], et plus récemment pour le cœur humain [Frindel *et al.*, 2009; Lombaert *et al.*, 2012; Wei *et al.*, 2013a;b; Wu *et al.*, 2009; Wu *et al.*, 2006; Yang *et al.*, 2012], ainsi que pour d'autres tissus et organes [Eyal *et al.*, 2012; Notohamiprodjo *et al.*, 2008; Raya *et al.*, 2012]. L'Imagerie du tenseur de diffusion devient donc un outil de plus en plus populaire et important pour la recherche médicale et pour le diagnostic.

Bien que prometteur pour l'étude de la microstructure des tissus in vivo, la performance et la potentialité de l'Imagerie du tenseur de diffusion sont entravées par la présence de bruit important dans les images pondérées en diffusion (DW images en anglais) [Basser *et al.*, 2000; Chen *et al.*, 2005; Ding *et al.*, 2005; Jones *et al.*, 2004]. Ces images sont corrompues si sévèrement que leurs caractéristiques, telles que les bords ou les détails, peuvent disparaitre sous forme de mosaïque mouchetée suscitée par le bruit, et l'analyse de DTI ultérieure telle que l'estimation du tenseur, le suivi des fibres et le calcul des cartographies de paramètres sont entachées d'incertitude et d'erreurs. Pour ces raisons, l'amélioration des données est devenue l'une des tâches primordiales dans l'étude de DTI.

Le prétraitement de ces données peut s'opérer soit sur les images DW soit sur les tenseurs. Jusqu'en 2007, de nombreux travaux ont porté sur la régularisation des tenseurs en étendant des méthodes classiques de traitement d'image scalaire et des champs de matrices [Burgeth *et al.*, 2011; Hamarnesh *et al.*, 2007; Welk *et al.*, 2007]. D'autres approches [Chou *et al.*, 2009; Coulon *et al.*, 2004] ont été développées pour lisser les champs de vecteurs dérivé des tenseurs. Cependant, sans prétraitement des DW images, ces tenseurs ne peuvent souvent pas être garantis d'être semi-définis positifs, sauf avec un traitement spécial, comme dans le cadre de Cholesky [Wang *et al.*, 2004c] ou de Log-euclidienne [Arsigny *et al.*, 2006]. Par conséquent, la régularisation des champs de tenseurs a une utilisation limitée.

D'autre part, le prétraitement ou le lissage des DW images consiste à traiter le problème en amont car il permet de réduire la propagation des erreurs dans le calcul ultérieur des grandeurs dérivées. Le filtrage par diffusion basé sur l'équation aux dérivées partielles (PDE) a été un premier choix pour lisser les images DW, en raison de sa solide base théorique et de sa bonne performance. Les auteurs [Parker *et al.*, 2000] ont utilisé le filtre de diffusion non linéaire proposé dans [Perona *et al.*, 1990] pour réduire le bruit dans les images DW. Dans [Ding *et al.*, 2005], le tenseur de structure dans le filtrage par diffusion anisotrope (ADF) [Weickert, 1999] a été reformulé afin de s'adapter aux structures des faisceaux de fibres dans les images de tenseur de diffusion. Des résultats illustratifs ont démontré que la technique de filtrage ou lissage anisotrope est supérieure à la méthode non linéaire [Parker *et al.*, 2000] dans la réduction de l'impact du bruit sur les mesures d'anisotropie et de la direction des images du tenseur de diffusion. Cette approche de lissage anisotrope [Ding *et al.*, 2005] a également été testée dans [Moraschi *et al.*, 2010] et est apparue plus adaptée aux données DTI. Récemment, la méthode de [Ding *et al.*, 2005] a été améliorée à la fois dans la stabilité et dans la précision temporelle [Xu *et al.*, 2010]. Outre le filtrage par diffusion basé sur PDE, d'autres méthodes de lissage ont également été développées qui concernent, par exemple, le lissage par TV-norm pondéré [Vemuri *et al.*, 2001] et le lissage adaptatif structurel basé sur la méthode de propagation-séparation [Tabelow *et al.*, 2008]. La plupart de ces techniques de lissage ont utilisé le filtrage par diffusion basé sur les équations aux dérivées partielles comme méthode de comparaison, et les résultats n'ont pas montré d'avantages évidents.

Malgré ces travaux, pour les images ayant un faible RSB comme les images DW, réduire le bruit tout en préservant les caractéristiques désirables demeure un défi persistant pour les méthodes de lissage existants. Dans ce chapitre, en nous appuyant sur un meilleur compromis entre la réduction du bruit et la préservation des caractéristiques dans l'image, nous proposons une nouvelle méthode de lissage, appelée filtrage adaptatif par non-stationnarité (nonstationarity adaptive filtering-NAF en anglais). Cette nouvelle méthode est décrite dans la Section 6.2. Ensuite, elle est évaluée dans la Section 6.3 sur des images DW de synthèse. Enfin, les résultats de traitement d'images DW du cœur humain par la méthode proposée sont donnés dans la Section 6.4, suivie d'une conclusion à la Section 6.5.

6.2 Nonstationarity adaptive filtering

Traditional averaging filters have undesirable side effect of blurring boundaries and details mainly because the average is performed on a fixed mask. In fact, for any pixel, a better operation to update its intensity is to average intensities of the pixels within its homogeneous neighborhood. Since the points in the homogeneous neighborhood have similar nature, the operation of averaging them can reduce noise without introducing any distortion caused by heterogeneous points. Therefore, such averaging can achieve a better compromise between the reduction of noise and the preservation of desirable features. The key point, especially for low-SNR images, is to appropriately choose the homogeneous neighborhood, in particular near boundaries.

Obviously, the homogeneous neighborhood has an adaptive shape. So the filtering based on the average within the homogeneous neighborhood is therefore called the adaptive neighborhood filtering, which is defined as

$$\tilde{f}(\boldsymbol{x}) = \frac{1}{M} \sum_{\boldsymbol{y} \in \mathbf{N}(\boldsymbol{x})} f(\boldsymbol{y}), \tag{6.1}$$

where $f(\boldsymbol{y})$ is the input image defined on a bounded domain $\Omega \subset \boldsymbol{R}^2$, $\tilde{f}(\boldsymbol{x})$ the smoothed image, $\mathbf{N}(\boldsymbol{x})$ the adaptive neighborhood of the pixel (or voxel for a 3-D volume) $\boldsymbol{x} \in \Omega$, and M the size of $\mathbf{N}(\boldsymbol{x})$.

The homogeneous neighborhood $\mathbf{N}(\boldsymbol{x})$ is composed of points $\boldsymbol{y} \in \Omega$ whose intensities and locations are close to those of $\boldsymbol{x}$. The points in $\mathbf{N}(\boldsymbol{x})$ are called the homogeneous points or members. The neighborhood $\mathbf{N}(\boldsymbol{x})$ can be expressed as

$$\mathbf{N}(\boldsymbol{x}) = \left\{ \boldsymbol{y} : R(\boldsymbol{x}, \boldsymbol{y}) \le Th, \boldsymbol{x}, \boldsymbol{y} \in \Omega \right\}, \tag{6.2}$$

where $R(\boldsymbol{x}, \boldsymbol{y})$ designates the rule which governs the relationship between the current point $\boldsymbol{x}$ and any neighborhood member $\boldsymbol{y}$, and Th representing the threshold is a positive real number. The design of $R(\boldsymbol{x}, \boldsymbol{y})$ is crucial since, for a fixed Th, it determines the adaptive neighborhood $\mathbf{N}(\boldsymbol{x})$, thus the smoothed image $\tilde{f}(\boldsymbol{x})$.

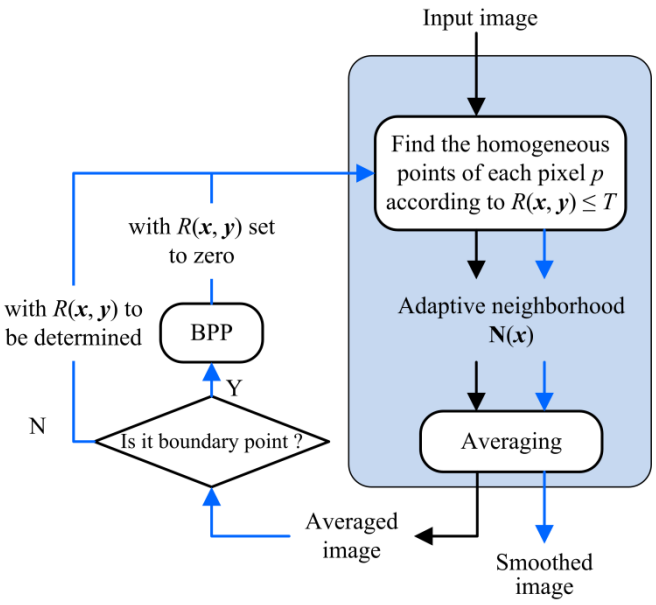

Fig. 6.1 Block diagram of the nonstationarity adaptive filtering (NAF) method.

For better understanding the proposed method, the block diagram of the nonstationarity adaptive filtering (NAF) is first given in Fig. 6.1. The block diagram consists of two parts. The blue rectangular block on the right represents the main part of the method, in which is involved the use of the image's local nonstationarity measure in determining the adaptive

neighborhood. The left part of the diagram mainly represents the boundary points processing (BPP). The flow of black arrows represents the first smoothing and that of blue arrows the refinement of the smoothing.

6.2.1 Adaptive neighborhood constrains

To obtain adaptive homogeneous neighborhood, we impose the following five constraints:

1) *Geometrical nearness:* the intensity of an image typically varies slowly over space (except highly textured images or regions), so near points are more likely to have similar nature than points far away, and they therefore lend themselves to be included in the neighborhood.
2) *Topological connectivity:* there should always be a path between $\boldsymbol{x}$ and $\boldsymbol{y}$ in the usual Euclidean topology, and any point in the path belongs to the neighborhood.
3) *Intensity similarity:* for scalar-valued images, homogeneous points usually have quasi-identical intensities. But image intensity is susceptible to noise. In the presence of heavy noise, originally homogenous points may have rather different intensities. Likewise, originally heterogeneous points may have similar intensities.
4) *Noise immunity:* factors immune to noise should be taken into account in the design of $R(\boldsymbol{x},\boldsymbol{y})$ in order to decrease the influence of noise on the computation of intensity similarity.
5) *Robustness design:* the design of $R(\boldsymbol{x},\boldsymbol{y})$ should be robust so that the adaptive neighborhood of the filter can exclude spurious points.

6.2.2 Homogeneous membership rule

Following the five constraints described above, we define the membership rule $R(\boldsymbol{x},\boldsymbol{y})$ as

$$R(\boldsymbol{x},\boldsymbol{y}) = L_\rho(\boldsymbol{x},\boldsymbol{y}) + D_\rho(nsm,\boldsymbol{x},\boldsymbol{y}), \tag{6.3}$$

where $\rho = (\boldsymbol{x}=\boldsymbol{y}_0,\boldsymbol{y}_1,\cdots,\boldsymbol{y}_{n-1},\boldsymbol{y}_n=\boldsymbol{y})$ is a path from the current pixel $\boldsymbol{x}$ (starting point) to its neighborhood member $\boldsymbol{y}$ (ending point) which has the smallest R value among all paths connecting the two points (topological connectivity), $L_\rho(\boldsymbol{x},\boldsymbol{y})$ is the geometric distance between $\boldsymbol{x}$ to $\boldsymbol{y}$ defined by

$$L_\rho(\boldsymbol{x},\boldsymbol{y}) = \sum_{i=1}^{n} l_{\boldsymbol{y}_{i-1},\boldsymbol{y}_i} = \sum_{i=1}^{n} \left\|\boldsymbol{y}_{i-1},\boldsymbol{y}_i\right\|_2, \tag{6.4}$$

which consists of n ordered segments $l_{\boldsymbol{y}_{i-1},\boldsymbol{y}_i}$ along the path ρ (geometrical nearness) calculated as the 2-norm distance between two contiguous points $\boldsymbol{y}_{i-1}$ and $\boldsymbol{y}_i$, and $D_\rho(nsm,\boldsymbol{x},\boldsymbol{y})$ is the intensity dissimilarity between the intensities of $\boldsymbol{x}$ and $\boldsymbol{y}$ defined by

$$D_\rho(nsm,\boldsymbol{x},\boldsymbol{y}) = \sum_{i=1}^{n} nsm(\boldsymbol{y}_i)\cdot\left|f(\boldsymbol{y}_{i-1}) - f(\boldsymbol{y}_i)\right|, \tag{6.5}$$

which consists of n weighted intensity differences $nsm(\boldsymbol{y}_i)\cdot\left|f(\boldsymbol{y}_{i-1})-f(\boldsymbol{y}_i)\right|$ (intensity similarity). The weighting coefficient $nsm(\boldsymbol{y})$ is a spatiodirectional NSM map explained in subsection 6.2.4. Simply speaking, when a point $\boldsymbol{y}$ is inside a region, $nsm(\boldsymbol{y})$ tends to have a small value near zero. On the contrary, $nsm(\boldsymbol{y})$ has a larger value when $\boldsymbol{y}$ locates near the boundary. Thus, within the region, if noise is present, $\left|f(\boldsymbol{y}_{i-1})-f(\boldsymbol{y}_i)\right|$ might be great, but $nsm(\boldsymbol{y}_i)$ is small. As a result, their product is much smaller than $\left|f(\boldsymbol{y}_{i-1})-f(\boldsymbol{y}_i)\right|$, which allows decreasing the dissimilarities $D_\rho(nsm,\boldsymbol{x},\boldsymbol{y})$ between $\boldsymbol{x}$ and $\boldsymbol{y}$ falsely caused by the noise and enables more homogeneous points $\boldsymbol{y}$ to be included in the adaptive neighborhood $\mathbf{N}(\boldsymbol{x})$ (noise immunity). The summation operation Σ in (6.5) is introduced for robustness since, if a boundary exists on the path ρ, the sum of the difference $nsm(\boldsymbol{y}_i)\cdot\left|f(\boldsymbol{y}_{i-1})-f(\boldsymbol{y}_i)\right|$ will remain great and consequently R is great and exceeds the threshold Th, which stops the neighborhood spreading beyond the boundary and avoids including, in the neighborhood, the pixels beyond the boundary (robustness design).

The adaptive homogeneous neighborhood $\mathbf{N}(\boldsymbol{x})$ corresponding to the rule thus defined has the following two properties:

Property 1 *Non-empty*

For each point $\boldsymbol{x}$, its neighborhood $\mathbf{N}(\boldsymbol{x})$ has at least one member $\boldsymbol{x}$. That is, $\mathbf{N}(\boldsymbol{x})\neq\varnothing$ and the size of the neighborhood $M\geq 1$.

Property 2 *Non-negative*

a. $L_\rho(\boldsymbol{x},\boldsymbol{y})\geq 0$

b. $nsm(\boldsymbol{y})\geq 0$

c. $D_\rho(nsm,\boldsymbol{x},\boldsymbol{y})\geq 0$

d. $R(\boldsymbol{x},\boldsymbol{y})>0,\boldsymbol{x}\neq\boldsymbol{y};\ R(\boldsymbol{x},\boldsymbol{y})=0,\boldsymbol{x}=\boldsymbol{y}.$

To sum up, the homogeneous membership rule (6.3) can be further expressed as

$$R(\boldsymbol{x},\boldsymbol{y})=\sum_{i=1}^{n}\left[\left\|\boldsymbol{y}_{i-1}-\boldsymbol{y}_i\right\|_2+nsm(\boldsymbol{y}_i)\cdot\left|f(\boldsymbol{y}_{i-1})-f(\boldsymbol{y}_i)\right|\right]. \tag{6.6}$$

Of course, this rule is also suitable for 3-D volumes if the point $\boldsymbol{x}$ or $\boldsymbol{y}$ represents the voxels of the 3-D volume.

6.2.3 Boundary points processing

After the first smoothing of the input image following the black arrows flow in Fig. 6.1, the noisy image is generally well smoothed inside regions except points on the boundary, whose intensities were not well smoothed, exhibiting mosaic effect on the boundary. These boundary points usually have neighborhoods of small sizes, which sometimes consist of themselves. The existence of such rough boundary points is mainly due to the fact that its 8-neighbors cannot become the members of its adaptive neighborhood since either the NSMs or the

intensity difference between the boundary point and its 8-neighbors or still both of them are so big that R exceeds the threshold Th [see (6.6)]. As a result, the pixels other than the 8-neighbors cannot be further handled due to the "topological connectivity" constraint. To cope with this problem, we set $R(\boldsymbol{x},\boldsymbol{y})=0$ for the homogeneous points in the 8 neighbors of the boundary point, which allows continuing the process of searching other possible members of the neighborhood (Fig. 6.1).

Our experiments showed that the homogeneous 8-neighhors whose $R(\boldsymbol{x},\boldsymbol{y})$ is set to zero usually have two characteristics in the gradient field of the boundary image: 1) they are located in the side opposite to the gradient direction of the boundary point; 2) they have the same gradient direction as the boundary point. For example, in Fig. 6.2, point no. 4 and no.5 circled by red dashed rectangles are homogeneous 8-neighbors of the point $\boldsymbol{p}$. Note the gradient is calculated according to

$$\begin{cases} G_{x_1} = f(x_1+1,x_2) - f(x_1-1,x_2) \\ G_{x_2} = f(x_1,x_2+1) - f(x_1,x_2-1) \end{cases}, \tag{6.7}$$

where x_1 and x_2 represent the coordinates of image points.

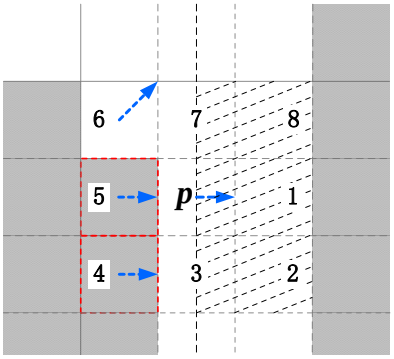

Fig. 6.2 Determination of homogeneous 8-neighbors of the boundary point.

According to the above two characteristics, the homogeneous 8-neighhors of a boundary point can be determined following the procedure below.

1) Obtain the binary boundary image by thresholding the spatiodirectional NSM map of the averaged image.
2) Calculate the gradient field of the binary boundary image, and find out the homogeneous 8-neighbors of each boundary point according to the two characteristics mentioned above, and set their $R(\boldsymbol{x},\boldsymbol{y})$ to zero.

Once the above BBP is achieved, based on the homogeneous 8-neighbors determined, we continue to find other homogeneous members according to (6.6) and (6.2) to finally determine the adaptive neighborhood of the boundary points.

6.2.4 Spatiodirectional NSM map

Compared to conventional imaging data, DTI data is a set of 3-D volumes, each of which corresponds to a diffusion gradient direction. Add to all that a b0 volume corresponding to the case the diffusion gradient is zero. To exploit both spatial and (diffusion gradient) directional information encoded in the DTI data, we construct a so-called spatiodirectional NSM map for each of the 3-D slices. The spatiodirectional NSM map for each 2-D slice is obtained following the steps: 1) calculate the NSM map of the DW image in each diffusion gradient direction, and then compute the average of the NSM maps in different directions; 2) calculate the NSM map of b0 image; 3) take the larger value between the two NSM maps obtained in the first two steps.

By doing so, the change information weakened in one image can be captured from others.

6.2.5 Selection of parameters

In the implementation of the NAF, three parameters need to be set: the weighting function g, the parameter estimation function h, and the threshold Th. Usually, rectangular windows of the same size are an effective and simple choice for g and h. The size $(2W+1)\times(2W+1)$ of the window depends on noise and to some extent image resolution. The selection of window width W can refer to Section 2.3.4. In smoothing DTI data, due to the poor resolution of the latter, we have chosen W as 1, which corresponds to a window size of 3×3. Concerning the choice of the threshold Th, it depends on the geometric distance and intensity dissimilarity in (6.6) and ranges from 5 to 9 for the cardiac DTI data in the present study. In principle, various window functions can be used for g and h.

6.3 Smoothing of synthetic DTI data

6.3.1 Production of synthetic data

A set of synthetic cardiac DW images of size 128×128 corresponding to six diffusion gradient directions were generated in order to both qualitatively and quantitatively evaluate the performance of the NAF. The synthetic images were designed such that they are similar to a slice of real human heart DTI volumes. Visually, each image mainly consists of three regions (Fig. 6.3): the cardiac region of interest, the perfluoropolyether fomblin (PF) and the air. In the air region, no diffusion tensor exists; in the PF region, isotropic diffusion tensors were designed with three equal eigenvalues 0.75; in the myocardium region, the three eigenvalues of anisotropic diffusion tensors were 1.5, 0.75, and 0.75, respectively. The principal eigenvectors of these anisotropic tensors make a fixed angle (45°) with the slice plane, and their projections on the plane take the direction of the tangents of the concentric circles centered on the center of the left ventricle (LV). In order to thoroughly analyze the smoothing performance of the NAF in Rician noisy cases, different level noises $\sigma_n = \{5,10,15,20,25\}$ were added to the ideal DW images.

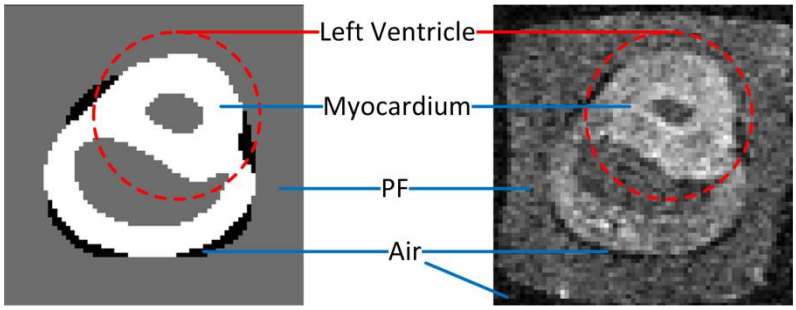

(a) (b)

Fig. 6.3 Generation of a synthetic DW image similar to a slice of a human cardiac DTI volume. (a) Synthetic DW image. (b) Human cardiac DW image. Image is courtesy of Pierre Croisille.

6.3.2 Experiments and results

For all the experiments, *g* and *h* were set as 2-D rectangular functions with size 3×3. Different *Th* values were chosen following different noise levels, as denoted by (σ_r, Th), to get better smoothing performance: (5, 5), (10, 5), (15, 6), (20, 6) and (25, 6.25). The proposed NAF is compared with an anisotropic diffusion filtering (ADF) recently used in DTI for the DW image smoothing [Xu *et al.*, 2010].

To illustrate the performance of the NAF in highly noisy cases, the result of smoothing synthetic data corrupted with Rician noise σ_r=25 is shown in Fig. 6.4. The images in the first column to the fourth column respectively correspond to the case of noise-free, noisy, smoothed by the ADF and smoothed by the NAF. To better observe the results of the two methods, the images in the first diffusion gradient direction are zoomed and shown in Fig. 6.5. Smoothed by the ADF [Fig. 6.5(c)], the DW image gains good visual appearances since the grainy aspect caused by the Rician noise is smoothed to a large degree. However, the smoothed areas show a little "wavy" and the sharp edges are blurred. In contrast, with the proposed NAF [Fig. 6.5(d)], the noise in flat regions is reduced to a larger degree, while the features such as edges are preserved very well. This can be more clearly seen in the profiles shown in Fig. 6.5(e)-(h).

Fig. 6.6 shows the tensor fields computed from the noise-free, noisy and smoothed DW images. Tensors are displayed as ellipsoids and colored according to the direction of their principal eigenvectors. The red color indicates a left-right direction, the green color the anterior-posterior direction, and the blue the inferior-superior direction. Note that the ellipsoids outside the myocardium region were masked since they are not of interest. The uniform tensor field computed from the noise-free data [Fig. 6.6(a), (e)] becomes disordered because of the heavy Rician noise in the noisy data [Fig. 6.6(b), (f)]. With the ADF, both the shapes and the colors of the ellipsoids become coherent [Fig. 6.6(c), (g)], but rather different from the original ones. In particular, the ellipsoids in the boundary areas between the myocardium and the PF become isotropic and smaller compared to the ellipsoids inside the myocardium, which reflects the presence of edge blurring effect. With the NAF, the shapes and the colors of the ellipsoids are close to those in the noise-free case, which indicates that the NAF preserve the characteristics of tensors while smoothing. It is worth mentioning that

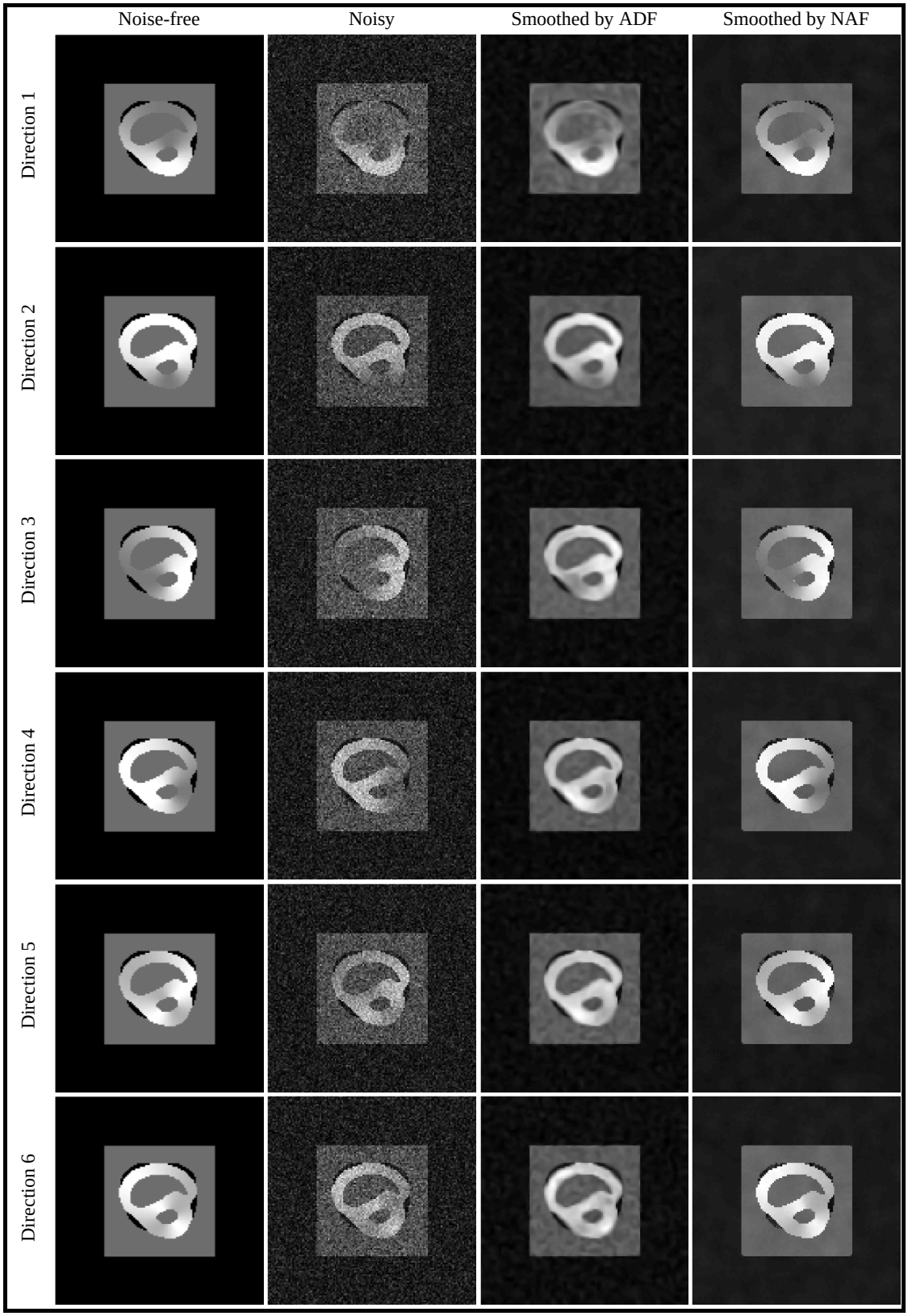

Fig. 6.4 Smoothing of synthetic human cardiac DW images in 6 diffusion gradient directions.

the ellipsoids in the boundary areas almost keep the same appearance as those inside the myocardium, which reflects that the edges in DW images are hardly blurred.

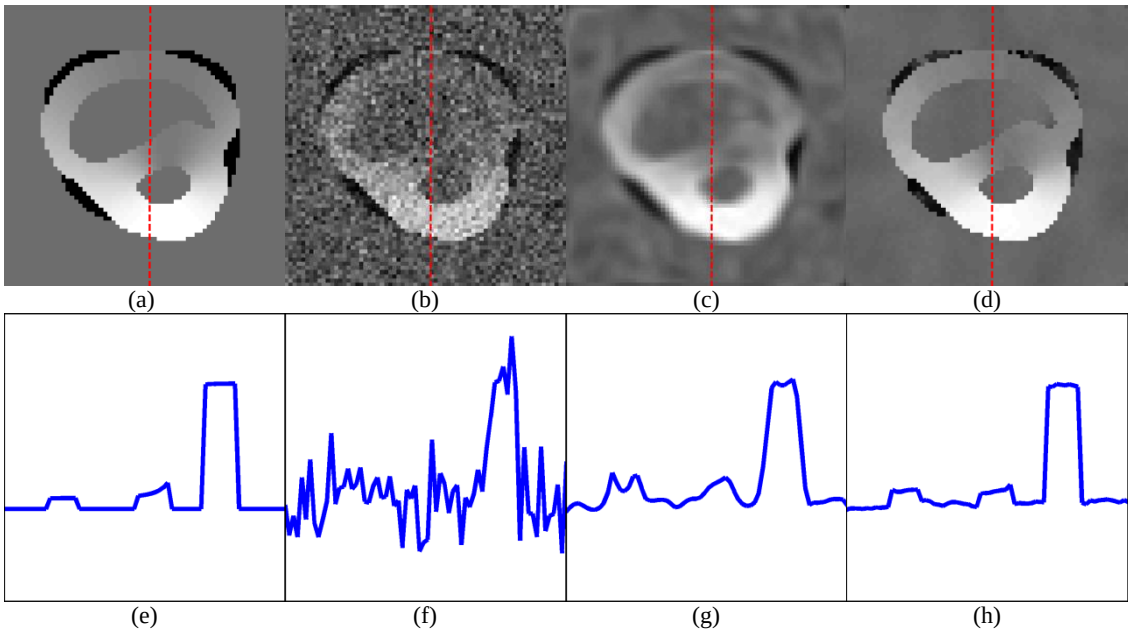

Fig. 6.5 Smoothing of synthetic cardiac DW images. (a) Noise-free DW image. (b) Noisy DW image. (c) Smoothed by the ADF. (d) Smoothed by the NAF. (e)-(h) Profiles marked by the red dashed lines in (a)-(d).

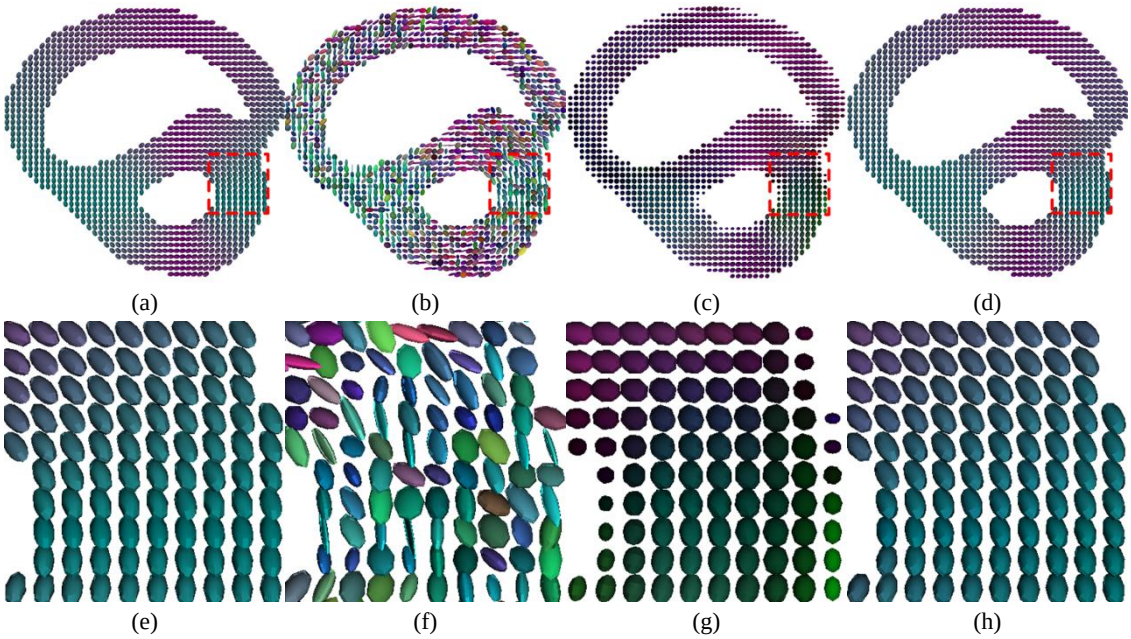

Fig. 6.6 Tensor fields in the Myocardium area before and after smoothing. (a)-(d) Tensor fields corresponding respectively to noise-free data, noisy, ADF smoothed and NAF smoothed cases. (e)-(h) Tensor fields in the red rectangles in (a)-(d).

6.3.3 Evaluation of smoothing results

Mean structural SIMilarity

Mean Structural SIMilarity (MSSIM) is an objective and effective measure to quantify the structural similarity between two images [Wang *et al.*, 2004a]. The MSSIM depends on the similarity of luminance, contrast and structure, and is defined as a mean structural similarity (SSIM) index to evaluate the overall image quality

$$\mathrm{MSSIM}(\mathbf{U},\mathbf{V})=\frac{1}{M}\sum_{j=1}^{M}\mathrm{SSIM}(\mathbf{u}_j,\mathbf{v}_j) \tag{6.8}$$

where **U** and **V** are the reference and smoothed or noisy images, respectively; SSIM the structural similarity of the image contents $\mathbf{u}_j$ and $\mathbf{v}_j$ at the j^{th} local window, and M the number of local windows of the image.

The MSSIM values calculated for the smoothing results are given in Table 6.1. With the two smoothing methods, the MSSIM values of the six DW images all increased significantly. By the ADF smoothing, the MSSIMs increased from 65.0% (for the DW image in the 6th direction) to 110.3% (for the DW image in the 1st direction). In contrast, using the NAF, the MSSIMs increased from 103.0% (for the same 6th direction image) to 164.9% (for the same 1st direction image). The average MSSIM of the DW images smoothed by the NAF are 22.6% up on that of the images smoothed by the ADF.

Table 6.1 MSSIMs of DW Images Smoothed by NAF and ADF ($\sigma_r = 25$)

Evaluation → Direction ↓	Noisy	Smoothed by the ADF	Smoothed by the NAF
1	0.350	0.736	0.927
2	0.466	0.786	0.952
3	0.384	0.752	0.934
4	0.452	0.769	0.946
5	0.449	0.796	0.947
6	0.468	0.772	0.950
Mean	0.428	0.769	0.943

When increasing noise levels, the MSSIMs of the resultant smoothed images are plotted in Fig. 6.7. It is observed that the NAF always outperforms the ADF and produces results with higher MSSIMs.

Diffusion anisotropy index

Fractional anisotropy (FA) and mean diffusivity (MD) are the two parametric indices commonly used in DTI study.

FA describes the spatial heterogeneity of the water molecules displacements that is related to the presence of orientated structures [Kingsley, 2006], it is defined as

$$\mathrm{FA}=\frac{\sqrt{3\left[(\lambda_1-\bar{\lambda})^2+(\lambda_2-\bar{\lambda})^2+(\lambda_3-\bar{\lambda})^2\right]}}{\sqrt{2(\lambda_1^{\,2}+\lambda_2^{\,2}+\lambda_3^{\,2})}}, \tag{6.9}$$

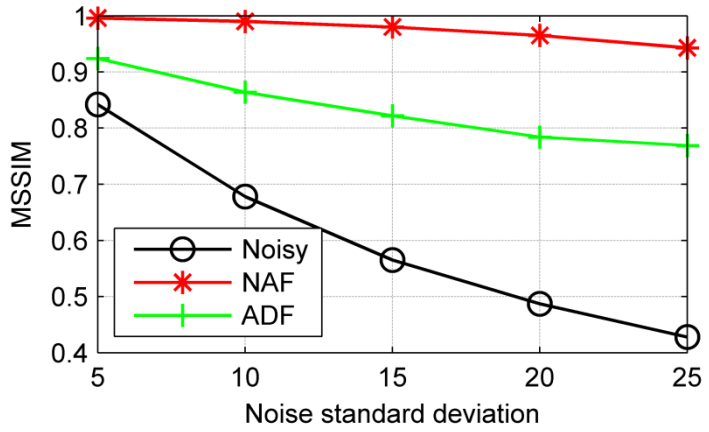

Fig. 6.7 Comparison of smoothing results obtained by the NAF and the ADF in terms of the MSSIM with different noise levels ranging from 5 to 25.

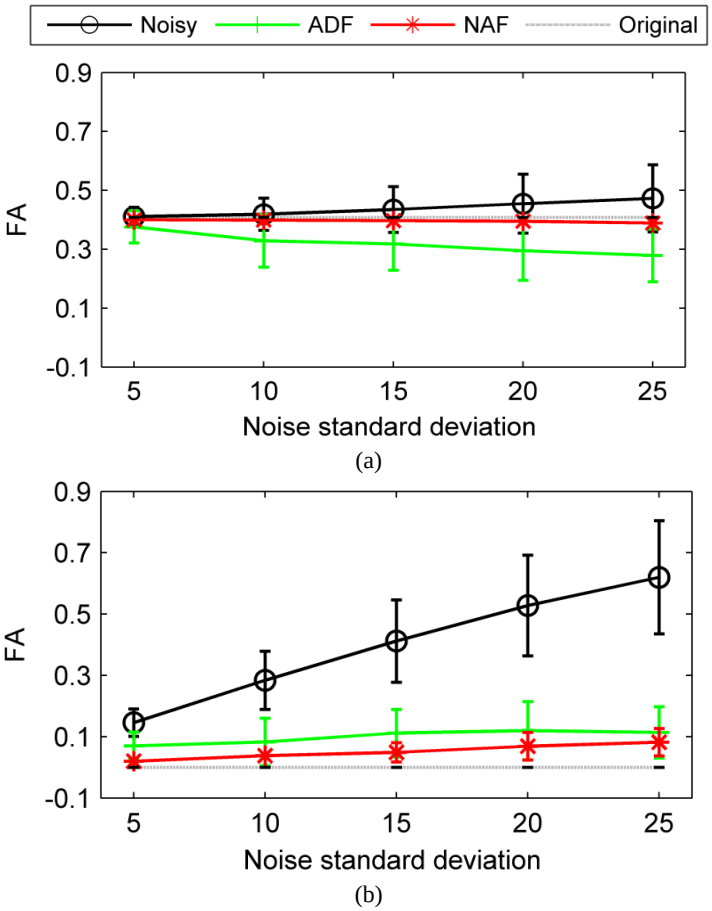

Fig. 6.8 Comparison of FA values of synthetic diffusion tensor data with different noise levels ranging from 5 to 25. (a) FA in the myocardium. (b) FA in the PF.

where $\bar{\lambda}$ represents MD which describes the overall mean-squared displacement of the water molecules [Bronshtein *et al.*, 2007]. It is defined by the average of the three apparent diffusion coefficients (ADC) respectively measured along the three axes of the tensor

$$\bar{\lambda} = \frac{\lambda_1 + \lambda_2 + \lambda_3}{3}. \tag{6.10}$$

The FAs in the myocardium and the PF region are plotted respectively in Fig. 6.8(a) and (b). The results show that: 1) both mean and variance of FA values increase with the increase of noise levels, and such increasing is much significant in the region where the diffusion is isotropic than in the region where the diffusion is anisotropic; 2) while smoothing reduces noise level, it induces the decreasing of FA values and generates FA values smaller than the true FA value in anisotropic regions; 3) for the same smoothing, the induced FA decrease is much significant in isotropic diffusion region (in the PF region) than in anisotropic region (in the myocardium region), but with the NAF, the mean FA is much closer to the true value with very small variance in comparison with the ADF smoothing that presents big variance; 4) for the image presenting both isotropic and anisotropic diffusion regions in Fig. 6.5, the ADF tends to over-smooth the anisotropic region and at the same time under-smooth the isotropic region, in which, after the ADF smoothing, the mean FA and variance remain big (while the FA in isotropic diffusion regions should be equal to zero). All these results demonstrate that the NAF can better preserve the anisotropy of original DTI data than the ADF.

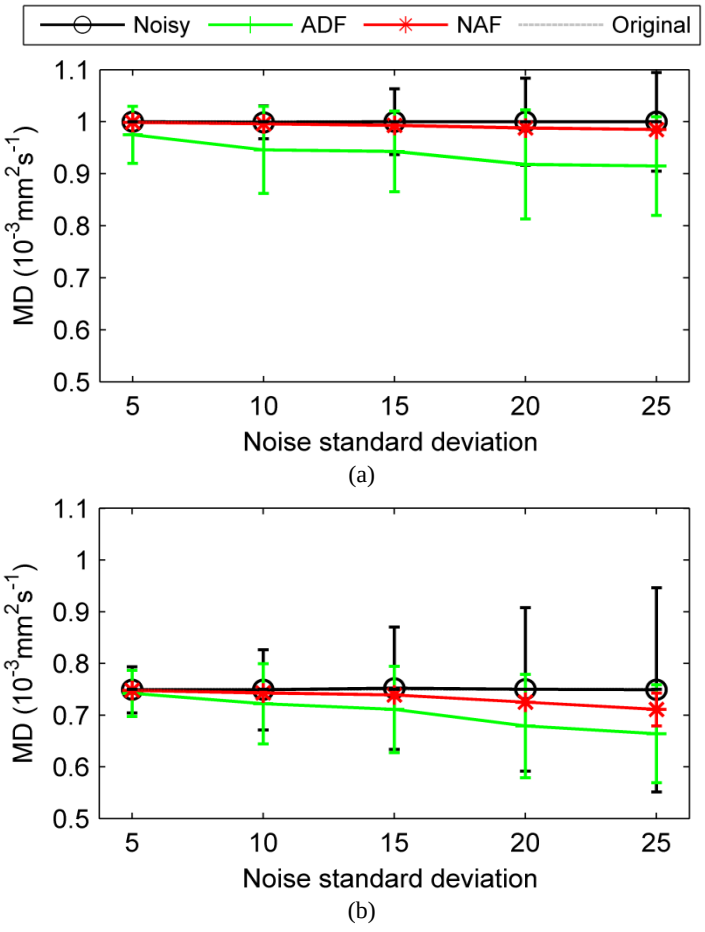

Fig. 6.9 Comparison of MD values of synthetic diffusion tensor data with different noise levels ranging from 5 to 25. (a) MD in the myocardium. (b) MD in the PF.

Regarding the smoothing effect on MD, the results are plotted in Fig. 6.9. It is seen that: 1) The mean of MD values varies little when the noise level increases, but the variance increases proportionally; 2) after both the ADF and the NAF smoothing, the mean of MD values decreases more or less, but the NAF has much less effect on MD values than the ADF while substantially reducing the variance; 3) in contrast to the FA case, the smoothing (with the ADF or NAF) has rather homogeneous effect on isotropic and anisotropic regions, but the NAF yields MD values much closer to the true MD value than the ADF that also exhibits big variance.

6.4 Smoothing of human cardiac DTI data

6.4.1 Acquisition of cardiac DTI data

Our real data come from a set of 38 acquisitions performed on eight *ex vivo* human hearts. These hearts were processed a few hours after death and not perfused with any fixing agent in order not to change their diffusion properties. Each heart was placed in a plastic container filled with the PF which help the heart maintain a diastolic shape.

The data were acquired with a Siemens Avanto 1.5T MR Scanner using echo planar acquisitions with the following parameters: 52 contiguous axial slices of 128×128/160×160 size, 2×2 mm^2 spatial resolution, 2 mm thickness, and 12/6 diffusion sensitizing directions.

6.4.2 Experiments and results

Three neighboring slices of 3-D real cardiac DTI datasets were processed in 3-D by the two methods. For the NAF, as in the case of synthetic data, spatiodirectional NSM maps were constructed and the averaged intensity of the 3-D homogeneous neighborhood of a voxel was calculated to substitute for its original intensity for the smoothing of DW images. The function g and h were set as 3×3 rectangular functions, and T took 9 in the black arrows flow and 6 in the blue arrows flow. The ADF was also applied to the same dataset for comparison.

In Fig. 6.10(a)-(c), we chose to show the noisy and smoothed LVs on a middle slice. As in the simulation case, the proposed NAF achieves a better compromise between the reduction of noise and the preservation of discontinuities at the boundaries or other desirable features than the ADF. Fig. 6.10(d)-(f) shows a zoomed version of the boxed region of the LV myocardium in Fig. 6.10(a)-(c). It is clearly seen that the red-dashed line corresponding to the NAF gives, compared to original noisy or ADF smoothed images, substantially more flat segments for homogeneous regions (within the myocardium and PF) in the image, and at the same time much sharper edges (at the endocardium and the epicardium).

The diffusion tensors corresponding to the zoomed parts of the myocardium in Fig. 6.10 (d)-(f) are shown in Fig. 6.11(a)-(c). A mask was used to show ellipsoids only in the myocardium. After smoothing with the two methods, the chaotic diffusion tensor field becomes orderly. With the ADF, the ellipsoids in the boundary areas between the myocardium and the PF become isotropic and larger compared to the ellipsoids inside the myocardium, which reflects the presence of edge blurring effect. In contrast, The NAF ensures a more consistent diffusion tensor field in the homogeneous region. All that implies that, compared to the ADF, the NAF can better reduce errors in the estimation of tensor

characteristics, such as the magnitude and the direction of principal eigenvectors. These errors present in the results smoothed by the ADF due to blurring lead to the spreading of fiber pathways into neighboring fiber bundles, as shown in Fig. 6.12(b).

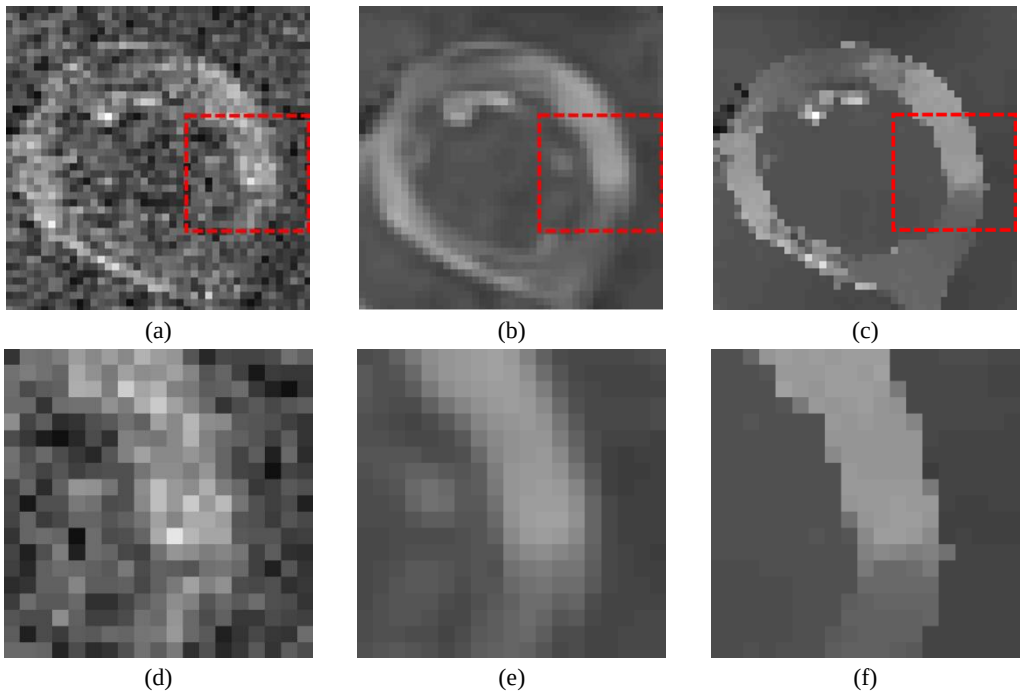

(a) (b) (c)

(d) (e) (f)

Fig. 6.10 Smoothing results of a real cardiac DW image. (a) Noisy DW image from an *ex vivo* human cardiac DTI datasets with 12 gradient directions. (b) Smoothed by the ADF. (c) Smoothed by the NAF. (d)-(f) Region circled by the red rectangles in (a)-(c). Images are courtesy of Pierre Croisille.

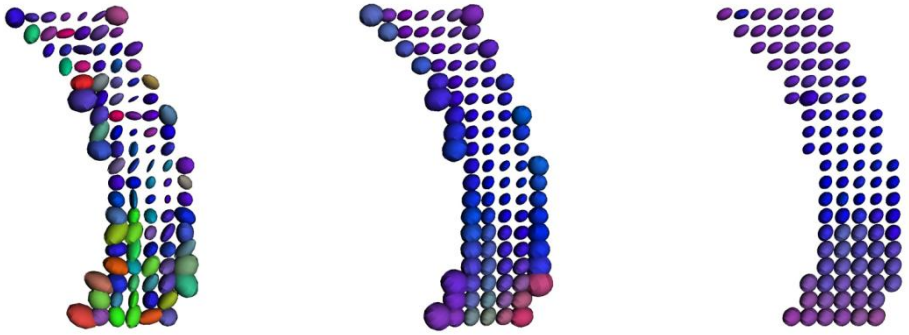

(a) (b) (c)

Fig. 6.11 Diffusion tensor fields corresponding to the region marked by the red rectangles in Fig. 6.10(a)-(c). (a) Noisy. (b) Smoothed by the ADF. (c) Smoothed by the NAF.

6.4.3 Evaluation of smoothing results

For the real data, the smoothing results are quantitatively evaluated using the coherent index (CI) [Basser *et al.*, 1996] as well as FA and MD. CI estimates the orientation coherence

of fibers and is defined as the mean dot product of the eigenvectors v and its 26 neighboring voxels v_{ij}

$$\mathrm{CI} = \frac{1}{26}\sum_{ij} v \cdot v_{ij} \ . \tag{6.11}$$

A high CI value reflects directional coherence of fibers in neighboring voxels.

Table 6.2 summarizes the values of FA, MD and CI. These quantitative results confirm the above qualitative analyses. It is seen that, in comparison with the FA values of the original noisy diffusion tensors, the FA values decrease after smoothing using both methods. Nevertheless, compared to the ADF, the NAF generates moderate decrease in FA while presenting a smaller variance of FA, which indicates that the NAF maintains the anisotropy of diffusion tensors while regularizing them effectively. In addition, the greater mean and much lower variance of CI also imply that, after smoothing by the NAF, the diffusion tensors of neighboring voxels have more consistency with respect to the orientation of their principal eigenvectors. Such directional coherence would advantage the subsequent fiber tracking.

Table 6.2 FA, MD and CI of the Diffusion Tensors in Fig. 6.11

Mean	FA		MD		CI	
	Mean	Var	Mean (10^{-3} mm^2s^{-1})	Var (10^{-6})	Mean	Var
Noisy	0.311	0.012	1.033	0.073	0.643	0.083
ADF	0.208	0.006	1.051	0.068	0.960	0.013
NAF	0.236	0.004	0.919	0.023	0.990	0.000

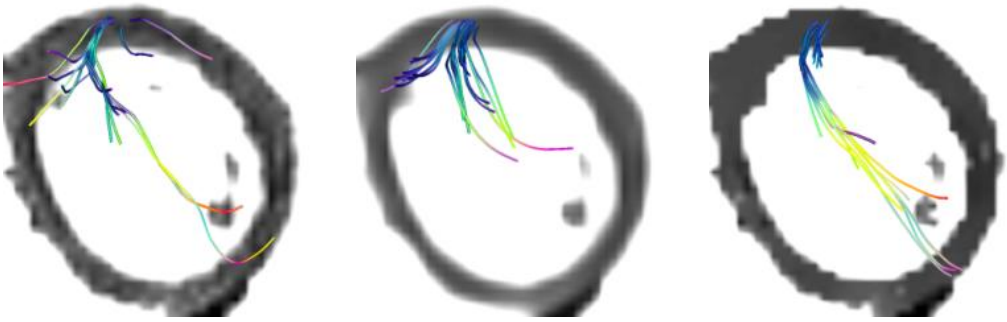

(a) (b) (c)

Fig. 6.12 Bundle of cardiac fibers lunching from a small patch of myocardium in the LV tracked from (a) the noisy data, (b) the smoothed data by the ADF, and (c) the smoothed data by the NAF. To indicate the locations of the fibers, they are overlapped with the original and the smoothed DW images, which are adjusted in color balance to highlight the fibers.

Fig. 6.12 shows fiber launching from the same petit patch of interest inside the LV. These fibers are colored according to their local orientation in the same manner as that used in Fig. 6.6. It is seen that the noisy raw data presents tousy fibers with diverse directions and lengths due to the presence of high-level noise. After smoothing by the ADF, the fibers become more

regular, but fiber spreading as a result of smoothing without adequate boundary preservation is visible in the sense that the fiber pathways spread into neighboring structures. The fiber bundles obtained after the NAF resemble the original ones but with more coherent and longer fibers, which is consistent with the fact that contiguous fibers would present similar features. Furthermore, the longer fibers in Fig. 6.12(c) imply the well preserved anisotropy of diffusion tensors by the NAF since the fiber tracking was stopped using the same FA value.

Finally, Table 6.3 reports the statistical results of FA, MD, and CI in the whole LV myocardium region of other seven DTI datasets with very high noises, before and after smoothing by the proposed NAF method. On average, FA means and variances decreased by 42.9% and 67.7%, and MD means and variances by 5.3% and 68.7%, while CI means increased by 92.1% and CI variances decreased by 35.7% after smoothing. After smoothing, the variances of the three indices for each heart decreased substantially, which implies that FA, MD and CI converge towards more consistent results.

Table 6.3 FA, MD and CI of Diffusion Tensors Calculated from Real Cardiac DTI Data in the LV Myocardium of Seven Human Hearts

Heart	FA		MD		CI	
	Mean	Var	Mean (10^{-3} mm^2s^{-1})	Var (10^{-6})	Mean	Var
1	0.327	0.014	0.707	0.038	0.589	0.148
	0.233	0.005	0.676	0.018	0.854	0.087
	-28.7%	-64.3%	-4.4%	-52.6%	+45.0%	-41.2%
2	0.356	0.018	0.738	0.072	0.506	0.178
	0.219	0.005	0.701	0.030	0.851	0.073
	-38.5%	-72.2%	-5.0%	-58.3%	+68.2%	-59.0%
3	0.369	0.021	0.994	0.070	0.401	0.142
	0.175	0.004	0.957	0.029	0.830	0.098
	-52.6%	-81.0%	-3.7%	-58.6%	+107.0%	-31.0%
4	0.266	0.022	1.450	0.128	0.403	0.156
	0.112	0.003	1.390	0.032	0.821	0.111
	-57.9%	-86.4%	-4.1%	-75.0%	+103.7%	-28.8%
5	0.219	0.008	1.537	0.071	0.339	0.135
	0.093	0.003	1.455	0.013	0.838	0.109
	-57.5%	-62.5%	-5.3%	-81.7%	+147.2%	-19.3%
6	0.267	0.016	0.666	0.066	0.447	0.119
	0.175	0.003	0.591	0.003	0.888	0.073
	-34.5%	-81.3%	-11.3%	-95.5%	+98.7%	-38.7%
7	0.668	0.049	0.908	0.118	0.474	0.143
	0.463	0.036	0.878	0.048	0.828	0.097
	-30.7%	-26.5%	-3.3%	-59.3%	+74.7%	-32.2%

For each heart, the first line corresponds to the DT-MRI data before smoothing, the second line to the data after smoothing using NAF, and the third line to the rate of change.

6.5 Conclusion

Nous avons proposé une nouvelle méthode de lissage, appelée filtrage adaptatif par non-stationnarité (nonstationarity adaptive filtering-NAF en anglais), en nous appuyant sur un meilleur compromis entre la réduction du bruit et la préservation des caractéristiques dans l'image. La méthode proposée consiste à estimer l'intensité d'un pixel en calculant la moyenne des intensités de ses voisins dans un voisinage homogène. Comme les points dans un voisinage homogène partagent la même caractéristique, le moyennage permet alors de réduire le bruit sans introduire des distorsions causées par les points hétérogènes.

Pour des images à faible RSB, il est particulièrement difficile de déterminer convenablement le voisinage homogène pour chaque pixel. Selon les cinq contraintes sur l'appartenance homogène, nous avons pu définir la règle d'appartenance basée sur NSM pour obtenir le voisinage homogène. Comme le NSM est insensible au bruit, il a été utilisé comme un facteur de pondération pour diminuer l'impact du bruit sur les différences d'intensité et pour ainsi améliorer la robustesse de la règle d'appartenance. Pour le traitement de points frontières, la cartographie de NSM a été utilisée afin d'obtenir l'image binaire de la frontière pour déterminer les huit voisins homogènes d'un point frontière, ainsi que son voisinage homogène. La NAF proposée réalise le moyennage dans les voisinages homogènes, et permet de ce fait un meilleur compromis entre la réduction du bruit et la préservation des caractéristiques désirable pour les images à faible RSB.

La NAF a été appliquée pour lisser des images DW cardiaques. Les résultats sur des images cardiaques synthétiques montrent que la moyenne de MSSIM des images DW lissées par la NAF est 120,3% plus élevée que celle des images bruitées, et est 22,6% plus élevée que celle des images lissées par le FAD. Les résultats sur des images cardiaques réelles montrent que la NAF proposée permet d'avoir un meilleure aspect visuel pour les images DW, de régulariser efficacement le champs de tenseurs de diffusion tout en restaurant l'anisotropie des tenseurs, et d'assurer une reconstruction plus fiable des fibres.

Chapter 7

7 Conclusions and perspectives

7.1 Conclusions

Cette thèse portrait sur l'étude de la mesure de la non-stationnarité des signaux et des images. Dans ce cadre, nous avons généralisé la définition de la non-stationnarité pour des signaux et des images, et développé une méthode générique pour mesurer le changement des caractéristiques d'un signal multidimensionnel quelconque.

En nous appuyant sur la nouvelle mesure de nonstationnarité, nous avons développé quatre méthodes de traitement de signaux et d'images: détection de changements dans un signal, détection de contours dans une image, segmentation d'images, et lissage adaptatif. Toutes ces méthodes ont pour mécanisme commun de se baser sur la mesure de changements des caractéristiques du signal ou de l'image.

Ces méthodes ont été appliquées à des signaux aléatoires de type ECG (électrocardiogramme) et EEG (électroencéphalogramme), à des images IRM pondérées en diffusion qui sont très bruitées et possèdent un faible contraste, et à des images ultrasonores de la carotide. Les résultats obtenus sur des images aussi bien synthétiques que réelles ont montré que ces méthodes sont particulièrement robustes au bruit, et que la mesure robuste du changement ainsi que les méthodes résultantes de traitement du signal et de l'image sont particulièrement intéressantes pour les signaux et les images biomédicaux.

Les contributions principales de ce travail de thèse sont résumées ci-dessous:

- Amélioration et généralisation de la mesure de non-stationnarité

  Nous avons d'abord proposé la notion de stationnarité d'un paramètre en général. Par rapport à la notion de stationnarité classique, cette nouvelle notion définit la stationnarité par rapport à un paramètre (caractéristique) statistique du signal, et n'impose pas de forme concrète pour le paramètre et pour le signal, ce qui rend cette nouvelle notion de stationnarité plus générale, adaptative et évolutive. A partir de la notion de stationnarité d'un paramètre en général, nous avons calculé des paramètres statistiques glissants à l'aide d'une fenêtre et construit ainsi un espace de paramètres statistiques glissant, ce qui nous a permis d'en déduire la mesure de non-stationnarité locale. Ensuite, le processus de construction de l'opérateur de mesure de la non-stationnarité a été formulé, et la réponse de l'opérateur à des signaux d'entrée typiques a été calculée analytiquement, ce qui nous a permis de démontrer de manière théorique la robustesse de l'opérateur d'ordre deux de mesure de la non-stationnarité. Enfin, le choix de la largeur de la fenêtre impliquée dans l'opérateur de mesure de non-stationnarité a été étudié en détail.

  L'extension à n-dimensions (n-D) de l'opérateur de mesure de non-stationnarité a également été effectuée. D'abord, nous avons défini la mesure de non-stationnarité pour des signaux n-D, et donné l'algorithme général de calcul de cette mesure. Ensuite, nous avons expliqué le principe de la mesure de non-stationnarité pour des données vectorielles et tensorielles, déduit les formules de calcul, et donné des illustrations à l'aide d'exemples. La méthode proposée permet ainsi de mesurer la non-stationnarité de signaux multidimensionnels quelconques (scalaires,

vectoriels, tensoriels) par rapport à un paramètre statistique, et en fait ainsi une mesure générique et robuste.

- Détection de changement dans un signal et de contours dans une image

  En vue d'adresser le problème des faux positifs et faux négatifs dans la détection de changement dans un signal ou une image, nous avons proposé des méthodes de détection du changement qui utilisent la mesure de non-stationnarité. Dans le cas des signaux 1D, la méthode de détection du changement consiste à générer une courbe de mesure de non-stationnarité, et à déterminer le changement à partir de cette courbe par rapport à un seuil. Quand la valeur de la mesure de non-stationnarité dépasse le seuil, un changement est alors considéré avoir lieu à l'instant correspondant. Par rapport à la méthode classique ΔBIC ou aux méthodes plus récentes telles que la Pearson divergence méthode et la DCPC méthode, la méthode proposée permet de détecter des instants de changements dans des signaux ECG et EEG de manière plus précise et avec un temps de traitement plus court, tout en réduisant les faux positifs et faux négatifs.

  Dans le cas des images, la méthode de détection de contours proposée utilise l'opérateur 2D de mesure de non-stationnarité pour mesurer l'amplitude du changement des contours, et détecter les contours par un seuillage des valeurs des mesures de non-stationnarité combinées avec la prise en charge du voisinage. Les résultats montrent que la méthode proposée est particulièrement efficace pour des images très bruitées telles que les images cardiaques pondérées en diffusion, en permettant d'obtenir des contours plus précis et de réduire le nombre de faux contours par rapport aux méthodes classiques ou récentes, telles que Canny, NLFS et FES.

- Segmentation d'images par mesure de non-stationnarité et contour actif géométrique

  Dans ce travail, nous nous sommes focalisés sur le problème des faux positifs et de la délocalisation des contours dans des images très bruitées. Nous avons proposé un model basé sur la mesure de la non-stationnarité locale et sur les contours actifs géométriques (NSM-GAC). Le mécanisme du modèle réside dans l'exploitation de la robustesse de l'opérateur 2D de mesure de non-stationnarité pour mesurer l'intensité du contour et guider le contour actif vers les contours cibles dans l'image. Les résultats sur des images de synthèses montrent que le modèle est particulièrement robuste au bruit gaussien et que le résultat de segmentation se dégrade peu avec l'augmentation du niveau de bruit. Sur des images ultrasonores de la carotide, la méthode proposée est plus performante que les méthodes DRLSE et C-V en termes de robustesse au bruit spatial de « speckle » propre aux images ultrasonores, de temps de calcul, et de précision de segmentation (moins de faux contours, moins de délocalisation de contours).

- Lissage adaptatif des images basé sur la mesure de non-stationnarité

  Pour aborder le difficile compromis entre lissage et préservation de caractéristiques de l'image ayant un faible rapport signal sur bruit (RSB), nous avons proposé une méthode de lissage basée sur la mesure de non-stationnarité, appelée NAF (nonstationarity adaptive filtering, en anglais). Utilisant l'hypothèse selon laquelle la meilleure estimation de l'intensité d'un pixel s'obtient par moyennage des intensités des pixels de son voisinage dit homogène, nous avons été conduits à formuler cinq contraintes qui nous ont permis de définir, à partir de la mesure de non-stationnarité, la règle d'appartenance d'un pixel au voisinage homogène. Selon cette règle d'appartenance, le voisinage homogène de chaque pixel est déterminé de manière adaptative. Ensuite, l'intensité du pixel courant est remplacée par la valeur moyenne du voisinage. Enfin, après un traitement spécifique pour les points frontières, on obtient le lissage final de l'image. Les résultats sur des images simulées de faible RSB montrent que la ressemblance selon le critère MSSIM entre l'image lissée par NAF et l'image originale sans bruit est de 0,943, ce qui correspond à une augmentation (amélioration) de 120,3% par rapport à la valeur de MSSIM de l'image bruitée. En comparaison avec la méthode de l'état de l'art ADF, la valeur de MISSIM a été augmentée de 22,6%. Sur des images réelles du cœur humain pondérées en diffusion, les résultats montrent que la méthode proposée permet un meilleur compromis entre réduction du bruit et préservation des contours et des détails, et conduit à une meilleure régularisation du champs de tenseurs tout en préservant l'anisotropie des tenseurs conduisant à des fibres plus cohérentes en termes de longueur et d'orientation. Le temps de calcul de la méthode proposée NAF dépend du nombre de pixels ou voxels à traiter et de la taille des voisinages homogènes. En pratique, on peut réduire de manière efficace le temps de calcul en imposant une limite supérieure à la taille du voisinage homogène.

7.2 Perspectives

La mesure de non-stationnarité développée dans cette thèse est une mesure générique capable de mesurer la non-stationnarité d'un signal par rapport à n'importe quelle caractéristique statistique et de quantifier la variation des données scalaires, vectorielles et tensorielles. Des études futures peuvent être poursuivies sur des points suivants:

1) Etude approfondie de la mesure de non-stationnarité des données tensorielles, étude de sa performance vis-à-vis du bruit, et exploration de son application à la segmentation et au lissage des champs de tenseurs en imagerie du tenseur de diffusion
2) Etude approfondie de la mesure de non-stationnarité des données vectorielles, analyse de sa performance en fonction du bruit, et exploration de son application pour la segmentation, le lissage des champs de vecteurs et pour la tractographie des fibres.

7.3 Author's publications

- **Yan-Li Zhang**, Wan-Yu Liu, Isabelle E. Magnin, Yue-Min Zhu, Feature-Preserving Smoothing of Diffusion Weighted Images Using Nonstationarity Adaptive Filtering, IEEE Trans. Biomedical Engineering, 60(6): 1693-1701. (**Cover page**; SCI, IDS Number: 147CD)

- **Yan-Li Zhang**, Wan-Yu Liu, Isabelle E. Magnin, Yue-Min Zhu, Enhancement of human cardiac DT-MRI data using locally adaptive filtering, IEEE ICSP'10, Proceedings, 744-747, Beijing, 2010. (EI, Accession number: 20110213573669)

- Liu W.Y., **Zhang Y.L.**, Liu W, Hu S, Zhu YM, Magnin I. E. A Robust algorithm based on Nonstationary Degree for ultrasonic data enhancement. IEEE SMC 07, Proceedings, 1061-1066, Montreal, 2007 (EI, Accession number: 20081311169382)

- Wan-Yu Liu, **Yan-Li Zhang**, Yue-Min Zhu, Isabelle E. Magnin, A General Scheme for the Detection of Changes in Noisy Signals, Signal processing. (SIGPRO-D-13-00014, Revision)

Appendices

A. Heights of the response peaks of NSM operators to the ideal step signal s_1

The ideal step signal s_1 is mathematically defined as

$$s_1(t) = u(t) = \begin{cases} 0, & t \le 0 \\ 1, & t > 0 \end{cases}. \tag{A.1}$$

Its 1st-order moment obtained with a rectangular window function $h(t)$ of width $2W$ is expressed as

$$\hat{\theta}_1(t) = \begin{cases} 0, & t < -W \\ \dfrac{t}{2W} + \dfrac{1}{2}, & -W \le t \le W \\ 1, & t > W \end{cases}. \tag{A.2}$$

The maximum of the output of the 2nd-order NSM operator is obtained at $t = 0$:

$$\begin{aligned} \hat{y}_{s_1}(0) &= [\hat{\theta}_1^2 * g](0) - (\hat{\theta}_1 * g)^2(0) \\ &= \int_{-W}^{W} \hat{\theta}_1^2(\tau) g(-\tau) d\tau - \left[\int_{-W}^{W} \hat{\theta}_1(\tau) g(-\tau) d\tau \right]^2. \end{aligned} \tag{A.3}$$

For the observation window function $g_1(t) = \dfrac{1}{2W} rect\left(\dfrac{t}{2W}\right)$, the first term of (A.3) is given by

$$\begin{aligned} \int_{-W}^{W} \hat{\theta}_1^2(\tau) g_1(-\tau) d\tau &= \frac{1}{2W} \int_{-W}^{W} \left(\frac{\tau}{2W} + \frac{1}{2} \right)^2 d\tau \\ &= \frac{1}{(2W)^3} \left[\frac{\tau^3}{3} + W\tau^2 + W^2\tau \right]_{-W}^{W} \\ &= \frac{1}{(2W)^3} \cdot \frac{8}{3} W^3 \\ &= \frac{1}{3} \end{aligned}. \tag{A.4}$$

For the second term of (A.3), we have

$$\begin{aligned}\int_{-W}^{W}\hat{\theta}_1(\tau)g(-\tau)d\tau &= \frac{1}{2W}\int_{-W}^{W}\left(\frac{\tau}{2W}+\frac{1}{2}\right)d\tau \\ &= \frac{1}{(2W)^2}\left[\frac{\tau^2}{2}+W\tau\right]_{-W}^{W} \\ &= \frac{1}{(2W)^2}\cdot 2W^2 \\ &= \frac{1}{2}\end{aligned} . \qquad (A.5)$$

Therefore, with the observation window function $g_1(t)$, the height of the response peak of the 2nd-order NSM operator to the ideal signal s_1 is

$$H_{11} = \frac{1}{3}-\left(\frac{1}{2}\right)^2 = \frac{1}{12}. \qquad (A.6)$$

For the observation window function $g_2(t)=\frac{1-\cos(\pi t/W)}{2W}$, the height of the response peak of the 2nd-order NSM operator to the ideal step signal s_1 can be expressed as:

$$\begin{aligned}H_{12} &= \int_{-W}^{W}\hat{\theta}_1^2(\tau)g_2(-\tau)d\tau-\left[\int_{-W}^{W}\hat{\theta}_1(\tau)g_2(-\tau)d\tau\right]^2 \\ &= \int_{-W}^{W}\hat{\theta}_1^2(\tau)\left[g_1(-\tau)-\frac{\cos(-\pi\tau/W)}{2W}\right]d\tau-\left\{\int_{-W}^{W}\hat{\theta}_1(\tau)\left[g_1(-\tau)-\frac{\cos(-\pi\tau/W)}{2W}\right]d\tau\right\}^2 \\ &= H_{11}-\int_{-W}^{W}\hat{\theta}_1^2(\tau)\cdot\frac{\cos(-\pi\tau/W)}{2W}d\tau+2\int_{-W}^{W}\hat{\theta}_1(\tau)g_1(-\tau)d\tau\cdot\int_{-W}^{W}\hat{\theta}_1(\tau)\cdot\frac{\cos(-\pi\tau/W)}{2W}d\tau \\ &\quad-\left[\int_{-W}^{W}\hat{\theta}_1(\tau)\cdot\frac{\cos(-\pi\tau/W)}{2W}d\tau\right]^2\end{aligned}, \qquad (A.7)$$

where

$$\begin{aligned}\int_{-W}^{W}\hat{\theta}_1^2(\tau)\cdot\frac{\cos(-\pi\tau/W)}{2W}d\tau &= \frac{1}{2\pi}\int_{-W}^{W}\hat{\theta}_1^2(\tau)\cdot d\sin(\pi\tau/W)\\ &= \frac{1}{2\pi}\left\{\left[\hat{\theta}_1^2(\tau)\cdot\sin(\pi\tau/W)\right]_{-W}^{W}-\int_{-W}^{W}\sin(\pi\tau/W)\cdot d\hat{\theta}_1^2(\tau)\right\}\\ &= \frac{1}{2\pi}\left\{0+\frac{1}{2W\pi}\int_{-W}^{W}\tau\cdot d\cos(\pi\tau/W)\right\}\\ &= \frac{1}{2\pi}\left\{0+\frac{1}{2W\pi}\left[\tau\cdot\cos(\pi\tau/W)\right]_{-W}^{W}\right\}\\ &= \frac{1}{2\pi}\cdot\frac{1}{2W\pi}\cdot(-2W)\\ &= -\frac{1}{2\pi^2}\end{aligned}, \quad \text{(A.8)}$$

$$\int_{-W}^{W}\hat{\theta}_1(\tau)g_1(-\tau)d\tau\cdot\int_{-W}^{W}\hat{\theta}_1(\tau)\cdot\frac{\cos(-\pi\tau/W)}{2W}d\tau=0, \quad \text{(A.9)}$$

$$\int_{-W}^{W}\hat{\theta}_1(\tau)\cdot\frac{\cos(-\pi\tau/W)}{2W}d\tau=0. \quad \text{(A.10)}$$

Therefore, with the observation window function $g_2(t)$, the height of the response peak of the 2nd-order NSM operator to the ideal signal s_1 is

$$H_{12}=H_{11}+\frac{1}{2\pi^2}=\frac{1}{12}+\frac{1}{2\pi^2} \quad \text{(A.11)}$$

For the observation window function $g_3(t)=\frac{1+\cos(\pi t/W)}{2W}$, the height of the response peak of the 2nd-order NSM operator to the ideal signal s_1 can be expressed as:

$$\begin{aligned}H_{13} &= \int_{-W}^{W}\hat{\theta}_1^2(\tau)g_3(-\tau)d\tau-\left[\int_{-W}^{W}\hat{\theta}_1(\tau)g_3(-\tau)d\tau\right]^2\\ &= \int_{-W}^{W}\hat{\theta}_1^2(\tau)\left[g_1(-\tau)+\frac{\cos(-\pi\tau/W)}{2W}\right]d\tau-\left[\int_{-W}^{W}\hat{\theta}_1(\tau)\left[g_1(-\tau)+\frac{\cos(-\pi\tau/W)}{2W}\right]d\tau\right]^2\\ &= H_{11}+\int_{-W}^{W}\hat{\theta}_1^2(\tau)\cdot\frac{\cos(-\pi\tau/W)}{2W}d\tau-2\int_{-W}^{W}\hat{\theta}_1(\tau)g_1(-\tau)d\tau\cdot\int_{-W}^{W}\hat{\theta}_1(\tau)\cdot\frac{\cos(-\pi\tau/W)}{2W}d\tau\\ &\quad-\left[\int_{-W}^{W}\hat{\theta}_1(\tau)\cdot\frac{\cos(-\pi\tau/W)}{2W}d\tau\right]^2\end{aligned}. \quad \text{(A.12)}$$

According to (A.8), (A.9) and (A.10), we arrive at

$$H_{13}=H_{11}-\frac{1}{2\pi^2}=\frac{1}{12}-\frac{1}{2\pi^2}. \quad \text{(A.13)}$$

B. Heights of the response peaks of NSM operators to the step signal with transition band s_2

The step signal with a transition band s_2 is mathematically defined as

$$s_2(t)=\begin{cases}-1/2, & t<-\alpha/2\\ t/\alpha, & -\alpha/2\le t\le\alpha/2\\ 1/2, & t>\alpha/2\end{cases}. \tag{B.1}$$

When $-(W+\alpha/2)\le t\le W+\alpha/2$, its 1st-order moment obtained with a rectangular window function $h(t)$ of width $2W$ is expressed as

$$\hat{\theta}_2(t)=\begin{cases}-\left(\frac{1}{2W}\int_{t-W}^{\alpha/2}\frac{\tau}{\alpha}d\tau+\frac{1}{2W}\int_{\alpha/2}^{t+W}\frac{1}{2}d\tau\right), & -\left(W+\frac{\alpha}{2}\right)<t\le-\left(W-\frac{\alpha}{2}\right)\\ -\left(\frac{1}{2W}\int_{t-W}^{-\alpha/2}-\frac{1}{2}d\tau+\frac{1}{2W}\int_{-\alpha/2}^{\alpha/2}\frac{\tau}{\alpha}d\tau+\frac{1}{2W}\int_{\alpha/2}^{t+W}\frac{1}{2}d\tau\right), & -\left(W-\frac{\alpha}{2}\right)\le t<0\\ \frac{1}{2W}\int_{t-W}^{-\alpha/2}-\frac{1}{2}d\tau+\frac{1}{2W}\int_{-\alpha/2}^{\alpha/2}\frac{\tau}{\alpha}d\tau+\frac{1}{2W}\int_{\alpha/2}^{t+W}\frac{1}{2}d\tau, & 0\le t\le W-\frac{\alpha}{2}\\ \frac{1}{2W}\int_{t-W}^{\alpha/2}\frac{\tau}{\alpha}d\tau+\frac{1}{2W}\int_{\alpha/2}^{t+W}\frac{1}{2}d\tau, & W-\frac{\alpha}{2}<t\le W+\frac{\alpha}{2}\end{cases}$$

$$=\begin{cases}-\frac{1}{4W\alpha}\left[\left(\frac{\alpha}{2}\right)^2-(t-W)^2\right]-\frac{1}{4W}\left(t+W-\frac{\alpha}{2}\right), & -\left(W+\frac{\alpha}{2}\right)<t\le-\left(W-\frac{\alpha}{2}\right)\\ -\frac{t}{2W}, & -\left(W-\frac{\alpha}{2}\right)\le t<0\\ \frac{t}{2W}, & 0\le t\le W-\frac{\alpha}{2}\\ \frac{1}{4W\alpha}\left[\left(\frac{\alpha}{2}\right)^2-(t-W)^2\right]+\frac{1}{4W}\left(t+W-\frac{\alpha}{2}\right), & W-\frac{\alpha}{2}<t\le W+\frac{\alpha}{2}\end{cases} \tag{B.2}$$

The maximum of the output of the 2nd-order NSM operator is obtained at $t=0$:

$$\begin{aligned}\hat{y}_{s_2}(0)&=[\hat{\theta}_2^2*g](0)-(\hat{\theta}_2*g)^2(0)\\&=\int_{-W}^{W}\hat{\theta}_2^2(\tau)g(-\tau)d\tau-\left[\int_{-W}^{W}\hat{\theta}_2(\tau)g(-\tau)d\tau\right]^2\end{aligned} \tag{B.3}$$

For the observation window function $g_1(t)=\frac{1}{2W}rect\left(\frac{t}{2W}\right)$, the height of the response peak of the 2nd-order NSM operator to s_2 is

$$H_{21} = \frac{1}{W}\int_0^{W-\frac{\alpha}{2}}\left(\frac{\tau}{2W}\right)^2 d\tau + \frac{1}{W}\int_{W-\frac{\alpha}{2}}^{W}\left\{\frac{1}{4W\alpha}\left[\left(\frac{\alpha}{2}\right)^2-(\tau-W)^2\right]+\frac{1}{4W}\left(\tau+W-\frac{\alpha}{2}\right)\right\}^2 d\tau \quad \text{, (B.4)}$$
$$= \frac{1}{12}-\frac{1}{24}\gamma^2+\frac{13}{960}\gamma^3$$

where $\gamma = \alpha/2W$ and $0<\gamma\le 1$.

For the observation window function $g_2(t)=\dfrac{1-\cos(\pi t/W)}{2W}$, the height of the response peak of the 2nd-order NSM operator to s_2 can be expressed as:

$$\begin{aligned} H_{22} &= \int_{-W}^{W}\hat{\theta}_2^2(\tau)g_2(-\tau)d\tau-\left[\int_{-W}^{W}\hat{\theta}_2(\tau)g_2(-\tau)d\tau\right]^2 \\ &= \int_{-W}^{W}\hat{\theta}_2^2(\tau)\left[g_1(-\tau)-\frac{\cos(-\pi\tau/W)}{2W}\right]d\tau-\left\{\int_{-W}^{W}\hat{\theta}_2(\tau)\left[g_1(-\tau)-\frac{\cos(-\pi\tau/W)}{2W}\right]d\tau\right\}^2 \\ &= H_{21}-\int_{-W}^{W}\hat{\theta}_2^2(\tau)\cdot\frac{\cos(-\pi\tau/W)}{2W}d\tau+2\int_{-W}^{W}\hat{\theta}_2(\tau)g_1(-\tau)d\tau\cdot\int_{-W}^{W}\hat{\theta}_2(\tau)\cdot\frac{\cos(-\pi\tau/W)}{2W}d\tau \\ &\quad -\left[\int_{-W}^{W}\hat{\theta}_2(\tau)\cdot\frac{\cos(-\pi\tau/W)}{2W}d\tau\right]^2 \end{aligned} \quad \text{, (B.5)}$$

where

$$\begin{aligned} &\int_{-W}^{W}\hat{\theta}_2^2(\tau)\cdot\frac{\cos(-\pi\tau/W)}{2W}d\tau \\ &=\frac{1}{4\pi^3}\sin(\gamma\pi)+\frac{\gamma}{16\pi^2}-\frac{3}{8\pi^4\gamma}-\frac{1}{4\pi^2}+\frac{3}{4\pi^4\gamma}\cos(\gamma\pi)-\frac{1}{4\pi^3\gamma}\sin(\gamma\pi)-\frac{3}{8\pi^5\gamma^2}\sin(\gamma\pi) \end{aligned} \quad \text{, (B.6)}$$

$$\int_{-W}^{W}\hat{\theta}_2(\tau)g_1(-\tau)d\tau\cdot\int_{-W}^{W}\hat{\theta}_2(\tau)\cdot\frac{\cos(-\pi\tau/W)}{2W}d\tau=0, \quad \text{(B.7)}$$

$$\int_{-W}^{W}\hat{\theta}_2(\tau)\cdot\frac{\cos(-\pi\tau/W)}{2W}d\tau=0. \quad \text{(B.8)}$$

Therefore, with the observation window function $g_2(t)$, the height of the response peak of the 2nd-order NSM operator to s_2 is given by:

$$\begin{aligned} H_{22} = \frac{1}{12}-\frac{\gamma^2}{24}+\frac{13\gamma^3}{960}-\Bigg[&\frac{1}{4\pi^3}\sin(\gamma\pi)+\frac{\gamma}{16\pi^2}-\frac{3}{8\pi^4\gamma}-\frac{1}{4\pi^2} \\ &+\frac{3}{4\pi^4\gamma}\cos(\gamma\pi)-\frac{1}{4\pi^3\gamma}\sin(\gamma\pi)-\frac{3}{8\pi^5\gamma^2}\sin(\gamma\pi)\Bigg] \end{aligned}. \quad \text{(B.9)}$$

For the observation window function $g_3(t)=\frac{1+\cos(\pi t/W)}{2W}$, the height of the response peak of the 2nd-order NSM operator to s_2 can be written as:

$$\begin{aligned} H_{23} &= \int_{-W}^{W}\hat{\theta}_2^2(\tau)g_3(-\tau)d\tau-\left[\int_{-W}^{W}\hat{\theta}_2(\tau)g_3(-\tau)d\tau\right]^2 \\ &= H_{21}+\int_{-W}^{W}\hat{\theta}_2^2(\tau)\cdot\frac{\cos(-\pi\tau/W)}{2W}d\tau-2\int_{-W}^{W}\hat{\theta}_2(\tau)g_1(-\tau)d\tau\cdot\int_{-W}^{W}\hat{\theta}_2(\tau)\cdot\frac{\cos(-\pi\tau/W)}{2W}d\tau. \\ &\quad-\left[\int_{-W}^{W}\hat{\theta}_2(\tau)\cdot\frac{\cos(-\pi\tau/W)}{2W}d\tau\right]^2 \end{aligned} \tag{B.10}$$

According to (B.6), (B.7) and (B.8), we arrive at:

$$\begin{aligned} H_{23} = \frac{1}{12}-\frac{\gamma^2}{24}+\frac{13\gamma^3}{960}+\left[\frac{1}{4\pi^3}\sin(\gamma\pi)+\frac{\gamma}{16\pi^2}-\frac{3}{8\pi^4\gamma}-\frac{1}{4\pi^2}\right. \\ \left.+\frac{3}{4\pi^4\gamma}\cos(\gamma\pi)-\frac{1}{4\pi^3\gamma}\sin(\gamma\pi)-\frac{3}{8\pi^5\gamma^2}\sin(\gamma\pi)\right]. \end{aligned} \tag{B.11}$$

C. Heights of the response peaks of NSM operators to the step signal mixed with a ramp s_3

The step signal mixed with a ramp s_3 is mathematically defined as:

$$s_3(t)=u(t)+\beta\cdot t. \tag{C.1}$$

When $-W\le t\le W$, its 1st-order moment obtained with a rectangular window function $h(t)$ of width $2W$ is given by:

$$\hat{\theta}_3(t)=\left(\beta+\frac{1}{2W}\right)\cdot t. \tag{C.2}$$

The maximum of the output of the 2nd-order NSM operator is obtained at $t=0$:

$$\begin{aligned} \hat{y}_{s_3}(0) &= [\hat{\theta}_3^2 * g](0)-(\hat{\theta}_3 * g)^2(0) \\ &= \int_{-W}^{W}\hat{\theta}_3^2(\tau)g(-\tau)d\tau-\left[\int_{-W}^{W}\hat{\theta}_3(\tau)g(-\tau)d\tau\right]^2. \end{aligned} \tag{C.3}$$

For the observation window function $g_1(t)=\frac{1}{2W}rect\left(\frac{t}{2W}\right)$, the height of the response peak of the 2nd-order NSM operator to s_3 is

$$H_{31} = \frac{1}{2W}\int_{-W}^{W}\left[\left(\beta+\frac{1}{2W}\right)\cdot\tau\right]^2 d\tau - \left[\frac{1}{2W}\int_{-W}^{W}\left(\beta+\frac{1}{2W}\right)\tau d\tau\right]^2 = \frac{(2\beta W+1)^2}{12} \quad (C.4)$$

For the observation window function $g_2(t)=\frac{1-\cos(\pi t/W)}{2W}$, the height of the response peak of the 2nd-order NSM operator to s_3 can be expressed as:

$$\begin{aligned} H_{32} &= \int_{-W}^{W}\hat{\theta}_3^2(\tau)g_2(-\tau)d\tau - \left[\int_{-W}^{W}\hat{\theta}_3(\tau)g_2(-\tau)d\tau\right]^2 \\ &= \int_{-W}^{W}\hat{\theta}_3^2(\tau)\left[g_1(-\tau)-\frac{\cos(-\pi\tau/W)}{2W}\right]d\tau - \left\{\int_{-W}^{W}\hat{\theta}_3(\tau)\left[g_1(-\tau)-\frac{\cos(-\pi\tau/W)}{2W}\right]d\tau\right\}^2 \\ &= H_{31} - \int_{-W}^{W}\hat{\theta}_3^2(\tau)\cdot\frac{\cos(-\pi\tau/W)}{2W}d\tau + 2\int_{-W}^{W}\hat{\theta}_3(\tau)g_1(-\tau)d\tau\cdot\int_{-W}^{W}\hat{\theta}_3(\tau)\cdot\frac{\cos(-\pi\tau/W)}{2W}d\tau \\ &\quad - \left[\int_{-W}^{W}\hat{\theta}_3(\tau)\cdot\frac{\cos(-\pi\tau/W)}{2W}d\tau\right]^2 \end{aligned} \quad (C.5)$$

where

$$\int_{-W}^{W}\hat{\theta}_3^2(\tau)\cdot\frac{\cos(-\pi\tau/W)}{2W}d\tau = -\frac{1}{\pi^2}(2\beta W+1)^2, \quad (C.6)$$

$$\int_{-W}^{W}\hat{\theta}_3(\tau)g_1(-\tau)d\tau\cdot\int_{-W}^{W}\hat{\theta}_3(\tau)\cdot\frac{\cos(-\pi\tau/W)}{2W}d\tau = 0, \quad (C.7)$$

$$\int_{-W}^{W}\hat{\theta}_3(\tau)\cdot\frac{\cos(-\pi\tau/W)}{2W}d\tau = 0. \quad (C.8)$$

Therefore, with the observation window function $g_2(t)$, the height of the response peak of the 2nd-order NSM operator to s_3 is calculated as:

$$H_{32} = H_{31} + \frac{1}{2\pi^2}(2\beta W+1)^2 = (2\beta W+1)^2\left(\frac{1}{12}+\frac{1}{2\pi^2}\right). \quad (C.9)$$

For the observation window function $g_3(t)=\frac{1+\cos(\pi t/W)}{2W}$, the height of the response peak of the 2nd-order NSM operator to s_3 can be expressed as:

$$
\begin{aligned}
H_{33} &= \int_{-W}^{W} \hat{\theta}_3^2(\tau) g_3(-\tau) d\tau - \left[\int_{-W}^{W} \hat{\theta}_3(\tau) g_3(-\tau) d\tau \right]^2 \\
&= \int_{-W}^{W} \hat{\theta}_3^2(\tau) \left[g_1(-\tau) + \frac{\cos(-\pi\tau/W)}{2W} \right] d\tau - \left\{ \int_{-W}^{W} \hat{\theta}_3(\tau) \left[g_1(-\tau) + \frac{\cos(-\pi\tau/W)}{2W} \right] d\tau \right\}^2 \\
&= H_{31} + \int_{-W}^{W} \hat{\theta}_3^2(\tau) \cdot \frac{\cos(-\pi\tau/W)}{2W} d\tau - 2 \int_{-W}^{W} \hat{\theta}_3(\tau) g_1(-\tau) d\tau \cdot \int_{-W}^{W} \hat{\theta}_3(\tau) \cdot \frac{\cos(-\pi\tau/W)}{2W} d\tau \\
&\quad - \left[\int_{-W}^{W} \hat{\theta}_3(\tau) \cdot \frac{\cos(-\pi\tau/W)}{2W} d\tau \right]^2
\end{aligned}
\tag{C.10}
$$

According to (C.6), (C.7) and (C.8), we get:

$$
\begin{aligned}
H_{33} &= H_{31} - \frac{1}{2\pi^2} (2\beta W + 1)^2 \\
&= (2\beta W + 1)^2 \left(\frac{1}{12} - \frac{1}{2\pi^2} \right)
\end{aligned}
\tag{C.11}
$$

D. Output SNRs of NSM operators corresponding to three representative observation window functions

From (2.29), it can be seen that the height of the response peak of the NSM operator to the ideal step signal $A \cdot u(t)$ and the square root of the mean-squared noise response are two important elements in the calculation of the output SNR.

The heights of the response peaks of the NSM operators corresponding to the three representative observation windows to the ideal step signal $A \cdot u(t)$ are respectively given by the following equations:

$$
H_{11} = \frac{A^2}{12}, \tag{D.1}
$$

$$
H_{12} = A^2 \cdot \left(\frac{1}{12} + \frac{1}{2\pi^2} \right), \tag{D.2}
$$

$$
H_{13} = A^2 \cdot \left(\frac{1}{12} - \frac{1}{2\pi^2} \right). \tag{D.3}
$$

To obtain the square root of the mean-squared noise response, we first estimate the variance of the response to the noise. In order to keep the theoretical analysis simple, we assume the noise $n(t)$ as a Gaussian white noise with zero mean. The response of the 2nd-order NSM to the noise $n(t)$ can be expressed as:

$$
\hat{y}_n(t) = \left[g * (h * n)^2 \right](t) - (g * h * n)^2(t), \tag{D.4}
$$

where the sliding window function $h(t)=\frac{1}{2W}rect\left(\frac{t}{2W}\right)$.

Let $U=\left(\left(n*h\right)^2*g\right)(t)$ and $V=\left(n*h*g\right)^2(t)$, then the variance of the noise response $D^2\left(\hat{y}_n(t)\right)$ can be expressed as:

$$\begin{aligned} D^2\left(\hat{y}_n(t)\right) &= E\left(\left(U-V\right)^2\right)-\left[E\left(U-V\right)\right]^2 \\ &= E\left(U^2\right)+E\left(V^2\right)-2E\left(UV\right)-\left[E\left(U-V\right)\right]^2 \end{aligned}, \tag{D.5}$$

where

$$E\left(U^2\right)=\sigma_n^4\left[\int_{\tau_1}h^2(\tau_1)d\tau_1\right]^2\left[\int_{\tau_2}g(\tau_2)d\tau_2\right]^2+2\sigma_n^4\int_{\tau}\left(h*h\right)^2\left(g*g\right)(\tau)d\tau, \tag{D.6}$$

$$E\left(V^2\right)=3\sigma_n^4\left[\int_{\tau}\left(h*g\right)^2(\tau)d\tau\right]^2, \tag{D.7}$$

$$E\left(UV\right)=\sigma_n^4\int_{\tau_1}h^2(\tau_1)d\tau_1\int_{\tau_2}\left(g*h\right)^2(\tau_2)d\tau_2\int_{\tau_3}g(\tau_3)d\tau_3+2\sigma_n^4\int_{\tau}g(\tau)\left(h*h*g\right)^2(\tau)d\tau, \tag{D.8}$$

$$E\left(U-V\right)=\sigma_n^2\left[\int_{\tau}h(\tau)g(\tau)d\tau-\int_{\tau}\left(h*g\right)^2(\tau)d\tau\right]. \tag{D.9}$$

For the observation window function $g_1(t)=\frac{1}{2W}rect\left(\frac{t}{2W}\right)$,

$$\left(h*h\right)(t)=\begin{cases}\frac{t}{4W^2}+\frac{1}{2W}, & -2W\le t\le 0\\ -\frac{t}{4W^2}+\frac{1}{2W}, & 0<t\le 2W\end{cases}. \tag{D.10}$$

So we have

$$E\left(U^2\right)=\frac{\sigma^4}{4W^2}+4\sigma_n^4\int_{-2W}^{0}\left(\frac{t}{4W^2}+\frac{1}{2W}\right)^3dt=\frac{\sigma_n^4}{2W^2}, \tag{D.11}$$

$$E\left(V^2\right)=3\sigma_n^4\left[2\int_{-2W}^{0}\left(\frac{\tau}{4W^2}+\frac{1}{2W}\right)^2d\tau\right]^2=\frac{\sigma_n^4}{3W^2}. \tag{D.12}$$

When $-W\le t\le 0$, the convolution in the $E\left(UV\right)$

$$
\begin{aligned}
&(h*h*g)(t)\\
&=\int_{t-W}^{0}\left(\frac{\tau}{4W^2}+\frac{1}{2W}\right)\frac{1}{2W}d\tau+\int_{0}^{t+W}\left(-\frac{\tau}{4W^2}+\frac{1}{2W}\right)\frac{1}{2W}d\tau\\
&=\frac{1}{2W}\left[-\frac{1}{8W^2}(t-W)^2-\frac{1}{2W}(t-W)\right]+\frac{1}{2W}\left[-\frac{1}{8W^2}(t+W)^2+\frac{1}{2W}(t+W)\right]\\
&=\frac{1}{2W}\left(\frac{3}{4}-\frac{t^2}{4W^2}\right)
\end{aligned}
\qquad \text{(D.13)}
$$

It follows that

$$
\begin{aligned}
E(UV)&=\frac{\sigma_n^4}{6W^2}+4\sigma_n^4\int_{-W}^{0}\frac{1}{8W^3}\left(\frac{3}{4}-\frac{t^2}{4W^2}\right)^2dt\\
&=\frac{47\sigma_n^4}{120W^2}
\end{aligned}
\qquad \text{(D.14)}
$$

In addition,

$$
\begin{aligned}
E(U-V)&=\sigma_n^2\left[\int_{\tau}h(\tau)g(\tau)d\tau-\int_{\tau}(h*g)^2(\tau)d\tau\right]\\
&=\sigma_n^2\left[\frac{1}{2W}-\frac{1}{3W}\right]\\
&=\frac{\sigma_n^2}{6W}
\end{aligned}
\qquad \text{(D.15)}
$$

So,

$$
\begin{aligned}
D^2(\hat{y}_n(t))&=E(U^2)+E(V^2)-2E(UV)-\left[E(U-V)\right]^2\\
&=\frac{\sigma_n^4}{2W^2}+\frac{\sigma_n^4}{3W^2}-2\times\frac{47\sigma_n^4}{120W^2}-\left(\frac{\sigma_n^2}{6W}\right)^2\\
&=\frac{\sigma_n^4}{45W^2}
\end{aligned}
\qquad \text{(D.16)}
$$

Therefore, for the observation window function $g_1(t)=\frac{1}{2W}rect\left(\frac{t}{2W}\right)$, the output SNR of the NSM operator is

$$
\Sigma_{\mathrm{NSM},1}=\frac{A^2/12}{\sqrt{\sigma_n^4/45W^2}}\approx 0.28\left(\frac{A}{\sigma_n}\right)^2(2W). \qquad \text{(D.17)}
$$

For the observation window function $g_2(t)=\frac{1-\cos(\pi t/W)}{2W}$, the convolution in the $E(U^2)$

$$(g*g)(t)=\begin{cases}\dfrac{1}{2W}+\dfrac{t}{4W^2}+\dfrac{5}{8\pi W}\sin\left(\dfrac{\pi t}{W}\right)+\dfrac{t}{8W^2}\cos\left(\dfrac{\pi t}{W}\right)+\dfrac{\cos(\pi t/W)}{4W}, & -2W\le t\le 0\\ \dfrac{1}{2W}-\dfrac{t}{4W^2}-\dfrac{5}{8\pi W}\sin\left(\dfrac{\pi t}{W}\right)-\dfrac{t}{8W^2}\cos\left(\dfrac{\pi t}{W}\right)+\dfrac{\cos(\pi t/W)}{4W}, & 0<t\le 2W\end{cases}.$$

(D.18)

As a result, we have

$$\begin{aligned}E(U^2)&=\frac{\sigma_n^4}{4W^2}+4\sigma_n^4\int_{-2W}^{0}\left(\frac{t}{4W^2}+\frac{1}{2W}\right)^2\left[\frac{1}{2W}+\frac{t}{4W^2}+\frac{5}{8\pi W}\sin\left(\frac{\pi t}{W}\right)+\frac{t}{8W^2}\cos\left(\frac{\pi t}{W}\right)+\frac{\cos(\pi t/W)}{4W}\right]dt\\&=\frac{\sigma_n^4}{4W^2}+4\sigma_n^4\int_{-2W}^{0}\left(\frac{t}{4W^2}+\frac{1}{2W}\right)^3dt\\&\quad+4\sigma_n^4\int_{-2W}^{0}\left(\frac{t}{4W^2}+\frac{1}{2W}\right)^2\left[\frac{5}{8\pi W}\sin\left(\frac{\pi t}{W}\right)+\frac{t}{8W^2}\cos\left(\frac{\pi t}{W}\right)+\frac{\cos(\pi t/W)}{4W}\right]dt\\&=\frac{\sigma_n^4}{2W^2}+4\sigma_n^4\left(-\frac{5}{32\pi^2W^2}+\frac{1}{32\pi^2W^2}+\frac{1}{16\pi^2W^2}\right)\\&=\left(2-\frac{1}{\pi^2}\right)\frac{\sigma_n^4}{4W^2}\end{aligned}$$

(D.19)

The convolution in the $E(V^2)$

$$(g*h)(t)=\begin{cases}\dfrac{t}{4W^2}+\dfrac{1}{2W}+\dfrac{\sin(\pi t/W)}{4\pi W}, & -2W\le t\le 0\\ -\dfrac{t}{4W^2}+\dfrac{1}{2W}-\dfrac{\sin(\pi t/W)}{4\pi W}, & 0<t\le 2W\end{cases}.$$

(D.20)

So,

$$\begin{aligned}E(V^2)&=3\sigma_n^4\left[2\int_{-2W}^{0}\left(\frac{\tau}{4W^2}+\frac{1}{2W}+\frac{\sin(\pi\tau/W)}{4\pi W}\right)^2d\tau\right]^2\\&=12\sigma_n^4\left[\int_{-2W}^{0}\left(\frac{\tau}{4W^2}+\frac{1}{2W}\right)^2d\tau+\int_{-2W}^{0}\left(\frac{\tau}{4W^2}+\frac{1}{2W}\right)\frac{\sin(\pi\tau/W)}{2\pi W}d\tau+\int_{-2W}^{0}\left(\frac{\sin(\pi\tau/W)}{4\pi W}\right)^2d\tau\right]^2\\&=12\sigma_n^4\left(\frac{1}{6W}-\frac{1}{4\pi^2W}+\frac{1}{16\pi^2W}\right)^2\\&=\frac{\sigma_n^4}{3W^2}-\frac{3\sigma_n^4}{4\pi^2W^2}+\frac{27\sigma_n^4}{64\pi^4W^2}\end{aligned}$$

(D.21)

When $-W \le t \le 0$, the convolution in the $E(UV)$

$$
\begin{aligned}
&(h*h*g)(t) \\
&= \int_{t-W}^{0}\left(\frac{\tau}{4W^2}+\frac{1}{2W}\right)\left(\frac{1}{2W}-\frac{\cos(\pi(t-\tau)/W)}{2W}\right)d\tau + \int_{0}^{t+W}\left(-\frac{\tau}{4W^2}+\frac{1}{2W}\right)\left(\frac{1}{2W}-\frac{\cos(\pi(t-\tau)/W)}{2W}\right)d\tau \\
&= \int_{t-W}^{0}\left(\frac{\tau}{4W^2}+\frac{1}{2W}\right)\frac{1}{2W}d\tau + \int_{0}^{t+W}\left(-\frac{\tau}{4W^2}+\frac{1}{2W}\right)\frac{1}{2W}d\tau + \int_{t-W}^{0}\left(\frac{\tau}{4W^2}+\frac{1}{2W}\right)\left(-\frac{\cos(\pi(t-\tau)/W)}{2W}\right)d\tau \\
&\quad + \int_{0}^{t+W}\left(-\frac{\tau}{4W^2}+\frac{1}{2W}\right)\left(-\frac{\cos(\pi(t-\tau)/W)}{2W}\right)d\tau \\
&= \frac{1}{2W}\left(\frac{3}{4}-\frac{t^2}{4W^2}\right)-\frac{1}{8\pi^2W}-\frac{\cos(\pi t/W)}{8\pi^2W}+\frac{\sin(\pi t/W)}{4\pi W}-\frac{1}{8\pi^2W}-\frac{\cos(\pi t/W)}{8\pi^2W}-\frac{\sin(\pi t/W)}{4\pi W} \\
&= \frac{1}{2W}\left[\frac{3}{4}-\frac{t^2}{4W^2}-\frac{1}{2\pi^2}-\frac{\cos(\pi t/W)}{2\pi^2}\right]
\end{aligned}
\tag{D.22}
$$

Consequently, we have

$$
\begin{aligned}
E(UV) &= \frac{\sigma_n^4}{4W^2}\left(\frac{2}{3}-\frac{3}{4\pi^2}\right)+2\sigma_n^4\int_{-W}^{W}\frac{1}{4W^2}\left[\frac{1}{2W}-\frac{\cos(\pi t/W)}{2W}\right]\left[\frac{3}{4}-\frac{t^2}{4W^2}-\frac{1}{2\pi^2}-\frac{\cos(\pi t/W)}{2\pi^2}\right]^2 dt \\
&= \frac{\sigma_n^4}{4W^2}\left(\frac{2}{3}-\frac{3}{4\pi^2}\right)+\frac{\sigma_n^4}{4W^2}\left(\frac{9}{10}-\frac{5}{3\pi^2}-\frac{23}{8\pi^4}\right) \\
&= \frac{\sigma_n^4}{4W^2}\left(\frac{47}{30}-\frac{29}{12\pi^2}-\frac{23}{8\pi^4}\right)
\end{aligned}
\tag{D.23}
$$

In addition,

$$
\begin{aligned}
E(U-V) &= \sigma_n^2\left[\int_{\tau}h(\tau)g(\tau)d\tau-\int_{\tau}(h*g)^2(\tau)d\tau\right] \\
&= \sigma_n^2\left\{\frac{1}{2W}-2\int_{-2W}^{0}\left[\frac{t}{4W^2}+\frac{1}{2W}+\frac{\sin(\pi t/W)}{4\pi W}\right]^2 dt\right\} \\
&= \sigma_n^2\left(\frac{1}{2W}-\frac{1}{3W}+\frac{3}{8\pi^2W}\right) \\
&= \frac{\sigma_n^2}{6W}+\frac{3\sigma_n^2}{8\pi^2W}
\end{aligned}
\tag{D.24}
$$

So,

$$D^2\left(\hat{y}_n(t)\right)=\left(2-\frac{1}{\pi^2}\right)\frac{\sigma_n^4}{4W^2}+\frac{\sigma_n^4}{3W^2}-\frac{3\sigma_n^4}{4\pi^2W^2}+\frac{27\sigma_n^4}{64\pi^4W^2}$$
$$-2\times\left[\frac{\sigma_n^4}{4W^2}\left(\frac{47}{30}-\frac{29}{12\pi^2}-\frac{23}{8\pi^4}\right)\right]-\left(\frac{\sigma_n^2}{6W}+\frac{3\sigma_n^2}{8\pi^2W}\right)^2. \quad \text{(D.25)}$$
$$=\frac{\sigma_n^4}{45W^2}+\frac{\sigma_n^4}{12\pi^2W^2}+\frac{55\sigma_n^4}{32\pi^4W^2}$$

Therefore, for the observation window function $g_2(t)=\frac{1-\cos\left(\pi t/W\right)}{2W}$, the output SNR of the NSM operator is

$$\Sigma_{\mathrm{NSM},2}=\frac{A^2\cdot\left(\frac{1}{12}+\frac{1}{2\pi^2}\right)}{\sqrt{\frac{\sigma_n^4}{45W^2}+\frac{\sigma_n^4}{12\pi^2W^2}+\frac{55\sigma_n^4}{32\pi^4W^2}}}\approx 0.30\left(\frac{A}{\sigma_n}\right)^2(2W). \quad \text{(D.26)}$$

For the observation window function $g_3(t)=\frac{1+\cos\left(\pi t/W\right)}{2W}$, the convolution in the $E\left(U^2\right)$

$$\left(g*g\right)(t)=\begin{cases}\frac{1}{2W}+\frac{t}{4W^2}-\frac{3}{8\pi W}\sin\left(\frac{\pi t}{W}\right)+\frac{t}{8W^2}\cos\left(\frac{\pi t}{W}\right)+\frac{\cos\left(\pi t/W\right)}{4W}, -2W\le t\le 0\\ \frac{1}{2W}-\frac{t}{4W^2}+\frac{3}{8\pi W}\sin\left(\frac{\pi t}{W}\right)-\frac{t}{8W^2}\cos\left(\frac{\pi t}{W}\right)+\frac{\cos\left(\pi t/W\right)}{4W}, 0<t\le 2W\end{cases}. \quad \text{(D.27)}$$

So, we have

$$E\left(U^2\right)=\left(2+\frac{3}{\pi^2}\right)\frac{\sigma_n^4}{4W^2}. \quad \text{(D.28)}$$

The convolution in the $E\left(V^2\right)$

$$\left(g*h\right)(t)=\begin{cases}\frac{t}{4W^2}+\frac{1}{2W}-\frac{\sin\left(\pi t/W\right)}{4\pi W}, & -2W\le t\le 0\\ -\frac{t}{4W^2}+\frac{1}{2W}+\frac{\sin\left(\pi t/W\right)}{4\pi W}, & 0<t\le 2W\end{cases}. \quad \text{(D.29)}$$

Thus, we get

$$E\left(V^2\right)=3\sigma_n^4\left[2\int_{-2W}^{0}\left(\frac{\tau}{4W^2}+\frac{1}{2W}-\frac{\sin\left(\pi\tau/W\right)}{4\pi W}\right)^2 d\tau\right]^2. \qquad (D.30)$$
$$=\frac{\sigma_n^4}{3W^2}+\frac{5\sigma_n^4}{4\pi^2W^2}+\frac{75\sigma_n^4}{64\pi^4W^2}$$

The convolution in the $E\left(UV\right)$

$$\begin{aligned}
&\left(h*h*g\right)(t)\\
&=\int_{t-W}^{0}\left(\frac{\tau}{4W^2}+\frac{1}{2W}\right)\left(\frac{1}{2W}+\frac{\cos\left(\pi(t-\tau)/W\right)}{2W}\right)d\tau+\int_{0}^{t+W}\left(-\frac{\tau}{4W^2}+\frac{1}{2W}\right)\left(\frac{1}{2W}+\frac{\cos\left(\pi(t-\tau)/W\right)}{2W}\right)d\tau\\
&=\int_{t-W}^{0}\left(\frac{\tau}{4W^2}+\frac{1}{2W}\right)\frac{1}{2W}d\tau+\int_{0}^{t+W}\left(-\frac{\tau}{4W^2}+\frac{1}{2W}\right)\frac{1}{2W}d\tau+\int_{t-W}^{0}\left(\frac{\tau}{4W^2}+\frac{1}{2W}\right)\frac{\cos\left(\pi(t-\tau)/W\right)}{2W}d\tau\\
&\quad+\int_{0}^{t+W}\left(-\frac{\tau}{4W^2}+\frac{1}{2W}\right)\frac{\cos\left(\pi(t-\tau)/W\right)}{2W}d\tau\\
&=\frac{1}{2W}\left(\frac{3}{4}-\frac{t^2}{4W^2}\right)+\frac{1}{8\pi^2W}+\frac{\cos\left(\pi t/W\right)}{8\pi^2W}-\frac{\sin\left(\pi t/W\right)}{4\pi W}+\frac{1}{8\pi^2W}+\frac{\cos\left(\pi t/W\right)}{8\pi^2W}+\frac{\sin\left(\pi t/W\right)}{4\pi W}\\
&=\frac{1}{2W}\left[\frac{3}{4}-\frac{t^2}{4W^2}+\frac{1}{2\pi^2}+\frac{\cos\left(\pi t/W\right)}{2\pi^2}\right]
\end{aligned} \qquad (D.31)$$

Hence,

$$\begin{aligned}
E\left(UV\right)&=\frac{\sigma_n^4}{4W^2}\left(\frac{2}{3}+\frac{5}{4\pi^2}\right)+2\sigma_n^4\int_{-W}^{W}\frac{1}{4W^2}\left[\frac{1}{2W}+\frac{\cos\left(\pi t/W\right)}{2W}\right]\left[\frac{3}{4}-\frac{t^2}{4W^2}+\frac{1}{2\pi^2}+\frac{\cos\left(\pi t/W\right)}{2\pi^2}\right]^2 dt\\
&=\frac{\sigma_n^4}{4W^2}\left(\frac{2}{3}+\frac{5}{4\pi^2}\right)+\frac{\sigma_n^4}{4W^2}\left(\frac{9}{10}+\frac{3}{\pi^2}+\frac{49}{8\pi^4}\right)\\
&=\frac{\sigma_n^4}{4W^2}\left(\frac{47}{30}+\frac{17}{4\pi^2}+\frac{49}{8\pi^4}\right)
\end{aligned} \qquad (D.32)$$

In addition,

$$
\begin{aligned}
E\left(U-V\right) &= \sigma_n^2\left[\int_\tau h(\tau)g(\tau)d\tau - \int_\tau \left(h*g\right)^2(\tau)d\tau\right] \\
&= \sigma_n^2\left\{\frac{1}{2W} - 2\int_{-2W}^{0}\left[\frac{t}{4W^2}+\frac{1}{2W}-\frac{\sin\left(\pi t/W\right)}{4\pi W}\right]^2 dt\right\}. \\
&= \sigma_n^2\left(\frac{1}{2W}-\frac{1}{3W}-\frac{5}{8\pi^2 W}\right) \\
&= \frac{\sigma_n^2}{6W}-\frac{5\sigma_n^2}{8\pi^2 W}
\end{aligned}
\tag{D.33}
$$

So,

$$
\begin{aligned}
D^2\left(\hat{y}_n(t)\right) &= \left(2+\frac{3}{\pi^2}\right)\frac{\sigma_n^4}{4W^2}+\frac{\sigma_n^4}{3W^2}+\frac{5\sigma_n^4}{4\pi^2W^2}+\frac{75\sigma_n^4}{64\pi^4W^2} \\
&\quad -2\times\left[\frac{\sigma_n^4}{4W^2}\left(\frac{47}{30}+\frac{17}{4\pi^2}+\frac{49}{8\pi^4}\right)\right]-\left(\frac{\sigma_n^2}{6W}-\frac{5\sigma_n^2}{8\pi^2W}\right)^2. \\
&= \frac{\sigma_n^4}{45W^2}+\frac{\sigma_n^4}{12\pi^2W^2}-\frac{73\sigma_n^4}{32\pi^4W^2}
\end{aligned}
\tag{D.34}
$$

Therefore, for the observation window function $g_3(t)=\dfrac{1+\cos\left(\pi t/W\right)}{2W}$, the output SNR of the NSM operator is given by

$$
\Sigma_{\mathrm{NSM},3} = \frac{A^2\cdot\left(\frac{1}{12}-\frac{1}{2\pi^2}\right)}{\sqrt{\frac{\sigma_n^4}{45W^2}+\frac{\sigma_n^4}{12\pi^2W^2}-\frac{73\sigma_n^4}{32\pi^4W^2}}} \approx 0.19\left(\frac{A}{\sigma_n}\right)^2(2W). \tag{D.35}
$$

Bibliographies

[Ajmera *et al.*, 2004] J. Ajmera, L. McCowan, and H. Bourlard, "Robust Speaker Change Detection," *IEEE Signal Processing Letters,* vol. 11, no. 8, pp. 649-651, Aug, 2004.

[Al-Assaf, 2006] Y. Al-Assaf, "Surface Myoelectric Signal Analysis: Dynamic Approaches for Change Detection and Classification," *IEEE Transactions on Biomedical Engineering,* vol. 53, no. 11, pp. 2248-2256, Nov, 2006.

[Alexander *et al.*, 2007] A. L. Alexander, J. E. Lee, M. Lazar, and A. S. Field, "Diffusion Tensor Imaging of the Brain," *Neurotherapeutics,* vol. 4, no. 3, pp. 316-329, Jul, 2007.

[Arsigny *et al.*, 2006] V. Arsigny, P. Fillard, X. Pennec, and N. Ayache, "Log-Euclidean Metrics for Fast and Simple Calculus on Diffusion Tensors," *Magnetic Resonance in Medicine,* vol. 56, no. 2, pp. 411-421, Aug, 2006.

[Assaf *et al.*, 2008] Y. Assaf, and O. Pasternak, "Diffusion Tensor Imaging (Dti)-Based White Matter Mapping in Brain Research: A Review," *Journal of Molecular Neuroscience,* vol. 34, no. 1, pp. 51-61, Jan, 2008.

[Bamber *et al.*, 1980] J. C. Bamber, and R. J. Dickinsont, "Ultrasonic B-Scanning: A Computer Simulation," *Phys. Med. Biol.,* vol. 25, no. 3, pp. 463-479, 1980.

[Barcelos *et al.*, 2003] C. A. Z. Barcelos, M. Boaventura, and E. C. Silva, "A Well-Balanced Flow Equation for Noise Removal and Edge Detection," *IEEE Transactions on Image Processing,* vol. 12, no. 7, pp. 751-763, Jul, 2003.

[Basser *et al.*, 1994] P. J. Basser, J. Mattiello, and D. Lebihan, "Mr Diffusion Tensor Spectroscopy and Imaging," *Biophysical Journal,* vol. 66, no. 1, pp. 259-267, Jan, 1994.

[Basser *et al.*, 2000] P. J. Basser, and S. Pajevic, "Statistical Artifacts in Diffusion Tensor Mri (Dt-Mri) Caused by Background Noise," *Magnetic Resonance in Medicine,* vol. 44, no. 1, pp. 41-50, Jul, 2000.

[Basser *et al.*, 1996] P. J. Basser, and C. Pierpaoli, "Microstructural and Physiological Features of Tissues Elucidated by Quantitative-Diffusion-Tensor Mri," *Journal of Magnetic Resonance Series B,* vol. 111, no. 3, pp. 209-219, Jun, 1996.

[Batchelor *et al.*, 2005] P. G. Batchelor, M. Moakher, D. Atkinson, F. Calamante, and A. Connelly, "A Rigorous Framework for Diffusion Tensor Calculus," *Magnetic Resonance in Medicine,* vol. 53, no. 1, pp. 221-225, Jan, 2005.

[Bouda *et al.*, 2008] B. Bouda, L. Masmoudi, and D. Aboutajdine, "Cvvefm: Cubical Voxels and Virtual Electric Field Model for Edge Detection in Color Images," *Signal Processing,* vol. 88, no. 4, pp. 905-915, Apr, 2008.

[Bronshtein *et al.*, 2007] I. N. Bronshtein, K. A. Semendyayev, G.Musiol, and H.Muehlig, *Handbook of Mathematics*, Berlin heidelberg New York: Springer, 2007.

[Burgeth *et al.*, 2007] B. Burgeth, S. Didas, L. Florack, and J. Weickert, "A Generic Approach to Diffusion Filtering of Matrix-Fields," *Computing,* vol. 81, no. 2-3, pp. 179-197, Nov, 2007.

[Burgeth *et al.*, 2011] B. Burgeth, L. Pizarro, M. Breuss, and J. Weickert, "Adaptive Continuous-Scale Morphology for Matrix Fields," *International Journal of Computer Vision,* vol. 92, no. 2, pp. 146-161, Apr, 2011.

[Canny, 1986] J. Canny, "A Computational Approach to Edge Detection," *IEEE Transactions on Pattern Analysis and Machine Intelligence,* vol. 8, no. 6, pp. 679-698, Nov, 1986.

[Caselles *et al.*, 1993] V. Caselles, F. Catte, T. Coll, and F. Dibos, "A Geometric Model for Active Contours in Image-Processing," *Numerische Mathematik,* vol. 66, no. 1, pp. 1-31, Oct, 1993.

[Castano-Moraga *et al.*, 2007] C. A. Castano-Moraga, C. Lenglet, R. Deriche, and J. Ruiz-Alzola, "A Riemannian Approach to Anisotropic Filtering of Tensor Fields," *Signal Processing,* vol. 87, no. 2, pp. 263-276, Feb, 2007.

[Chan *et al.*, 2001] T. F. Chan, and L. A. Vese, "Active Contours without Edges," *IEEE Transactions on Image Processing*, vol. 10, no. 2, pp. 266-277, Feb, 2001.
[Chelani, 2011] A. B. Chelani, "Change Detection Using Cusum and Modified Cusum Method in Air Pollutant Concentrations at Traffic Site in Delhi," *Stochastic Environmental Research and Risk Assessment*, vol. 25, no. 6, pp. 827-834, Aug, 2011.
[Chen *et al.*, 2005] B. Chen, and E. W. Hsu, "Noise Removal in Magnetic Resonance Diffusion Tensor Imaging," *Magnetic Resonance in Medicine*, vol. 54, no. 2, pp. 393-401, Aug, 2005.
[Chen *et al.*, 1998] S. Chen, and P. Gopalakrishnan, "Speaker, Environment and Channel Change Detection and Clustering Via the Bayesian Information Criterion." p. 8.
[Chen, 2008] T. Chen, "Derivative Operator on Smoothed Images," *Image Processing: Algorithms and Systems Vi*, Proceedings of Spie, 2008.
[Cheng *et al.*, 2010] S. S. Cheng, H. M. Wang, and H. C. Fu, "Bic-Based Speaker Segmentation Using Divide-and-Conquer Strategies with Application to Speaker Diarization," *IEEE Transactions on Audio Speech and Language Processing*, vol. 18, no. 1, pp. 141-157, Jan, 2010.
[Chou *et al.*, 2009] H. F. Chou, and L. Younes, "Smoothing Directional Vector Fields Using Dual Norms," *Siam Journal on Imaging Sciences*, vol. 2, no. 1, pp. 41-63, 2009.
[Chuang *et al.*, 1993] E. R. Chuang, and D. Sher, "Chi 2 Test for Feature Detection," *Pattern Recognition*, vol. 26, no. 11, pp. 1673-1681, Nov., 1993.
[Coulon *et al.*, 2004] O. Coulon, D. C. Alexander, and S. Arridge, "Diffusion Tensor Magnetic Resonance Image Regularization," *Medical Image Analysis*, vol. 8, no. 1, pp. 47-67, Mar, 2004.
[Delacourt *et al.*, 2000] P. Delacourt, and C. J. Wellekens, "Distbic: A Speaker-Based Segmentation for Audio Data Indexing," *Speech Communication*, vol. 32, no. 1-2, pp. 111-126, Sep, 2000.
[Demirci, 2007] R. Demirci, "Similarity Relation Matrix-Based Color Edge Detection," *Aeu-International Journal of Electronics and Communications*, vol. 61, no. 7, pp. 469-477, 2007.
[Desobry *et al.*, 2005] F. Desobry, M. Davy, and C. Doncarli, "An Online Kernel Change Detection Algorithm," *IEEE Transactions on Signal Processing*, vol. 53, no. 8, pp. 2961-2974, Aug, 2005.
[Ding *et al.*, 2005] Z. H. Ding, J. C. Gore, and A. W. Anderson, "Reduction of Noise in Diffusion Tensor Images Using Anisotropic Smoothing," *Magnetic Resonance in Medicine*, vol. 53, no. 2, pp. 485-490, Feb, 2005.
[Direkoglu *et al.*, 2011] C. Direkoglu, and M. S. Nixon, "Moving-Edge Detection Via Heat Flow Analogy," *Pattern Recognition Letters*, vol. 32, no. 2, pp. 270-279, Jan 15, 2011.
[Elad, 2002] M. Elad, "On the Origin of the Bilateral Filter and Ways to Improve It," *IEEE Transactions on Image Processing*, vol. 11, no. 10, pp. 1141-1151, Oct, 2002.
[Ensign *et al.*, 2010] D. L. Ensign, and V. S. Pande, "Bayesian Detection of Intensity Changes in Single Molecule and Molecular Dynamics Trajectories," *Journal of Physical Chemistry B*, vol. 114, no. 1, pp. 280-292, Jan, 2010.
[Eyal *et al.*, 2012] E. Eyal, M. Shapiro-Feinberg, E. Furman-Haran, D. Grobgeld, T. Golan, Y. Itzchak, R. Catane, M. Papa, and H. Degani, "Parametric Diffusion Tensor Imaging of the Breast," *Investigative Radiology*, vol. 47, no. 5, pp. 284-291, May, 2012.
[Frindel *et al.*, 2009] C. Frindel, M. Robini, P. Croisille, and Y. M. Zhu, "Comparison of Regularization Methods for Human Cardiac Diffusion Tensor Mri," *Medical Image Analysis*, vol. 13, no. 3, pp. 405-418, Jun, 2009.
[Gao *et al.*, 2011] X. Gao, B. Wang, D. Tao, and X. Li, "A Relay Level Set Method for Automatic Image Segmentation," *IEEE Transactions on Systems Man and Cybernetics Part B-Cybernetics*, vol. 41, no. 2, pp. 518-525, Apr, 2011.
[Gish *et al.*, 1994] H. Gish, and M. Schmidt, "Text-Independent Speaker Identification," *IEEE Signal Processing Magazine*, vol. 11, no. 4, pp. 18-32, Oct, 1994.
[Gonzalez *et al.*, 2002] R. C. Gonzalez, and R. E. Woods, *Digital Image Processing, 2nd Ed.*, pp. 568–584: Prentice Hall, 2002.
[Grazzini *et al.*, 2009] J. Grazzini, and P. Soille, "Edge-Preserving Smoothing Using a Similarity Measure in Adaptive Geodesic Neighbourhoods," *Pattern Recognition*, vol. 42, no. 10, pp. 2306-2316, Oct, 2009.

[Guo *et al.*, 2008] W. H. Guo, Y. M. Chen, and Q. G. Zeng, "A Geometric Flow-Based Approach for Diffusion Tensor Image Segmentation," *Philosophical Transactions of the Royal Society a-Mathematical Physical and Engineering Sciences,* vol. 366, no. 1874, pp. 2279-2292, Jul, 2008.

[Hamarnesh *et al.*, 2007] G. Hamarnesh, and J. Hradsky, "Bilateral Filtering of Diffusion Tensor Magnetic Resonance Images," *IEEE Transactions on Image Processing,* vol. 16, no. 10, pp. 2463-2475, Oct, 2007.

[Heric *et al.*, 2007] D. Heric, and D. Zazula, "Combined Edge Detection Using Wavelet Transform and Signal Registration," *Image and Vision Computing,* vol. 25, no. 5, pp. 652-662, May 1, 2007.

[Hou *et al.*, 2003] Z. J. Hou, and T. S. Koh, "Robust Edge Detection," *Pattern Recognition,* vol. 36, no. 9, pp. 2083-2091, Sep, 2003.

[Huang *et al.*, 2005] C. C. Huang, J. F. Wang, and D. J. Wu, "Automatic Scene Change Detection for Composed Speech and Music Sound under Low Snr Noisy Environment," *IEEE Transactions on Speech and Audio Processing,* vol. 13, no. 5, pp. 689-699, Sep, 2005.

[Huang *et al.*, 2006] R. Q. Huang, and J. H. L. Hansen, "Advances in Unsupervised Audio Classification and Segmentation for the Broadcast News and Ngsw Corpora," *IEEE Transactions on Audio Speech and Language Processing,* vol. 14, no. 3, pp. 907-919, May, 2006.

[Jähne, 1997] B. Jähne, *Digital Image Processing: Concepts, Algorthms, and Scientific Applications, Fourth Ed.*, Berlin: Springer, 1997.

[Jones *et al.*, 2004] D. K. Jones, and P. J. Basser, ""Squashing Peanuts and Smashing Pumpkins": How Noise Distorts Diffusion-Weighted Mr Data," *Magnetic Resonance in Medicine,* vol. 52, no. 5, pp. 979-993, Nov, 2004.

[Kawaguchi *et al.*, 2003] T. Kawaguchi, and M. Rizon, "Iris Detection Using Intensity and Edge Information," *Pattern Recognition,* vol. 36, no. 2, pp. 549-562, Feb, 2003.

[Ke *et al.*, 2011] W. Ke, X. Pengfeng, F. Xuezhi, and W. Guiping, "Image Feature Detection from Phase Congruency Based on Two-Dimensional Hilbert Transform," *Pattern Recognition Letters,* vol. 32, no. 15, pp. 2015-2024, 1 Nov., 2011.

[Khalil *et al.*, 2000] M. Khalil, and J. Duchene, "Uterine Emc Analysis: A Dynamic Approach for Change Detection and Classification," *IEEE Transactions on Biomedical Engineering,* vol. 47, no. 6, pp. 748-756, Jun, 2000.

[Kim *et al.*, 2004] D. S. Kim, W. H. Lee, and I. S. Kweon, "Automatic Edge Detection Using 3 X 3 Ideal Binary Pixel Patterns and Fuzzy-Based Edge Thresholding," *Pattern Recognition Letters,* vol. 25, no. 1, pp. 101-106, Jan 5, 2004.

[Kingsley, 2006] P. B. Kingsley, "Introduction to Diffusion Tensor Imaging Mathematics: Part Ii. Anisotropy, Diffusion-Weighting Factors, and Gradient Encoding Schemes," *Concepts in Magnetic Resonance Part A,* vol. 28A, no. 2, pp. 123-154, Mar, 2006.

[Konishi *et al.*, 2003a] S. Konishi, A. Yuille, and J. Coughlan, "A Statistical Approach to Multi-Scale Edge Detection," *Image and Vision Computing,* vol. 21, no. 1, pp. 37-48, Jan 10, 2003a.

[Konishi *et al.*, 2003b] S. Konishi, A. L. Yuille, J. M. Coughlan, and S. C. Zhu, "Statistical Edge Detection: Learning and Evaluating Edge Cues," *IEEE Transactions on Pattern Analysis and Machine Intelligence,* vol. 25, no. 1, pp. 57-74, Jan, 2003b.

[Kovesi, 2000] P. Kovesi, "Phase Congruency: A Low-Level Image Invariant," *Psychological Research-Psychologische Forschung,* vol. 64, no. 2, pp. 136-148, Dec, 2000.

[Kuncheva, 2013] L. I. Kuncheva, "Change Detection in Streaming Multivariate Data Using Likelihood Detectors," *IEEE Transactions on Knowledge and Data Engineering,* vol. 25, no. 5, pp. 1175-1180, May, 2013.

[Kuo *et al.*, 2007] C. T. Kuo, and S. C. Cheng, "Fusion of Color Edge Detection and Color Quantization for Color Image Watermarking Using Principal Axes Analysis," *Pattern Recognition,* vol. 40, no. 12, pp. 3691-3704, Dec, 2007.

[La Rosa *et al.*, 2008] P. S. La Rosa, A. Nehorai, H. Eswaran, C. L. Lowery, and H. Preissi, "Detection of Uterine Mmg Contractions Using a Multiple Change Point-Estimator and the K-Means Cluster Algorithm," *IEEE Transactions on Biomedical Engineering,* vol. 55, no. 2, pp. 453-467, Feb, 2008.

[Laligant *et al.*, 2010] O. Laligant, and F. Truchetet, "A Nonlinear Derivative Scheme Applied to Edge Detection," *IEEE Transactions on Pattern Analysis and Machine Intelligence,* vol. 32, no. 2, pp. 242-257, Feb, 2010.

[Laurent *et al.*, 1998] H. Laurent, and C. Doncarli, "Stationarity Index for Abrupt Changes Detection in the Time-Frequency Plane," *IEEE Signal Processing Letters,* vol. 5, no. 2, pp. 43-45, Feb, 1998.

[Lavielle, 1999] M. Lavielle, "Detection of Multiple Changes in a Sequence of Dependent Variables," *Stochastic Processes and Their Applications,* vol. 83, no. 1, pp. 79-102, Sep, 1999.

[Lavielle, 2005] M. Lavielle, "Using Penalized Contrasts for the Change-Point Problem," *Signal Processing,* vol. 85, no. 8, pp. 1501-1510, Aug, 2005.

[Law *et al.*, 2007] M. W. K. Law, and A. C. S. Chung, "Weighted Local Variance-Based Edge Detection and Its Application to Vascular Segmentation in Magnetic Resonance Angiography," *IEEE Transactions on Medical Imaging,* vol. 26, no. 9, pp. 1224-1241, Sep, 2007.

[Lebarbier, 2005] E. Lebarbier, "Detecting Multiple Change-Points in the Mean of Gaussian Process by Model Selection," *Signal Processing,* vol. 85, no. 4, pp. 717-736, Apr, 2005.

[Lenglet *et al.*, 2006a] C. Lenglet, and M. Rousson, "Dti Segmentation by Statistical Surface Evolution," *IEEE Transactions on Medical Imaging,* vol. 25, no. 6, pp. 685-700, Jun, 2006a.

[Lenglet *et al.*, 2006b] C. Lenglet, M. Rousson, R. Deriche, and O. Faugeras, "Statistics on the Manifold of Multivariate Normal Distributions: Theory and Application to Diffusion Tensor Mri Processing," *Journal of Mathematical Imaging and Vision,* vol. 25, no. 3, pp. 423-444, Oct, 2006b.

[Lerallut *et al.*, 2007] R. Lerallut, E. Decenciere, and F. Meyer, "Image Filtering Using Morphological Amoebas," *Image and Vision Computing,* vol. 25, no. 4, pp. 395-404, Apr, 2007.

[Li *et al.*, 2010] C. M. Li, C. Y. Xu, C. F. Gui, and M. D. Fox, "Distance Regularized Level Set Evolution and Its Application to Image Segmentation," *IEEE Transactions on Image Processing,* vol. 19, no. 12, pp. 3243-3254, Dec, 2010.

[Liu *et al.*, 2012] S. Liu, M. Yamada, N. Collier, and M. Sugiyama, "Change-Point Detection in Time-Series Data by Relative Density-Ratio Estimation," *Lecture Notes in Computer Science (including subseries Lecture Notes in Artificial Intelligence and Lecture Notes in Bioinformatics).* pp. 363-372.

[Liu, 1994] W. Y. Liu, "Detection De Rupture Par Mesure De Non Stationnarite Locale: Application a La Segmentation De Signaux Multidimensionnels," Institut National des Sciences Appliquées (INSA), 1994.

[Liu *et al.*, 1993a] W. Y. Liu, I. Dautraix-Ricard, I. E. Magnin, and G. Gimenez, "A Statistic Based Preprocessing Technique for Ultrasonic Stereoechography," in Int. Conf. on Signal Processing' 93, Beijing, P.R. China, 1993a, pp. 916–919.

[Liu *et al.*, 1992] W. Y. Liu, I. E. Magnin, and G. Gimenez, "A Statistic Based Approach for Segmentation," in Conf Proc IEEE Eng Med Biol Soc, Paris, France, 1992, pp. 1924–1925.

[Liu *et al.*, 1993b] W. Y. Liu, I. E. Magnin, and G. Gimenez, "A New Approach for the Segmentation of Stochastic Processes," in Int. Conf. on Signal Processing' 93, Beijing, P.R. China, 1993b, pp. 584–587.

[Liu *et al.*, 1995] W. Y. Liu, I. E. Magnin, and G. Gimenez, "Un Nouvel Opérateur Pour La Détection De Rupture Dans Des Signaux Bruités," *Traitement du Signal,* vol. 12, no. 3, pp. 226-236, 1995.

[Lombaert *et al.*, 2012] H. Lombaert, J. M. Peyrat, P. Croisille, S. Rapacchi, L. Fanton, F. Cheriet, P. Clarysse, I. Magnin, H. Delingette, and N. Ayache, "Human Atlas of the Cardiac Fiber Architecture: Study on a Healthy Population," *IEEE Transactions on Medical Imaging,* vol. 31, no. 7, pp. 1436-1447, Jul, 2012.

[Lopez-Molina *et al.*, 2010] C. Lopez-Molina, H. Bustince, J. Fernandez, P. Couto, and B. De Baets, "A Gravitational Approach to Edge Detection Based on Triangular Norms," *Pattern Recognition,* vol. 43, no. 11, pp. 3730-3741, Nov, 2010.

[Lopez-Molina *et al.*, 2011] C. Lopez-Molina, B. De Baets, and H. Bustince, "Generating Fuzzy Edge Images from Gradient Magnitudes," *Computer Vision and Image Understanding,* vol. 115, no. 11, pp. 1571-1580, Nov, 2011.

[Lukac *et al.*, 2007] R. Lukac, and K. N. Plataniotis, "Vector Edge Operators for Cdna Microarray Spot Localization," *Computerized Medical Imaging and Graphics,* vol. 31, no. 7, pp. 510-522, Oct, 2007.

[Malcolm *et al.*, 2007] J. Malcolm, Y. Rathi, and A. Tannenbaum, "A Graph Cut Approach to Image Segmentation in Tensor Space," *IEEE Conference on Computer Vision and Pattern Recognition.* pp. 3096-3103.

[Malegaonkar *et al.*, 2006] A. Malegaonkar, A. Ariyaeeinia, P. Sivakumaran, and J. Fortuna, "Unsupervised Speaker Change Detection Using Probabilistic Pattern Matching," *IEEE Signal Processing Letters,* vol. 13, no. 8, pp. 509-512, Aug, 2006.

[Malegaonkar *et al.*, 2007] A. S. Malegaonkar, A. M. Ariyaeeinia, and P. Sivakumaran, "Efficient Speaker Change Detection Using Adapted Gaussian Mixture Models," *IEEE Transactions on Audio Speech and Language Processing,* vol. 15, no. 6, pp. 1859-1869, Aug, 2007.

[Malladi *et al.*, 1995] R. Malladi, J. A. Sethian, and B. C. Vemuri, "Shape Modeling with Front Propagation - a Level Set Approach," *IEEE Transactions on Pattern Analysis and Machine Intelligence,* vol. 17, no. 2, pp. 158-175, Feb, 1995.

[Mallat, 2009] S. Mallat, *A Wavelet Tour of Signal Processing: The Sparse Way, 3rd Ed.*, p.^pp. 205–262: Academic Press, 2009.

[Mallat *et al.*, 1992] S. Mallat, and S. Zhong, "Characterization of Signals from Multiscale Edges," *IEEE Transactions on Pattern Analysis and Machine Intelligence,* vol. 14, no. 7, pp. 710-732, Jul, 1992.

[Meer *et al.*, 2001] P. Meer, and B. Georgescu, "Edge Detection with Embedded Confidence," *IEEE Transactions on Pattern Analysis and Machine Intelligence,* vol. 23, no. 12, pp. 1351-1365, Dec, 2001.

[Moraschi *et al.*, 2010] M. Moraschi, G. E. Hagberg, M. Di Paola, G. Spalletta, B. Maraviglia, and F. Giove, "Smoothing That Does Not Blur: Effects of the Anisotropic Approach for Evaluating Diffusion Tensor Imaging Data in the Clinic," *Journal of Magnetic Resonance Imaging,* vol. 31, no. 3, pp. 690-697, Mar, 2010.

[Morrone *et al.*, 1988] M. C. Morrone, and D. C. Burr, "Feature Detection in Human Vision: A Phase Dependent Energy Model," *Proc. R. Soc. Lond. B, Biol. Sci. 235,* vol. 1280, pp. 221-245, 1988.

[Morrone *et al.*, 1987] M. C. Morrone, and R. A. Owens, "Feature Detection from Local Energy," *Pattern Recognition Letters,* vol. 6, no. 5, pp. 303-313, Dec, 1987.

[Morrone *et al.*, 1986] M. C. Morrone, J. Ross, D. C. Burr, and R. Owens, "Mach Bands Are Phase Dependent," *Nature,* vol. 324, no. 6094, pp. 250-253, Nov, 1986.

[Nes, 2012] P. G. Nes, "Fast Multi-Scale Edge-Detection in Medical Ultrasound Signals," *Signal Processing,* vol. 92, no. 10, pp. 2394-2408, Oct, 2012.

[Noble *et al.*, 2006] J. A. Noble, and D. Boukerroui, "Ultrasound Image Segmentation: A Survey," *IEEE Transactions on Medical Imaging,* vol. 25, no. 8, pp. 987-1010, Aug, 2006.

[Notohamiprodjo *et al.*, 2008] M. Notohamiprodjo, C. Glaser, K. A. Herrmann, O. Dietrich, U. I. Attenberger, M. F. Reiser, S. O. Schoenberg, and H. J. Michaely, "Diffusion Tensor Imaging of the Kidney with Parallel Imaging: Initial Clinical Experience," *Investigative Radiology,* vol. 43, no. 10, pp. 677-685, Oct, 2008.

[Pal *et al.*, 1993] N. R. Pal, and S. K. Pal, "A Review on Image Segmentation Techniques," *Pattern Recognition,* vol. 26, no. 9, pp. 1277-1294, Sep, 1993.

[Paris *et al.*, 2008] S. Paris, P. Kornprobst, J. Tumblin, and F. Durand, "Bilateral Filtering: Theory and Applications," *Foundations and Trends in Computer Graphics and Vision,* vol. 4, no. 1, pp. 1-73, 2008.

[Park *et al.*, 1995] D. J. Park, K. M. Nam, and R. H. Park, "Multiresolution Edge Detection Techniques," *Pattern Recognition,* vol. 28, no. 2, pp. 211-229, Feb, 1995.

[Parker *et al.*, 2000] G. J. M. Parker, J. A. Schnabel, M. R. Symms, D. J. Werring, and G. J. Barker, "Nonlinear Smoothing for Reduction of Systematic and Random Errors in Diffusion Tensor Imaging," *Journal of Magnetic Resonance Imaging,* vol. 11, no. 6, pp. 702-710, Jun, 2000.

[Pennec *et al.*, 2006] X. Pennec, P. Fillard, and N. Ayache, "A Riemannian Framework for Tensor Computing," *International Journal of Computer Vision,* vol. 66, no. 1, pp. 41-66, Jan, 2006.

[Perona *et al.*, 1990] P. Perona, and J. Malik, "Scale-Space and Edge-Detection Using Anisotropic Diffusion," *IEEE Transactions on Pattern Analysis and Machine Intelligence,* vol. 12, no. 7, pp. 629-639, Jul, 1990.

[Raya *et al.*, 2012] J. G. Raya, A. Horng, O. Dietrich, S. Krasnokutsky, L. S. Beltran, P. Storey, M. F. Reiser, M. P. Recht, D. K. Sodickson, and C. Glaser, "Articular Cartilage: In Vivo Diffusion-Tensor Imaging," *Radiology,* vol. 262, no. 2, pp. 550-559, Feb, 2012.

[Rigaill *et al.*, 2012] G. Rigaill, E. Lebarbier, and S. Robin, "Exact Posterior Distributions and Model Selection Criteria for Multiple Change-Point Detection Problems," *Statistics and Computing,* vol. 22, no. 4, pp. 917-929, Jul, 2012.

[Rousson *et al.*, 2004] M. Rousson, C. Lenglet, and R. Deriche, "Level Set and Region Based Surface Propagation for Diffusion Tensor Mri Segmentation," *Computer Vision and Mathematical Methods in Medical and Biomedical Image Analysis,* Lecture Notes in Computer Science M. Sonka, I. A. Kakadiaris and J. Kybic, eds., pp. 123-134, 2004.

[Saintmarc *et al.*, 1991] P. Saintmarc, J. S. Chen, and G. Medioni, "Adaptive Smoothing - a General Tool for Early Vision," *IEEE Transactions on Pattern Analysis and Machine Intelligence,* vol. 13, no. 6, pp. 514-529, Jun, 1991.

[Scharcanski *et al.*, 1997] J. Scharcanski, and A. N. Venetsanopoulos, "Edge Detection of Color Images Using Directional Operators," *IEEE Transactions on Circuits and Systems for Video Technology,* vol. 7, no. 2, pp. 397-401, Apr, 1997.

[Severo *et al.*, 2006] M. Severo, and J. Gama, "Change Detection with Kalman Filter and Cusum," *Discovery Science, Proceedings,* Lecture Notes in Artificial Intelligence L. Todorovski, N. Lavrac and K. P. Jantke, eds., pp. 243-254, 2006.

[Shacham *et al.*, 2007] O. Shacham, O. Haik, and Y. Yitzhaky, "Blind Restoration of Atmospherically Degraded Images by Automatic Best Step-Edge Detection," *Pattern Recognition Letters,* vol. 28, no. 15, pp. 2094-2103, Nov 1, 2007.

[Shui *et al.*, 2012] P.-L. Shui, and W.-C. Zhang, "Noise-Robust Edge Detector Combining Isotropic and Anisotropic Gaussian Kernels," *Pattern Recognition,* vol. 45, no. 2, pp. 806-820, Feb, 2012.

[Somkantha *et al.*, 2011] K. Somkantha, N. Theera-Umpon, and S. Auephanwiriyakul, "Boundary Detection in Medical Images Using Edge Following Algorithm Based on Intensity Gradient and Texture Gradient Features," *IEEE Transactions on Biomedical Engineering,* vol. 58, no. 3, pp. 567-573, Mar, 2011.

[Struc *et al.*, 2009] V. Struc, and N. Pavesic, "Phase Congruency Features for Palm-Print Verification," *Iet Signal Processing,* vol. 3, no. 4, pp. 258-268, Jul, 2009.

[Sun *et al.*, 2007] G. Sun, Q. Liu, Q. Liu, C. Ji, and X. Li, "A Novel Approach for Edge Detection Based on the Theory of Universal Gravity," *Pattern Recognition,* vol. 40, no. 10, pp. 2766-2775, Oct, 2007.

[Sun *et al.*, 2004] J. X. Sun, D. B. Gu, Y. Z. Chen, and S. Zhang, "A Multiscale Edge Detection Algorithm Based on Wavelet Domain Vector Hidden Markov Tree Model," *Pattern Recognition,* vol. 37, no. 7, pp. 1315-1324, Jul, 2004.

[Tabelow *et al.*, 2008] K. Tabelow, J. Polzehl, V. Spokoiny, and H. U. Voss, "Diffusion Tensor Imaging: Structural Adaptive Smoothing," *Neuroimage,* vol. 39, no. 4, pp. 1763-1773, Feb, 2008.

[Theoharatos *et al.*, 2005] C. Theoharatos, G. Economou, and S. Fotopoulos, "Color Edge Detection Using the Minimal Spanning Tree," *Pattern Recognition,* vol. 38, no. 4, pp. 603-606, Apr, 2005.

[Tomasi *et al.*, 1998] C. Tomasi, and R. Manduchi, "Bilateral Filtering for Gray and Color Images." pp. 839-846.

[Tourneret, 1998] J. Y. Tourneret, "Detection and Estimation of Abrupt Changes Contaminated by Multiplicative Gaussian Noise," *Signal Processing,* vol. 68, no. 3, pp. 259-270, Aug, 1998.

[Trahanias *et al.*, 1993] P. E. Trahanias, and A. N. Venetsanopoulos, "Color Edge Detection Using Vector Order Statistics," *IEEE Transactions on Image Processing,* vol. 2, no. 2, pp. 259-264, Apr, 1993.

[Trahanias *et al.*, 1996] P. E. Trahanias, and A. N. Venetsanopoulos, "Vector Order Statistics Operators as Color Edge Detectors," *IEEE Transactions on Systems Man and Cybernetics Part B-Cybernetics,* vol. 26, no. 1, pp. 135-143, Feb, 1996.

[Vemuri *et al.*, 2001] B. C. Vemuri, Y. Chen, M. Rao, T. McGraw, Z. Wang, and T. Mareci, "Fiber Tract Mapping from Diffusion Tensor Mri," in IEEE Workshop on Variational and Level Set Methods in Computer Vision, Proceedings, 2001, pp. 81-88.

[Vincent Arsigny, 2005] P. F. Vincent Arsigny, Xavier Pennec,Nicholas Ayache, *Fast and Simple Computations on Tensors with Log-Euclidean Metrics*, 5584, Unité de recherche INRIA Sophia Antipolis, 2005.

[Wang *et al.*, 2004a] Z. Wang, A. C. Bovik, H. R. Sheikh, and E. P. Simoncelli, "Image Quality Assessment: From Error Visibility to Structural Similarity," *IEEE Transactions on Image Processing*, vol. 13, no. 4, pp. 600-612, Apr, 2004a.

[Wang *et al.*, 2004b] Z. Z. Wang, and B. C. Vemuri, "Tensor Field Segmentation Using Region Based Active Contour Model," in Computer Vision - Eccv 2004, Pt 4, 2004b, pp. 304-315.

[Wang *et al.*, 2005] Z. Z. Wang, and B. C. Vemuri, "Dti Segmentation Using an Information Theoretic Tensor Dissimilarity Measure," *IEEE Transactions on Medical Imaging*, vol. 24, no. 10, pp. 1267-1277, Oct, 2005.

[Wang *et al.*, 2004c] Z. Z. Wang, B. C. Vemuri, Y. M. Chen, and T. H. Mareci, "A Constrained Variational Principle for Direct Estimation and Smoothing of the Diffusion Tensor Field from Complex Dwi," *IEEE Transactions on Medical Imaging*, vol. 23, no. 8, pp. 930-939, Aug, 2004c.

[Wang *et al.*, 2004d] Z. Z. Wang, B. C. Vemuri, and I. C. Society, "An Affine Invariant Tensor Dissimilarity Measure and Its Applications to Tensor-Valued Image Segmentation," *Proceedings - IEEE Computer Society Conference on Computer Vision and Pattern Recognition.* pp. 228-233.

[Wei *et al.*, 2013a] H. J. Wei, M. Viallon, B. M. A. Delattre, V. M. Pai, H. Wen, H. Xue, C. Guetter, M.-P. Jolly, T. Feiweier, P. Croisille, and Y. M. Zhu, "In Vivo Cardiac Diffusion Tensor Imaging in Free-Breathing Conditions," in Society for Cardiovascular Magnetic Resonance (SCMR) 2013, San Francisco, CA, 2013a, pp. 382-383.

[Wei *et al.*, 2013b] H. J. Wei, M. Viallon, B. M. A. Delattre, V. M. Pai, H. Wen, H. Xue, C. Guetter, M.-P. Jolly, T. Feiweier, P. Croisille, and Y. M. Zhu, "Quantitative Investigation of Cardiac Motion Effects on in-Vivo Diffusion Tensor Parameters: A Simulation Study," in Society for Cardiovascular Magnetic Resonance (SCMR) 2013, San Francisco, CA, 2013b, pp. 397-398.

[Weickert, 1998] J. Weickert, *Anisotropic Diffusion in Image Processing*, B.G. Teubner: Stuttgart, 1998.

[Weickert, 1999] J. Weickert, "Coherence-Enhancing Diffusion Filtering," *International Journal of Computer Vision*, vol. 31, no. 2-3, pp. 111-127, Apr, 1999.

[Welk *et al.*, 2007] M. Welk, J. Weickert, F. Becker, C. Schnorr, C. Feddern, and B. Burgeth, "Median and Related Local Filters for Tensor-Valued Images," *Signal Processing*, vol. 87, no. 2, pp. 291-308, Feb, 2007.

[Wiegell *et al.*, 2003] M. R. Wiegell, D. S. Tuch, H. B. W. Larsson, and V. J. Wedeen, "Automatic Segmentation of Thalamic Nuclei from Diffusion Tensor Magnetic Resonance Imaging," *Neuroimage*, vol. 19, no. 2, pp. 391-401, Jun, 2003.

[Wong *et al.*, 2008] A. Wong, and W. Bishop, "Efficient Least Squares Fusion of Mri and Ct Images Using a Phase Congruency Model," *Pattern Recognition Letters*, vol. 29, no. 3, pp. 173-180, Feb 1, 2008.

[Wu *et al.*, 2009] M. T. Wu, M. Y. M. Su, Y. L. Huang, K. R. Chiou, P. C. Yang, H. B. Pan, T. G. Reese, V. J. Wedeen, and W. Y. I. Tseng, "Sequential Changes of Myocardial Microstructure in Patients Postmyocardial Infarction by Diffusion-Tensor Cardiac Mr Correlation with Left Ventricular Structure and Function," *Circulation-Cardiovascular Imaging*, vol. 2, no. 1, pp. 32-40, Jan, 2009.

[Wu *et al.*, 2006] M. T. Wu, W. Y. I. Tseng, M. Y. M. Su, C. P. Liu, K. R. Chiou, V. J. Wedeen, T. G. Reese, and C. F. Yang, "Diffusion Tensor Magnetic Resonance Imaging Mapping the Fiber Architecture Remodeling in Human Myocardium after Infarction - Correlation with Viability and Wall Motion," *Circulation*, vol. 114, no. 10, pp. 1036-1045, Sep, 2006.

[Xu *et al.*, 2010] Q. Xu, A. W. Anderson, J. C. Gore, and Z. Ding, "Efficient Anisotropic Filtering of Diffusion Tensor Images," *Magnetic Resonance Imaging*, vol. 28, no. 2, pp. 200-211, Feb, 2010.

[Xu *et al.*, 2009a] Q. Xu, A. W. Anderson, J. C. Gore, and Z. H. Ding, "Unified Bundling and Registration of Brain White Matter Fibers," *IEEE Transactions on Medical Imaging*, vol. 28, no. 9, pp. 1399-1411, Sep, 2009a.

[Xu *et al.*, 2009b] X. Xu, Z. Yang, and Y. Wang, "A Method Based on Rank-Ordered Filter to Detect Edges in Cellular Image," *Pattern Recognition Letters*, vol. 30, no. 6, pp. 634-640, Apr 15, 2009b.

[Yang *et al.*, 2012] F. Yang, Y. M. Zhu, I. E. Magnin, J. H. Luo, P. Croisille, and P. B. Kingsley, "Feature-Based Interpolation of Diffusion Tensor Fields and Application to Human Cardiac Dt-Mri," *Medical Image Analysis*, vol. 16, no. 2, pp. 459-481, Feb, 2012.

[Yang *et al.*, 2006] P. Yang, G. Dumont, and J. M. Ansermino, "Adaptive Change Detection in Heart Rate Trend Monitoring in Anesthetized Children," *IEEE Transactions on Biomedical Engineering*, vol. 53, no. 11, pp. 2211-2219, Nov, 2006.

[Yu *et al.*, 2002] Y. J. Yu, and S. T. Acton, "Speckle Reducing Anisotropic Diffusion," *IEEE Transactions on Image Processing*, vol. 11, no. 11, pp. 1260-1270, Nov, 2002.

[Yu *et al.*, 2004] Y. J. Yu, and S. T. Acton, "Edge Detection in Ultrasound Imagery Using the Instantaneous Coefficient of Variation," *IEEE Transactions on Image Processing*, vol. 13, no. 12, pp. 1640-1655, Dec, 2004.

[Zhang *et al.*, 2011] C. Zhang, and J. H. L. Hansen, "Whisper-Island Detection Based on Unsupervised Segmentation with Entropy-Based Speech Feature Processing," *IEEE Transactions on Audio Speech and Language Processing*, vol. 19, no. 4, pp. 883-894, May, 2011.

[Zhang *et al.*, 2012] L. Zhang, L. Zhang, D. Zhang, and Z. Guo, "Phase Congruency Induced Local Features for Finger-Knuckle-Print Recognition," *Pattern Recognition*, vol. 45, no. 7, pp. 2522-2531, Jul, 2012.

[Zhang *et al.*, 2010] W. Zhang, F. Liu, L. Jiao, B. Hou, S. Wang, and R. Shang, "Sar Image Despeckling Using Edge Detection and Feature Clustering in Bandelet Domain," *IEEE Geoscience and Remote Sensing Letters*, vol. 7, no. 1, pp. 131-135, Jan, 2010.

[Zhou *et al.*, 2005] B. W. Zhou, and J. H. L. Hansen, "Efficient Audio Stream Segmentation Via the Combined T(2) Statistic and Bayesian Information Criterion," *IEEE Transactions on Speech and Audio Processing*, vol. 13, no. 4, pp. 467-474, Jul, 2005.

[Zhu *et al.*, 1996] S. C. Zhu, and A. Yuille, "Region Competition: Unifying Snakes, Region Growing, and Bayes/Mdl for Multiband Image Segmentation," *IEEE Transactions on Pattern Analysis and Machine Intelligence*, vol. 18, no. 9, pp. 884-900, Sep, 1996.

FOLIO ADMINISTRATIF

THESE SOUTENUE DEVANT L'INSTITUT NATIONAL DES SCIENCES APPLIQUEES DE LYON

NOM : ZHANG **DATE de SOUTENANCE :** 04/10/2013

Prénoms : Yanli

TITRE : Une mesure de non-stationnarité générale: application en traitement d'images et de signaux biomédicaux

NATURE : Doctorat **Numéro d'ordre :** 2013-ISAL-0090

École doctorale : École Doctorale Électronique, Électrotechnique, Automatique

Spécialité : Image et System

RESUME :

La variation des intensités est souvent exploitée comme une propriété importante du signal ou de l'image par les algorithmes de traitement. La grandeur permettant de représenter et de quantifier cette variation d'intensité est appelée « mesure de changement », elle est couramment employée dans les méthodes de détection de ruptures d'un signal, en détection de contours d'une image, dans les modèles de segmentation basés sur les contours, et dans les méthodes de lissage d'images avec préservation de discontinuités.

En traitement des images et des signaux biomédicaux, les mesures de changement existantes fournissent des résultats peu précis lorsque le signal ou l'image présentent un fort niveau de bruit ou un fort caractère aléatoire, ce qui conduit à des artefacts indésirables dans le résultat des méthodes basées sur la mesure de changement. D'autre part, de nouvelles techniques d'imagerie médicale produisent de nouveaux types de données dites à valeurs multiples, qui nécessitent le développement de mesures de changement adaptées. Mesurer le changement dans des données de tenseur pose alors de nouveaux problèmes.

Dans ce contexte, une mesure de changement, appelée « mesure de non-stationnarité (NSM) », est améliorée et étendue pour permettre de mesurer la non-stationnarité de signaux multidimensionnels quelconques (scalaires, vectoriels, tensoriels) par rapport à un paramètre statistique, ce qui en fait ainsi une mesure générique et robuste.

Une méthode de détection de changements basée sur la NSM et une méthode de détection de contours basée sur la NSM sont respectivement proposées et appliquées aux signaux ECG et EEG, ainsi qu'a des images cardiaques pondérées en diffusion (DW). Les résultats expérimentaux montrent que les méthodes de détection basées sur la NSM permettent de fournir la position précise des points de changement et des contours des structures tout en réduisant efficacement les fausses détections.

Un modèle de contour actif géométrique basé sur la NSM (NSM-GAC) est proposé et appliqué pour segmenter des images échographiques de la carotide. Les résultats de segmentation montrent que le modèle NSM-GAC permet d'obtenir de meilleurs résultats comparativement aux outils existants avec moins d'itérations et un temps de calcul plus faible tout en réduisant les faux contours et les ponts.

Enfin, et plus important encore, une nouvelle approche de lissage préservant les caractéristiques locales, appelée filtrage adaptatif de non-stationnarité (NAF), est proposée et appliquée pour améliorer les images DW cardiaques. Les résultats expérimentaux montrent que la méthode proposée peut atteindre un meilleur compromis entre le lissage des régions homogènes et la préservation des caractéristiques désirées telles que les bords ou frontières, ce qui conduit à des champs de tenseurs plus homogènes et par conséquent à des fibres cardiaques reconstruites plus cohérentes.

Laboratoire (s) de recherche :

Creatis (CNRS UMR 5520, INSERM U1044)

Directeur de thèse : Isabelle Magnin, Wan-Yu Liu, Yue-Min Zhu

Président de jury : Jin LI

Composition du jury : Jean-Marc CHASSERY, Isabelle E. MAGNIN, Yue-Min ZHU, Jin LI, Ping LI, Wan-Yu LIU